THE UNIVERSITY *of* EDINBURGH

This thesis has been submitted in fulfilment of the requirements for a postgraduate degree (e.g. PhD, MPhil, DClinPsychol) at the University of Edinburgh. Please note the following terms and conditions of use:

This work is protected by copyright and other intellectual property rights, which are retained by the thesis author, unless otherwise stated.
A copy can be downloaded for personal non-commercial research or study, without prior permission or charge.
This thesis cannot be reproduced or quoted extensively from without first obtaining permission in writing from the author.
The content must not be changed in any way or sold commercially in any format or medium without the formal permission of the author.
When referring to this work, full bibliographic details including the author, title, awarding institution and date of the thesis must be given.

Cell cycle regulation of microtubule nucleation in fission yeast *Schizosaccharomyces pombe*

Weronika Ewa Borek

Doctor of Philosophy
The University of Edinburgh
September 2013

Acknowledgments

First, I would like to thank my supervisor Ken Sawin for having me in the lab. I am very grateful for his guidance, patience, and infinite curiosity and enthusiasm that were invaluable to my PhD research and development as a scientist. I am also very grateful to past and present members of Sawin lab: Hilary Snaith, Andreas Anders, Itaru Samejima, Lynda Groocock, Claudia Bicho, Vicky Miller, Su Ling Leong, Xun Bao, Sanju Ashraf, Eric Lynch, Delyan Mutavchiev and Harish Thakur for the helpful discussion and advice.

I am grateful to CR UK for the financial support and the opportunity to communicate my research to CR UK fundraisers.

During my project, I have been privileged to supervise Christian Wiggam (University of Edinburgh), and his work contributed directly to the research presented in this thesis.

I would also like to thank the groups of Adele Marston, Julie Welburn, Kevin Hardwick and Hiro Okura, with whom I had the opportunity to discuss my research. During my PhD, I collaborated with the Juri Rappsilber group, and I am grateful to him for the opportunity to learn about mass spectrometry, and to Juan Zou for sample processing.

I am very grateful to David Kelly for his help with the microscopy and for cheering me up while I spent hours in COIL. I also need to thank Alastair Kerr for help with the statistics.

Finally, I am very grateful to my family and friends who supported me over these years. These include several people living their lives in the Swann Building as well as many non-scientists. Mamo, bardzo Ci dziękuję za wszystko. Dziękuję też mojemu rodzeństwu (w liczbie trzech) i przyjaciołom, za wsparcie, wspólnie spędzony czas, wycieczki, imprezy i rozmowy do świtu. Dziękuję Ci, Paweł, za wsparcie przez te wszystkie lata. I wam wszystkim za to, że czasem potrafiłam po prostu zapomnieć o laboratorium i tym moim naukowym życiu, i mieć potem więcej siły, żeby się z nim zmagać.

Declaration

I declare that this thesis has been composed by myself and the research presented is my own original work. Where other individuals have made contributions, this has been clearly stated within the text.

Weronika Borek

Abstract

In fission yeast, microtubule (MT) nucleation is regulated in space and time. In interphase, MTs are nucleated in the cytoplasm to regulate cell polarity, whereas in mitosis, nucleation takes place inside the nucleus to form a mitotic spindle. We hypothesize that several non-exclusive mechanisms may be responsible for this differential regulation of MT nucleation.

Two fission yeast proteins, Mto1 and Pcp1, are involved in MT nucleation in interphase and mitosis, respectively. These proteins share a sequence motif, called CM1 that is responsible for interaction with the γ-tubulin complex (γ-TuC). In the first part of my project, I tested whether sequence differences between Mto1 and Pcp1 CM1 regions contribute to the differential regulation of MT nucleation in interphase vs. mitosis. I showed that the two CM1 regions are interchangeable and play no role in differential regulation of Mto1 and Pcp1. By generating Pcp1-9A1 mutant, where conserved residues within the Pcp1 CM1 region was replaced with alanines, I showed that Pcp1 CM1 region is required for its function. Moreover, using CM1 regions from two human proteins that are implicated in schizophrenia and microcephaly development, MMGL and CDK5RAP2, I showed that human CM1 domains could rescue yeast protein function, demonstrating that the CM1 region is conserved across evolution.

In the second part of my project, I focused on regulation of cytoplasmic MT nucleation. In fission yeast, cytoplasmic MT nucleation occurs from several distinct sites in the cell and is promoted by the Mto1/2 complex. The Mto1/2 complex is composed of multiple copies of Mto1 and Mto2 and interacts with the γ-TuC. Disruption of the interaction of Mto1/2 with the γ-TuC, or of the Mto1-Mto2 interaction, results in a complete loss of interphase cytoplasmic nucleation. As cells enter mitosis, Mto2 is hyperphosphorylated, and the Mto1-Mto2 interaction is disrupted, leading to abolishment of cytoplasmic nucleation. This led to a hypothesis that Mto2 phosphorylation regulated the Mto1/2 complex mitotic disassembly. I showed that Mto2 phosphorylation is used to control levels of cytoplasmic nucleation in both interphase and mitosis. During interphase, I found that Mto2 is phosphorylated in order to reduce levels of MT nucleation. When Mto2 phosphorylation is prevented by mutation of phosphorylatable residues to alanines, Mto1/2 mutant complexes show a more robust interaction with the γ-TuC, and more

MTs are nucleated in the cytoplasm. During mitosis, hyperphosphorylation of Mto2 plays a role in the disassembly of Mto1/2 complexes. In particular, while the interaction of wild-type Mto2 with Mto1 is disrupted during mitosis, Mto2-alanine mutants, in which phosphorylation was nearly abolished, are still able to interact with Mto1 in mitosis. Interestingly, Mto1/2 complexes containing Mto2-alanine mutants are still disassembled in mitosis by disruption of Mto2 self-interaction.

I used SILAC phosphoproteomics to show that Mto2-alanine is still phosphorylated in mitosis, suggesting the Mto2 self-interaction might also be controlled by phosphorylation. While doing so, I developed a novel SILAC quantification method that is particularly useful for quantification of multiply phosphorylated proteins and peptides. Using data obtained by SILAC, I generated additional Mto2 alanine mutants with more phosphorylation sites mutated. Preliminary analysis showed that these mutants are similar to the alanine mutants analysed previously; however, more analysis is required to generate more definitive conclusions.

In summary, in this study I have uncovered the functional conservation of the CM1 region from yeast to human. I also showed that Mto2 phosphorylation regulates cytoplasmic MT nucleation in both interphase and mitosis, by regulating the Mto2-Mto1 interaction and the Mto2-Mto2 self-interaction and therefore remodelling the Mto1/2 complex.

Lay summary

Microtubules (MTs) are dynamic polymers that play many different roles in cells. During cell division, they form a mitotic spindle, the cellular machine that distributes DNA to two daughter cells. In interphase, which occurs between cell divisions, MTs facilitate cell growth and transport within cells. This research investigated how cells control formation of new MTs; we used fission yeast, a model eukaryote, to do so. In fission yeast, the proteins Mto1 and Pcp1 are responsible for MT formation in interphase and mitosis respectively. I looked at what Mto1 and Pcp1 proteins have in common - a fragment known as CM1 that is also present in two human proteins that play a role in schizophrenia and microcephaly. I swapped the CM1 regions of Mto1 and Pcp1 with(?) the human protein. I showed that human CM1 substitutes for yeast CM1, demonstrating that MT formation machinery is very similar in yeast and humans.

In interphase, Mto1 and another protein, Mto2, form the Mto1/2 complex that promotes MT formation. I showed that this complex is controlled in cells by the attachment of small groups called phosphates to Mto2 – a process called phosphorylation. Mto2 phosphorylation makes the Mto1/2 complex less active, and therefore fewer MTs are formed. Mto2 de-phosphorylation makes the Mto1/2 complex more active, and thus, more MTs are formed. This research also suggests that phosphorylation of Mto2 plays a role in switching off the Mto1/2 complex in mitosis. In humans, defects in MT formation are implicated in several human diseases. Understanding how MT formation is regulated may ultimately lead to new therapies.

Table of Contents

Acknowledgments ..... **iii**
Declaration ..... **iv**
Abstract ..... **v**
Lay summary ..... **vii**
List of tables ..... **xii**
List of figures ..... **xiv**
List of abbreviations ..... **xvii**

Chapter 1 Introduction **1**

1.1 Microtubule structure and function 1
1.2 Microtubule polymerisation 4
1.3 Microtubule organising centres 6
1.4 MT nucleation by the γ-tubulin complex 8
1.5 Regulation of the γ-TuC 12
1.6 Microtubules in *S. Pombe* 15
1.6.1 Microtubule organisation in fission yeast 15
1.6.2 γ-tubulin complex in *S. pombe* 17
1.6.2.1 γ-tubulin complex adaptor proteins in *S. pombe* 18
1.6.2.1.1 The Mto1/2 complex 18
1.6.2.1.2 Pcp1 21
1.7 Human CM1 proteins and associated diseases 21

Project Aims **24**

Chapter 2 Materials and methods **25**

2.1 Generation of plasmids for *pcp1(CM1)* mutant construction 25
2.2 Generation of plasmids for Pcp1 bacterial expression 26
2.3 Growth of *E. coli* strains 27
2.4 Preparation of *E. coli* competent cells 27
2.5 Transformation of *E. coli* strains 28
2.6 Isolation of plasmid DNA from *E. coli* 28
2.7 DNA sequencing 29
2.8 Exo-AP reaction 30
2.9 Ethanol DNA precipitation 30
2.10 Restriction digestion 31
2.11 Ligation of DNA 31
2.12 Gene synthesis 32
2.13 Gateway Cloning 32
2.13.1 Generation of PCR products containing attB1-attB2 flanking sites 32
2.13.2 BP recombination reaction 32
2.14 LR recombination reaction 33
2.15 Large scale bacterial protein expression 33
2.16 Isolation of bacterially expressed proteins from inclusion bodies 34
2.17 Nickel purification of Pcp1(604)-His_6 and Pcp1(605-1208)-His_6 34
2.18 Growth of fission yeast strains 35
2.19 Genetic crosses 36
2.20 Strain construction using PCR-based gene targeting 36
2.21 Strain construction using two-step gene-replacement and 5-FOA counterselection 38
2.22 Strain construction using pMONO integration system 39

2.23 Fission yeast DNA extracts....39
2.24 PCR amplification of DNA....39
2.25 Colony PCR....41
2.26 Microscopy....41
2.27 Cell morphology assay....42
2.28 *cdc25-22* block and release....43
2.28.1 cdc25-22 block and release for biochemical analysis of Mto2 phosphorylation....43
2.28.2 cdc25-22 block and release for microscopy analysis of Mto1[bonsai]-GFP puncta formation in mto2-NT2 cells....44
2.29 *cdc10-129* block and release and MBC treatment....44
2.30 *nda3-KM311* block and release....45
2.31 Fission yeast boiled protein extracts....45
2.32 Fission yeast native protein extracts....46
2.33 SDS-PAGE....47
2.34 Coomassie staining....47
2.35 Western blotting....48
2.36 TAP affinity tag pulldown....49
2.37 Coupling anti-GFP antibody to Protein G-Dynabeads....49
2.38 Anti-GFP immunoprecipitation....50
2.39 λ-Phosphatase treatment....51
2.40 CDK1-Cyclin B treatment of purified Mto1/2[A] complexes....51
2.41 Trypsin digestion and Stage-Tip purification....52
2.42 LC-MS^2 analysis....52

Chapter 3 Analysis of the role of the Centrosomin Motif 1 in the regulation of Mto1 and Pcp1 nucleation activity during the cell cycle..63

3.1 Introduction....63
3.2 Results....66
3.2.1 Introduction of heterologous CM1 domains into Mto1....66
3.2.1.1 CM1 regions of Pcp1 and MMGL fully rescue Mto1 function whereas CM1 region of CDK5RAP2 does not....66
3.2.1.2 Mto1(CM1)-GFP proteins interact with different amounts of the γ-TuC....72
3.2.1.3 Mto1(bonsai-CM1)-GFP aggregates colocalise with iSPB in *CM1:Pcp1* and *CM1:MMGL* background....74
3.2.2 Introduction of heterologous CM1 regions into Pcp1....82
3.2.2.1 Despite low expression levels, all three heterologous CM1 regions rescue Pcp1 function....82
3.2.2.2 Cell cycle progression and mitosis timing is normal in *pcp1(CM1)-GFP* cells 85
3.2.2.3 Introduction of heterologous CM1 regions into Pcp1 has no effect on cytoplasmic MT networks....88
3.3 Discussion....91
3.3.1 The role of the CM1 region in cell-cycle regulation of MT nucleation....91
3.3.2 Evolutionary conservation of the CM1 region....93

Chapter 4 Analysis of the role of Mto2 phosphorylation in regulation of Mto1/2 complex activity....95

4.1 Introduction....95
4.2 Results....98
4.2.1 Mto1-Mto2 is interaction is regulated in the cell cycle....98
4.2.2 MT depolymerisation does not affect Mto2 phosphorylation state....102

4.2.3 Unlike wild-type Mto2, Mto2[alanine] mutants interact with Mto1 in both interphase *and* mitosis....104
4.2.4 Mto2 phosphorylation is perturbed in *mto1[bonsai]-TAPC* cells....109
4.2.5 Mto2 phosphorylation is independent of Mto1....111
4.2.6 Human CDK1-Cyclin B phosphorylates wild-type, Mto2-6A and Mto2-13A *in vitro* 113
4.2.7 MT nucleation is more efficient in *mto2[alanine]* cells compared to wild-type cells 115
4.2.8 Post-anaphase array formation is advanced in *mto2[alanine]* cells....117
4.2.9 The Mto1/2 complex size and intensity are comparable in wild-type and *mto2[alanine]* cells....119
4.2.10 The Mto1/2 complex is disassembled in mitosis in wild-type and *mto2[alanine]* cells....122
4.2.11 The Mto1/2[NE] complex size and intensity increase with increasing number of alanine substitutions in Mto2 sequence....122
4.2.12 Localisation of Mto1[NE]-GFP to the NE is disrupted in mitosis in *mto2[alanine]* cells....124
4.2.13 The Mto1/2[bonsai] complex size and intensity increase with increasing number of alanine substitutions in Mto2 sequence....125
4.2.14 Mto1[bonsai]-GFP puncta disappear in mitosis in *mto2[alanine]* cells....127
4.2.15 Mto2 self-interaction is regulated in the cell cycle....127
4.2.16 Lambda phosphatase treatment confirms that Mto2-17A is phosphorylated in mitosis....130
4.3 Discussion....132
4.3.1 Mto2 phosphorylation acts as a dial to fine-tune cytoplasmic MT nucleation levels in interphase....132
4.3.2 Mto2 phosphorylation plays a role in regulation of the interaction between the Mto1/2 complex and its NE receptor....138
4.3.3 Mto2 phosphorylation acts as a switch to abolish cytoplasmic MT nucleation in mitosis....139

Chapter 5 Identification and mutagenesis of mitosis-specific phosphorylation sites in Mto2-17A....142

5.1 Introduction....142
5.2 Results....144
5.2.1 Optimisation of SILAC methodology for large-scale immunoprecipitation..144
5.2.2 Design of Mto2 phosphomutants....147
5.2.2.1 Identification of mitotic phosphorylation sites in Mto2-17A-GFP using SILAC 147
5.2.2.2 Quantification of phosphopeptides and their corresponding unmodified peptides 151
5.2.2.3 Design of Mto2 phosphomutants....157
5.2.3 Analysis of Mto2 phosphomutants....159
5.2.3.1 Mto2-NT2 is not hyperphosphorylated in mitosis....159
5.2.3.2 Mto1[NE]-GFP puncta disappear from the NE in *mto2-NT2* cells....160
5.2.3.3 *mto2-NT2* and *mto2-17A* cells nucleate more MTs than wild-type cells in *mto1[NE]-GFP* background....161
5.2.3.4 Mto1[bonsai]-GFP aggregate formation in *mto2-17A* and *mto2-NT2* cells impairs interphase MT networks....163
5.2.3.5 Analysis of Mto1[bonsai]-GFP puncta in *mto2-NT2* mitotic cells....165
5.3 Discussion....169

Chapter 6 Structure-function mutagenesis of Mto2 conserved regions to reveal Mto2 domains important for its function.....172

6.1 Introduction.....172
6.2 Results.....174
6.2.1 Design of *mto2* alanine-scanning (*mto2-asc*) mutants.....174
6.2.2 Mutations in three regions of Mto2 affect interphase MT networks.....176
6.2.3 Mutations in three Mto2 regions affect Mto1-Mto2 and Mto1/2-γ-TuC interactions.....179
6.3 Discussion.....183

Appendix 1. Identification of phosphorylation sites in Mto1.....187
Appendix 2. Arginine-10 conversion to other amino acids.....191
Appendix 3. Generation of anti-Pcp1 antibodies.....198
References.....200

List of tables

Table 1.1. Summary of γ-tubulin complex proteins in various species.
Table 2.1. Conditions used for microscopy.
Table 2.2. List of antibodies and dilutions used during this study.
Table 2.3. List of plasmids used during this study.
Table 2.4. List of yeast strains used during this study.
Table 2.5. List of oligonucleotides used during this study.
Table 3.1. Two of three heterologous CM1 regions substitute for the Mto1 CM1 region.
Table 3.2. *mto1(bonsai-CM1)-GFP* cells are statistically different from both *mto1-GFP* and *mto1(bonsai-9A1)-GFP cells*
Table 3.3. Heterologous CM1 regions substitute for the Pcp1 CM1.
Table 4.1. Residues mutated in *mto2[alanine]* cells.
Table 4.2. *mto2[alanine]* cells contain more MT bundles than wild-type cells.
Table 4.3. MT nucleation frequency increases with increasing number of alanine substitutions in Mto2 sequence.
Table 4.4. Comparison of Mto1-GFP puncta size in *mto2*$^+$ and *mto2[alanine*] cells.
Table 4.5. Comparison of Mto1-GFP puncta intensity in *mto2*$^+$ and *mto2[alanine*] cells.
Table 4.6. Comparison of Mto1[NE]-GFP puncta size in *mto2*$^+$ and *mto2[alanine*] cells.
Table 4.7. Comparison of Mto1[NE]-GFP puncta size in *mto2*$^+$ and *mto2[alanine*] cells.
Table 4.8. Comparison of Mto1[bonsai]-GFP puncta size in *mto2*$^+$ and *mto2[alanine*] cells.
Table 4.9. Comparison of Mto1[bonsai]-GFP puncta size in *mto2*$^+$ and *mto2[alanine*] cells.
Table 4.10. Comparison of Mto2-GFP and Mto2-17A-GFP puncta size in *mto1*$^+$ and *mto1*Δ cells.
Table 4.11. Comparison of Mto2-GFP and Mto2-17A-GFP puncta intensity in *mto1*$^+$ and *mto1*Δ cells.
Table 5.1. Experimental design of four MS runs summarised.
Table 5.2. Phosphorylation sites identified during MS analysis of Mto2-17A-GFP.
Table 5.3. Three quantification methods give different results
Table 5.4. Mto2 phosphomutants design based on unmodified peptide data.
Table 5.5. *mto2-NT2 mto1[NE]-GFP* and *mto2-NT2 mto1[NE]-GFP* cells contain more MT bundles than *mto2*$^+$ *mto1[NE]-GFP* cells.
Table 5.6. *mto2-NT2 mto1[bonsai]-GFP* and *mto2-17A mto1[bonsai]-GFP* cells contain fewer MT bundles than *mto2*$^+$ *mto1[bonsai]-GFP* cells.
Table 6.1. Summary of Mto2 truncation analysis.
Table 6.2. Statistical analysis of MT bundles number in *mto2-asc* cells when compared to *mto2*$^+$ and *mto2*Δ cells.
Table A1.1. Experimental design MS runs summarised.

Table A1.2. Quantification of phosphorylated and unmodified peptides detected during SILAC analysis of Mto1.
Table A1.3. Mto1 phosphorylation sites detected in previously published studies.
Table A2.1. Heavy-labelled amino acid conversion in fission yeast.
Table A3.1. Generation of anti-Pcp1 antibodies.

List of figures

Figure 1.1. Assembly intermediates of MTs.
Figure 1.2. The revised template model of the g-TuRC.
Figure 1.3. Changes in MT cytoskeleton during cell cycle progression in fission yeast.
Figure 3.1. Schematic representation of Mto1 and Pcp1.
Figure 3.2. Sequence alignment of CM1 regions of human CDK5RAP2 and MMGL and fission yeast Mto1 and Pcp1.
Figure 3.3. Two of three mto1(CM1)-GFP mutants show normal cell morphology.
Figure 3.4. Localisation of Mto1(CM1)-GFP proteins.
Figure 3.5. Cytoplasmic MT networks in mto1(CM1)-GFP mutants.
Figure 3.6. Quantification of MT arrays in mto1(CM1)-GFP cells.
Figure 3.7. The efficiency of the Mto1-Gtb1 interaction is affected by the CM1 region substitution.
Figure 3.8. Cell morphology is abnormal in mto1(bonsai-CM1)-GFP mutants.
Figure 3.9. Cytoplasmic MT networks in mto1(bonsai-CM1)-GFP mutants.
Figure 3.10. Quantification of MT arrays in mto1(bonsai-CM1)-GFP cells.
Figure 3.11. Functional Mto1(bonsai-CM1)-GFP mutants localise to iSPB but not to mSPB.
Figure 3.12. The various Mto1(bonsai-CM1)-GFP proteins mutants interact with the γ-TuC at different levels.
Figure 3.13. Cross and Loss assay.
Figure 3.14. Pcp1(CM1)-GFP protein levels are lower relative to wild-type.
Figure 3.15. Mitosis timing is normal in pcp1(CM1)-GFP cells.
Figure 3.16. Cell cycle progression is normal in pcp1(CM1) mutants.
Figure 3.17. Cytoplasmic MT networks in pcp1(CM1)-GFP mutants in pcp1+ background.
Figure 3.18. Introduction of heterologous CM1 regions into Pcp1 has no effect on cytoplasmic MT networks.
Figure 3.19. Models for cell cycle-regulation of MT nucleation.
Figure 4.1. Mto1-Mto2 interaction is disrupted in metaphase-arrested cells.
Figure 4.2. Mto1-Mto2 interaction is regulated in a cell cycle-dependent manner.
Figure 4.3. Absence of MTs does not affect Mto2 phosphorylation.
Figure 4.4. Unlike wild-type Mto2, Mto2-alanine mutants interact with Mto1-TAPS in mitosis
Figure 4.5. Unlike wild-type Mto2, Mto2-alanine mutants can interact with Mto1-NE-TAPS in mitosis.
Figure 4.6. Mto2-alanine mutants interact with Mto1-bonsai-TAPC in mitosis, but wild-type Mto2 phosphorylation is perturbed.
Figure 4.7. Mto2 phosphorylation is abnormal in mto1[bonsai]-TAPC background.
Figure 4.8. Human CDK1-Cyclin B phosphorylates purified Mto1/2-alanine complexes in vitro.
Figure 4.9. mto2-alanine cells contain more MT bundles and nucleate more MTs than wild-type.

Figure 4.10. Post-anaphase array (PAA) formation is advanced in mto2-alanine cells.
Figure 4.11. mto1-GFP mto2-17A cells show defects in cytokinesis.
Figure 4.12. Localisation of Mto1-NE-GFP to the NE is disrupted in mitosis in mto2-alanine mutants.
Figure 4.13. Mto1-bonsai-GFP puncta are disassembled in mitosis in wild-type and mto2-alanine cells.
Figure 4.14. Mto2-17A-GFP forms puncta in the absence of Mto1 in a cell cycle-regulated manner.
Figure 4.15. λ-protein phosphatase treatment on Mto2-17A confirms that Mto2-17A-GFP is phosphorylated in mitosis.
Figure 4.16. Mto2 phosphorylation regulates Mto1-Mto2 interaction and Mto2-Mto2 self- interaction in vivo.
Figure 4.17. Model of how Mto1/2 complexes in mto2[alanine] cells are better MT nucleators.
Figure 4.18. Post-mitotic re-assembly of the Mto1/2 complex is advanced in mto2[alanine] cells resulting in premature PAA formation.
Figure 4.19. Mto2 phosphorylation negatively regulates interphase MT nucleation.
Figure 4.20. Model of the Mto1/2 complex disruption upon mitotic entry.
Figure 5.1. SILAC experimental set-up.
Figure 5.2. Optimisation of immunoprecipitation procedure for SILAC.
Figure 5.3. Mto2-17A phosphorylation sites identified by mass spectrometry analysis.
Figure 5.4. Methods to quantify abundance of phosphorylation in the heavy sample relative to the light sample.
Figure 5.5. Manual quantification of phosphopeptides abundance.
Figure 5.6. Quantification of SILAC data based on unmodified peptides.
Figure 5.7. Mitotic phosphorylation of Mto2-NT2 is almost completely abolished in mitosis relative to Mto2-17A.
Figure 5.8. Mto1[NE]-GFP delocalises from the NE upon mitotic entry in mto2+, mto2-17A and mto2-NT2 cells.
Figure 5.9. Microscopy analysis of Mto1[NE]-GFP in mto2-17A and mto2-NT2 interphase cells.
Figure 5.10. Microscopy analysis of Mto1[bonsai]-GFP in mto2-alanine and mto2-NT2 interphase cells.
Figure 5.11. Mto1[bonsai]-GFP puncta in early mitosis in mto2+, mto2-17A and mto2-NT2 cells.
Figure 5.12. Mto1[bonsai]-GFP puncta in mitotic cells in mto2+ cdc25-22, mto2-17A cdc25-22 and mto2-NT2 cdc25-22 cells.
Figure 6.1. Design of mto2-asc mutants.
Figure 6.2. Cytoplasmic MT networks in mto2-asc mto1[bonsai]-GFP cells.
Figure 6.3. Quantitative analysis of MT bundles in mto2-asc cells.
Figure 6.4. Mto1-Mto2 and Mto1/2-Gtb1 interactions are impaired in some of the mto2-asc mutants.
Figure A2.1. Arginine conversion.
Figure A2.2. Nitric Oxide Synthase-catalysed reaction of NO synthesis from L-arginine.
Figure A2.3. Griess test used to detect nitrite ions.

Figure A3.1. Testing of anti-Pcp1 antibodies.

List of abbreviations

ABC	Ammonium bicarbonate
ACN	Acetonitrile
AEBSF	4-(2-Aminoethyl) benzenesulfonyl fluoride
ATP	Adenosine Triphosphate
bp	Base pair
BSA	Bovine serum albumin
cAMP	Cyclic adenosine monophosphate
CM1	Centrosomin motif 1
CMT	Cortical MTs
Da	Dalton
DAPI	4',6-diamidino-2-phenylindole
DMP	Dimethyl pimelidate
DMSO	Dimethylsulfoxide
DNA	Deoxyribonucleic Acid
DNTP	Deoxyribonucleotide
DTT	Dithiothreitol
EDTA	Ethylenediaminetetraacetic acid
EM	Electron microscopy
EMM	Edinburgh Minimal Media
eMTOC	Equatorial MTOC
EtOH	Ethanol
FOA	5-Fluoroorotic acid
FL	Full length
g	X gravity
γ-TuRC	Gamma tubulin ring complex
γ-TuSC	Gamma tubulin small complex
γ-TuC	Gamma tubulin complex
GCP	Gamma tubulin complex protein
GDP	Guanosine diphosphate
GFP	Green fluorescent protein
GTP	Guanosine triphosphate
h	Hour

HFG	His6 FLAG GFP
HMT	Home made Taq
HPLC	High pressure liquid chromatography
IgG	Immunoglobulin G
iMTOC	Interphase MTOC
IP	Immunoprecipitation
IPTG	Isopropylthio-β-D-galactosidase
kDa	Kilodaltons
L	Litre
L-NAME	L-N^G-Nitroarginine methyl ester
LSB	Laemmli Sample Buffer
MASC	Mto1 and Spc72 C-terminus
MBP	Maltose binding protein
min	Minute
MPP	Multiply phosphorylated peptide
MS	Mass Spectrometry
MT	Microtubule
MTOC	MT organising centre
NE	Nuclear envelope
nmt	No message in thiamine
NusA	N-utilising substance A
OD	Optical Density
O/N	Overnight
ORF	Open reading frame
PAGE	Polyacrylamide Gel Electrophoresis
PAA	Post-Anaphase Array
PBS	Phosphate Buffered Saline
PCR	Polymerase Chain Reaction
PEG	Polyethylene glycol
PMSF	Phenylmethanesulphonyl fluoride
PCM	Pericentriolar matrix
PTM	Post-translational modification
RT	Room temperature
rpm	Revolutions per minute
sec	Second

SDS	Sodium dodecyl sulfate
SILAC	Stable isotope labeling with amino acid in cell culture
SPA	Synthetic Sporulation Agar
SPB	Spindle Pole Body
TAP	Tandem affinity purification
TBS	Tris Buffered Saline
TEMED	N,N,N',N'-Tetramethylethylenediamine
TFA	Trifluoroacetic acid
WT	Wild-type
YES	Yeast Extract Supplemented

Chapter 1
Introduction

1.1 Microtubule structure and function

Microtubules (MTs) are essential components of the eukaryotic cytoskeleton and are vital for spatial organisation of eukaryotic cells. MTs play a myriad of roles in the cell including cell division, when they form mitotic and meiotic spindles, and other processes as diverse as cell signalling, cell motility, transport of organelles and establishment of cell polarity.

MTs are hollow, cylindrical polymers, composed of laterally associated protofilaments that are assembled from α-and β-tubulin heterodimers (Fig. 1.1) (Ludueńa et al., 1977). A MT was first shown to be composed of 13 protofilaments in an electron microscopy (EM) study demonstrating a MT is made of 13 equally spaced 'subunits' (Tilney et al., 1973). Further experiments have shown that the exact number of protofilaments within the MT lattice depends on *in vitro* polymerisation conditions, and can vary from 9 to 16 (Chrétien and Wade, 1991; Evans et al., 1985; Langford, 1980; McEwen and Edelstein, 1980). However, the majority of MTs nucleated either *in vivo* or *in vitro* from centrosomes have 13 protofilaments, suggesting that the protofilament number can be accurately controlled (Evans et al., 1985; Tilney et al., 1973). An exception is, for instance, *C. elegans*, in which majority of neuronal MTs consist of 11 protofilaments (Chalfie and Thomson, 1982).

The two tubulins are approximately ~50% identical at the primary sequence level and have strikingly similar structures (Burns, 1991; Löwe et al., 2001; Luduena and Woodward, 1973; Nogales et al., 1998). The tubulin subunits make two types of contacts: longitudinal contacts along the length of protofilaments, and lateral contacts between protofilaments (typically, α-tubulin to α-tubulin and β-tubulin to β-tubulin). Within a 13-protofilament MT, α- and β-tubulin monomers follow a left-handed three-start helix, which leads to MTs having a "seam" where α- and β-tubulin monomers interact laterally (Fig. 1.2) (Li et al., 2002; Mandelkow et al., 1986). MTs are dynamic polymers that grow and shrink actively; the longitudinal orientation of α,β-tubulin heterodimers within a MT provides MTs with an intrinsic polarity with the β-tubulin molecule exposed at the fast-growing "plus-end", and the α-tubulin

exposed at the slow-growing “minus-end”. Importantly, MTs are known to switch between phases of slow growth and rapid shrinkage that interconvert stochastically, a property referred to as dynamic instability (Mitchison and Kirschner, 1984a, 1984b). Because all of the MT-dependent processes require MTs to be organised in arrays with defined geometry, the polarity of MT lattice is central for MT functions. Processes like cell division, differentiation or migration require rapid re-modelling of the MT cytoskeleton (therefore exploiting dynamic properties of MTs), while cell polarity establishment and maintenance or cell shape control rely largely on polar properties of MTs.

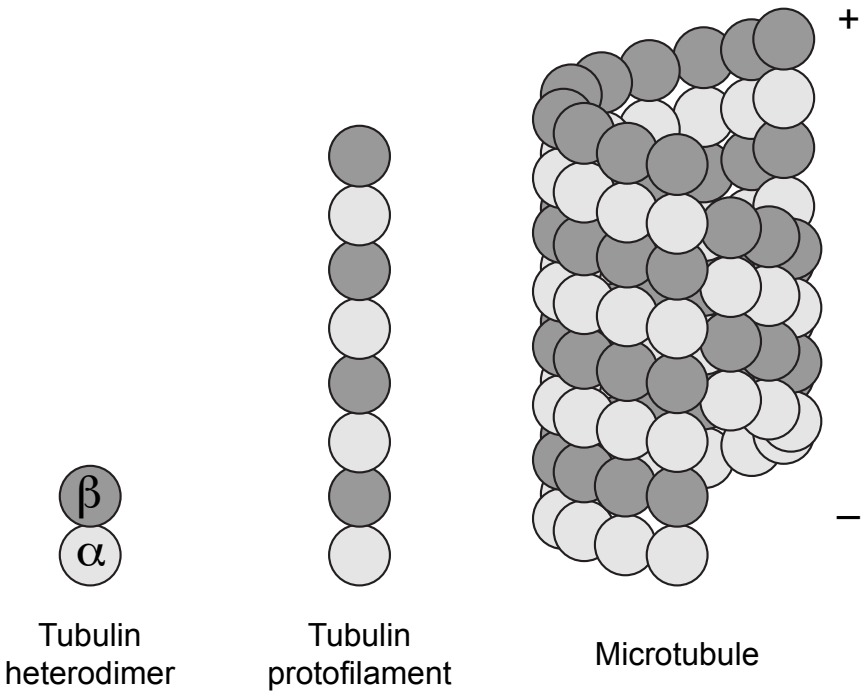

Figure 1.1. Assembly intermediates of MTs.
Left: an α,β-tubulin heterodimer. Middle: a tubulin protofilament made of logitudinally associated tubulin heterodimers. During MT assembly, protofilaments associate such that α-tubulin molecules are exposed at the MT minus-end, whereas β-tubulin molecules at the MT plus-end. Right: an assembled MT, composed of 13 protofilaments, with a 3-start helix. In a MT lattice, homotypic interactions occur: α-tubulins interact laterally with α-tubulins and β-tubulins with β-tubulins, apart from the “seam” present between protofilaments 1 and 13, where α-tubulin and β-tubulin molecules interact laterally (heterotypic interaction). Plus and minus end of MT are indicated.

MTs facilitate processes such as endocytosis and exocytosis, by the formation of a scaffold that is used for motor-driven transport of vesicles around the cell

(Caviston and Holzbaur, 2006; Soldati and Schliwa, 2006; Vale, 2003). MTs also contribute to positioning of organelles, such as Golgi apparatus and mitochondria; this was first observed in giant squid axon extracts where organelles moved along MTs in an ATP-dependent manner (Vale et al., 1985). MT networks, along with actin cytoskeleton, are important for establishment and maintenance of cell polarity, which is in turn important for cell division, differentiation and morphogenesis (Li and Gundersen, 2008). Regulation of cell polarity is achieved by delivery of numerous polarity factors to sites of cell growth. In specialised motile cells such as neuronal or epithelial cells, MTs and the actin cytoskeleton act together to promote cell protrusion and migration (Gibney and Zheng, 2003).

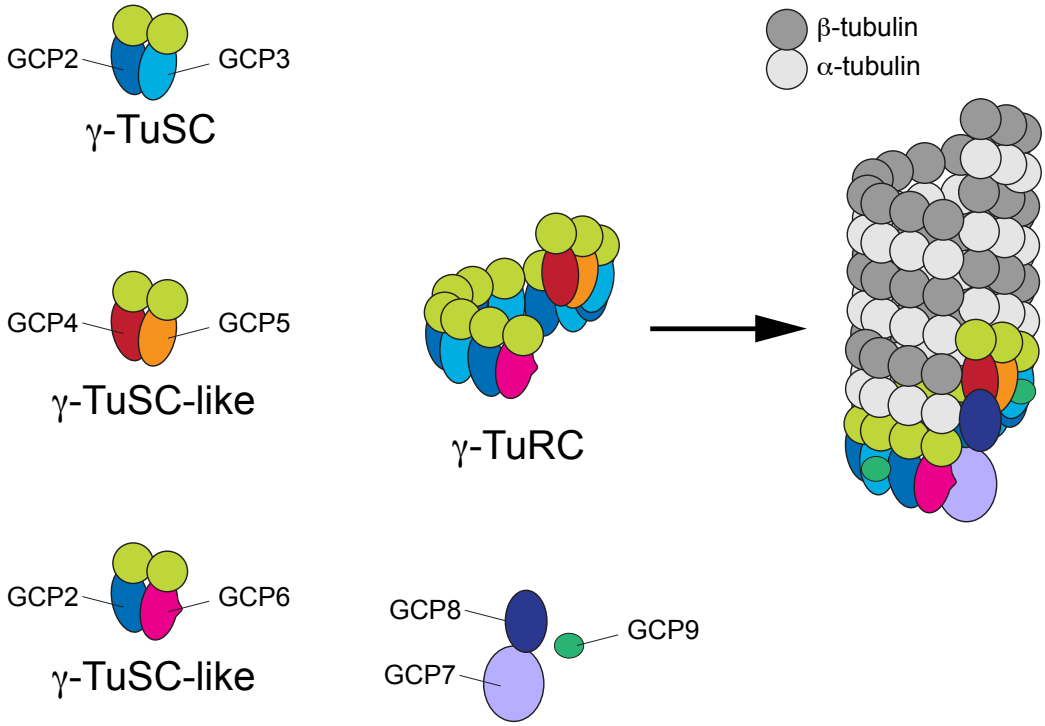

Figure 1.2. The revised template model of the γ-TuRC.
One copy of GCP2 and GCP3 associate with one molecule of γ-tubulin each to form the canonical γ-TuSC. GCPs 4-6 have silimar structures to GCP2 and GCP3, suggesting that they can form γ-TuSC-like complexes and be integrated into the ring structure made of γ-TuSCs. The low abundance of GCPs 4-6 relative to GCP2 and GCP3 suggests that they might play specific roles to ensure the ring is of a proper size and geometry, by acting as ring assembly initiators or terminators. Recently discovered GCPs 7-9 can provide a cap and mediate γ-TuRC localisation to specific foci or binding to adaptor proteins. Exact positions of GCPs 4-9 within the ring remain to be shown experimentally and are speculative.

The role of MTs is perhaps most prominent during cell division, where they form mitotic and meiotic spindles. In most of interphase animal cells, MTs are arranged in radial arrays with minus ends anchored at or in vicinity of the centrosome, and plus ends extending towards the cell periphery (Wade, 2007). Upon mitotic entry, the interphase MT networks disassemble and the mitotic spindle is formed to facilitate chromosome segregation into two daughter cells. In most cell types, spindle MT nucleation takes place primarily at two centrosomes that become spindle poles, but MTs can also be generated by the chromosomes and within the spindle itself (Gadde and Heald, 2004; Wadsworth et al., 2011; Wittmann et al., 2001). Dynamic instability of MTs, that is, the lengthening and shortening of spindle MTs, determines to a large extent the proper alignment of chromosomes at the spindle midzone (Gardner et al., 2013). Mitotic microtubule-associated proteins (MAPs) associate with the spindle poles and spindle midzone to regulate MT dynamics (Kline-Smith and Walczak, 2004). The organisation of MTs into bipolar mitotic spindle requires a variety of MAPs ensuring that minus ends of MTs focus at spindle poles whereas the dynamic plus ends extend outward (Jiang and Akhmanova, 2011). Activity of motor proteins, such as the plus end-directed kinesin-5 and the minus end-directed dynein, is required for the establishment and maintenance of the bipolar spindle. The role of kinesin-5 motors is to crosslink and slide antiparallel MTs (Ferenz et al., 2010), while the dynein acts to position chromosomes and to organise and position the spindle (Kikkawa, 2013). Other kinesins exhibit a plethora of functions, including kinetochore alignment and MT polymerase activity (Welburn, 2013). This highly regulated interplay between MTs, MAPs and motor proteins ensures functional cell division.

1.2 Microtubule polymerisation

Within a MT, α,β-heterodimers interact in a head-to-tail manner to form a protofilament, while the interaction between protofilaments is a result of lateral interactions between tubulin subunits. *In vitro*, MT polymerisation was first shown using rat brain tubulin, and it required GTP to occur (Weisenberg, 1975; Weisenberg and Deery, 1976; Weisenberg et al., 1968). Both α- and β-tubulin molecules binds one molecule of GTP each; however, only one of the GTP molecules is available for hydrolysis and exchange. During addition of an α,β-tubulin dimer to a MT lattice, the newly arriving α-tubulin molecule hydrolyses the GTP molecule present on the β-

tubulin that is already built into the MT (Nogales et al., 1999). The GDP molecule made in this reaction is hidden in the subunit interface and not available for exchange. α-tubulin also binds GTP but it is bound in a non-exchangeable manner (Spiegelman et al., 1977). Experiments using a non-hydrolysable analogue of GTP, GMPCPP, showed that the GTP hydrolysis, even though it normally occurs during MT polymerisation, is not actually required for polymerisation (Hyman et al., 1992). Instead, GMPCPP-MTs were shown to be hyperstable and did not exhibit dynamic instability, suggesting that the GTP hydrolysis might play a role in MT depolymerisation rather than polymerisation. Indeed, when buffer conditions were used that triggered hydrolysis of GMPCPP, the MT lattice destabilised which led to rapid MT depolymerisation (Caplow et al., 1994). Tubulin exists in two conformations: straight when bound to GTP and bent when bound to GDP. Docking of the α,β-tubulin dimer structure onto the protofilaments lattice showed that tubulin dimers have straight conformation when present in the lattice (Löwe et al., 2001; Nogales et al., 1999), which is most likely promoted by lateral associations between protofilaments. Dimers isolated from pre-formed protofilaments, on the other hand, adopt a curved conformation (Ravelli et al., 2004). GTP hydrolysis in the MT lattice leads to curving of protofilaments (Wang and Nogales, 2005), which destabilises the lattice and initiates MT depolymerisation. Such curved protofilaments were observed by EM at the ends of depolymerising MTs (Arnal et al., 2000)..

Collectively, those observations led to an elegant model of MT dynamic instability. In the polymerisation phase, addition of GTP-bound subunits to the plus end of a growing MT is followed by GTP hydrolysis. When the GTP hydrolysis rate is slower than the rate of subunit addition, a GTP “cap” is formed at the plus end. which protects MT from shrinking (Desai and Mitchison, 1997; Mitchison and Kirschner, 1984a). When the hydrolysis rate exceeds the polymerisation rate, the cap is not formed (or is “eaten up”), leading to a change in curvature of the protofilaments and, as a result, a catastrophe event, in which a MT switches from growth to shrinkage (Gardner et al., 2013). During shrinking, GDP subunits are released from the MT lattice. The rescue event, in which MTs recover from catastrophe and resume growth, occurs when GTP subunits are added to the end of a depolymerising MT (Gardner et al., 2013). Cellular MTs are believed to have islands of GTP-bound tubulin within their lattices that promote the rescue events (Dimitrov et al., 2008; Tropini et al., 2012).

1.3 Microtubule organising centres

In vitro, MT formation occurs in two phases, referred to as nucleation and elongation. During the nucleation phase, multiple tubulin dimers bind to form a seed that allows for further polymerisation to occur. These seeds are not stable at low (<10 μM) tubulin concentrations (Fygenson DK et al., 1995; Mitchison and Kirschner, 1984b), resulting in a slow MT growth. Once a sufficiently large tubulin oligomer is formed, polymerisation becomes energetically favourable and addition of further tubulin heterodimers (therefore, MT elongation) proceeds rapidly. This is most likely due to a stabilisation effect provided by lateral and longitudinal interactions within the MT lattice, which also ensure a straight tubulin conformation (Gardner et al., 2011; Rice et al., 2008).

Significantly, *in vivo,* MT nucleation occurs at specific foci in cells, referred to as MT organising centres (MTOCs). Because of the low tubulin concentration in cells, the cellular context is highly unfavourable for spontaneous MT formation. The role of MTOCs is to allow bypassing the early, slow MT growth phase. The spatial and temporal control of MT nucleation allows formation of distinct MT arrays *in vivo*. A variety of MTOCs exists, and their formation and localisation depends on the species, the cell type, and the cell division stage, but they can generally be classified as either centrosomal or non-centrosomal.

The most studied MTOC is the centrosome, the main MTOC in animal cells. It is a small spherical structure, made of a pair of centrioles surrounded by the pericentriolar material (PCM). Purified centrosomes promote nucleation at tubulin concentrations lower than the concentration required for *in vitro* MT assembly (Mitchison and Kirschner, 1984b). In many animal cells, the centrosome is the main MTOC: a central anchor point for radial MT array in interphase cells, as well as a main MTOC in mitosis. Within the centrosome, centrioles have defined dimensions and are built on an ordered cylindrical array of nine MT triplets (Avidor-Reiss and Gopalakrishnan, 2013; Delattre and Gönczy, 2004). The two centrioles are structurally and functionally different, which stems from the generational difference between them. The old “mother” centriole is distinguished by two sets of nine appendages at its distal end, while the young “daughter” centriole is shorter than mother and has no appendages. The PCM, a proteinaceous, electron dense material surrounding the centriole pair, is a key structure that anchors and nucleates most MTs of the cell. PCM is made of a lattice-like structure built of many coiled-coil

proteins including pericentrin and AKAP450. This structure docks several regulatory components involved in MT nucleation, such as the γ-tubulin complex and γ-tubulin adaptor proteins (described in detail in Sections 1.4 and 1.5) (Bettencourt-Dias and Glover, 2007).

However, centrosomes are not the only MTOCs found in eukaryotic cells. In fact, after depletion of centrosomes by laser ablation or microsurgery cells are still able to form the mitotic spindle (Khodjakov et al., 2000; La Terra et al., 2005). Moreover, fungi and plants do not have centrosomes and yet contain organised MT networks. In fungi, the functional equivalent of the centrosome is the spindle pole body (SPB), which forms the two poles of the mitotic spindle. In budding yeast, EM studies have shown that the NE-embedded SPB is made of three disks: an inner plaque that faces the nucleoplasm and associates with nuclear MTs; the central plaque that crosses the nuclear membrane and the outer plague, that faces the cytoplasm and associates with cytoplasmic MTs (Jaspersen and Winey, 2004). In fission yeast, the SPB remains attached to the nuclear envelope (NE) in interphase, and it gets inserted into the NE in mitosis (Ding et al., 1997; McIntosh and O'Toole, 1999). SPBs are made of scaffold proteins, such as calmodulin, and several other proteins involved in complex processes of SPB duplication, insertion, as well as proteins involved in MT nucleation (Jaspersen and Winey, 2004). In *Saccharomyces cerevisiae*, the SPB is the sole MTOC and nucleates nuclear MTs from its inner plaque and cytoplasmic MTs from its outer plaque (Knop et al., 1999). By contrast, in fission yeast *Schizosaccharomyces pombe*, MTs are nucleated not only from SPBs, but also from other cytoplasmic foci, such as the NE, cell equator during cytokinesis or existing MT bundles (described in more detail in Section 1.6) (Hagan, 1998; Sawin and Tran, 2006).

Plant cells do not have any centrosome analogue, but do organise acentrosomal MT arrays (Ehrhardt, 2008; Fishel and Dixit, 2013; Murata and Hasebe, 2007; Wasteneys and Ambrose, 2009). The interphase cortical MTs (CMTs) of plant cells create a two-dimensional array, with MTs aligned along the cell cortex and absent from the cell body. Conventional MTOCs are not observed in majority of plant cells, but the γ-TuC accumulates at specific locations allowing focused MT nucleation: the bulk of nucleation of CMTs takes place from the lattice of previously established MTs and from the NE and the cell cortex. Nucleation also occurs along newly formed cell edges following cytokinesis (Ambrose and Wasteneys, 2011). Microtubules were shown to be nucleated by the isolated nuclei

from the NE (Seltzer et al., 2007). The NE is also an MTOC in animal cell myotubes, (differentiated muscle cells). During muscle differentiation, centrosomal proteins such as pericentrin, ninein and MT-nucleating γ-tubulin are redistributed to the nuclear membrane independently of MTs and promote MT nucleation (Bugnard et al., 2005; Srsen et al., 2009).

Non-centrosomal MT nucleation occurs simultaneously with centrosomal MT nucleation in other types differentiated cells, such as epithelial cells or neurons, (Bartolini and Gundersen, 2006). In both of these cell types cells proper MT organisation is crucial for the cell function. In epithelial cells, MTs are organised in a linear acentrosomal array, in which MT bundles are aligned such that the minus ends of MTs are located apically whereas plus ends are basal. The Golgi apparatus serves as a MTOC, and it is believed to be important in the establishment of cell MT asymmetry (Efimov et al., 2007; Vinogradova et al., 2009). In neurons, axon extension and maintenance depends on the MT cytoskeleton; in addition, MTs are also required for the motor-driven cargo transport within axon. Axons and dendrites have distinct arrays of MTs: axon MTs are long and their plus ends are exposed towards the axon tip, whereas dendrite MTs are shorter and are of mixed polarity (Bartolini and Gundersen, 2006; Prokop, 2013). During neural development, the neuronal centrosome loses its function as a MTOC and the acentrosomal MT nucleation organises the cytoskeleton. Recent experiments, in which the centrosome was removed from developing neurons by laser ablation showed that that the centrosomal MT nucleation is not necessary for axon extension (Stiess and Bradke, 2011; Stiess et al., 2010). Acentrosomal MT nucleation within the axon seems to be important as tubulin import into the axon is required for axon formation (Stiess and Bradke, 2011). It was recently suggested that the hyperstable (polyaminated) MTs could act as nucleation sites for new MTs along axons (Baas, 2013; Song et al., 2013).

1.4 MT nucleation by the γ-tubulin complex

The physical properties of each type of MTOCs (e.g. shape, size and spatial distribution) determine the organisation of MT arrays. Efficient MT polymerisation under physiological conditions at MTOCs requires a nucleator that will mimic the MT seed formed by multiple tubulin subunits during spontaneous polymerisation. Such a nucleator is another member of the tubulin family, γ-tubulin, which is ubiquitous

component of all known MTOCs and is required for their function. γ-tubulin was initially identified in *A. nidulans* as a suppressor of β-tubulin mutation and was subsequently found to be conserved in all eukaryotes (Oakley and Oakley, 1989; Stearns et al., 1991; Weil et al., 1986; Zheng et al., 1991). Crystallography revealed that γ-tubulin is structurally very similar to α- and β-tubulin (Aldaz et al., 2005).

Although essential for MT nucleation, γ-tubulin alone is unable to promote nucleation. Instead, in order to form a template for MT nucleation, γ-tubulin associates with a variety of evolutionary conserved proteins, termed "gamma-tubulin complex proteins", or GCPs, where γ-tubulin itself is designated GCP1. In most eukaryotes, γ-tubulin complexes (γ-TuCs) contain five GCPs: GCPs 2-6, in addition to γ-tubulin. GCPs 2-6 belong to a single family characterised by the presence of two highly conserved "γ-tubulin ring protein" motifs: an N-terminal "grip1" and a C-terminal "grip2", which are unique for the *grip* family. More recent studies have identified additional proteins, such as GCP-WD (NEDD1), GCP8 (MZT2) and GCP9 (MZT1), that are not members of the *grip* family, yet are γ-TuC components (that is, they co-purify with the γ-TuC components stoichiometrically, colocalise with γ-tubulin *in vivo* and co-fractionate with the γ-TuC on sucrose gradients). Two types of γ-TuCs are generally found in eukaryotes. The γ-tubulin small complex (γ-TuSC) is a tetramer made of two molecules of γ-tubulin bound to laterally associated GCP2 and GCP3. By contrast, the 2.2-MDa γ-tubulin ring complex (γ-TuRC) contains several other proteins, including GCPs 4-6, GCP8 (MZT2), GCP-WD and GCP9 (MZT1) (the GCP nomenclature is used throughout, however, species-specific names for each of the GCP proteins exist and are summarised in Table 1.1). In humans, *Drosophila* and *Xenopus,* electron microscopy showed that the complex forms a ring-like structure leading to the name γ-TuRC (Keating and Borisy, 2000; Moritz et al., 2000; Zheng et al., 1995). Importantly, the γ-TuRC is much more efficient MT nucleator than the γ-TuSC (Oegema et al., 1999).

Table 1.1. Summary of γ-tubulin complex proteins in various species. The γ-TuSC components are indicated in yellow, and the γ-TuRC-specific components in green.

GCP name	*H. sapiens*	*X. leavis*	*D. melanogaster*	*A. thaliana*	*S. pombe*	*A. nidulans*	*S. cerevisiae*
γ-tubulin (GCP1)	γ-tubulin	γ-tubulin	γ-tubulin	γ-tubulin	Gtb1/Tubg 1	MipA	Tub4
GCP2	GCP2	Xgrip110	Dgrip84	AtSpc97	Alp4	AnGCP2	Spc97
GCP3	GCP3	Xgrip109	Dgrip91	AtSpc98	Alp6	AnGCP3	Spc98
GCP4	GCP4	Xgrip76	Dgrip75	AtGCP4	Gfh1	AnGCP4	-
GCP5	GCP5	Xgrip133	Dgrip128	AtGCP5	Mod21	AnGCP5	-
GCP6	GCP6	Xgrip210	Dgrip163	AtGCP6	Alp16	AnGCP6	-
GCP7	GCP-WD NEDD1	NEDD1	Dgp71WD	AtNEDD1	-	-	-
GCP8	MOZART2A MOZART2B	Mzt2	-	-	-	-	-
GCP9	MOZART1	Mzt1	Mzt1	Gip1	Mzt1	-	-

The precise stoichiometry of the γ-TuRC remains unclear and varies between species. In humans, an average complex contains approximately 14 copies of γ-tubulin, 6 copies of each GCP2 and GCP3, in addition 2-3 copies of GCP4, one copy of GCP5 and less than one copy of GCP6, which suggests that GCP6 is found in only a subset of γ-TuRCs (Choi et al., 2010). GCP7 and GCP8 are believed to play a regulatory rather than a structural role, and are present at lower stoichiometries. GCP7, found in plants and animals, but not fungi, is non-essential for γ-TuRC assembly and acts to target the γ-TuRC to MTOCs (Gunawardane et al., 2003; Haren et al., 2006). GCP8 is a small protein conserved only in deuterostomes and is also dispensable for γ-TuRC assembly; instead, it acts to recruit the γ-TuRC to interphase centrosomes (Teixidó-Travesa et al., 2010). Human GCP9 is required for γ-TuRC recruitment to mitotic centrosomes (Hutchins et al., 2010). The fission yeast GCP9^{Mzt1} is essential, interacts directly with GCP3^{Alp6} and is present in cells and at SPBs in similar to GCP2^{Alp4} (Dhani et al., 2013; Masuda et al., 2013). In plants, GCP9^{Gip1} interacts only with GCP7-free γ-TuRCs, and at lower stoichiometries than those observed in fission yeast (Janski et al., 2012; Nakamura et al., 2012).

Historically, there were two models of the γ-TuRC assembly. In the *protofilament model*, the γ-TuRC unfolds to form a γ-tubulin protofilament that nucleates a MT through lateral interactions with α,β-tubulin protofilaments (Erickson, 2000; Erickson and Stoffler, 1996). In the *template model*, the γ-TuRC acts as a

direct template for MT nucleation by forming a ring of γ-tubulin molecules and therefore enhancing the intrinsically weak lateral interactions between α,β-tubulin heterodimers. Initially, it was believed that the γ-TuSC proteins form the ring, while the γ-TuRC-specific proteins (GCPs 4-6) create a cap located at the base of the complex (Moritz et al., 2000). Recent crystallographic work suggested that *grip* domains of GCPs 2-6 form a structural core that is common for all *grip*-GCPs (Guillet et al., 2011). This led to a *revised template model*, in which GCPs 4-6 are integrated in the γ-TuRC structure, potentially at the start or end of the γ-TuRC helix. Recently discovered *non-grip*-GCPs (GCPs 7-9) could form a structural cap that mediates γ-TuRC localisation to cellular MTOCs (Fig 1.2) (Remy et al., 2013).

Unlike other organisms, budding yeast appear to have lost their γ-TuRC-specific proteins, and contain only GCPs 1-3. This suggests that the γ-TuSC is the core of the nucleation machinery; this notion is additionally supported by the fact that the γ-TuRC proteins are nonessential in a variety of biological systems, such us the fission yeast *Schizosaccharomyces pombe* or *Drosophila.* Recombinant γ-TuSCs from *S. cerevisiae* are V-shaped and consist of two molecules of γ-tubulin at tips, which interact with C-termini of GCP2 and GCP3. Interestingly, γ-TuSCs can oligomerise *in vitro* to form a 22S complex, comparable in size to the 25-35S γ-TuRC, but this process is sensitive to buffer conditions (Vinh et al., 2002). EM studies showed that *in vitro*, in the presence of a short N-terminal fragment of a γ-TuC adaptor protein Spc110 and glycerol, budding yeast γ-TuSCs assemble into multimeric structures with a slight helical pitch (Kollman et al., 2010). Assembly of γ-TuSC helices allowed single particle reconstruction at 8 Å resolution. Strikingly, γ-TuSCs oligomer structure revealed that there are 6.5 γ-TuSCs (which equals 13 γ-tubulin molecules) per helix turn, which matches perfectly the *in vivo* symmetry of the MT, made of 13 protofilaments. The 13-fold symmetry of the multimeric γ-TuSC is a result of conformations of GCP2 and GCP3 alone, with a very little contribution of the γ-tubulin itself. γ-TuSCs use lateral associations to assemble into a helix, positioning the γ-tubulin in a such way that it is oriented to expose its putative binding site allowing for interaction with α-tubulin longitudinally, but not laterally (Kollman et al., 2010). This rules out the *protofilaments* model in which the lateral associations between the γ-tubulin protofilaments and the α,β-tubulin heterodimers promoted MT nucleation (Erickson, 2000). Similar helical pitch is also observed in *Drosophila* γ-TuRCs; therefore, it seems plausible that the γ-TuSC and the γ-TuRC

use the same assembly mechanism (Moritz et al., 2000). In higher eukaryotes, GCPs 4-6 might occupy specific positions at the start and end of this helix to determine its exact size. Potentially GCP 4-6 can also play a role in complex stabilisation (Fig. 1.2) (Remy et al., 2013).

The symmetry of the γ-TuSC oligomer does not, however, perfectly match the 13-fold symmetry of a MT (Kollman et al., 2010, 2011). The γ-tubulin molecules within the oligomer are not in contact with each other, which is required to match the MT 13-fold symmetry. This might explain the low nucleation activity of purified γ-TuSCs *in vitro* - they might be in an "off" state and require a conformational change in order to become nucleation-competent. The γ-tubulin molecules bound to GCP3 are out of alignment with those bound to GCP2, and would require a conformational change in GCP3 in order to properly align. Rotation of approximately 20º around a hinge present in GCP3 would be sufficient to align the γ-tubulin molecules into optimal positions (Guillet et al., 2011). The crystal structure of GCP4 showed that *grip1* motif is likely to form interface promoting lateral GCP interaction, while *grip2* interacts with the γ-tubulin. Importantly, the interaction between GCP4 and γ-tubulin was confirmed by immunoprecipitation, and required the C-terminus of GCP4, similarly to GCP2 and GCP3 (Cala et al., 2013; Guillet et al., 2011). When oligomerisation of γ-TuSCs is blocked by buffer conditions, they loose all their nucleation capacity, suggesting that some degree of multimerisation is essential to promote nucleation. How this conformational control is achieved is currently not clear, however it was suggested that allosteric activation might occur upon binding of γ-TuRC adaptor proteins.

1.5 Regulation of the γ-TuC

All of the GCPs were identified in co-precipitation experiments, but it is important to note that many proteins co-purify with the γ-TuRC at lower molecular ratios. These include attachment factors and regulatory subunits.

Attachment factors localise the γ-TuC to prospective MTOCs. In animal cells, there are several proteins that target the γ-TuRC to the centrosome, the main MTOC (Teixidó-Travesa et al., 2012). These proteins include AKAP450 (often referred to as AKAP9) (Takahashi et al., 2002), pericentrin (Zimmerman et al., 2004), CDK5RAP2 (also known as Cep215) (Fong et al., 2008) and myomegalin (MMGL, also known as PDE4DIP) (Roubin et al., 2013). Pericentrin and AKAP450 both bind

directly to GCP2 and GCP3 and tether the γ-TuRC to mitotic centrosomes. They also recruit other γ-TuRC-interacting proteins to MTOCs; CDK5RAP2 localisation to centrosomes depends on pericentrin (Andersen et al., 2003; Bond et al., 2005; Wang et al., 2010), while MMGL localises to centrosomes in an AKAP450-dependent manner (Roubin et al., 2013).

In humans, GCP-WD has been shown to be required for interphase and mitotic localisation of the γ-TuRC to the centrosome, but itself it localises to the centrosome independently of the γ-TuRC (Haren et al., 2006). GCP8 is required for γ-TuRC localisation to interphase centrosomes only, but its centrosomal localisation is GCP-WD-dependent (Teixidó-Travesa et al., 2010). In budding yeast, two γ-TuC adaptor proteins, Spc110 and Spc72 recruit the γ-TuC to the nucleoplasmic and cytoplasmic faces of the SPB, respectively (Knop and Schiebel, 1998). In fission yeast, a similar phenomenon is observed: Pcp1 recruits the γ-TuC to the nucleoplasmic face of the SPB while Mto1 recruits the γ-TuC to the cytoplasmic face of the SPB as well as other interphase MTOCs (Flory et al., 2002; Samejima et al., 2010; Sawin et al., 2004; Venkatram et al., 2004).

To localise to the centrosome, human γ-tubulin needs to be assembled into the γ-TuRC (Izumi et al., 2008; Teixidó-Travesa et al., 2012). By contrast, in lower eukaryotes such as *S. pombe, A. nidulans* or *D. melanogaster*, the γ-TuRC specific components are dispensable for γ-tubulin localisation to the centrosome (Anders et al., 2006; Fujita et al., 2002; Venkatram et al., 2004; Vérollet et al., 2006; Xiong and Oakley, 2009). Moreover, the budding yeast *S. cerevisiae* completely lack γ-TuRC-specific proteins and yet is able to nucleate MTs from the SPB. Potentially, in these organisms the ring-like structure is formed from γ-TuSCs only, with an aid of γ-TuRC localising factors. Quantitative analysis of budding yeast MT nucleating complexes *in vivo* showed that they contain approximately seven γ-TuSCs (Erlemann et al., 2012), which corresponds to one γ-TuRC. In fission yeast, the actively nucleating γ-TuCs also contain approximately seven γ-TuSCs (Lynch et al., 2013, unpublished).

Several factors act to target the γ-TuC to non-centrosomal MTOCs, such as the Golgi apparatus, the NE or the MT lattice. In vertebrates in mitosis, a multi-subunit augmin complex recruits the γ-TuRC to spindle MTs via GCP-WD as an adaptor protein. Augmin-dependent localisation of the γ-TuRC promotes MT nucleation along existing MTs thereby amplifying the density of MTs within the spindle, independently of centrosomal nucleation (Goshima and Kimura, 2010;

Kamasaki et al., 2013; Petry et al., 2013). The MT lattice serves as MTOC also in lower eukaryotes (Janson et al., 2005; Murata et al., 2005) and potentially neurons (Baas, 2013; Song et al., 2013). The Golgi apparatus is another non-centrosomal MTOC and is believed to be important to create asymmetric MT networks in motile cells (Vinogradova et al., 2009). AKAP450, which anchors the γ-TuRC and its adaptor proteins at the centrosome, has also a role in tethering the γ-TuRC to the Golgi apparatus. The Golgi apparatus localisation of CDK5RAP2 and MMGL depends on AKAP450 (Roubin et al., 2013; Wang et al., 2010).

As mentioned previously, to induce MT nucleation, the γ-TuRC is predicted to undergo conformational changes to align the 13 molecules of γ-tubulin laterally, which would allow it to serve as a template (Kollman et al., 2010, 2011). This requires a conformational change in GCP3. While the γ-TuRC anchoring mechanisms are now partly understood, how the conformational change In GCP3 occurs remains to be shown. An immediate hypothesis is that it might be induced by an activator protein that is present only at MTOCs. Such a γ-TuRC activator could be CDK5RAP2. One of the CDK5RAP2 conserved motifs, referred to as CM1 (Centrosomin Motif 1, will be discussed in more detail in Section 1.6.2.1), is conserved in several other γ-tubulin tethering proteins, including human MMGL, *Drosophila* centrosomin, fission yeast Mto1 and Pcp1 (Fong et al., 2008; Roubin et al., 2013; Sawin et al., 2004). Together, these proteins are referred to as CM1 proteins. Full length CDK5RAP2 as well as a short CM1-containing fragment increases the MT nucleation capacity of γ-TuRC in cells and *in vitro* (Choi et al., 2010). In fission yeast, mutations within the Mto1 CM1 region abolish γ-TuC-Mto1 binding and completely abolish cytoplasmic MT nucleation (mitotic spindle MTs are nucleated by the action of Mto1 paralogue, Pcp1) (Flory et al., 2002; Samejima et al., 2008).

An alternative hypothesis is that the conformational change in the γ-TuRC structure could be achieved by post-translational modification (PTM) of *grip*-GCP proteins (Kollman et al., 2011). The most commonly occurring PTM is phosphorylation; γ-tubulin itself was shown to be phosphorylated in budding yeast, and this regulated the γ-TuC MT nucleation activity (Keck et al., 2011; Lin et al., 2011; Vogel et al., 2001). The γ-TuSC subunits are also phosphorylated, but the significance of this phosphorylation remains to be studied (Keck et al., 2011; Lin et al., 2011). In humans, γ-tubulin is also phosphorylated which might play a role in

formation of centriolar MTs (Alvarado-Kristensson et al., 2009). In polarised epithelial cells, GCP6 phosphorylation regulates γ-TuRC localisation (Oriolo et al., 2007). In addition, GCPs 2-4 contain several uncharacterised phosphorylation sites that could contribute the γ-TuRC regulation, but their role remains to be studied (Hegemann et al., 2011; Kettenbach et al., 2011). Thus far, it appears that phosphorylation of γ-TuRC components plays a regulatory rather than activating role.

γ-TuRC attachment factors also undergo phosphorylation, which regulates the γ-TuRC nucleation activity. In *Drosophila*, the CDK5RAP2 homologue, centrosomin (Cnn) phosphorylation by Plk1 is required for γ-tubulin recruitment to the centrosome (and centrosome maturation) (Dobbelaere et al., 2008). In vertebrates, Plk1 phosphorylates several centrosomal proteins including CDK5RAP2 and pericentrin (Haren et al., 2009; Lee and Rhee, 2011), which plays a role in recruitment of these proteins to PCM as well as recruitment of the γ-TuRC. GCP-WD phosphorylation by Cdk1 and Plk1 is required for the recruitment of the γ-TuRC to spindle MTs, and abolishment of phosphorylation by Cdk1 leads to phenotype resembling augmin depletion (Lüders et al., 2006; Uehara et al., 2009).

1.6 Microtubules in *S. Pombe*

1.6.1 Microtubule organisation in fission yeast

Fission yeast is a haploid unicellular organism with relatively complex network of MTs that changes dramatically during the cell cycle. Owing its genetic tractability, high recombination rates and short generation time, it has become an attractive model to study MT organisation and dynamics. *S. pombe* are rod-shaped cells that typically measure 3-4 μm in width and 7-14 μm in length. Upon reaching 14 μm, cells stop growing and commit to mitosis. The cell shape is defined by the way cells grow: they elongate exclusively through the cell tips and divide by medial fission, which leads to generation of two identical daughter cells.

An interphase fission yeast cell contains from three to five spatially discrete MT bundles that align with the long axis of the cell such that their plus ends are facing the cell tips and minus ends are oriented towards the nucleus (Hagan, 1998; Sawin and Tran, 2006) (Figure 1.3). This polar arrangement ensures the establishment of the cell polarity and facilitates bipolar growth by delivery of polarity factors to cell tips (Piel and Tran, 2009). MT bundles consist of many MTs that are

arranged in an atiparallel manner with their minus ends located in the vicinity of MTs as well as further away from iMTOCs (interphase MTOCs) (Höög et al., 2007). MTs are held together within bundles by bundling proteins such as Ase1 and Dis1 (Janson et al., 2007; Roque et al., 2010). Interphase MTs are nucleated from the interphase SPB (iSPB) and from a variety of iMTOCs that are located along pre-existing MTs, at the NE and in the cytoplasm. Upon mitotic entry, the interphase MT network disassembles and intranuclear spindle MTs are formed at the nucleoplasmic face of the SPB. Fission yeast undergoes a "closed" mitosis; therefore, to promote spindle MT nucleation the SPB gets inserted into a fenestra that form within the nuclear membrane during mitotic commitment (Ding et al., 1997). The SPB insertion process was recently suggested to be similar to nuclear pore insertion into the NE (Jaspersen and Ghosh, 2012)

In anaphase, astral MTs are nucleated from the cytoplasmic face of the SPB, which was suggested to play a role in spindle positioning along the long axis of the cell to ensure the genetic material is distributed evenly following mitosis (Tolić-Nørrelykke et al., 2004). However, the spindle alignment is largely unaffected in the absence of astral MTs (Zimmerman and Chang, 2005). Following completion of mitosis and initiation of mitotic spindle disassembly, a post-anaphase array (PAA) of MTs is nucleated from equatorial MTOCs (eMTOCs) at the site of septation. PAA formation depends on the formation of the contractile actomyosin ring, which is positioned medially in the cell to ensure the two daughter cell are identical (Feierbach and Chang, 2001; Pardo and Nurse, 2003). The exact position of the actomyosin ring is defined by the release of the protein Mid1 by the nucleus. Mid1 binds to the cell cortex and recruits actomyosin ring components (Daga and Chang, 2005; Sohrmann et al., 1996). Cells lacking the PAA are viable (Sawin et al., 2004; Venkatram et al., 2005), but PAA MTs maintain the medial position of the actomyosin ring, and can also play a role in separating diving nuclei (Hagan and Yanagida, 1997; Pardo and Nurse, 2003).

During fission yeast meiosis, MTs are organised in a radial array, and originate from the radial MTOC located at the cytoplasmic face of the SPB (Funaya et al., 2012; Sawin, 2005).

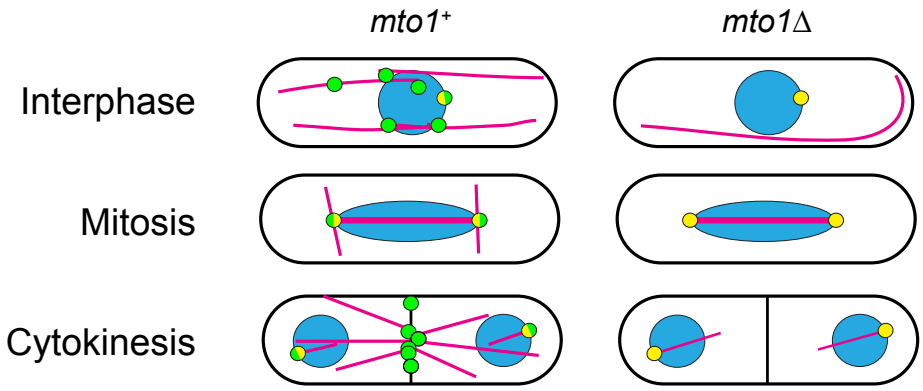

Figure 1.3. Changes in MT cytoskeleton during cell cycle progression in fission yeast. MTOCs containing Mto1 are shown in green while MTOCs containing Pcp1 in yellow. In wild type cells, interphase MTs (magenta) are nucleated from iMTOCs (green) localised along pre-existing MTs, at the NE and from cytoplasmic face of the SPB (yellow/green). Upon mitotic entry, cytoplasmic MT network is disassembled to give place to mitotic spindle. In mitosis, spindle and astral MTs are nucleated from the duplicated SPBs. During cell division, MTs are nucleated from eMTOCs. In *mto1*Δ cells, all *de novo* cytoplasmic nucleation is abolished; abnormal MTs, often observed in interphase *mto1*Δ cells are remnants of mitotic spindle that persisted from previous mitosis.

1.6.2 γ-tubulin complex in *S. pombe*

The fission yeast homologues of γ-TuSC components: γ-tubulin, GCP2 and GCP3 (known as Gtb1, Alp4 and Alp6, respectively) are essential for viability (Horio et al., 1991; Stearns et al., 1991; Vardy and Toda, 2000). However, the GCPs 4-6 proteins (Gfh1, Mod21 and Alp16, respectively) are dispensable for both interphase and mitotic MT nucleation (Anders et al., 2006; Fujita et al., 2002; Venkatram et al., 2004). Even though the ring-like structure was never observed in fission yeast (therefore, I do not use the term "γ-TuRC" to describe *S. pombe* "large" γ-TuC, and only use this term to describe those complexes where the ring has been directly observed by EM), GCPs 4-6 colocalise with the γ-TuSC components at nucleation sites, implying that the γ-TuRC might exist in this organism (Anders and Sawin, 2011). Alternatively, GCPs 4-6 might play regulatory role, which is supported by the observation that both individual and simultaneous deletion of GCPs 4-6 showed no apparent defects in interphase MT architecture, but resulted in decreasing the number of interphase MT bundles, while the stability of MT bundles increased (Anders et al., 2006). No additive effect was observed upon simultaneous deletion of GCPs 4-6, implicating that these proteins share a common role in the γ-TuC assembly or regulation. These results suggest that in fission yeast the γ-TuSC

components in association with its adaptors: the Mto1/2 complex and Pcp1 (see below), are sufficient for promoting MT formation.

1.6.2.1 γ-tubulin complex adaptor proteins in *S. pombe*

In fission yeast, cytoplasmic and nuclear MT nucleation is spatially and temporally separated. Cytoplasmic γ-TuC localisation is promoted by the Mto1/2 complex, which is required for all interphase cytoplasmic MT nucleation. In mitosis, the protein Pcp1 is required for spindle MT formation.

1.6.2.1.1 The Mto1/2 complex

Regulation of cytoplasmic γ-TuC activity was shown to dependent on two auxiliary proteins, Mto1 and Mto2, which form the Mto1/2 complex recruiting the γ-TuC to prospective MTOCs (Samejima et al., 2005, 2008, 2010; Sawin et al., 2004; Venkatram et al., 2004, 2005). Both proteins, which localise to all cytoplasmic MTOCs and are essential for non-SPB MT nucleation, were identified in an insertional mutagenesis screen designed to find nonessential genes regulating cell shape and cell polarity (Samejima et al., 2005; Sawin et al., 2004; Snaith and Sawin, 2003). Deletion of either *mto1* or *mto2* leads to formation of abnormal interphase MT arrays, with a greatly reduced total number of interphase MT bundles that curve around the cell tips (Fig. 1.3).

In wild-type cells, Mto1 and Mto2 colocalise with the γ-TuC at all cytoplasmic MTOCs (along MTs, at the NE, at the iSPB, at the eMTOCs). In *mto1*Δ cells, Mto2 and γ-TuC localisation to iMTOCs and eMTOCs is abolished, although the γ-TuC still localises to SPBs in a process believed to be mediated by Pcp1 (mitosis-specific Mto1 paralogue; discussed in more detail in Section 1.6.2.1.2) (Flory et al., 2002; Samejima et al., 2005; Sawin et al., 2004; Venkatram et al., 2004, 2005). Live-cell imaging revealed that deletion of *mto1* results in a complete loss of MT nucleation from iMTOCs, eMTOCs and the cytoplasmic face of the SPB (responsible for nucleating interphase MTs as well as astral MTs in mitosis). In *mto1*$^{+}$ cells, cold-depolymerised MTs start to form approximately one minute after shifting to warm temperature, while in *mto1*Δ cells first cytoplasmic MTs are first observed after 15 minutes (Sawin et al., 2004). These MTs originate from spindle MTs nucleated in a Pcp1-dependent manner in mitosis. Following nucleation inside the nucleus, these MTs break through the NE and persist in the cytoplasm through subsequent interphase (Sawin et al., 2004; Zimmerman and Chang, 2005).

In *mto2*Δ cells, unlike in *mto1*Δ cells, MT nucleation from the cytoplasmic face of the SPB is preserved. Astral MTs are observed in anaphase, and SPB-derived MTs are nucleated in interphase. Moreover, the ability to nucleate PAA MTs is partially retained, however, the MT nucleation from eMTOCs is severely reduced in *mto2*Δ cells when compared to wild-type cells (Samejima et al., 2005; Venkatram et al., 2005). Mto1 localisation to MTOCs is only partially affected in *mto2*Δ cells: the SPB localisation is unaffected, and reduced levels of Mto1 are also observed at eMTOCs and on MTs. Similarly, the γ-TuC localises normally to the SPB, while its localisation to eMTOCs is reduced, and to the MT lattice – abolished. Overexpression of Mto1 in *mto2*Δ cells is sufficient to rescue Mto1 localisation to cytoplasmic MTOCs leading to decoration of MTs and the NE (Samejima et al., 2005). Mto2, on the other hand, requires simultaneous overexpression of Mto1 to mirror the localisation pattern of overexpressed Mto1. These observations suggest that Mto2 localisation to MTs and to the NE is an Mto1-dependent process.

Co-immunoprecipitation experiments demonstrated that Mto1 and Mto2 strongly interact to form the Mto1/2 complex (Samejima et al., 2005; Venkatram et al., 2005). The Mto2 interaction domain of Mto1 is located in the central part of Mto1 within the coiled-coil regions. Attempts to find the Mto1 interaction domain of Mto2 by truncation analysis failed, because generated Mto2 truncations exhibited lower protein stability (Groocock PhD Thesis, 2010).

A detailed analysis of Mto1 showed that the protein contains several interaction and localisation domains that are responsible for the recruitment of the Mto1/2 complex to cytoplasmic MTOCs and for binding of the γ-TuC. The NE-localisation domain, located at the N-terminus, is followed by the CM1 (centrosomin motif 1) domain (Lynch et al., 2013, unpublished; Samejima et al., 2008). The Mto2 binding region Is located centrally, in the region of predicted coiled-coils (Samejima et al., 2008). Abolition of the Mto1-Mto2 interaction in *mto1-334* mutant leads to an *mto2*Δ-like phenotype: a partial loss of Mto1 and γ-TuC localisation to iMTOCs and abolition of MT nucleation from these sites.

The CM1 region of Mto1 is also required for the Mto1/2 complex function. The CM1 is an approximately sixty amino-acid sequence motif conserved in most organisms. CM1 proteins – including *Drosophila* centrosomin (cnn), human CDK5RAP2 (mutated in a form of primary autosomal microcephaly), and MMGL (implicated in schizophrenia), and fission yeast Mto1 and Pcp1 – have been implicated in γ-TuC binding in several systems (Bond et al., 2005; Flory et al., 2002;

Kim et al., 2012; Megraw et al., 1999; Roubin et al., 2013; Samejima et al., 2008; Sawin et al., 2004; Verde et al., 2001; Zhang and Megraw, 2007). A small region of CDK5RAP2 encompassing the CM1 stimulated γ-TuRC-dependent MT nucleation *in vitro* (Choi et al., 2010). *mto1-9A1* cells, in which nine conserved residues within the CM1 region were mutated to alanines to eliminate the γ-TuC-Mto1/2 interaction, phenocopy *mto1*Δ with respect to MT nucleation and γ-TuC localisation (Samejima et al., 2008). However, unlike the CM1 region of CDK5RAP2, the CM1 domain of Mto1 is not sufficient to promote the interaction between the γ-TuC and Mto1. This is because both the Mto2-binding domain and the CM1 region must be present within Mto1 for normal Mto1/2 function (Samejima et al., 2008).

Mutagenesis of Mto1 C-terminus identified a conserved region referred to as MASC (Mto1 and Spc72 C-terminus), which is found at the C-terminus of a single protein in a variety of yeast species (Samejima et al., 2010). One of the proteins containing MASC is Spc72, an Mto1 functional homologue in budding yeast that is responsible for nucleating MTs from the outer plague of budding yeast SPB (Knop and Schiebel, 1998). The MASC region promotes Mto1/2 complex localisation to interphase and mitotic SPBs and to eMTOCs (Samejima et al., 2010). Different subregions of MASC target Mto1 to distinct subcellular sites; however, GFP-tagged MASC fragments only localise to MTOCs when they are multimeric, which most likely increases the avidity of Mto1 binding to MTOCs.

The Mto1/2 complex formation is essential for non-SPB MT nucleation (Samejima et al., 2008). Interestingly, work of E. Lynch in Sawin lab showed that the Mto1/2 complex is able to stimulate MT formation by the γ-TuC independently of its localising it (Lynch, unpublished). In *mto1[bonsai]* cells, where Mto1 is truncated at both termini, and is not able to bind to any conventional MTOCs, the Mto1/2[bonsai] complex promotes robust MT nucleation occurring freely in the cytoplasm. Fluorescence quantification revealed that the Mto1/2[bonsai] complex consists of approximately thirteen copies of both Mto1 and Mto2 *in vivo*. Formation of the Mto1/2 complex and subsequent recruitment of the γ-TuC and MT nucleation does not require γ-TuRC specific proteins. In fission yeast, $GCP6^{Alp16}$ is required for association of GCP4 and GCP5 with the γ-TuSC; therefore, deletion of $GCP6^{Alp16}$ phenocopies simultaneous deletion of *GCPs 4-6* genes. In $GCP6^{Alp1}\Delta$ cells, MTs are nucleated with near to wild-type frequency. These results suggested that fission yeast γ-TuRC assembly might be promoted by the Mto1/2 complex, independently of γ-TuRC specific components.

1.6.2.1.2 Pcp1

Pcp1 is an essential Mto1 paralogue that is thought to be responsible for spindle MT nucleation. It contains several predicted coiled-coil regions and localises to the inner face of the SPB throughout the cell cycle (Flory et al., 2002). Moderate overexpression of Pcp1 leads to formation of ectopic SPB-like structures, defects in spindle architecture and chromosome missegregation. Pcp1 localisation to SPB is mediated by the PACT (pericentrim-AKAP450 centrosomal targeting) domain located towards the C-terminus and conserved in several centrosomal/SPB proteins such as kendrin, pericentrin, AKAP450 or Spc110 (Flory et al., 2000; Geiser et al., 1993; Gillingham and Munro, 2000). The PACT domain interacts with calmodulin, an SPB scaffold protein (Muller et al., 2005). The centrally located extensive coiled-coil regions are dispensable for Pcp1 function, as *pcp1Δ(400-900)* cells are viable and show only mild mitotic delay (Rajagopalan et al., 2004). Similarly to other CM1 proteins, Pcp1 contains the CM1 domain at its N-terminus.

Pcp1 is thought to interact with the γ-TuC throughout the cell cycle; yet, Pcp1-mediated nucleation is restricted to the mitotic phase of the cell cycle, therefore suggesting that MT nucleation is regulated independently of the γ-TuC-Pcp1 interaction (Flory et al., 2002; Fong et al., 2010). However, a *pcp1* temperature sensitive allele containing two point-mutations, one of which is within the CM1 region, fails to recruit the γ-TuC to mSPBs but not iSPBs, suggesting that the γ-TuC is recruited to the nucleoplasmic face of iSPBs in Pcp1-independent manner (note that this localisation is also Mto1-independent) (Fong et al., 2010). Another *pcp1* temperature sensitive allele fails to recruit polo kinase (Plo1) to mSPBs resulting in defective reorganisation of the NE upon mitotic entry, implying a role of Pcp1 in mitotic entry (Fong et al., 2010).

1.7 Human CM1 proteins and associated diseases

In humans, there are several γ-TuRC anchoring proteins (discussed in Section 1.5). Two of them, CDK5RAP2 and MMGL, are functional homologues of fission yeast Mto1 and Pcp1, and belong to the family of CM1 proteins that consists of proteins possessing a conserved γ-tubulin binding CM1 domain. Both MMGL and CDK5RAP2 CM1 regions were shown to interact with the γ-TuC (Choi et al., 2010; Roubin et al., 2013).

CDK5RAP2 (CDK5 regulatory subunit associated protein 2), also known as Cep215 (Centrosomal Protein 215 kDa), was initially identified in a rat brain yeast two hybrid screen to identify interactors of Cdk5R1 (Ching et al., 2000; Wang et al., 2000). In 2005, CDK5RAP2 was linked to microcephaly (MCPH), when sequencing of genomic DNA of families with MCPH revealed that one of the seven MCPH loci (MPCH3) encodes CDK5RAP2 (Bond et al., 2005). CDK5RAP2 localizes to the centrosome and Golgi apparatus throughout the cell cycle in a pericentrin- and AKAP450-dependent manner (Andersen et al., 2003; Bond et al., 2005; Graser et al., 2007; Wang et al., 2010). In developing embryos it is expressed mainly in the brain and spinal cord (Bond et al., 2005). Primary expression takes place in the neuroepithelium, and the expression pattern is consistent with a role in regulating neurogenic mitosis (Bond et al., 2005). Interestingly, MMGL has an expression pattern complementary to CDK5RAP2 (Verde et al., 2001). In human cells, endogenous and ectopically expressed CDK5RAP2 colocalises with the γ-tubulin at the centrosome throughout the cell cycle. When overexpressed, CDK5RAP2 forms aggregates that recruit centrosomal proteins: γ-tubulin, pericentrin and Cep250. In co-immunoprecipitation experiments, CDK5RAP2 coprecipitates and cosediments with the γ-TuRC. However, sedimentation analysis demonstrated that CDK5RAP2 depletion by siRNA does not influence γ-TuRC structure, indicating that it is not required for the γ-TuRC integrity. Instead, depletion of CDK5RAP2 strongly decreases γ-tubulin and pericentrin staining at the centrosome and leads to disruption of interphase MT arrays. In mitosis, cells lacking CDK5RAP2 are incapable of formation of astral MT and display chromosome missegregation (Fong et al., 2008; Haren et al., 2009; Zhang et al., 2009). Importantly, a small region of CDK5RAP2 encompassing the CM1 is able to promote γ-TuRC-dependent nucleation *in vitro* (Choi et al., 2010).

Myomegalin (MMGL) was first identified in 2001 (Soejima et al., 2001; Verde et al., 2001) in a screen designed to identify PDE4-interacting proteins (Verde et al., 2001). PDE4 is a cyclic nucleotide phosphodiesterase, and is a part of cAMP signalling pathway. Several isoforms of PDE enzymes degrade cAMP by hydrolysing phosphodiester bond. PDE4 is implicated in several human diseases including Alzheimer's disease and autoimmune diseases such as arthritis (García-Osta et al., 2012; Kumar et al., 2013; Michalski et al., 2012).

Verde and colleagues showed that myomegalin is highly expressed in rat muscles and heart. Given the protein high abundance in muscles the large size of

the protein (2324 amino acids, 262 kDa) this newly identified gene was termed myomegalin (Verde et al., 2001). There are several isoforms of MMGL expressed in different tissues, many of them containing domains implicated in MT-related functions such as MT nucleation of MT dynamics (Overlack et al., 2011; Roubin et al., 2013; Verde et al., 2001). MMGL is mostly made of coiled coils and α-helices; it contains a leucine zipper at its N-terminus, homologous to *Drosophila* centrosomin leucine zipper (Verde et al., 2001). Some of the isoforms contain the CM1 region (shown in other systems to be required for γ-tubulin binding), the CM2 region (mediating localisation to Golgi and the centrosome) and a region homologous to dynactin (Choi et al., 2010; Samejima et al., 2008; Verde et al., 2001; Wang et al., 2010). This region in dynactin is responsible for interaction within a complex involved in trafficking vesicles along MTs (Burkhardt, 1998). Moreover, MMGL contains a helix-loop-helix domain homologous to MT-binding protein CLIP-170 (Pierre et al., 1992; Verde et al., 2001). Analysis of primary MMGL sequence revealed the presence of three SxI/LP motifs, which promote MMGL binding to the plus-end tracking protein EB1 (Jiang and Akhmanova, 2011; Roubin et al., 2013). Two human isoforms of MMGL have been shown to play a role in regulation of MT nucleation and dynamics at the Golgi apparatus (Roubin et al., 2013). Isoform one, referred to as CM-MMG, containing the CM1 region, colocalises with γ-TuRC components (γ-tubulin, GCP2, NEDD1) at the centrosome and *cis*-side of the Golgi apparatus in the CM1-dependent manner. Depletion of CM-MMG resulted in a decrease in centrosomal MT nucleation and a complete abrogation of Golgi-derived nucleation of MTs. Isoform six, called EB-MMG, binds to EB1 through 3 SxI/LP motifs at its N-terminus.

MMGL has been implicated in several human diseases. Anti-myomegalin antibodies were detected in patients with esophageal squamous cell, and can be used as a tumour marker (Shimada et al., 2007). In 2011, MMGL was suggested to play a role in Usher syndrome, one of the most frequent causes of combined hereditary deaf-blindness (Overlack et al., 2011). A protein complex consisting of MMGL and Usher syndrome protein SANS might play a role in MT-dependent cargo transport towards the ciliary base of photoreceptor cells. It was also suggested MMGL might be a potential target for therapeutic intervention in schizophrenia, bipolar disorder and depression (Kim et al., 2012; Shapshak, 2012).

Project Aims

Many of the proteins involved in spatial and temporal regulation of MT nucleation have been identified. In fission yeast the interphase vs. mitosis regulation is achieved by the use of two different γ-TuC adaptor proteins, Mto1 and Pcp1. Both of these proteins contain a conserved γ-TuC binding region, the CM1. We hypothesised that the sequence differences between CM1 regions of Mto1 and Pcp1 contribute to the differential regulation of these two proteins, for example by allowing for interaction only with a subset of the total γ-TuC pool. In the first part of my project, I aimed to generate mutants with CM1 domains swapped. If the chimeric Mto1 and Pcp1 proteins changed their nucleation activities during the cell cycle (for example, if Pcp1 promoted nucleation during interphase, or Mto1 promoted MT nucleation in mitosis), this would provide evidence that the CM1 region plays a role in regulation of Mto1 vs. Pcp1 nucleation activity.

In the second part of my project, I focused on the role of Mto2 in the regulation of interphase MT nucleation. In interphase, the multimeric Mto1/2 complex is required for all MT nucleation from iMTOCs. The Mto1/2 complex formation is driven by multimerisation of Mto2. The complex is disassembled upon mitotic entry, which coincides with a loss of interaction between Mto1 and Mto2, as well as with Mto2 hyperphosphorylation. We hypothesised that Mto2 phosphorylation upon mitotic entry could lead to disruption of the Mto1-Mto2 interaction, which "switches off" cytoplasmic nucleation in mitosis. To address this hypothesis, I aimed to generate an Mto2 phosphomutant in which the Mto1-Mto2 interaction is maintained in mitosis. We later hypothesised that Mto2 self-interaction, in addition to the Mto1-Mto2 interaction, might also be disrupted by phosphorylation in mitosis. To address this possibility, I aimed to generate a completely non-phosphorylatable Mto2 phosphovariant. Finally, as Mto2 multimerisation is required for Mto1/2 complex formation and MT nucleation, I aimed to identify Mto2 regions that are crucial the Mto1-Mto2 interaction.

Chapter 2
Materials and methods

2.1 Generation of plasmids for *pcp1(CM1)* mutant construction

Construction of plasmids used for *pcp1(CM1)* mutant generation required few steps. First, additional restriction sites were introduced into *pcp1-GFP* sequence in a pALKS_pcp1-GFP plasmid. Second, heterologous CM1 region sequences were cloned into this plasmid. Third, a pMONO yeast integration plasmid was generated to allow for stable integration of *pcp1* alleles at *leu1* locus. Finally, heterologous *pcp1* genes were cloned into pMONO.

Generation of pALKS_pcp1(R)-GFP

Megaprimer PCR was performed to introduce 4 unique restriction sites into Pcp1 sequence by introducing silent mutations into *pcp1* sequence. The sites introduced were: BspEI, AvrII, XhoI and NruI. Oligonucleotides OKS2117-OKS2126 were used and pKS480 (pALKS_pcp1-GFP) was used as a DNA template. PCR was performed using Phusion polymerase as described below. The resulting PCR product, containing also AatII and StuI sites (present in *pcp1* gene), was blunt-cloned into pJet1,2 [Thermo Scientific] and sequenced as described below, giving rise to pKS1153. AatII-StuI insert was excised from pKS1153 and gel purified. pKS480 was also digested with AatII-StuI and the vector was isolated. To screen for positive clones, colony PCR was performed as described below. Colony PCR was performed using OKS2187-OKS2126, and the amplified region was approximately 1 kb long. The parent vector, pKS480 and the desired cloning product sequences were only different by a few point mutations, and both would give an identical PCR product. To distinguish between pKS480 and the cloning product, PCR product obtained by colony PCR were treated with XhoI, as XhoI restriction site was present in the insert, but not the parent vector. The obtained positive clone was sequenced and added to lab collection (pKS1154).

Generation of pALKS_pcp1(CM1)-GFP

To introduce heterologous CM1 regions and 9A1 mutation into Pcp1, pKS1154 was digested with AvrII-XhoI, as those sites flanked the CM1 region. Inserts containing heterologous CM1 sequences were also generated by AvrII-XhoI, from plasmids containing synthetic genes obtained from GENEART. Following ligation and

transformation, colony PCR was used to screen for desired clones; OKS2126, OKS2151-OKS2153 were used. Obtained plasmids were sequences and added to lab collection (pKS1155-pKS1157). DNA fragment containing 9A1 mutation was generated by PCR using OKS2117, OKS2126, OKS2176 and OKS2177. This was the cloned into pJet1,2 [Thermo Scientific], sequenced and added to lab collection (pKS1163). Following ligation and transformation, colony PCR was used to screen for desired clones; OKS2126 and OKS2176 primers were used. The resulting plasmid was sequenced and added to lab collection (pKS1192).

Generation of pMONO yeast integration plasmid

pDUAl vectors are multipurpose vectors, and allow for introducing the gene of interest either for episomal expression, but also allow for integration into the fission yeast genome (Matsuyama et al., 2004). The episomal expression can be verified by cells requirement for uracil, as the plasmid contains *ura4* gene. The expression plasmid is converted to an integration fragment by digestion with NotI. Resulting fragments are integrated at *leu1* locus, rendering cell prototrophic for leucine. Several attempts to clone DNA fragments containing *pcp1(CM1)-GFP* alleles into pDUAL were unsuccessful, perhaps because of the large size of both the vector and the insert (7.9 and 5.1 kb, respectively).

Therefore, a pMONO plasmid was generated, in which the part of pDUAL that was required for episomal maintenance was removed. The *ars1-ura4* fragment was excised by NotI digest, and a linker containing unique AgeI and KpnI sites was introduced that also removed the NotI sites. The obtained plasmid was sequenced and added to lab collection (pKS1200).

Generation of pMONO_pcp1(CM1)-GFP plasmids

Plasmids pKS1154-pKS1157 and pKS1192 were digested with BssHII to generate inserts. The vector was obtained by pKS1200 digest with BssHII. Following ligation and transformation, colony PCR was used to screen for positive clones (OKS2194, OKS2195 were used). Resulting plasmids (pKS1202-pKS1206) were sequenced.

2.2 Generation of plasmids for Pcp1 bacterial expression

pcp1 fragments flanked by attB1-attB2 sites were generated using pKS1154 as a DNA template and OKS2278-OKS2281 (for Pcp1 N-termnal fragment) or OKS2274-OKS2277 (for Pcp1 C-terminal fragment). These were then cloned to pJET1,2 and

sequenced (to give pKS1208, pKS1209). pKS1208 and pKS1209 were the used as templates for PCR reaction to amplify the attB-attB2 flanked fragments; OKS2274-OKS2276 and OKS2278-OKS2280 primer pairs were used. Obtained Pcp1 products were subjected to BP Clonase II reaction with pKS535 (pDONR™221) donor vector as descried below. Colony PCR was used toidentify desired contructs, which were later sequences and added to laboratory collection (pKS1211, pKS1212). pKS1211, pKS1212 were then subjected to LR reaction with pKS537 (Busso et al., 2005), desired constructs were identified by colony PCR, sequenced and added to the lab collection (pKS1213, pKS1214).

2.3 Growth of *E. coli* strains

All *Escherichia coli* (*E. coli*) strains were grown at 37ºC in liquid LB media (10 g/L Difco Bacto tryptone, 5 g/L Difco Bacto yeast extract, 5 g/L NaCl, pH 7.2) or on solid LB-agar plates (LB + 2% Difco Bacto agar). DH5α [Invitrogen] or TOP10 [Invitrogen] *E. coli* strains were used for cloning and amplification of plasmids. BL21-CodonPlus[DE3]-RIL *E. coli* strain [Stratagene] was used for protein expression. Antibiotics were added to media; ampicillin was used at 100 mg/mL, while kanamycin at 50 mg/mL.

Stain genotypes:

TOP10 Chemically competent *E. coli* [Invitrogen]

F- mcrA Δ(mrr-hsdRMS-mrcBC) φ80lacZΔM15 ΔlacX74 nupG recA1 araD139 Δ(ara-leu)7697 galE15 galK16 rpsL(Str^R) endA1 λ-

DH5α Chemically competent *E. coli* [Invitrogen]

F$^-$ endA1 glnV44 thi-1 recA1 relA1 gyrA96 deoR nupG Φ80d*lacZ*ΔM15 Δ(*lacZYA-argF*)U169, hsdR17(r_K^- m_K^+), λ–

BL21-CodonPlus[DE3]-RIL *E. coli* [Stratagene]

F– *ompT hsdS*(r_B^- m_B^+), *dcm*$^+$ Tet^r *gal endA* Hte (*argU ileY leuW* Cam^r)

2.4 Preparation of *E. coli* competent cells

5mL of LB medium was inoculated with a single *E. coli* colony and grown ON at 37°C. The culture was diluted 1:200 into pre-warmed 100 mL LB supplemented with 20mM $MgSO_4$. The culture was grown at 37°C with shaking until OD_{600} = 0.48. The

cells were then transferred to chilled 250 ml centrifuge bottle and incubated on ice for 10 min. Cells were then harvested by centrifugation in JA14 rotor for 5 min at 5000 rpm at 4°C. The supernatant was discarded and 40 ml of cold sterile-filtered TFB1 buffer (30 mM KOAc, 100 mM RbCl, 10 mM $CaCl_2$, 50 mM $MnCl_2$, 15% glycerol) was added. Cells were resuspended by gentle pipetting, incubated on ice for 5 min and then centrifuged for 10 min at 3000 rpm at 4°C. The supernatant was rejected and 4 ml cold TFB2 (10 mM MOPS, 75 mM $CaCl_2$, 10 mM RbCl, 15% glycerol) was added. Cells were resuspended by gentle pipetting, incubated on ice for 15 min, and then 100 μl portions were aliquoted into pre-chilled Eppendorf tubes and transferred into -80°C for storage. Cells with competency 10^9 [cfu] are obtained when this protocol is used.

2.5 Transformation of *E. coli* strains

100 μl of chemically competent *E. coli* cells were thawed on ice. 20 – 50 ng of plasmid DNA or 100 – 250 ng of DNA obtained in ligation reaction was added to the cells and incubated on ice for 30 minutes. Cells were placed in 42°C heating block for 45 sec and then incubated on ice for further 2 minutes. 900 μL of SOC medium was added and cells were incubated with agitation on an incubation shaker at 37°C for 1 hour. Cells were centrifuged for 30 sec at 13,000 g at RT, the supernatant was discarded, and the pellet was resuspended in 200 μL of SOC. Cells were then split 9:1 and plated on two LB agar plates containing 100 μg/L of an appropriate antibiotic. Glass beads were used to spread cells on plates. Plates were incubated ON at 37°C.

2.6 Isolation of plasmid DNA from *E. coli*

When plasmid DNA was required for PCR or cloning, the DNA was extracted from bacteria using the Nucleospin Plasmid Kit [Machery-Nagel, Germany]. Cells from up to 5 ml of bacterial culture grown in an appropriate antibiotic were centrifuged for 1 minute at 13000 g and re-suspended in 250 μl of cold P1 containing RNAse. 250 μl of buffer P2 was added, tube was mixed by inversion, and the debris was removed by centrifugation for 10 minutes at 13000 g. The clear supernatant was applied to a QIAprep spin column and the then centrifuged for 1 minute at 13000 g to bind the plasmid DNA to the column. The eluate was discarded and the column was washed

twice with 750 μL of PE buffer by centrifugation (2x1 minute at 13000 g). The column was pre-warmed in 65ºC heating block, transferred to a Treff tube and 20-50 μl of warm (65ºC) EB buffer was applied to the centre of the column matrix and left to stand at 65ºC for 1 min. The plasmid DNA was eluted into the microfuge tube by centrifugation 1 minute at 13000 g, the DNA concentration was measured by NanoDrop [Thermo Scientific] and the sample was stored at -20°C.

When plasmid DNA purity was not of a great importance, for example when a large number of colonies were screened to identify positive clones, the DNA was isolated from bacteria using the Zyppy Plasmid Miniprep Kit [Zymo Research]. 1.5 mL of bacterial culture was centrifuged at 13000 g for 2 minutes, the supernatant was discarded and, if the DNA concentration was expected to be low, another 1.5 mL of culture was centrifuged in the same way. The supernatant was discarded and the pellet was resuspended in 550 μl of TE buffer (10 mM Tris, pH=8.0, 1mM EDTA). 100 μL of 7X Lysis Buffer was added and lysis was allowed to proceed for up to 2 minutes, until the solution became clear. 350 μL of cold Neutralization Buffer (containing 100 μg/mL RNase A) was then added and the tube was mixed by inversion. The debris was removed by centrifugation for 5 minutes at 13000 g. The clear supernatant was applied to a Zymo-Spin column. The column was washed with 200 μL of Endo-Wash Buffer followed by 400 μL of Zyppy Wash Buffer. The column was then place in a Treff tube and 20-50 μl of Zyppy Elution Buffer was applied to the centre of the column matrix. The plasmid DNA was eluted into the microfuge tube by centrifugation 1 minute at 13000 g, the DNA concentration was measured by NanoDrop [Thermo Scientific, USA] and the sample was stored at -20°C.

2.7 DNA sequencing

When fission yeast strains were sequenced, colony PCR followed by Exo-AP reaction was used to generate DNA template. Plasmid DNA was used directly. The sequencing reaction contained:

100 ng of DNA (for plasmid) or 250 ng of DNA (for PCR product),

3.2 pmol of primer,

1X BigDye Terminator v3.1 [Applied Biosystems],

10 mM Tris-HCl pH 8.5,

2.5 mM $MgCl_2$

in a final volume of 10 µl.

The sequencing reaction was carried out according to the following programme:

1. 96°C 30 sec
2. 50°C 15 sec
3. 60°C 4 min
4. Repeat steps 1-3 24 times
5. Hold at 4ºC

Sequencing was then carried out on by the University of Edinburgh GenePool sequencing facility, using ABI 3730 capillary sequencing instruments [Applied Biosystems, USA]. The sequencing files were analysed using Seqman sequence analysis software [DNASTAR Inc.].

2.8 Exo-AP reaction

Exo-AP reaction was used to remove excess dNTPs and primers prior to sequencing. 10 µL of mix containing 0.1 U/µL Exonuclease I (NEB) and $1.25x10^{-2}$ U/µL Antarctic Phosphatase (NEB) were added to 25 µL of PCR reaction. Sample was then incubated at 37°C for 30 minutes and then 95°C for 5 minutes in a PCR machine. Samples were stored at -20°C until needed.

2.9 Ethanol DNA precipitation

3 M NaOAc was added to DNA solution to final concentration 0.3 M. The solution was mixed by tube inversion, and two volumes of 96% EtOH was added. The solution was mixed by tube inversion, incubated at RT for 5 minutes, and centrifuged at 13000 g for 5 min at RT. The supernatant was discarded and the DNA pellet was washed with 70% EtOH and centrifuged at 13000 g for 5 min at RT. The Supernatant was discarded and 30-100 µL of TE buffer was added to the tube. The tube was then placed in 65ºC heat block and kept at 65ºC until no EtOH smell was observed indicating complete removal of EtOH from the sample. The DNA concentration was measured by NanoDrop {Thermo Scientific, USA], and the DNA was stored at -20ºC.

2.10 Restriction digestion

Restriction digest was performed using enzymes purchased from New England Biolabs (NEB), unless stated otherwise, using buffers provided with enzymes. The digestion reactions were generally carried out according to the New England BioLabs guideline, but the amount of the restriction enzyme used was increased tenfold. For cloning purposes, 1-5 μg of plasmid DNA was used. For analytical purposes, for instance to verify the presence or absence of an insert, or the plasmid size, approximately 100 ng of plasmid DNA was used. If products of the digestion reaction were to be used in further experiments, they were purified by gel extraction using the QIAquick Gel Extraction Kit [Qiagen]. Total reaction volume was subject to electrophoresis on regular or low-melting agarose gel containing ethidium bromide. The gel concentration depended on the size of the DNA fragment of interest and was kept as low as possible to facilitate gel extraction. The band corresponding to the desired DNA fragment was excised from the gel using a clean microscope coverslip. 300 μL of buffer QG was added for each 100 μg of gel slice. The gel slice was then dissolved in QG buffer during incubation at 50ºC for 15 minutes, interrupted with vortexing. Following dissolving, one gel volume of isopropanol was added, and the sample was mixed by inversion. The sample was then loaded onto a QIAquick silica column, and centrifuged for 1 minute at 13000 to bind DNA. The column was then washed with QG buffer followed by PE buffer. The column was heated to 65ºC, the DNA was eluted into using warm (65ºC) EB buffer (10 mM Tris, pH 8.5). The DNA concentration was estimated by electrophoresis, and the sample was kept at -20ºC.

2.11 Ligation of DNA

Both blunt-end and sticky-end ligation into plasmids was carried out using the Quick T4 Ligation Kit [NEB]. 20 μl ligation reactions were performed, containing: 1 μl Quick T4 DNA ligase, 10 μl 2X Quick Ligase Buffer (132 mM Tris-HCl, 20 mM $MgCl_2$, 2 mM dithiothreitol, 2 mM ATP, 15% Polyethylene glycol, pH=7.6), 50-100 ng of plasmid DNA, and a 3-fold molar excess of insert DNA. Ligation reactions were incubated at RT for 1 h, chilled on ice, and then transformed into *E. coli* or stored at -20ºC.

2.12 Gene synthesis

mto1(CM1), *pcp1(CM1)* and *mto2* mutants were purchased from GENEART [Life Technologies]. Lyophilised plasmid DNA was re-suspended in 1X TE to 100 ng/µL final. This DNA was used as a template for PCR amplification and transformed into yeast or cloned into other plasmids.

2.13 Gateway Cloning

The Gateway® cloning Technology [Invitrogen] is based on Phage I site-specific recombination system used to integrate DNA into *E. coli* genome. Both Phage and *E. coli* DNA contain specific recombination sites, *attP* and *att*B, respectively. After integration into the bacterial genome, recombination occurs between *attB* and *attP* sites to generate *attL* and *attR* sites flanking the integrated piece of DNA on the *E. coli* chromosome (Landy, 1989). This reaction has been used to develop an *in vitro* system, which allows efficient transfer of DNA between plasmids containing modified versions of the recombination sites (Hartley et al., 2000).

2.13.1 Generation of PCR products containing attB1-attB2 flanking sites

To generate DNA fragments flanked by *attB-attB2* sites, PCR primers were purchased that contained 31 bp of *attB-attB2* sequences and ~20 bp of template-specific sequence. Nested PCR was used to avoid using long primers. In the first PCR reaction, primers complementary to the template DNA with only a short fragment of *attB* sites were used. In the second round of PCR, the product from the first round of PCR was used along with primers covering the whole *attB* sequence Extra nucleotides were added between the *attB1* sequence and the START codon to maintain the reading frame. PCR reaction was carried out as described above.

2.13.2 BP recombination reaction

The reaction mix containing 50-100 fmoles of *attB1/2* flanked PCR product and 50 fmoles of pDONR™221 donor vector, 1XTE Buffer pH 7.5 and 2 µL BP Clonase™ II enzyme mix in a final volume of 10 µL. The recombination mix was incubated at RT O/N. The reaction was stopped by adding 2 µg of Proteinase K [Invitrogen] and

incubating the mix at 37°C for 1 hr. 2x5 μL of the reaction was then transformed into DH5α *E. coli*, where the *ccdB* gene from the pDONR™211 plasmid provided negative selection against empty vector, and plated onto LB-agar supplemented with kanamycin. Colonies were analysed by colony PCR, and plasmids were sequenced.

2.14 LR recombination reaction

The 10 μl reaction mix contained: 150 ng of pDONR™221 containing the intert of interest flanked by *attL1-attL2* sites, 150 ng of Destination vector containing *attR1/2* sites, TE pH 8.0 and 2 µl of LR Clonase™ II enzyme mix. Treff tube was gently agitated and then incubated O/N at 25°C. 2 µg of Proteinase K was added to the mixture and incubated for 1 hr at 37°C to stop the reaction. The whole reaction mix was then transformed into DH5α *E. coli*, which were plated onto LB agar containing the appropriate antibiotic. The *ccdB* gene from the pDONR™211 plasmid and destination vectors provided negative selection against empty vector. P0GWA was used as destination vector (Busso et al., 2005). Colonies were analysed by colony PCR, and plasmids were sequenced.

2.15 Large scale bacterial protein expression

BL21-CodonPlus competent *E. coli cells* [Stratagene, USA] were chosen for expression because they allow high-level expression of heterologous proteins in *E. coli.* BL21-CodonPlus cells contain a pACYC-based plasmid containing *argU*, *ileY*, *leuW* tRNA genes to provide extra copies of rare tRNAs, as the limited availability of these rare tRNAs often stalls translation during high-level expression. This *E. coli* strain contains also the T7 promoter, that allows from expression of the T7 phage RNA polymerase only in response to IPTG.

Stationary culture was diluted 1:30 (200 mL in the final volume of 4 L) and grown at 37°C until OD reached 0.08. Protein expression was then induced using 0.05 mM IPTG [Melford, UK] for 2.5 h. Cells were then harvested using Beckmann Avanti J-26 centrifuge and JLA 8.1000 rotor at 5000 rpm for 15 min at 4°C. Cell pellet was collected with a spatula, transferred into a polythene bag and snap-frozen in liquid nitrogen. Bags were stored at -80°C.

2.16 Isolation of bacterially expressed proteins from inclusion bodies

The cell pellets were resuspended in 2 cell volumes (with the assumption that 1 g cells equals 1 mL) of lysis buffer (20 mM Tris pH 8.0, 1 mM EDTA, 5 mM MgCl2, 0.3 mM PMSF, 8 U/ml benzonase, 400 μg/ml lysozyme) and incubated with stirring for 20 min at RT. The French press at 3 x 1500 psi Gauge pressure was used to disrupt cells for 10 min at RT. NaCl to 300 mM final and TX-100 to 1% final was added to the extract, followed by addiotion of an equal volume of resuspension buffer (RB) [50 mM Tris 8.0, 300 mM NaCl, 1 mM EDTA, 1% TX-100, 0.3 mM PMSF]. The solution was vortexed and inclusion bodies were harvested Beckmann Avanti J-25 centrifuge and JA 25.500 rotor at 10000 rpm for 10 min at 4°C. Inclusion bodies were then washed twice by resuspending in RB using Dounce pestle and centrifugation using Beckmann Avanti J-25 centrifuge and the JA 25.500 rotor at 10000 rpm for 10 min at 4°C. After the last spin, the supernatant was discarded and the pellet was resuspended in 4 volumes of PBS [(Phosphate Buffered Saline; 1.5 mM KH_2PO_4, 5.1 mM Na_2HPO_4, 150 mM NaCl, pH 7.4). The resulting solution was aliquoted to screw-cap tubes, snap-frozen in liquid nitrogen, and kept in -80°C. Small amount was analysed by SDS-PAGE and compared to known amounts of BSA and IgG to estimate protein concentration and assess its purity.

2.17 Nickel purification of Pcp1(604)-His_6 and Pcp1(605-1208)-His_6

Four buffers were prepared: AU (25 mM Tris pH=8.0, 75 mM NaCl, 8 M urea), AG (25 mM Tris pH=8.0, 75 mM NaCl, 6 M guanidinium hydrochloride), BU (25 mM Tris pH=8.0, 75 mM NaCl, 8 M urea, 0.3 M imidazole), BG (25 mM Tris pH=8.0, 75 mM NaCl, 6 M guanidinium hydrochloride, 0.3 M imidazole).

For each protein, 2 mL of His-bind Fractogel (Merck) bead suspension were washed three times with 15 mL of water and incubated with 4 mL of 0.3 M $NiSO_4$ for 10 min with end-over-end rotation. Beads were then washed three times with 15 mL of water and twice with 10 mL of 3% BG in AG buffer.

The inclusion bodies suspension was solubilised in 3% BG buffer (20X the volume of inclusion bodies suspension was used), heated for 5 min in 65ºC in water bath and spun for 10 min in JA-14 rotor for 5 min at 4700 rpm at 4°C. The supernatant

was recovered; the beads were incubated with the sample for 45 min at RT with end-over-end rotation. The extract was separated from the beads, and beads with bound protein were then placed in a polypropylene column and washed with 25 mL of 3% BU in AU, and then 55 mL of 10% BU in AU. Elution was performed with 4 mL of BU buffer.

2 mL of “old” beads (used in previous steps) and 1 mL of freshly prepared beads were incubated with the extract for another hour, and the washes and elution were performed as above.

Elution fractions containing the desired protein were pooled and SDS-PAGE was used to estimate protein concentration by comparing to known BSA concentrations. An appropriate volume of 5XLSB was then added to samples, which were then boiled for 5 min and loaded onto preparative SDS-PAGE gel [Protean, II System, BioRad, UK]. The gels were run at 175 mA each, for approximately 4 h. Following very brief Coomassie staining, a band containing the protein was excised, lyophilised and manually ground to a fine powder in a mortar chilled on dry ice. Approximately 1 g of gel powder was obtained for each protein.

2.18 Growth of fission yeast strains

Fission yeast strains were grown in rich medium (YE5S/4XYE5S) or minimal medium (EMM), supplemented with appropriate amino acids. Media composition:

YE5S/4XYE5S: 0.5% (w/v) Difco Yeast Extract, 3.0% (w/v) glucose, 250 mg/L each of adenine, histidine, leucine, lysine hydrochloride, and uracil. 4X applies to all ingredients.

EMM: 2.2 g/L NH_4Cl or 3.75 g/L sodium L-glutamate, 14.7 mM potassium hydrogen phthalate, 15.5 mM Na_2HPO_4, 2% glucose, 1X salts (50X salt stock solution: 52.5 g/L $MgCl_2•6H_2O$, 0.735 mg/L $CaCl_2•2H_2O$, 50 g/L KCl, 2 g/L Na_2SO_4), 1X vitamins (1000X vitamin stock: 1 g/L pantothenic acid, 10 g/L nicotinic acid, 10 mg/L biotin), 1X minerals (10,000X mineral stock: 5 g/L boric acid, 4 g/L $MnSO_4$, 4 g/L $ZnSO_4•7H_2O$, 2 g/L $FeCl_2•6H_2O$, 0.4 g/L molybdic acid, 1 g/L KI, 0.4 g/L $CuSO_4•5H_2O$, 10 g/L citric acid), and. Amino acid supplements are added as required. Adenine, histidine, leucine, lysine hydrochloride, and uracil were supplemented at 200 mg/L.

For SILAC experiments EMM was supplemented with arginine at 80 mg/L, lysine at 60 mg/L, and NH_4Cl at 6 mM.

2% Difco Bacto agar was added for growth on solid plates. G418 (Geneticin), nourseothricin (ClonNat), and hygromycin were added at 100 mg/ml where required.
YE5S + 5 mg/L Phloxin B was used to check for dead and diploid cells.
EMM + uracil at 50 mg/L + 0.2% 5-FOA + other required amino acids was used for *ura4* counterselection.
Non-*ts* strains were grown at 30°C or 32°C. Strains were stored at -80°C in 75%YE5S/25%Glycerol. From -80°C storage, yeast cells were grown on YE5S-agar until colonies were visible.

2.19 Genetic crosses

Genetic crosses were performed on SPA solid medium.
SPA: glucose (30 g/L), KH2PO4 (5 g/L), Difco Bacto agar (2 % w/v); 1X vitamins (1000X vitamin stock: 1 g/L pantothenic acid, 10 g/L nicotinic acid, 10 mg/L biotin); 250 mg/L each of adenine, histidine, leucine, lysine hydrochloride, and uracil.
h- and h+ strains to be mated were spotted onto SPA plate and mixed with 8 μL of distilled water. After the water dried, the SPA plate was placed at 25ºC for 2 days or 28ºC for 1 day to allow mating. Asci from the mating plate were streaked onto YE5S and placed at 32ºC for at least an hour minutes to allow for ascus wall breakdown with the plate oriented “top up”, which facilitated drying of the agar surface. Spores from individual tetrads were then dissected using a Singer MSM 300 dissection microscope [Singer Instruments, UK] and placed at an appropriate temperature (32ºC for non-*ts* strains, 25ºC for *ts* strains) to germinate. After 2-3 days, when colonies were approximately 3-4 mm in diameter, they were replica-plated to appropriate selective media in order to identify genotypes. Mating type of thus obtained clones was examined by crossing to a strain of a known mating type followed by iodine vapour treatment, whereby the iodine stains spore walls, therefore allowing to distinguish which strains have mated.

2.20 Strain construction using PCR-based gene targeting

C-terminal tagging and deletions were created using a PCR-base method (Bähler et al., 1998). Oligonucleotides with 5’ ends containing about 80 nucleotides of homology to the genomic sequence and 3’ ends contained 20-22 nucleotides of

homology to tagging cassettes were used. The amplified sequences contained: antibiotic resistance (G418, hygromycin, nourseothricin) and/or an appropriate tag (GFP, TAP), or, in case of gene deletion, the *ura4*$^+$ gene. The DNA fragments were then incorporated into fission yeast genome using homologous recombination to generate C-terminal truncation mutants with or without GFP tags. The same approach was used for tagging genes at their C-termini and marking them with antibiotic resistance cassette and creating deletion strains where the gene of interest was replaced with *ura4*$^+$ gene.

Yeast strains were grown in YE5S medium at 32°C to an OD_{595nm}=0.8. 20 mL of culture, corresponding to approximately 10^7 cells per 1 mL of culture, was used per transformation. Cells were harvested by centrifugation at 4,000 g for 2 min, at RT, and the pellet was re-suspended in an equal volume of water and spun again at 4,000 g for 2 min, at RT. Pellet was re-suspended in 1 ml dH_2O and transferred to a Treff tube. Cells were spun again (13000 g, 1 min, RT) then re-suspended in 1 ml 100 mM LiOAc, 1X TE pH 7.5. Cells were spun again at 13000 g, 1 min, at RT and re-suspended in 100 mM LiOAc, 1X TE pH 7.5, to a final volume of 100 μL. 30 μL of DNA in 1XTE buffer was added, containing 20-40 μg of DNA, and the solution was gently mixed by pipetting and incubated at RT for 10 min. 260 μL of 40% (w/v) PEG-4000 in 100 mM LiOAc, 1X TE pH 7.5, was then added, mixed then incubated at 30°C for 1 h. Following incubation, 43 μL of DMSO was added and cells were heat-shocked at 42°C for 5 min. Transformed cells were then centrifuged (13000 g, 1 min, RT) and washed in 1 mL of water, centrifuged again and re-suspended in 0.5 mL of water . 2 X 250 μL of cell suspension were then plated out onto YE5S plates using sterilised glass beads to spread the cells. Following O/N incubation at 32°C, cells were replica-plated to YE5S containing appropriate antibiotic(s) (G418, hygromycin, or nourseothricin) for selection. The replica plating onto selective media was repeated after two days, and cells were grown O/N. Colonies were then streaked onto YE5S, grown 2XO/N, and replica-plated to selective media to check stable integration. Colony PCR and Western blotting or fluorescence microscopy was used to confirm the genotype of the desired strain.

2.21 Strain construction using two-step gene-replacement and 5-FOA counterselection

Genes deleted using a PCR-base method contain *ura4*$^+$ gene instead of the gene of interest or its fragment (Bähler et al., 1998). To re-introduce the gene of interest into its genomic locus (for example, to allow expression of mutated version of the gene from its endogenous promoter), a yeast strain is tranformed with DNA homologous to regions flanking the *ura4* gene. To select for positive clones, 5-FOA (5-fluoroorotic acid) is added to solid media, which allows for growth of Ura- but not Ura+ cells, therefore selecting for positive transformants that lack the *ura4* gene. *In* vivo, 5-FOA is converted 5-fluoro-2'-doexyuridine monophosphate (FdUMP), which is a potent inhibitor of thymidylate synthase. Inhibition of this enzyme causes cessation of DNA synthesis, leading to cell death. Therefore, only cells that had replaced the *ura4* gene with the transformed DNA fragment are able to grow on 5-FOA plates.

Yeast strains were grown in YE5S medium at 32°C to an OD_{595nm}=0.8. 10 mL of culture, corresponding to approximately $0.5x10^7$ cells, was used per transformation. Cells were harvested by centrifugation at 4,000 g for 2 min, at RT, and the pellet was re-suspended in an equal volume of water and spun again at 4,000 g for 2 min, at RT. Pellet was re-suspended in 1 ml dH_2O and transferred to a Treff tube. Cells were spun again (13000 g, 1 min, RT) then re-suspended in 1 ml 100 mM LiOAc, 1X TE pH 7.5. Cells were spun again at 13000 g, 1 min, at RT and re-suspended in 100 mM LiOAc, 1X TE pH 7.5, to a final volume of 100 μL. 30 μL of DNA in 1XTE buffer was added, containing 20-40 μg of DNA, and the solution was gently mixed by pipetting and incubated at RT for 10 min. 260 μL of 40% (w/v) PEG-4000 in 100 mM LiOAc, 1X TE pH 7.5, was then added, mixed then incubated at 30°C for 1 h. Following incubation, 43 μL of DMSO was added and cells were heat-shocked at 42°C for 5 min. Transformed cells were then centrifuged (13000 g, 1 min, RT) and washed in 1 mL of water, centrifuged again and re-suspended in 1 mL of water . 10 X 100 μL of cell suspension were then plated out onto EMM-5-FOA plates (containing only 25% of the standard amount of uracil) using sterilised glass beads to spread the cells. Cells were allowed to grow until colonies are formed. Typically, colonies would appear in two batches, the first after 4-5 days and the second after approximately a week from transformation. After the second batch of colonies appeared, cells were replica-plated onto EMM-5-FOA plates and allowed to grow for

another day or two. The replica plating onto selective media was repeated after two days, and cells were grown O/N. Colonies were then streaked onto YE5S, grown 2XO/N, and replica-plated to EMM-5-FOA plates to check stable integration. Colony PCR and Western blotting or fluorescence microscopy was used to confirm the genotype of the desired strain. In the case of Mto2 mutagenesis obtained Mto2 mutant strains were sequenced.

2.22 Strain construction using pMONO integration system

5 µg of pMONO plasmids containing *pcp1(CM1)* genes was subject to KpnI restriction enzyme digestion, then the linear DNA was transformed into *pcp1*Δ strain rescued by *pcp1*$^{+}$ plasmid containing *ura4* gene. Following transformation, yeast cells were spread onto EMM-5-FOA plates. The selection was performed as described in Section 2.1.19.

2.23 Fission yeast DNA extracts

A single colony was picked following transformation and patched on YE5S plate. The following day, an approximately 0.5 cm^2 sized fresh patch of cells was collected using a yellow tip and suspended in 50 µL of 0.25% (w/v) SDS in 1X TE pH 8.0. This suspension was incubated at 98°C for 5 min and then centrifuged at 13,000 g for 1 min at RT. 40 µL of the supernatant was transferred to a fresh tube and used as a DNA template for PCR.

2.24 PCR amplification of DNA

Polymerase chain reaction (PCR) amplification of DNA was performed using a MJ Research Thermal Cycler. For cloning and gene tagging purposes, reactions were performed using Phusion High-Fidelity DNA Polymerase (Thermo Scientific). For colony PCR homemade Taq (HMT) polymerase was used. The annealing temperature for each primer pair was determined by performing gradient PCR, that involved testing a range of annealing temperatures. The following reaction/cycling conditions were used:

Phusion Polymerase PCR

Template DNA	0.4 ng/μL
HF or GC buffer	1X
Forward ptimer	0.5 μM
Reverse primer	0.5 μM
dNTPs	200 μM each
Phusion	0.02U/μL

GC buffer was used for GC-rich templates, for example templates containing nourseothricin resistance gene.

The reaction was carried out according to the following programme:

1. 98°C	2 min
2. 98°C	15 sec
3. 50-70°C	20 sec
3. 72°C	45 sec/kb
4. Repeat steps 2-4 34 times	
5. 72°C	5 min
6. Hold at 20ºC	

HMT Polymerase PCR

Template DNA	2 μL of DNA extract
Buffer IV	1X
Forward ptimer	0.2 μM
Reverse primer	0.2 μM
dNTPs	200 μM each
$MgCl_2$	3.5 mM
HMT Polymerase	0.2U/μL

The reaction was carried out according to the following programme:

1. 95°C	2 min
2. 95°C	15 sec
3. 50-70°C	30 sec
3. 68°C	3 min
4. Repeat steps 2-4 34 times	
5. 68°C	5 min

6. Hold at 20ºC

Products were analysed by electrophoresis on agarose gels in TAE buffer (40 mM Tris, 0.1% glacial acetic acid, 1 mM EDTA) with 0.4 μg/mL ethidium bromide. The gel concentration was appropriate to product size. Samples were prepared in 1X orange G buffer (10X stock: 0.2% Orange G, 30% Glycerol) and gels were run at ~100V and visualized by UV illumination. A 1 kb or 100 bp DNA ladder (NEB) was used to determine PCR product size.

2.25 Colony PCR

In yeast, colony PCR was used to verify integration of transformed DNA at the correct position in the genome. One PCR primer was homologous to the integrated resistance gene in the cassette, while the other was homologous to sequence upstream or downstream of the gene. Preparation of the template DNA is described in Section 2.1.22 and the PCR conditions are described in Section 2.1.23 (HMT Polymerase was used).

In bacteria, colony PCR was used to screen for colonies containing a desired plasmid construct. A yellow tip was used to transfer bacterial colony into a PCR tube containing the reaction mix. PCR conditions were used as described in Section 2.1.23 (HMT Polymerase was used).

Typical reaction volume was 25 μL. The generation of a DNA product of the correct size was confirmed by electrophoresis.

2.26 Microscopy

Wide-field microscopy was carried out using a Nikon TE300 inverted microscope with a Nikon 20X/0.75 NA Plan Apo or a Nikon 100x/1.40 NA Plan Apo objective. This was attached to a Coolsnap HQCCD camera [Photometrics]. Spinning-disc confocal microscopy was carried out using a Nikon TE2000 inverted microscope with a Nikon 100x/1.45 NA Plan Apo objective, attached to a Yokogawa CSU-10 spinning disc confocal head [Visitech] and an Andor Du888 EMCCD camera. Images were then processed using Metamorph imaging software [Molecular Devices], ImagePro Photoshop [Adobe]. Maximum projections of eight Z-sections with a step size of 0.6 μm were acquired for all imaging presented in this study.

Images wee subject to 2x2 pixel binning. Compared samples were imaged under identical conditions and adjusted using consistent values to allow for direct comparison. Imaging was performed at 25ºC in a heat box, with the exception of Pcp1-GFP imaging to measure SPB separation dynamics, where imaging was performed at 30ºC.

For live-cell imaging, samples were prepared as described (Snaith et al., 2010). Cells were grown 2X O/N overnight in EMM at 25ºC, with diluting to maintain expotential growth. 1 mL of early log-phase cultures was spun for 15 sec, the supernatant was discarded, and the cell pellet was pipetted onto EMM-2% agarose pads and covered with a coverslip. The coverslip edges were sealed with a mixture of vaseline, lanolin and paraffin in 1:1:1 ratio. If only GFP was imaged, the coverslip was completely sealed. When both GFP and RFP were imaged, only two out of four edges were sealed. The conditions used for fluorescence microscopy are shown in Table 2.1

Table 2.1. Conditions used for microscopy.

Figure(s)	488 laser power/ acquisition time	561 laser power/ acquisition time
3.2, 3.3, 3.6, 3.10, 3.11, 3.17, 3.18, 5.8-5.11, 5.12a	25%, 1000 ms	25%, 1000 ms
3.13, 4.8-4.12	25%, 1000 ms	-
4.2	Full illumination, 200 ms	
4.13	70%, 200 ms	
5.12b		25%, 200 ms
6.2	50%, 500 ms	50%, 500 ms

2.27 Cell morphology assay

A large patch of cells was resuspended in water and the resulting suspension was spread evenly on a YE5S plate and incubated at 32ºC for 2-3 days. After 3 days, cells were already in stationary phase, which caused partial depolarization. Cells were then replica-plated onto a fresh YE5S plate for 3 h at 32ºC, which allowed observation of any polarity phenotypes. Cells were then washed from plates using water. The total volume (V_T) of cell suspension was measured and $1/9V_t$ of formalin was added, which resulted in final concentration of 3.7%. Cells were incubated in this solution for 30 min, washed in water to remove excess formalin and imaged by wide-field DIC microscopy with a 20X objective (as described in Section 2.27).

2.28 *cdc25-22* block and release

2.28.1 cdc25-22 block and release for biochemical analysis of Mto2 phosphorylation

2000 mL *cdc25-22* strain were grown at 25°C O/N to an OD_{595}=0.2 in YE5S. Cultures were then split to seven flasks, each flask containing 250 mL of culture, a volume corresponding to two time points. One flask was allowed to grow at 25°C, while for the other six the temperature was shifted to 36°C and cultures were grown for 3 h 30 min. Cultures were then returned to permissive temperature by brief incubation in an ice slurry, then into a water bath at 25°C. "Cycling" and T_0 time points were taken upon temperature shift; the "cycling" sample was taken from the culture grown at 25°C. Successive time points were taken every 15 min for 225 min. At each time point 100 mL of culture was collected by centrifugation for 1 min 30 sec at 4000 rpm at 4°C and washed with 125 mL ice-cold STOP buffer (25mM $Na_xH_yPO_4$, 150 mM NaCl, 50 mM NaF, 10 mM EDTA, 1 mM NaN3). Following centrifugation (1 min 30 sec at 4000 rpm at 4°C) cells were re-suspended in 1 mL (time points 1-7) or 1.5 mL (time points 8-15) of IP buffer (25mM $Na_xH_yPO_4$, 100 mM KCl, 5 mM EDTA pH=8.0, 0.2% TritonX-100, 10 µg/ml CLAAPE, 2 mM AEBSF, 2 mM benzamidine, 2 mM PMSF, 50 mM Na β-glycerophosphate, 1 mM NaF, 0.1 mM Na_3VO_4, 50 nM calyculin A, 50 nM okadaic acid). The resulting cell suspension was split into two (time points 1-7) or three (time points 8-15) screw-cap tubes, that were centrifuged at 13000 g for 30 sec at RT. The supernatant was discarded and the pellet snap-frozen in liquid nitrogen.

For scoring septation index, 500 µL aliquots were taken from each cell cycle block and release time point. Cells were centrifuged at 13000 g for 30 sec at RT, the supernatant was discarded and the pellet re-suspended in ice-cold MeOH and kept in -20ºC. 5µl of cell solution were incubated with 5 µL fluorescent brightener (0.1% fluorescent brightener, 10 mM Tris HCl pH 7.5) for 5 min at RT. 5 µL of cell suspension were then placed on a microscope slide and examined under the wide-field microscope using a DAPI filter set. 200 cells were scored and the percentage of cells containing septum was calculated for each time point. Cells that had formed a septum but had started to separate or had been released from sister cells were not counted.

2.28.2 cdc25-22 block and release for microscopy analysis of Mto1[bonsai]-GFP puncta formation in mto2-NT2 cells

100 mL *cdc25-22* strain were grown at 25°C O/N to an OD_{595}=0.2 in EMM. Cultures were then shifted to 36°C and grown for 5 h 15 min. Cultures were then returned to permissive temperature by brief incubation in an ice slurry, then into a water bath at 25°C. Cells were imaged 50 min following the release.

2.29 *cdc10-129* block and release and MBC treatment

2000 mL *cdc10-129* strains were grown at 25°C O/N to an OD_{595}=0.2 in EMM. Cultures were then split to five flasks, each flask containing 250 mL of culture. One flask was allowed to grow at 25°C, while for the other four the temperature was shifted to 36°C and cultures were grown for 5 h 15 min. Cultures were then incubated in an ice slurry for 30 min, after which 2.5 mL of 5 mg/mL MBC was added, and cells were kept on ice for additional 15 min and moved into a water bath at 25°C. As a control, the same strain was treated with DMSO alone. T_0 time point was taken upon temperature shift; the “cycling” sample was taken from the culture grown at 25°C. Successive time points were taken every 30 min for 120 min. At each time point 50 mL of culture was collected by centrifugation for 1 min at 4000 rpm at 4°C and resuspended in 1 mL ice-cold PBS supplemented with 50 mM NaF. The resulting cell suspension was transferred into a 2 mL screw-cap tube and centrifuged at 13000 g for 30 sec at 4°C. The supernatant was discarded and the pellet snap-frozen in liquid nitrogen.

For scoring mitotic index, 1 mL aliquots were taken from each cell cycle block and release time point. Cells were centrifuged at 13000 g for 30 sec at 4°C resuspended in PBS and placed on a microscope slide and examined under the wide-field microscope using a GFP filter set. Cells were expressing *nmt81:*GFPα-tubulin to visualize MTs. 100 cells were scored and the percentage of cells containing mitotic spindle was calculated for each time point. Cells with intact spindles were counted as mitotic, regardless at what mitosis stage they were.

2.30 *nda3-KM311* block and release

nda3-KM311 allele was used to arrest cells in metaphase. Cultures were grown at 32°C to an $OD_{595\ nm}$ = 1.0. Cultures were then cooled to 18°C on ice, and incubated at 18°C for 6 h in YE5S or 8 h in EMM (including SILAC growth medium).

2.31 Fission yeast boiled protein extracts

Boiled extracts were used for Western blot analysis of fission yeast proteins, primarily to check expression levels of mutant proteins. Typically, 20 mL of cells were grown overnight to an OD_{595}=0.8 in YE5S. Cells were then centrifuged at 4000 rpm for 2 minutes, the cell pellet was then resuspended in 1 mL of PBS ant the resulting suspension was transferred to a 2 mL screw-cap tube. Samples were then spun for 1 minute at 13000 rpm at RT. The supernatant was discarded, and the pellet was resuspended in the small remaining volume by vortexing. The pellet was then boiled for 5 min and 0.5 mm Zirconia/Silica beads [BioSpec Products, USA] were added. Samples were the bead-beat in a Ribolyser [Hybaid, UK] (2x30 sec at a speed of 6.5). The bottoms of the tubes were pierced with a hot needle, tubes were placed into a 5 mL polyethylene tube, and lysates were collected by centrifuging for 1 min at 1000 rpm at RT. 200 μL of PBS was added to the flow-through, the tube was vortexed and the liquid transferred to a fresh tube. An equal volume of 2X Laemmli sample buffer (4% SDS, 20% glycerol, 120 mM Tris-HCl, pH 6.8) was added and samples were then boiled for 5 minutes, and cleared by centrifugation at 13000 rpm for 5 minutes. The boiled extract was recovered and stored at -20ºC. Prior to running on SDS-PAGE, bromophenol blue (~0.01 %) and DTT (0.1 M) were added to samples.

Protein concentration in boiled extracts was determined by Bicinchoninic acid (BCA) assay. 20 μL of reagent B (4% $CuSO_4$) was added per 1 mL of reagent A (containing BCA). 2-5 μL of boiled extract was added to 1 mL of BCA reagent mixture, incubated at 65ºC for 15 minutes, and then immediately placed on ice. OD_{562} was measured and the protein concentration was calculated based on previous calibration with BSA (not shown) where 1 mg/mL of protein gives an OD_{562} of 0.04.

2.32 Fission yeast native protein extracts

Grinding and bead-beating was used to disrupt cells. Ground cell powder was used in all SILAC experiments, in PPase treatments on Mto2[A] and in all Mto1-TAP pulldowns, apart from Mto1-TAPS pulldown following *cdc25-22* block and release experiment, where bead-beating was used to disrupt cells.

Grinding

Culture was grown to an OD_{595} = 2 (YE5S, EMM) or OD_{595} = 12 (4XYE5S). Cells were harvested using a Beckmann Avanti J-25 centrifuge using a JLA 8.1000 rotor (5000 rpm, 8 min, 4°C). Pellet was re-suspended in 200 mL of 10 mM $Na_xH_yPO_4$, pH 7.5, 0.5 mM EDTA and cells were collected using Beckmann Avanti J-25 centrifuge with a JLA 10-500 rotor (5000 rpm, 8 min, 4°C). Cell pellet was then weighted and resuspended in 10 mM $Na_xH_yPO_4$, pH 7.5, 0.5 mM EDTA (0.3 mL of buffer per 1 g of cell pellet). Cell suspension was then frozen, drop-wise into liquid nitrogen. Balls of cells were then stored at -80°C. 10-30 g of frozen cell balls were placed in the Retsch RM100 electric mortar-grinder [Retsch, Germany], which had been pre-cooled to ~190°C with liquid nitrogen, and ground to powder for 30 min. Cell powder was then stored at -80°C. The required amount of cell powder was acquired by weighing aliquots into a cooled tube 24 h before the experiment. The tube was then placed at -20ºC overnight. Tubes were then placed on ice and an appropriate buffer was added. The sample was incubated on ice until the powder was completely thawed. The tubes were then spun twice (1x5 min, 1x15 min) at 13000 rpm for at 4ºC to remove cell debris. If Falcon tubes were used, they were spun twice (1x5 min, 1x15 min) at 14000 rpm for at 4ºC.

Bead-beating

Tube containing approximately 0.15 g of cells (prepared as described in Section 2.28.1) was placed on dry ice. 1.2 mL of 0.5 mm Zirconia/Silica beads [BioSpec Products, USA], pre-chilled O/N to -20ºC, was added. 0.2 mL of IP buffer (25mM $Na_xH_yPO_4$, 100 mM KCl, 5 mM EDTA pH=8.0, 0.2% TritonX-100, 10 µg/ml CLAAPE, 2 mM AEBSF, 2 mM benzamidine, 2 mM PMSF, 50 mM Na β-glycerophosphate, 1 mM NaF, 0.1 mM Na_3VO_4, 50 nM calyculin A, 50 nM okadaic acid) was added. Samples were the bead-beat in a Ribolyser [Hybaid, UK] (1x45 sec at a speed of 4.0, 3x20 sec at a speed of 4.0), with chilling on dry ice for 2 min between cycles. The bottoms of the tubes were pierced with a hot needle, tubes were placed into a 5 mL polyethylene tube, and lysates were collected by centrifuging for 1 min at 1000

rpm at 4ºC. 200 μL of IP buffer was added to the flow-through, the tube was vortexed and the liquid transferred to a fresh tube. The tubes were then spun twice (1x5 min, 1x15 min) at 13000 rpm for at 4ºC to remove cell debris.

Determining protein concentration

Protein concentration in soluble native extracts was determined by the Bradford Assay. 2 μL of extract was added to 1 ml of the 1X Bradford reagent [BioRad, U.S.A.]. was measured and the protein concentration was calculated based on previous calibration with BSA (not shown) where 1 mg/mL of BSA gave an OD_{595} = 0.027.

2.33 SDS-PAGE

All sodium dodecyl sulphate polyacrylamide gel electrophoresis (SDS-PAGE) was performed with 5% acrylamide stacking gels and 10-12% acrylamide resolving gels in 1X Laemmli running buffer (25 mM Tris-base, 192 mM glycine, 0.1% SDS, pH 8.3). Two types of SDS-PAGE gels, referred to as Laemmli gels and Anderson gels were used. The acrylamide to bis-acrylamide ratio is 37.5:1 for Laemmli gels, and 150:1 for Anderson gels. Anderson gels at 12% were used for Western blotting of Mto2 (shown in Chapter 4). Laemmli gels at 10% were used for all other experiments. Mini-gels [BioRad, USA] or "low-wide" 10x20 cm gels [Scie-Plas, UK] were run at 35 mA and 100 mA per gel, respectively. Protein samples were prepared in Laemmli sample buffer (LSB, 2% SDS, 10% glycerol, 60 mM Tris-HCl pH 6.8, 0.01% bromophenol blue, 100 μM DTT), boiled and centrifuged for 1 min at 13000 g before loading. Resolving gel was poured and overlayed with a small volume of water-saturated n-butanol, and gel was incubated until gel polymerised. Resolving gel was then rinsed three times with water, and the stacking gel was poured on top. Appropriate comb was inserted into the stacking gel and incubated at until gel polymerised.

2.34 Coomassie staining

Following electrophoresis, gels were transferred to a glass staining solution (25% isopropanol, 10% acetic acid, 0.05% Brilliant Blue R-250) and heated for 1 min in a microwave on high power. The tray was then placed on a gyro-rocker for 10-15 minutes. Staining solution was replaced with Coomassie destain (10% acetic acid),

absorbent paper towel was placed in the tray, and the gel was again heated in the microwave for 1 min at high power. Gels were left in destaining solution until adequate contrast between bands and gel was achieved. If the gel was left for O/N destaining, the paper towel was removed from the tray.

2.35 Western blotting

A wet-transfer system was used to transfer SDS-PAGE gels onto nitrocellulose membrane using CAPS transfer buffer (10 mM CAPS, 10% MeOH). Minigels were transferred for 60 min at 90 V, and low-wide gels wee transferred for 180 min at 50V. Protein transfer was confirmed by brief Ponceau S staining (0.2% Ponceau S, 3% trichloroacetic acid, 3% sulfosalicylic acid), followed by destaining with 5% acetic acid. Membranes were then blocked with 2% non-fat dried milk (NFM) in TBST (TBS supplemented with 0.025% Tween-20) for 30 min. Membranes were then incubated with an appropriate primary antibody diluted in 2% NFM in TBST for 2 h - O/N. Antibody concentrations used are listed in Table 2.2. Following incubations, membranes were washed 3x10 min with TBST. For primary antibodies raised in sheep, a monoclonal GT-34 (mouse anti-sheep) was used as a secondary antibody, and membranes were incubated with it for 60 minutes. Following incubations, membranes were washed 3x10 min with TBST. Finally, membranes were incubated with tertiary anti-mouse IRDue800 fluorescent antibody for an hour. For primary antibodies raised in mouse, this was the secondary antibody. Following incubations, membranes were washed 2x10 min with TBST and for additional 10 min with TBS without Tween20. For quantification, a rectangle was drawn around the band of interest, and the integrated intensity that region was obtained. Background subtraction was chosen adequately.

Table 2.2. List of antibodies and dilutions used during this study.

Antibody	Dilution
PRIMARY ANTIBODIES	
anti-GFP, sheep polyclonas (Sawin lab)	1:1000
anti-Mto1, sheep polyclonas (Sawin lab)	1:1000
anti-Mto2, sheep polyclonas (Sawin lab)	1:1000
anti-Gtb1, GTU88, mouse monoclonal [Sigma, USA]	1:1000 for IP 1:4000 for WCE
SECONDARY ANTIBODIES	
GT-34, mouse andi-goat monoclonal [Sigma, USA]	1:30000
Donkey-anti-mouse, IRDye 800[LiCOR Bioscience, USA]	1:10000

2.36 TAP affinity tag pulldown

This protocol was used for all pulldown experiments where various truncations of Mto1 were tagged with either TAPS or TAPC tag.

2 mL of IP buffer (25mM $Na_xH_yPO_4$, 100 mM KCl, 5 mM EDTA pH=8.0, 0.2% TritonX-100, 10 µg/ml CLAAPE, 2 mM AEBSF, 2 mM benzamidine, 2 mM PMSF, 50 mM Na β-glycerophosphate, 1 mM NaF, 0.1 mM Na_3VO_4, 50 nM calyculin A, 50 nM okadaic acid) was added per 1 g of cell powder. Extracts were spun twice for 15 min at 13000 g at 4ºC to remove cell debris. The protein content was normalised per volume unit using Bradford assay (2 µL of extract analysed); if the difference between samples was smaller than 20%, the concentration was not adjusted. 50 µl of each extract was kept as whole cell extract, and was added to 2XLSB. Pre-washed with IP buffer (2 x 1 mL), IgG-linked-Protein G-Dynabeads were then added to extracts. 100 µL of bead suspension for 1 g of cell powder. Extracts were incubated with beads for 1.5 h at 4ºC, with rotation. The beads were then recovered and washed three times with 1 mL of IP buffer. Beads were then transferred to a new tube (Treff tube) and washed twice with 0.5 mL of buffer. The tube was then vortexed, briefly spun and all the remaining buffer was removed, Beads were then resuspended in 20-40 µL of 1X LBS without DTT and BPB and incubated at 50˚C for 15 minutes, with vortexing after 10 min. Tubes were then briefly spun and the eluate was transferred to a fresh tube. DTT (final 100 mM) and BPB (final 0.01%) were added and samples were boiled at 100˚C for 5 minutes, and stored at -20ºC.

2.37 Coupling anti-GFP antibody to Protein G-Dynabeads

2000 µL of beads was washed with 10 mL of PBST (PBS + 0.025% Tween20) and incubated with 160 µL of home-made anti-GFP antibody for 30 min at RT in two separate Falcon tubes containing 5 mL of bead suspension each. The content of the two tubes was then combined, washed three times with 10 mL of PBST and then two times with 10 mL of 0.2 M sodium borate pH=9.0. 100 µL was kept for SDS PAGE (these are non-crosslinked beads, NC, correspond to 20 µl of bead suspension), while the rest of beads was then resuspended with 10 mL of fresh DMP, made by dissolving 52 µg of DMP in 10 mL of 0.2 M sodium borate pH=9.0. The bead suspension was again split into two tubes, and mixed with an end-over-

end rotation for 30 min at RT. The content of the two tubes was again combined, and the beads were resuspended in 10 mL of fresh DMP, again split into two tubes and incubated for 30 min at RT. The content of the two tubes was again combined and the reaction was stopped by washing the beads with 10 mL of 0.2 M ethanolamine pH=8.0. The beads were then washed two times with 10 mL of 50 mM glycine pH=2.5, followed by two washes with 10 mL of PBST. Beads were then resuspended in 9.9 mL of PBST, and 100 μL was kept for SDS-PAGE (these are crosslinked beads, C, corresponds to 20 μL of bead suspension). Beads were then resuspended in 2 mL of PBST supplemented with 0.02% sodium azide and stored at 4ºC.

Control samples were split in halves, one half incubated with PBS and the other with 1X Laemmli sample buffer (LSB), for 10 min at 65ºC. The supernatant was collected, processed for SDS-PAGE (2X LSB was added to PBS, DTT and bromophenol blue were added) and analysed on 10% Laemmli gel. The absence of IgG bands in sample C (with concurrent presence of those bands in sample NC) was taken as a confirmation that crosslinking was successful.

2.38 Anti-GFP immunoprecipitation

This protocol was used for all immunoprecipitation experiments where Mto1-GFP, Mto2-GFP or Mto2-17A-GFP were immunoprecipitated.

1.8 mL (for cultures grown in EMM or YE5S) or 2 mL (for cultures grown in 4XYE5S) of IP buffer (25mM $Na_xH_yPO_4$, 100 mM KCl, 5 mM EDTA pH=8.0, 0.2% TritonX-100, 10 μg/ml CLAAPE, 2 mM AEBSF, 2 mM benzamidine, 2 mM PMSF, 50 mM Na β-glycerophosphate, 1 mM NaF, 0.1 mM Na_3VO_4, 50 nM calyculin A, 50 nM okadaic acid) was added per 1 g of cell powder. Extracts were spun one time for 5 min, and once for 15 min at 4000 rpm at 4ºC to remove cell debris. The protein content was normalised per volume unit using Bradford assay (2 μL of extract analysed); if the difference between samples was smaller than 20%, the concentration was not adjusted. 50 μl of each extract was kept as whole cell extract, and was added to 2XLSB. Pre-washed with IP buffer (2 x 1 mL), Protein G-Dynabeads with anti-GFP crosslinked to beads were then added to extracts. 20 μL of bead suspension for each mL of extract if the OD_{595} in Bradford assay was greater than one; 15 μL of bead suspension for each mL of extract if the OD_{595} in Bradford assay was below one. Extracts were incubated with beads for 1.5 h at 4ºC, with rotation. The beads

were then recovered and washed once with 3 mL, than twice with 1 mL of IP buffer. Beads were then transferred to a new tube (Treff tube) and washed twice with 0.5 mL of buffer. The tube was then vortexed, briefly spun and the entire remaining buffer was removed. Beads were then resuspended in 20-55 μL of 1X LBS without DTT and BPB and incubated at 50˚C for 15 minutes, with vortexing after 10 min. Tubes were then briefly spun and the eluate was transferred to a fresh tube. DTT (final 100 mM) and BPB (final 0.01%) were added and samples were boiled at 100˚C for 5 minutes, and stored at -20ºC.

2.39 λ-Phosphatase treatment

Two samples of 100 μg of cell powder was resuspended in 200 μL of either B- buffer (20 mM Tris-HCl pH=7.5, 150 mM NaCl, 0.1 mM EGTA, 2 mM DTT, 0.01% TX-100, 2mM $MgCl_2$, 10 μg/ml CLAAPE, 1 mM AEBSF, 2 mM benzamidine, 2mM PMSF) or B+ buffer (B- with the addition of 100mM Na β-glycerophosphate, 50 mM NaF, 10 mM Na_3VO_4, 50 nM calyculin A, 50 nM okadaic acid, 50 mM EDTA, 5 mM NaN_3). All samples were centrifuged twice at 13000 g, RT for 15 min to remove cell debris. 3x50 μL was taken from each extract, which gave six samples for each strain (3xB- samples, 3xB+ samples, will refer to them as 1-6, with samples 1-3 not containing PPase inhibitors, and samples 4-6 containing PPase inhibitors). Heat inactivated (HI) PPase was prepared by incubation of PPase in 10 mM EDTA for 1 h at 65ºC. $MnCl_2$ was added to tubes 2, 3, 5 and 6 to a final concentration of 2 mM. 400U of HI PPase was added to tubes 2 and 5, and 400U of PPase was added to tubes 3 and 6. Samples were incubated at 30ºC for 60 min and then processed for western blot analysis.

2.40 CDK1-Cyclin B treatment of purified Mto1/2[A] complexes

0.5 g of cell powder was resuspended in lysis buffer (20 mM Tris-HCl pH 7.5, 6 mM $MgCl_2$, 150 mM NaCl, 0.05% Triton X-100, 2 mM DTT, 10% glycerol, 1 mM PMSF, 1 mM benzamidine, 10 μg/ml CLAAPE). TAP affinity tag purification was performed as described in Section 2.36. After incubation of beads with extracts, the beads were transferred into a fresh screw-cap tube re-suspended in 80 μL of lysis buffer and 200 μM final concentration of ATP was added to each sample. The sample was

split into two halves, and 100 ng of CDK1-Cyclin B [Invitrogen, U.S.A.] was added one of the two samples; both samples were then agitated for 60 min at 30ºC. The supernatant was recovered into a fresh tube. 40 μL of 2XLSB was added and incubated at 100°C for 5 min. The remaining beads were washed 3 times with 0.2 ml of lysis buffer. Dynabeads were re-suspended in 80 μL of 1XLSB and incubated at 50°C for 15 min. The eluate was recovered and incubated at 100°C for 5 min and samples were processed for western blot analysis.

2.41 Trypsin digestion and Stage-Tip purification

Coomassie stained band corresponding to the expected molecular weight was excised from the gel cut into small pieces using microscope coverslip. Gel pieces were then placed in a microcentrifuge tube, treated with 50 mM ABC (ammonium bicarbonate) for 5 min, and the solution was discarded. Gel pieces were then shrunk with ACN (acetonitrile) for 5 min, and the solution was discarded. The treatment with ABC/ACN was repeated. Proteins were then reduced in 10 mM DTT in 50 mM ABC for 30 min at 37°C. The solution was removed, and the gel pieces were again treated with ABC followed by ACN. Proteins were then alkylated in 55 mM iodoacetamide in 50 mM ABC for 30 min at RT in the dark, and the solution was discarded. The treatment with ABC/ACN was repeated. Gel pieces were then incubated in trypsin buffer (13 ng/μL trypsin, 10 mM ABC, 10% ACN) on ice for 15 min. This was followed by an O/N at 37°C. The digestion medium was then acidified by adding an equal volume of 0.1 % (v/v) of trifluoroacetic acid (TFA) and spun onto StageTips (Rappsilber et al., 2003). Peptides were eluted in 2x10 μL 80% ACN in 0.1% TFA and were concentrated to 4 μL (concentrator 5301 [Eppendorf AG, Hamburg, Germany]). 1 μL of 0.1% TFA was added and LC-MS^2 analysis was performed.

2.42 LC-MS^2 analysis

Dr Juan Zhou from Rappsilber group performed experiments described in this Section.

Before running Mto2-17A-GFP samples, 10% of total volume (0.5 μL) was subjected to MS analysis (so called survey-run). After the survey run, H/L ratio was estimated,

and if needed, unequal volumes of heavy and light samples were loaded during the analytical run to obtain a near to 1:1 H/L ratio.

An analytical column with a spray emitter (75-µm inner diameter, 8-µm opening, 250-mm length; New Objectives) that was packed with C18 material (ReproSil-Pur C18-AQ 3 µM; Dr Maisch GmbH, Ammerbuch-Entringen, Germany) using an air pressure pump (Proxeon Biosystems). Mobile phase A consisted of water and 0.1% formic acid. Mobile phase B consisted of 80% ACN and 0.1% formic acid. Peptides were loaded onto the column with 2% B at 500 nL/min flow rate and eluted at 300 nL/min flow rate with two gradients: linear increase from 2% B to 40% B in 79 minutes; then increase from 40% to 90% B in 11 minutes. The eluted peptides were directly sprayed into an Q-Exactive mass spectrometer (Thermo Fisher Scientific). Full MS Scans were acquired on the Q-Exactive mass analyser over the range m/z 300–1750 with a mass resolution of 70 000 (at m/z 200). The target value was 1.0E+06. The ten most intense peaks with charge state ≥2 were fragmented in the HCD collision cell with normalized collision energy of 25%, and MS2 spectra were with a mass resolution of 35,000 at m/z 200. The target value was 5.0E+05. The ion selection threshold was 2.1E+04 counts, and the maximum allowed ion accumulation times were 20 ms for full MS scans and 120 ms for MS2 spectra. The dynamic exclusion time was set to 45 second and repeat count equal to 1.

The data acquisition was performed in a data dependent manner over the range m/z 300-1800 on Orbitrap Velos. From each MS survey scan, 10 most intense precursor ions were selected for fragmentation. MS and MS/MS scans were acquired in an Orbitrap mass analyser and the peptides were fragmented (charge state ≥2) by HCD with normalized collision energy of 40%. MS scans were acquired at a resolution of 100,000 at 400 m/z, while MS/MS scans were acquired at a resolution of 7500. The automatic gain control for full FT MS was set to 5.0E+05 ions and for FT MS/MS was set to 1.0E+05 ions with maximum time of accumulation of 500 ms and 200 ms, respectively.

The generated peak lists were searched against protein databases using Mascot 2.0. The results were parsed through MSQuant [http://msquant.sourceforge.net/].

Table 2.3. List of plasmids used during this study.

Database name	Description	Source
pDUAL	pDUAL-AmpR	(Matsuyama et al., 2004)
pKS103	pFA6a-TAPC-kanMX6	(Tasto et al., 2001)

pKS422	pFA6a-TAPS-kanMX6	(Tagwerker et al., 2006)
pKS535	pDONR221	[Invitrogen]
pKS537	p0GWA	(Busso et al., 2005)
pKS694	pFA6a-hphMX6	(Hentges et al., 2005)
pKS700	pFA6a-GFP(S65T)-natMX6	(Van Driessche et al., 2005)
pKS1148	pMA-T_mto1_ CDK5RAP2CM1	GENEART
pKS1149	pMA-T_mto1_ myomegalinCM1	GENEART
pKS1150	pMA-T_pcp1_ myomegalinCM1	GENEART
pKS1151	pMA-T_pcp1_ mto1CM1_pcp1	GENEART
pKS1152	pMA-T_pcp1_ CDK5RAP2CM1	GENEART
pKS1153	pJET1.2_pcp1	This study
pKS1154	pAL-KS_pcp1_GFP	This study
pKS1155	pAL-KS_pcp1_ CDK5RAp2CM1_ pcp1_GFP	This study
pKS1156	pAL-KS_pcp1_ mto1 CM1_ pcp1_GFP	This study
pKS1157	pAL-KS_pcp1_ myomeg CM1_ pcp1_GFP	This study
pKS1158	pMK_mto1_ pcp1CM1	GENEART
pKS1163	pJET-pcp1_9A1	This study
pKS1164	pJET-pcp1_I172T	This study
pKS1192	pALKS_pcp1_9A1	This study
pKS1193	pALKS_pcp12_I172T	This study
pKS1200	pDUALΔUra4	This study
pKS1202	pMONO_PCP1	This study
pKS1203	pMONO_PCP1_CM1_CDK5RAP2	This study
pKS1204	pMONO_PCP1_CM1_Mto1	This study
pKS1205	pMONO_PCP1_CM1_MMGL	This study
pKS1206	pMONO_PCP1_9A1	This study
pKS1207	pMONO_PCP1_I172T	This study
pKS1208	pJET_attb1_Pcp1(1-1812)_attb2	This study
pKS1209	pJET_attb1_Pcp1(1813-3624)_attb2	This study
pKS1210	pJET_half_attb1_Pcp1(1813-3624)_half_attb2	This study
pKS1211	pDONR221_Pcp1(1813-3624)	This study
pKS1212	pDONR221_Pcp1(1-1812)	This study
pKS1213	p0GWA_Pcp1(1-1812)	This study
pKS1214	p0GWA_Pcp1(1813-3624)	This study
pKS1227	pMA_mto2_009_DRE_AAA	GENEART
pKS1228	pMA_mto2_014_ED_AA	GENEART
pKS1229	pMA_mto2_103_EHK_AAA	GENEART
pKS1230	pMA_mto2_112_EK2EK_AA2AA	GENEART
pKS1231	pMA_mto2_129_ELE2RER_AAA2AAA	GENEART
pKS1232	pMA_mto2_192_RLR_AAA	GENEART
pKS1233	pMA_mto2_056_ED_AA	GENEART
pKS1234	pMA_mto2_129_ELE_AAA	GENEART
pKS1235	pMA_mto2_134_RER_AAA	GENEART
pKS1236	pMA_mto2_009_DRE2ED_AAA2AA	GENEART
pKS1237	pMA_mto2_344_RYRSD_AAAAA	GENEART
pKS1238	pMA_mto2_226_D3R3E_A3A3A	GENEART

pKS1276	pMA-T_Mto2(17A)	GENEART
pKS1277	pMA-T_Mto2-FCC	GENEART
pKS1278	pMA-T_Mto2-NT1	GENEART
pKS1279	pMA-T_Mto2-CT1	GENEART
pKS1280	pMA-T_Mto2-NT2	GENEART
pKS1281	pMA_Mto2-CT2	GENEART

Table 2.4. List of yeast strains used during this study.

Database name	Genotype	Source
349	h+kanMX6 nmt81::GFP-atb2 cdc10-129	Lab. stock
515	h+ ade6-M216 ura4-D18 leu1-32	Lab. stock
516	h- ade6-M210 ura4-D18 leu1-32	Lab. stock
566	h- cdc25-22 ade6-M216 leu1-32 ura4-D18	Lab. stock
567	h+ cdc25-22 ade6-M216 leu1-32 ura4-D18	Lab. stock
819	h+ mto1-GFP:kanMX ura4-D18 leu1-32 ade6-M216	Lab. stock
1158	h- mto1Δ::kanMX ade6-210 leu1-32 ura4-D18	Lab. stock
1235	h+ kanMX:nmt81:GFP-atb2 ade6-? leu1-32 ura4-D18	Lab. stock
1239	h- mto1Δ::kanMX nda3-km311 ade6-210 leu1-32 ura4-D18	Lab. stock
1459	mto2-GFP:KanMX mto1Δ::kanM X6 ade6-M216 leu1-32 ura4-D18	Lab. stock
1740	h+ nda3-KM311 ade6-M216 leu1-32 ura4-D18	Lab. stock
1866	h- pcp1-GFP:kanMX6 ade6-210 leu1-32 ura4-D18	Lab. stock
1950	h+ mto1-GFP:kanMX ura4-D18 leu1-32 ade6-M216, mto1::ura4	Lab. stock
2076	h+ mto1(9A1)-GFP:kanMX6 ade6-216 leu1-32 ura4-D18	Lab. stock
2767	h- natMX6:nmt81:mCh-atb2 ade6-M210 leu1-32 ura4-D18	Lab. stock
2789	h+ hphMX6:nmt81:mCh-atb2 ade6-210 leu1-32 ura4-D18	Lab. stock
2853	h+ mto1-GFP:kanMX6 hphMX6:nmt81:mCh-atb2 ade6-210 leu1-32 ura4-D18	Lab. stock
2973	h- pcp1Δ::natMX6 ade6-216 leu1-32 ura4-D18 + pUR19-pcp1	Lab. stock
3472	h+ mto1-TAPS:kanMX6 ade6-216 leu1-32 ura4-D18	Lab. stock
3524	h+ mto1-TAPS:kanMX6 ade6-216 leu1-32 ura4-D18	Lab. stock
3575	h+ mto1-TAPS:kanMX6 nda3-km311 ade6-216 leu1-32 ura4-D18	Lab. stock
5201	h- pcp1-GFP::kanMX hphMX:nmt81:mCh-atb2 ade6-216 leu1-32 ura4-D18	Lab. stock
5209	h- mto1(1-549)-GFP:kanMX6 ade6-210 leu1-32 ura4-D18	Lab. stock
5335	h+ mto1Δ::kanMX6 natMX6:nmt81:RFP-atb2 ade6-210 leu1-32 ura4-D18	Lab. stock
5514	h+ cut12-RFP:kanMX6 ade6-210 leu1-32 ura4-D18	Lab. stock
5607	h+ mto1(1-549)::kanMX6 ade6-M216 ura4-D18 leu1-32	Lab. stock
5922	h- mto1(131-549)-GFP:kanMX6 ade6-M210 ura4-D18 leu1-32	Lab. stock
6032	h+ mto1(1-549)-TAPS:KanMX6 ade6-M216 ura4-D18 leu1-32	Lab. stock
6080	h+ mto1(131-9A1-549)-GFP:kanMX6 ade6-216 leu1-32 ura4-D18	Lab. stock
6100	h- mto1(131-9A1-549)-GFP:kanMX6 hphMX6:nmt81:mCh-atb2 ade6-? leu1-32 ura4-D18	Lab. stock
6160	h+ mto1(mto1_CM1::MMGL_CM1)-GFP:kanMX ura4-D18 leu1-32 ade6-M216)	Lab. stock
6161	h+ mto1(mto1_CM1::CDK5RAP2_CM1)-GFP:kanMX ura4-D18 leu1-32 ade6-M216)	Lab. stock
6171	h- Mto1-TAPC::kanMX ade6-M210 ura4-D18 leu1-32	Lab. stock
6175	h- Mto1 (1-549)-TAPC::kanMX ade6-M210 ura4-D18 leu1-32	Lab. stock
6193	h– mto1(1-549)-TAPS:kanMX6 nda3-KM311 ade6-216 leu1-32 ura4-D18	Lab. stock
6197	h+ Mto1-TAPC::kanMX mto2Δ::kanMX6 ade6-? ura4-D18 leu1-32	Lab. stock

6201	h+ Mto1 (1-549)-TAPC::kanMX mto2Δ::kanMX6 ade6-? ura4-D18 leu1-32	Lab. stock
6234	h+ mto1(mto1_CM1::MMGL_CM1)-GFP:kanMX natMX:nmt81:mCh-atb2 ura4-D18 leu1-32 ade6-210	This study
6235	h90 mto1(mto1_CM1::CDK5RAP2_CM1)-GFP:kanMX natMX:nmt81:mCh-atb2 ura4-D18 leu1-32 ade6-216	This study
6237	h+ mto1(mto1_CM1::pcp1_CM1)-GFP:kanMX ura4-D18 leu1-32 ade6-M216)	This study
6266	h- mto1(131-549)-TAPC ade6-M210 ura4-D18 leu1-32	Lab. stock
6267	h- mto1(131-549, CM1_Mto1::CM1_Pcp1)-GFP:kanMX6 ade6-M210 ura4-D18 leu1-32	This study
6269	h- mto1(131-549, CM1_Mto1::CM1_CDK5RAP2)-GFP:kanMX6 ade6-M210 ura4-D18 leu1-32	This study
6270	h- mto1(131-549, CM1_Mto1::CM1_MMGL)-GFP:kanMX6 ade6-M210 ura4-D18 leu1-32	This study
6294	h+ mto1(131-549)-TAPC::kanMX6 mto2Δ::kanMX6 ade6-? ura4-D18 leu1-32	Lab. stock
6295	h+ mto1(mto1_CM1::Pcp1_CM1)-GFP:kanMX natMX:nmt81:mCh-atb2 ura4-D18 leu1-32 ade6-210	This study
6303	h– mto2-v1 nda3-KM311 ade6-210 leu1-32 ura4-D18	Lab. stock
6304	h– mto2-v12 nda3-KM311 ade6-210 leu1-32 ura4-D18	Lab. stock
6309	h– mto2-v22 nda3-KM311 ade6-210 leu1-32 ura4-D18	Lab. stock
6332	h- mto2-v22 mto1(1-549)-TAPS:kanMX6 nda3-KM311 ade6-216 leu1-32 ura4-D18	Lab. stock
6335	h+ mto2-v1 mto1(1-549)-TAPS:kanMX6 nda3-KM311 ade6-216 leu1-32 ura4-D18	Lab. stock
6336	h+ mto2-v12 mto1(1-549)-TAPS:kanMX6 nda3-KM311 ade6-216 leu1-32 ura4-D18	Lab. stock
6339	h- mto1(131-549)-GFP:kanMX6 hphMX6:nmt81:mCh-atb2 ade6-M210 ura4-D18 leu1-32	This study
6340	h- mto1(131-549, CM1_Mto1::CM1_Pcp1)-GFP:kanMX6 hphMX6:nmt81:mCh-atb2 ade6-M210 ura4-D18 leu1-32	This study
6342	h- mto1(131-549, CM1_Mto1::CM1_CDK5RAP2)-GFP:kanMX6 hphMX6:nmt81:mCh-atb2 ade6-M210 ura4-D18 leu1-32	This study
6344	h+ mto1(131-549, CM1_Mto1::CM1_MMGL)-GFP:kanMX6 hphMX6:nmt81:mCh-atb2 ade6-M210 ura4-D18 leu1-32	This study
6346	h+ mto1(131-549)-GFP:kanMX6 cut12-RFP:kanMXade6-M210 ura4-D18 leu1-32	This study
6348	h+ mto1(131-549, CM1_Mto1::CM1_Pcp1)-GFP:kanMX6 cut12-RFP:kanMX ade6-M210 ura4-D18 leu1-32	This study
6350	h+ mto1(131-549, CM1_Mto1::CM1_CDK5RAP2)-GFP:kanMX6 cut12-RFP:kanMX ade6-M210 ura4-D18 leu1-32	This study
6352	h+ mto1(131-549, CM1_Mto1::CM1_MMGL)-GFP:kanMX6 cut12-RFP:kanMX ade6-M210 ura4-D18 leu1-32	This study
6353	h+ hphMX6:nmt81:mCh-atb2 ade6-210 ura4-D18 (pcp1_CM1::CDK5RAP2_CM1)-GFP intergrated at leu1 locus	This study
6355	h+ hphMX6:nmt81:mCh-atb2 ade6-210 ura4-D18 (pcp1_CM1::MMGL_CM1)-GFP intergrated at leu1 locus	This study
6357	h+ hphMX6:nmt81:mCh-atb2 ade6-210 ura4-D18 pcp1-9A1-GFP intergrated at leu1 locus	This study
6361	h+ pcp1Δ::natMX6 hphMX6:nmt81:mCh-atb2 ade6-216 ura4-D18 (pcp1_CM1::CDK5RAP2_CM1)-GFP intergrated at leu1 locus	This study
6363	h- pcp1Δ::natMX6 hphMX6:nmt81:mCh-atb2 ade6-??? ura4-D18 (pcp1_CM1::MMGL_CM1)-GFP intergrated at leu1 locus	This study
6364	h+ hphMX6:nmt81:mCh-atb2 ade6-210 ura4-D18 (pcp1_CM1::Mto1_CM1)-GFP intergrated at leu1 locus	This study
6366	h+ hphMX6:nmt81:mCh-atb2 ade6-210 ura4-D18 Pcp1-GFP intergrated at leu1 locus	This study
6383	h+ pcp1Δ::natMX6 hphMX6:nmt81:mCh-atb2 ade6-210 ura4-D18 (pcp1_CM1::Mto1_CM1)-GFP intergrated at leu1 locus	This study
6384	h+ pcp1Δ::natMX6 hphMX6:nmt81:mCh-atb2 ade6-210 ura4-D18 pcp1-GFP intergrated at leu1 locus	This study
6385	h+ pcp1Δ::natMX6 hphMX6:nmt81:mCh-atb2 ade6-210 ura4-D18 pcp1(I172T)-GFP intergrated at leu1 locus	This study

6387	h– mto2-v12:hphMX6 nda3-KM311 ade6-210 leu1-32 ura4-D18	This study
6388	h+ mto2-v1:hphMX6 mto1(1-549)-TAPS:kanMX6 nda3-KM311 ade6-216 leu1-32 ura4-D18	This study
6390	h+ mto2-v12:hphMX6 mto1(1-549)-TAPS:kanMX6 nda3-KM311 ade6-216 leu1-32 ura4-D18	This study
6391	h– mto2-v12:hphMX6 nda3-KM311 ade6-210 leu1-32 ura4-D18	This study
6394	h– mto2-v22;hphMX6 nda3-KM311 ade6-210 leu1-32 ura4-D18	This study
6396	mto2-v22:hphMX mto1(1-549)-TAPS:kanMX6 nda3-KM311 ade6-216 leu1-32 ura4-D18	This study
6397	h- mto2-v22:hphMX mto1(1-549)-TAPS:kanMX6 nda3-KM311 ade6-216 leu1-32 ura4-D18	This study
6398	h+ mto2-v12:hphMX6 nda3-KM311 ade6-? leu1-32 ura4-D18	This study
6401	h+ mto2-v22:hphMX6 nda3-KM311 ade6-? leu1-32 ura4-D18	This study
6407	h- mto2-v12:hphMX6 kanMX:nmt81:GFP-atb2 ade6-? leu1-32 ura4-D18	This study
6411	h– mto2-v22;hphMX6 mto1-TAPS:kanMX nda3-KM311 ade6-216 leu1-32 ura4-D18	This study
6412	h+ mto2-v22;hphMX6 mto1-TAPS:kanMX nda3-KM311 ade6-216 leu1-32 ura4-D18	This study
6413	h+ mto2-v1:hphMX6 mto1(1-549)-TAPS:kanMX6 ade6-216 leu1-32 ura4-D18	This study
6414	h90 mto2-v1:hphMX6 mto1(1-549)-TAPS:kanMX6 ade6-210 leu1-32 ura4-D18	This study
6415	h- mto2-v1:hphMX6 nda3-KM311 ade6-210 leu1-32 ura4-D18	This study
6434	h+ mto2-v12:hphMX6 mto1(131-549)-GFP:kanMX ade6-210 leu1-32 ura4-D18	This study
6440	h+ mto2-v22:hphMX6 mto1(131-549)-GFP:kanMX ade6-216 leu1-32 ura4-D18	This study
6446	h+ mto2-v22:hphMX6 mto1(131-549)-TAPC:kanMX nda3-KM311 ade6-210 leu1-32 ura4-D18	This study
6447	h- mto2-v22:hphMX6 mto1(131-549)-TAPC:kanMX ade6-216 leu1-32 ura4-D18	This study
6448	h+ mto2-v22:hphMX6 mto1(131-549)-TAPC:kanMX ade6-216 leu1-32 ura4-D18	This study
6450	h- mto2-v12:hphMX6 mto1(131-549)-TAPC:kanMX nda3-KM311 ade6-210 leu1-32 ura4-D18	This study
6451	h- mto2-v12:hphMX6 mto1(131-549)-TAPC:kanMX ade6-210 leu1-32 ura4-D18	This study
6452	h- mto2-v12:hphMX6 mto1(131-549)-TAPC:kanMX ade6-210 leu1-32 ura4-D18	This study
6454	h+ mto1(131-549)-TAPC:kanMX ade6-210 nda3-KM311 leu1-32 ura4-D18	This study
6455	h+ mto1(131-549)-TAPC:kanMX ade6-210 leu1-32 ura4-D18	This study
6474	h+ mto2-v12:hphMX6 mto1(1-549)-TAPS:kanMX6 ade6-216 leu1-32 ura4-D18	This study
6485	h- mto2-v22:hphMX6 mto1(1-549)-GFP:kanMX ade6-210 leu1-32 ura4-D18	This study
6486	h+ mto2-v22:hphMX mto1(1-549)-TAPS:kanMX6 ade6-210 leu1-32 ura4-D18	This study
6496	h+ mto2-v1:hphMX6 mto1(131-549)-TAPC:kanMX nda3-KM311 ade6-210 leu1-32 ura4-D18	This study
6498	h+ mto2-v1:hphMX6 mto1(131-549)-TAPC:kanMX ade6-210 leu1-32 ura4-D18	This study
6510	h+ mto2-v1:hphMX6 mto1-GFP:kanMX ade6-210 leu1-32 ura4-D18	This study
6512	h+ mto2-v1:hphMX6 kanMX:nmt81:GFP-atb2 ade6-216 leu1-32 ura4-D18	This study
6521	h- pcp1Δ::natMX6 (pcp1_CM1::Mto1_CM1)-GFP:leu1 ade6-210 ura4-D18	This study
6523	h+ pcp1Δ::natMX6 (pcp1_CM1::CDK5RAP2_CM1)-GFP:leu1 ade6-210 ura4-D18	This study
6525	h+ pcp1Δ::natMX6 pcp1-GFP:leu1 ade6-210 ura4-D18	This study
6529	h- pcp1Δ::natMX6 Pcp1(CM1:MMGL)-GFP:leu1 ade6-210 ura4-D18	This study
6600	h+ mto2v1:hphMX mto1(131-549)-GFP:kanMX ade6-216 ura4-D18 leu1-32	This study
6626	h- mto1(131-549):kanMX6 ade6-M210 ura4-D18 leu1-32	Lab. stock

6677	h+ mto1(1-549)-GFP:kanMX6 Z:ADH15:mCherry-Atb2:natMX6 ade6-M210 leu1-32 ura4-D18	Lab. stock
6678	h+ mto1(131-549)-GFP:kanMX6 Z:ADH15:mCherry-Atb2:natMX6 ade6-M210 leu1-32 ura4-D18	Lab. stock
6737	h+ mto2-v22:hphMX6 kanMX:nmt81:GFP-atb2 ade6-210 leu1-32 ura4-D18	This study
6742	h- mto1-TAPS:kanMX6 mto2v1:hphMX nda3-KM311 ade6-216 leu1-32 ura4-D18	This study
6743	h+ mto1-TAPS:kanMX6 mto2v1:hphMX ade6-216 leu1-32 ura4-D18	This study
6746	h- mto1-TAPS:kanMX6 mto2v22:hphMX nda3-KM311 ade6-210 leu1-32 ura4-D18	This study
6747	h+ mto1-TAPS:kanMX6 mto2v22:hphMX ade6-210 leu1-32 ura4-D18	This study
6749	h+ mto1-TAPS:kanMX6 mto2v12:hphMX nda3-KM311 ade6-210 leu1-32 ura4-D18	This study
6751	h+ mto1-TAPS:kanMX6 mto2v12:hphMX ade6-216 leu1-32 ura4-D18	This study
6760	h+ mto1-TAPS:kanMX6 cdc25-22 ade6-216 leu1-32 ura4-D18	This study
6828	h+ Mto1(1-549)-TAPC::kanMX nda3-KM311 ade6-M210 ura4-D18 leu1-32	This study
6909	h- mto1(131-549)-TAPS:kanMX ade6-M210 ura4-D18 leu1-32	This study
6910	h- mto1(131-549)-TAPS:kanMX ade6-M210 ura4-D18 leu1-32	This study
6928	h- mto2Δ::ura4+:hphMX6 mto1(131-549)-GFP:kanMX6 Z:ADH15:mCherry-Atb2:natMX6 ade6-M210 leu1-32 ura4-D18	Lab. stock
6949	h+ mto1(131-549)-TAPS:kanMX nda3-KM311 ade6-M210 ura4-D18 leu1-32	This study
6975	h+ mto2:hphMX kanMX::nmt81:GFP-atb2 ade6-210 leu1-32 ura4-D18	This study
6977	h- mto2v1:hphMX mto1(1-549)-GFP:kanMX ade6-210 ura4-D18 leu1-32	This study
7057	h- mto2(009_DRE_AAA):hphMX6 mto1(131-549)-GFP:kanMX6 Z:ADH15:mCherry-Atb2:natMX6 ade6-M210 leu1-32 ura4-D18	This study
7059	h- mto2(014_ED_AA):hphMX6 mto1(131-549)-GFP:kanMX6 Z:ADH15:mCherry-Atb2:natMX6 ade6-M210 leu1-32 ura4-D18	This study
7061	h- mto2(103_EHK_AAA) hphMX6 mto1(131-549)-GFP:kanMX6 Z:ADH15:mCherry-Atb2:natMX6 ade6-M210 leu1-32 ura4-D18	This study
7063	h- mto2(112_EK2EK_AA2AA) hphMX6 mto1(131-549)-GFP:kanMX6 Z:ADH15:mCherry-Atb2:natMX6 ade6-M210 leu1-32 ura4-D18	This study
7065	h- mto2(129_ELE2RER_AAA2AAA) hphMX6 mto1(131-549)-GFP:kanMX6 Z:ADH15:mCherry-Atb2:natMX6 ade6-M210 leu1-32 ura4-D18	This study
7067	h- mto2(192_RLR_AAA) hphMX6 mto1(131-549)-GFP:kanMX6 Z:ADH15:mCherry-Atb2:natMX6 ade6-M210 leu1-32 ura4-D18	This study
7069	h- mto2(056_ED_AA) hphMX6 mto1(131-549)-GFP:kanMX6 Z:ADH15:mCherry-Atb2:natMX6 ade6-M210 leu1-32 ura4-D18	This study
7071	h- mto2(129_ELE_AAA) hphMX6 mto1(131-549)-GFP:kanMX6 Z:ADH15:mCherry-Atb2:natMX6 ade6-M210 leu1-32 ura4-D18	This study
7073	h- mto2(134_RER_AAA) hphMX6 mto1(131-549)-GFP:kanMX6 Z:ADH15:mCherry-Atb2:natMX6 ade6-M210 leu1-32 ura4-D18	This study
7075	h- mto2(009_DRE2ED_AAA2AA) hphMX6 mto1(131-549)-GFP:kanMX6 Z:ADH15:mCherry-Atb2:natMX6 ade6-M210 leu1-32 ura4-D18	This study
7077	h- mto2(344_RYRSD_AAAAA) hphMX6 mto1(131-549)-GFP:kanMX6 Z:ADH15:mCherry-Atb2:natMX6 ade6-M210 leu1-32 ura4-D18	This study
7079	h- mto2(226_D3R3E_A3A3A) hphMX6 mto1(131-549)-GFP:kanMX6 Z:ADH15:mCherry-Atb2:natMX6 ade6-M210 leu1-32 ura4-D18	This study
7081	h- mto2-GFP:natMX ade6-M210 ura4-D18 leu1-32	This study
7083	h– mto2(17A)-GFP:natMX nda3-KM311 ade6-210 leu1-32 ura4-D18	This study
7087	h+ mto2-GFP:natMX ade6-M210 arg1-230	This study
7092	h+ mto2(17A)-GFP:natMX car2Δ:kanMX arg1-230 lys3-37 nda3-KM311	This study
7093	h+ mto2(17A)-GFP:natMX car2Δ:kanMX arg1-230 lys3-37 nda3-KM311	This study
7096	h- Mto1-9A1-GFP:kanMX hphMX6:nmt81:mCh-atb2 ade6-? leu1-32 ura4-D18	This study
7099	h+ mto2(17A)-GFP:natMX ade6-? leu1-32 ura4-D18	This study
7121	h+ SPAC1783.01Δ::kanMX ade6-210	This study
7122	h+ SPBC12C2.03CΔ::kanMX ade6-210	This study

7152	h- SPAC1783.01Δ::kanMX arg1-230 car2Δ::KanMX4 lys3-37	This study
7153	h- SPAC1783.01Δ::kanMX arg1-230 car2Δ::KanMX4 lys3-37 nda3-KM311	This study
7154	h- SPBC12C.03CΔ::kanMX arg1-230 car2Δ::KanMX4 lys3-37 nda3-KM311	This study
7155	h- SPBC12C.03CΔ::kanMX arg1-230 car2Δ::KanMX4 lys3-37 nda3-KM311	This study
7158	h+ mto2(17A)-GFP:natMX mto1Δ::kanMX ade6-? leu1-32 ura4-D18	This study
7183	h- SPAC1783.01Δ::kanMX SPBC12C.03CΔ::kanMX arg1-230 car2Δ::KanMX4 lys3-37 nda3-km311	This study
7184	h- SPAC1783.01Δ::kanMX SPBC12C.03CΔ::kanMX arg1-230 car2Δ::KanMX4 lys3-37 nda3-km311	This study
7185	h- SPAC1783.01Δ::kanMX SPBC12C.03CΔ::kanMX arg1-230 car2Δ::KanMX4 lys3-37 nda3-km311	This study
7186	h+ mto2Δ::ura4+:hphMX6 nda3-KM311 ade6-210 leu1-32 ura4-D18	This study
7221	h+ Mto2-FCC:hphMX6 nda3-KM311 ade6-210 leu1-32 ura4-D18	This study
7223	h+ Mto2-NT1:hphMX6 nda3-KM311 ade6-210 leu1-32 ura4-D18	This study
7225	h+ Mto2-CT1:hphMX6 nda3-KM311 ade6-210 leu1-32 ura4-D18	This study
7227	h+ Mto2-NT2:hphMX6 nda3-KM311 ade6-210 leu1-32 ura4-D18	This study
7229	h+ Mto2-CT2:hphMX6 nda3-KM311 ade6-210 leu1-32 ura4-D18	This study
7241	h- mto2-6A:hphMX mto1(131-549)-GFP:kanMX6 Z:ADH15:mCherry-Atb2:natMX6 ade6-M210 leu1-32 ura4-D18	This study
7246	h+ mto2-13A:hphMX mto1(131-549)-GFP:kanMX6 Z:ADH15:mCherry-Atb2:natMX6 ade6-M210 leu1-32 ura4-D18	This study
7249	h+ mto2-17A:hphMX mto1(131-549)-GFP:kanMX6 Z:ADH15:mCherry-Atb2:natMX6 ade6-M210 leu1-32 ura4-D18	This study
7253	h+ Mto2-NT2:hphMX6 ade6-210 leu1-32 ura4-D18	This study
7260	h+ mto2-NT2:hphMX6 mto1(131-549)-GFP:kanMX6 Z:ADH15:mCherry-Atb2:natMX6 ade6-M210 leu1-32 ura4-D18	This study
7266	h+ Mto2-NT2-GFP:natMX:hphMX6 ade6-210 leu1-32 ura4-D18	This study
7268	h+ mto2-NT2:hphMX6 mto1(131-549)-GFP:kanMX6 Z:ADH15:mCherry-Atb2:natMX6 cdc25-22 ade6-? leu1-32 ura4-D18	This study
7270	h+ mto1(131-549)-GFP:kanMX6 Z:ADH15:mCherry-Atb2:natMX6 cdc25-22 ade6-? leu1-32 ura4-D18	This study
7272	h- mto2-17A:hphMX6 mto1(131-549)-GFP:kanMX6 Z:ADH15:mCherry-Atb2:natMX6 cdc25-22 ade6-? leu1-32 ura4-D18	This study
7282	h+ mto2-NT2:hphMX6 mto1(1-549)-GFP:kanMX6 Z:ADH15:mCherry-Atb2:natMX6 ade6-M210 leu1-32 ura4-D18	This study
7284	h- mto2-17A:hphMX6 mto1(1-549)-GFP:kanMX6 Z:ADH15:mCherry-Atb2:natMX6 ade6-M210 leu1-32 ura4-D18	This study

Table 2.5. List of oligonucleotides used during this study.

Database name	5'-3' sequence
pJET1,2 Fwd	CGACTCACTATAGGGAGAGCGGC
pJET1,2 Rev	AAGAACATCGATTTTCCATGGCAG
OKS204	GCTAGGATACAGTTCTCACATCACATCCG
OKS241	GTGCAAGAATCTCTTGCAAATTCGAGCTTGGTCTTGCAACTGTTTATTCTAATCC TCCAGCGTCTTGCTGGTGGTTTCGCCGGATCCCCGGGTTAATTAA
OKS248	CGTCCTAGTAGGATTAGCAACTTCTT
OKS249	GAGCAAGCAATGCAGCAAATAGAGAT
OKS258	TCCTCAATCAATGTTTGTATGAACTTACATGTATGAGAAGAACCTGATTTACTTG ATAAACACAAAGAAAAATTGATTCAGAATTCGAGCTCGTTTAAAC
OKS503	CACGTTGTGCCTGAATAAAACTCGATTC
OKS504	TGCGCAGTAAAATTTACTTAAAAAAGGT
OKS916	CAGGAAAACTTCGTGGATC
OKS928	CTTGAAAATCTCCGAGAACGC
OKS1230	GTAAAACGACGGCCAG

OKS1231	CAGGAAACAGCTATGAC
OKS1355	GATGTTCGGGGATTCCCAATAC
OKS1356	GACTGCCCCGAAGTCCGGCACC
OKS1802	ATTTGCCACTGAGGTTCT
OKS1804	GGCTTCGTGGTCATCTCGT
OKS2117	CTAAAGGGAACAAAAGCTGGGTACC
OKS2118	TAAATACATGCATCCGGAGTTACGTTATG
OKS2119	CATAACGTAACTCCGGATGCATGTATTTA
OKS2120	ATACAACGGGAGCCTAGGCGATAAAGGCT
OKS2121	AGCCTTTATCGCCTAGGCTCCCGTTGTAT
OKS2122	GCGCATTCGTTTTCTCGAGAATGCCTTGG
OKS2123	CCAAGGCATTCTCGAGAAAACGAATGCGC
OKS2124	AGAAGACGAAATCGCGACCCTGAAAAGAC
OKS2125	GTCTTTTCAGGGTCGCGATTTCGTCTTCT
OKS2126	GTACTTGCATGGAATCTGTCAAACC
OKS2127	TTAGATTCATGTTTACGTTTTG
OKS2128	GAGATTTTAATACGCAATCTCCCA
OKS2129	TCATTAACCTTAGATAAATAATCGAC
OKS2130	TACGATTATACTTCGGACCCTTCA
OKS2131	CGTTCGTTATCAAGCATATTTGAC
OKS2150	CTTACTCTTCGTGAGCAAGAAAAGGT
OKS2151	CGGAACATGAAGGACTTTGAAAATCA
OKS2152	TTAACTTTAAAGGAACAAGCAAACGT
OKS2153	CAGGCTCTTCGAGACTTTGAGAAGCA
OKS2164	AGAATAATTCGTCTTCTTTGA
OKS2165	ATTTGGATGATGAAGATGATT
OKS2175	AACACCAAATTTTAGAAGCTAATCACTCTCATCATAATCGTCTACATCCTCATCG TTATCGACGATAAAAGAATCATCTTGAATTCGAGCTCGTTTAAAC
OKS2176	GCAGCAGCCGCAGCAGCCGCCGCAGCAATCAAAATTGTATGTTTGGAAAAGCG A
OKS2177	TGCTGCGGCGGCTGCTGCGGCTGCTGCTTTCTCAAGGACCTTTTCTTGCTCAC G
OKS2178	TTCGAATCAAAACTGTATGTTTGGA
OKS2179	TCCAAACATACAGTTTTGATTCGAA
OKS2180	AAGCTGAAGCTGTAAGTTTGCTC
OKS2188	CTTCTCTAGATCAGTTACCTCATTTG
OKS2189	CTTCCTTTTCCCGCCGTTCGTTAT
OKS2190	CACCAAATTTTAGAAGCTAATCACTCTCATCATAATCGTCTACATCCTCATCGTT ATCGACGATAAAAGAATCATCTTACGAATTCGAGCTCGTTTAAAC
OKS2193	GAGTTGCTCATCCTATTATCCCCCAGAGGGCGTCTCCAGCATCACAGTCTTTTC CTTCTCTTCAAGACACTCCTTCCCCCCGGATCCCCGGGTTAATTAA
OKS2194	TCACACAGGAAACAGCTATG
OKS2195	CATAAATCATAAGAAATTCG
OKS2196	CAACGGCTCGTTGAAGCTCC
OKS2197	CGGCTCGTTGAAGCTCCATAG
OKS2206	CTATACAATGGCTGAGGCAGAAC
OKS2207	CCACATGGTCCTTCTTGAGTTTG
OKS2212	AACGTGATTGATAATTTGAG
OKS2213	TAAGGGTCTTCAAATCGATG
OKS2214	ATCTCAGCCCGGCTCCTCC

OKS2215	TTAACTTTAAAGGAACAAGCAAACGT
OKS2216	CAACGGCTCGTTGAAGCTCC
OKS2219	TTAACTTTAAAGGAACAAGCAAACGT
OKS2220	CAACGGCTCGTTGAAGCTCC
OKS2232	GGCCAGACCGGTGGTACCTA
OKS2233	GGCCTAGGTACCACCGGTCT
OKS2234	GCATGGTACCACCGGTCCCGGG
OKS2235	CGCGCCCGGGACCGGTGGTACC
OKS2236	GGCCAGACCGGTGGTACCTA
OKS2237	GGCCTAGGTACCACCGGTCT
OKS2238	GCATGGTACCACCGGTCCCGGG
OKS2239	CGCGCCCGGGACCGGTGGTACC
OKS2244	GCCTGAAATCGTTGAAGGTGTCG
OKS2253	CATGGGTACCACCGGTCCCGGG
OKS2254	TCGAGGTACCACCGGTCCCGGG
OKS2268	CTCTTATTGACCACACCTCTACC
OKS2269	GGTCATAAAGTTGAACGGATGTCG
OKS2270	GCAACTGTTTATTCTAATCC
OKS2271	ACCTGATTTACTTGATAAAC
OKS2272	TTGCTCATCCTATTATCCCCCAGAGGGCGTCTCCAGCATCACAGTCTTTTCCTT CTCTTCAAGACACTCCTTCCCCCTAGCGGATCCCCGGGTTAATTAA
OKS2274	GGGGACAAGTTTGTACAAAAAAGCAGGCTTCATGAAAT
OKS2275	AAGCAGGCTTCATGAAATTACAAGATCGAGAGAAAGAGT
OKS2276	GGGGACCACTTTGTACAAGAAAGCTGGGTCGTAGTTTGC
OKS2277	AAAGCTGGGTCGTAGTTTGCGGTCTTTGCCTTTGCG
OKS2278	GGGGACAAGTTTGTACAAAAAAGCAGGCTTCATGTCT
OKS2279	AAGCAGGCTTCATGTCTGAACGAGATTTTAATACGC
OKS2280	GGGGACCACTTTGTACAAGAAAGCTGGGTCATTAATGGA
OKS2281	AAAGCTGGGTCATTAATGGATTCATGAAACCGCCGC
OKS2282	CCAGATCTCGATCCCGCG
OKS2283	CCAACTCAGCTTCCTTTCG
OKS2292	GGGGAAGGAGTGTCTTGAAGAG
OKS2293	CTAGGGGGAAGGAGTGTCTT
OKS2344	ATAAAAACTAGCAAGTTATCCTAACGAAC
OKS2345	ATTAAAATAGACGTCCTAGTAGGATTAGC
OKS2366	GAGTTGCTCATCCTATTATCCCCCAGAGGGCGTCTCCAGCATCACAGTCTTTTC CTTCTCTTCAAGACGCTCCTGCTCCCCGGATCCCCGGGTTAATTAA
OKS2407	GGGATTTCTCATGGTTAATGAATTCTC
OKS2409	CCGAGCAAATCGAGGTTCTTGAGAACG
OKS2410	GTCAGCCGAATCTTTGTTACATAACAC
OKS2411	CCTTCATTAAGTCTTCCTCGGTAATGACC
OKS2412	GGAGTCATATCAATGGTAGGAAGATC
OKS2416	GGCAGAGATCCTACCATCTCCGCGTACC
OKS2417	CGGAACCTCATGAATCGGCCAATGTCG
OKS2418	CAAGAGGAAGTTGAACACTAGGGAAAGC
OKS2419	CGTCGTTGCACAAAACCTCTAAAGGGAGC
OKS2420	GTTAAGGATACGTCTTGTTTGAAGGTTCG
OKS2421	CGATATTACAGCAATCATTCTCATGGGC

OKS2422	CCTGCCTGAAATCGGAAAGAGCTAAAAGG
OKS2423	CGTGGCTTATCTTCTCCCCAGATAGTG
OKS2424	CTCTAAAAAAACAGATACCTAAATTG
OKS2425	GGAATTGCACTGATGTAACAGAATCAGC
OKS2426	CGAAAATAATGTGAAAAGATAGTAAAC
OKS2427	GCCCAAGCCAATATAGAATTAAAATGCC

Chapter 3
Analysis of the role of the Centrosomin Motif 1 in the regulation of Mto1 and Pcp1 nucleation activity during the cell cycle

3.1 Introduction

In eukaryotes, the specific tethering or "adaptor" proteins are involved in recruiting the γ-TuC to prospective MTOCs. In fission yeast, Mto1 and Pcp1 are the only γ-TuC tethering proteins. Like many other γ-TuC adaptors, both Mto1 and Pcp1 are relatively large coil-coiled proteins (1115 and 1208 amino acids, respectively) (Flory et al., 2002; Sawin et al., 2004; Venkatram et al., 2004), and each contains a γ-TuC-binding Centrosomin Motif 1 (CM1) (Sawin et al., 2004; Zhang and Megraw, 2007) (Fig. 3.1). Mto1- and Pcp1-promoted MT nucleation is almost mutually exclusive both spatially and temporally. Pcp1 function is limited to within the nucleus, and specifically during mitosis, when it promotes formation of mitotic spindle MTs from the inner face of the SPB (Flory et al., 2002; Fong et al., 2010). In contrast, Mto1 promotes MT cytoplasmic nucleation from several distinct cytoplasmic MTOCs, specifically during interphase (Sawin et al., 2004; Venkatram et al., 2004). The mechanisms regulating the spatial and temporal division of labour between Mto1 and Pcp1 remain largely unknown.

A similar differential regulation is observed between budding yeast γ-TuC receptors, Spc110 and Spc72, whereby Spc110 nucleates MTs from the inner, and Spc72 the other plaque of the SPB (Knop and Schiebel, 1997, 1998). Recently, human MMGL was also suggested to be interphase-specific (as opposed to its paralogue CDK5RAP2, which functions both in interphase and mitosis (Fong et al., 2008)). MMGL RNAi had no mitotic phenotype in RPE1 cells (Roubin et al., 2013); however, RNAi is never absolute and it is possible that residual MMGL might be sufficient to perform its mitotic function.

Pcp1, presumably due to its role in spindle formation, is an essential protein, and localises to the inner face of the SPB (Flory et al., 2002). The N-terminal CM1 domain is followed by central coiled-coils; SPB-localisation domains are located towards the Pcp1 C-terminus. Pcp1 is though to interact with the γ-TuC throughout the cell cycle; yet, Pcp1-mediated nucleation is restricted to the mitotic phase of the

cell cycle, therefore suggesting that MT nucleation is regulated independently of the γ-TuC-Pcp1 interaction (Flory et al., 2002; Fong et al., 2010).

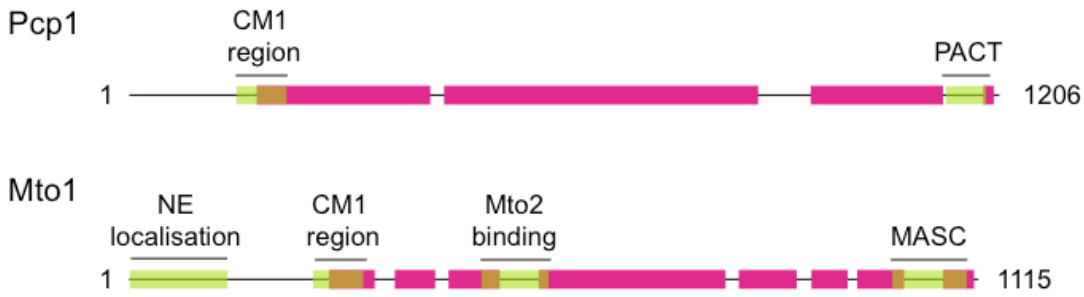

Figure 3.1. Schematic representation of Mto1 and Pcp1 with predicted coiled-coil regions shown in magenta and interaction domains indicated in green. MASC region is required for Mto1 localisation to SPBs and MTOCs; PACT domain promotes Pcp1 interaction with calmodulin.

Unlike Pcp1, Mto1 is non-essential and localises to and promotes nucleation from distinct cytoplasmic foci such as MTs, the NE, the outer face of the SPB and eMTOCs. Comprehensive Mto1 characterisation showed that the protein contains multiple localisation and interaction domains. The NE-localisation domain is located at the N-terminus and is followed by the CM1 and more centrally located Mto2-binding region; the C-terminus promotes localisation to interphase and mitotic SPBs, MTs and to eMTOCs (Samejima et al., 2008, 2010; Sawin et al., 2004). Previous work revealed that Mto1 needs an intact CM1 domain to perform its function; *mto1-9A1* cells, in which nine conserved residues within the CM1 were mutated to alanines to eliminate the γ-TuC-Mto1 interaction, are completely defective in MT nucleation from cytoplasmic MTOCs, phenocopying *mto1*Δ (Samejima et al., 2008).

The CM1 is an approximately sixty amino acids sequence motif conserved in most eukaryotes. CM1 proteins – including *Drosophila* centrosomin (cnn), human CDK5RAP2, mutated in a form of primary autosomal microcephaly, and MMGL, recently implicated in schizophrenia, as well as *S. pombe* Mto1 and Pcp1 – display various MT nucleation-related functions (Bond et al., 2005; Flory et al., 2002; Kim et al., 2012; Megraw et al., 1999; Roubin et al., 2013; Samejima et al., 2008; Sawin et al., 2004; Verde et al., 2001; Zhang and Megraw, 2007). In humans, both MMGL and CDK5RAP2 CM1 regions were shown to interact with the γ-TuC (Choi et al., 2010; Roubin et al., 2013). Importantly, a small truncation of CDK5RAP2

encompassing the CM1, termed γ-TuNA (γ-TuRC-mediated Nucleation Activator), stimulated γ-TuRC-dependent nucleation *in vitro* (Choi et al., 2010). In budding yeast, a truncated CM1-containing fragment of Spc110, a Pcp1 orthologue, promotes γ-TuSC multimerization into γ-TuRC-like structures (Kollman et al., 2010). In the template model of MT nucleation, such multimerization is required for MT formation.

We hypothesised that the Mto1 vs. Pcp1-promoted nucleation regulation might rely on different Mto1 and Pcp1 CM1 structures. There are several ways this could be achieved. Firstly, the γ-TuC components are known to be post-translationally modified (Alvarado-Kristensson et al., 2009; Kim et al., 2005; Lin et al., 2011; Pereira et al., 1998; Vogel et al., 2001). One could imagine two distinct, differently modified γ-TuC pools existed: intranuclear – that could only interact with or be activated by Pcp1, and cytoplasmic – that could interact exclusively with Mto1. Secondly, the γ-TuC modification could be cell cycle-regulated, allowing it to interact with Mto1 only in interphase and with Pcp1 only in mitosis. The possibility of two functionally distinct γ-TuC pools has been suggested in other studies (Khodjakov and Rieder, 1999; Schiebel, 2000). Finally, the CM1 regions of Mto1 and Pcp1 could themselves be differentially modified (e.g. phosphorylated) in a cell cycle-dependent manner. The CM1 alignment reveals that both proteins contain phosphorylatable residues specific to only one of them (Fig 3.2)

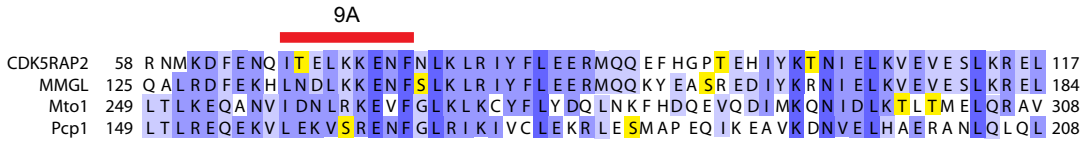

Figure 3.2. Sequence alignment of CM1 regions of human CDK5RAP2 and MMGL and fission yeast Mto1 and Pcp1. The alignment was generated using Clustal W 2.0 (Larkin, 2007) and visualised using Jalview (www.jalview.org). Different shades of blue correspond to different degrees of conservation. Non-conserved phosphorylatable residues within are indicated in yellow. Red bar indicates conserved residues mutated to alanines in *mto1-9A1* mutant.

In this chapter, my aim was to address whether CM1 regions of Mto1 and Pcp1 contribute to the differential regulation of Mto1 vs. Pcp1-promoted nucleation. To do this, I used a reciprocal domain-swap approach to generate Mto1 and Pcp1 chimeric proteins containing heterologous CM1 regions. Using this method, I additionally investigated the functional conservation of the CM1 region from yeast to human, by introducing CM1 regions of MMGL and CDK5RAP2 into fission yeast γ-

TuC adaptors and analysing the functional and biochemical interaction of chimeric proteins with the γ-TuC. I found that the CM1 region of Pcp1 is essential for viability, and that CM1 region sequence differences have no role in the Mto1 vs. Pcp1-mediated MT nucleation regulation. Importantly, I showed that the human CM1 regions rescue yeast proteins function, suggesting that the γ-TuC-CM1 interaction is functionally conserved across evolution.

3.2 Results

3.2.1 Introduction of heterologous CM1 domains into Mto1

3.2.1.1 CM1 regions of Pcp1 and MMGL fully rescue Mto1 function whereas CM1 region of CDK5RAP2 does not

In Mto1, similarly to other centrosomin-related proteins, the CM1 domain is located towards the Mto1 N-terminus (Sawin et al., 2004). Using two-step gene replacement method, I introduced three heterologous CM1 regions into *mto1-GFP* at endogenous locus, to produce *mto1(CM1:Pcp1)-GFP*, *mto1(CM1:MMGL)-GFP* and *mto1(CM1:CDK5RAP2)-GFP* (in figures and legends referred to as *CM1:Pcp1*, *CM1:MMGL* and *CM1:CDK5RAP2*, respectively).

As a first method to assess *mto1* function in *mto1:CM1* cells, I used cell morphology assay. Both *mto1*Δ and nucleation-deficient *mto1-9A1* cells, as a result of impaired MT organization, exhibit a curved morphology, a phenotype that is more prominent during recovery from stationary phase (Sawin et al., 2004; Venkatram et al., 2004, 2005). Wild-type and mutant cells were thus grown to stationary phase and then re-introduced into fresh medium, fixed with formaldehyde solution and imaged using DIC (Differential Interference Contrast) microscopy.

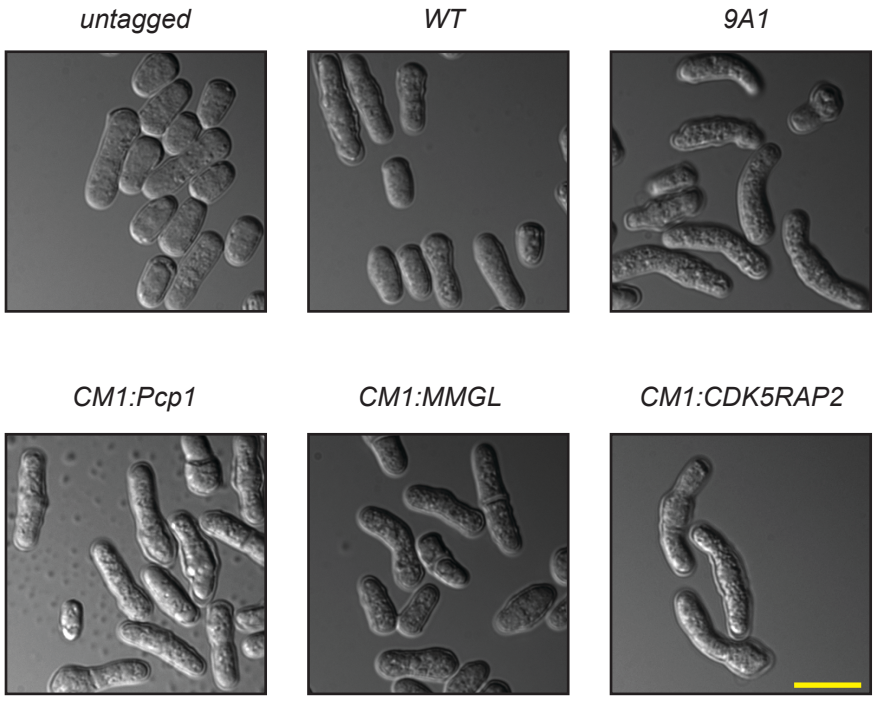

Figure 3.3. Two of three *mto1(CM1)-GFP* mutants show normal cell morphology. Cell morphology was assayed after growing cells to stationary phase and re-introduction into fresh medium. Wild-type cells showed normal, straight cell phenotype. Introduction of the CM1 region of Pcp1 and MMGL had no effect on cell morphology, whereas introduction of the CDK5RAP2 CM1 region produced the curved cell phenotype, characteristic of nucleation-deficient *mto1-9A1-GFP*. Bar, 5 µm. [Strains: KS516, KS819, KS2076, KS6237, KS6160 and KS6161]

As expected, *mto1*$^{+}$ (untagged) and *mto1-GFP* (WT) cells were straight while *mto1-9A1-GFP* exhibited abnormal, curved cell shape. Introduction of CM1 regions of Pcp1 and MMGL had no effect on cell morphology, showing that Mto1 function is maintained in these mutants. Introduction of CDK5RAP2 CM1 region lead to curved cell phenotype, suggesting that Mto1 function is lost or impaired (Fig. 3.3).

By fluorescence microscopy, Mto1(CM1:Pcp1)-GFP and Mto1(CM1:MMGL)-GFP proteins showed localisation patterns similar to wild-type Mto1-GFP (Fig 3.4). By contrast, Mto1(CM1:CDK5RAP2)-GFP was enriched at the NE, reminiscent of Mto1(9A1)-GFP. This suggested that MT networks are altered in *mto1(CM1:CDK5RAP2)-GFP* but not in *mto1(CM1:Pcp1)-GFP* and *mto1(CM1:MMGL)-GFP* background.

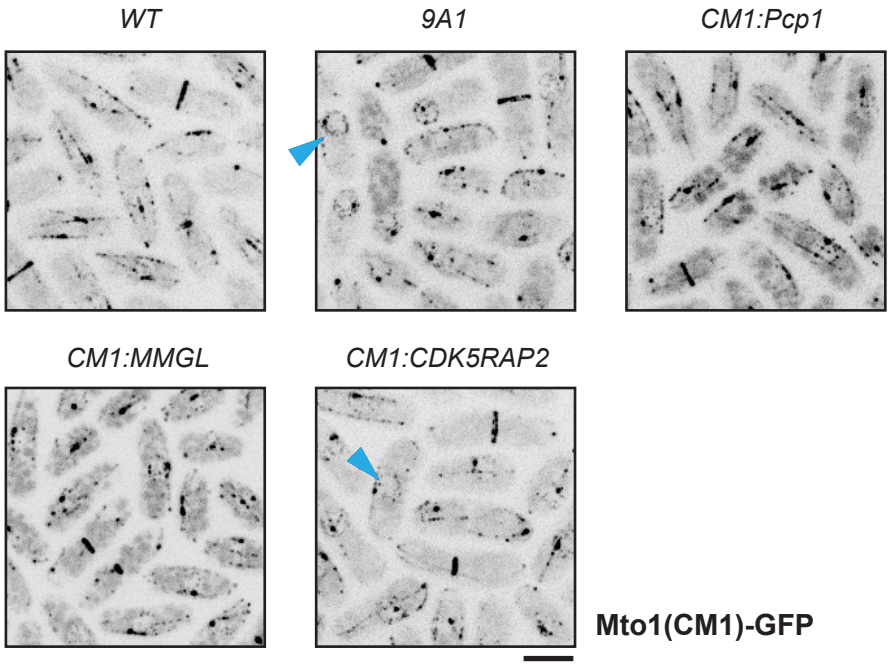

Figure 3.4. Localisation of Mto1(CM1)-GFP proteins. Mto1-GFP localizes to the SPB, the NE, along MTs and to eMTOCs. Mto1-9A1-GFP localizes to the same foci, and is enriched at the NE, as compared to wild-type (blue arrowhead). *CM1:Pcp1* and *CM1:MMGL* mutants exhibit wild-type Mto1-GFP localisation, while *CM1:CDK5RAP2* shows NE enrichment, reminiscent of *mto1-9A1-GFP*. Bar, 5 μm. [Strains: KS2853, KS6234, KS6235, KS6295 and KS7096]

In order to address whether MT arrays are normal in *mto1(CM1)-GFP* cells, live-cell imaging of mCherry-α-tubulin was used to directly compare MT networks in *mto1-GFP* and *mto1(CM1)-GFP* mutant strains (Fig. 3.5). As expected, *mto1-GFP* interphase cells expressing *nmt81*:mCherry-α-tubulin showed normal MT arrays. By contrast, *mto1-9A1-GFP* cells contained fewer microtubules, as a result of total absence of Mto1-dependent MT nucleation in this genetic background; the few existing MTs are thought to be nucleated by Pcp1 in mitosis and then subsequently 'escape' into the cytoplasm (Sawin et al., 2004; Venkatram et al., 2004; Zimmerman and Chang, 2005). *mto1(CM1:Pcp1)-GFP* and *mto1(CM1:MMGL)-GFP* cells clearly showed normal MT arrays, while *mto1(CM1:CDK5RAP2)-GFP* cells exhibited *mto1-9A1*-like phenotype. To obtain more quantitative information, the number of MT bundles per cell was counted for each mutant, and compared to that of *mto1-GFP* and *mto1-9A1-GFP* (Fig. 3.6 A). Since the data was non-parametric, Wilcoxon rank-sum test was used to statistically compare mutants (Mann and Whitney, 1947), and out of the three *mto1(CM1)-GFP* strains only *mto1(CM1:CDK5RAP2)-GFP* was statistically different than wild-type (Table 3.1).

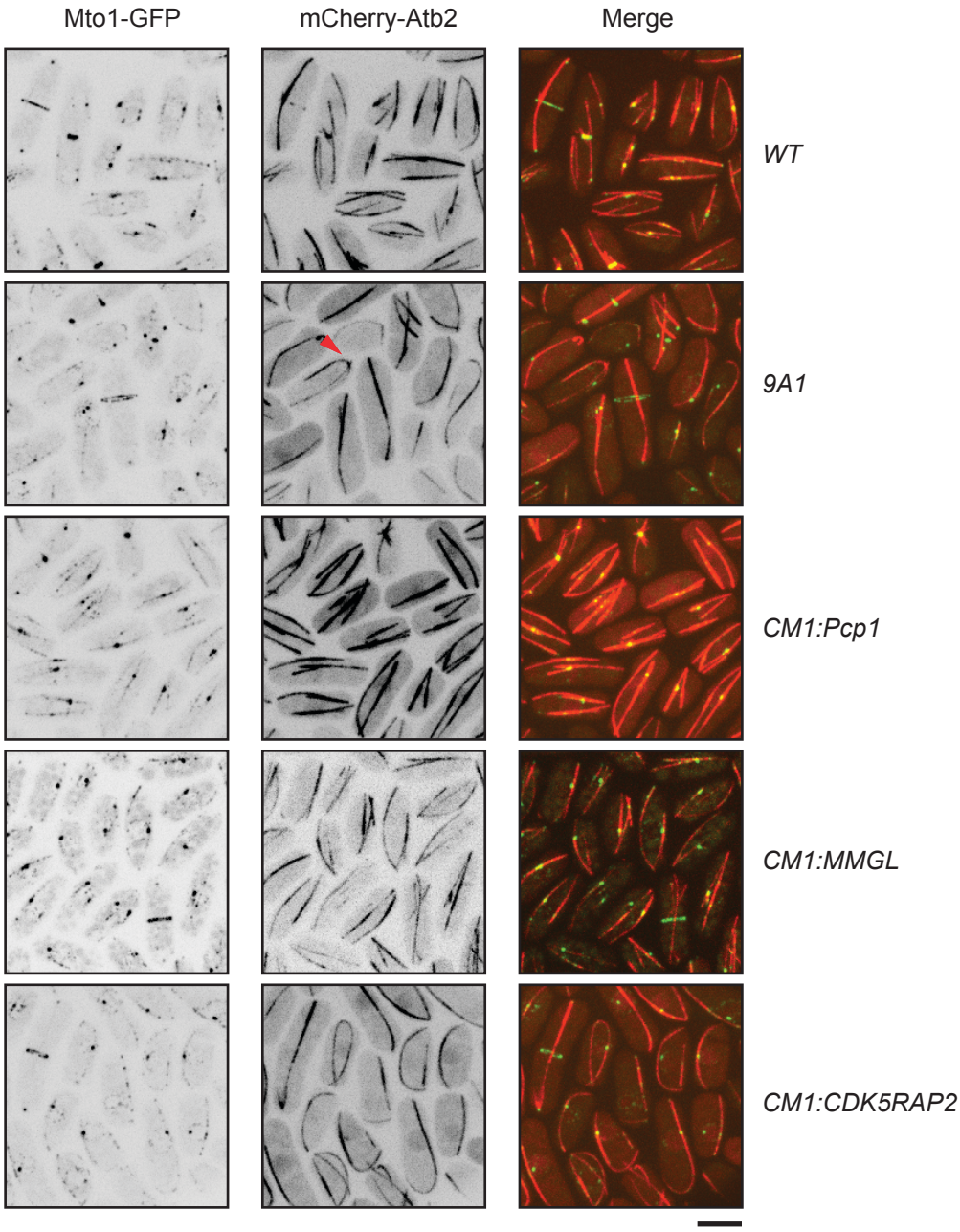

Figure 3.5. Cytoplasmic MT networks in *mto1(CM1)-GFP* mutants. Interphase MTs (mCherry-α-tubulin, red) in strains expressing Mto1(CM1)-GFP (green). Interphase *mto1-GFP* cells contained three to five MT bundles that extended along the long axis of the cell, while in *mto1-9A1-GFP* the number of MT bundles per cell was lower, and they often curved around cell tips (red arrowhead). *CM1:Pcp1* and *CM1:MMGL* cells exhibited wild-type MT phenotypes whereas *CM1:CDK5RAP2* showed reduced number of MTs, characteristics of *mto1-9A1-GFP*. Bar, 5 μm. [Strains: KS2853, KS5335, KS6234, KS6235, KS6295, KS7096]

Table 3.1. Two of three heterologous CM1 regions substitute for the Mto1 CM1 region. Wilcoxon rank-sum test was used for comparison between each mutant (Mann and Whitney, 1947). P values are shown.

	Δ	9A1	WT	CM1: Pcp1	CM1: MMGL
CM1: CDK5RAP2	0.1244	0.0174	2.20E-16	2.40E-15	2.20E-16
CM1:MMGL	6.65E-14	4.22E-14	0.08278	0.7309	
CM1:Pcp1	1.48E-12	1.34E-12	0.06502		
WT	9.39E-15	7.13E-15			
9A1	0.446				

Another characteristic of impaired *mto1* function is the shape of MT bundles: in wild-type (*mto1*$^{+}$) cells, MT bundles extend along the long axis of the cell and terminate at cell tips, whereas in *mto1*Δ and *mto1-9A1* they often curve abnormally around cell ends (Samejima et al., 2008; Sawin et al., 2004; Venkatram et al., 2004; Zimmerman and Chang, 2005). The percentage of abnormal MT bundles was counted for each mutant (Fig. 3.6 B), defining an abnormal MT as one that curves around more than 75% of the cell tip. As expected, *mto1-GFP* cells contained virtually no abnormal MTs, while in *mto1*Δ and *mto1-9A1-GFP* cells abnormal MTs were present in approximately half of the cells. As before, MTs in *mto1(CM1:Pcp1)-GFP* and *mto1(CM1:MMGL)-GFP* cells resembled wild-type, whereas *mto1(CM1:CDK5RAP2)-GFP* cells showed a *mto1-9A1*-like phenotype. This further suggested that MT nucleation is either severely impaired or abolished in *mto1(CM1:CDK5RAP2)-GFP* background.

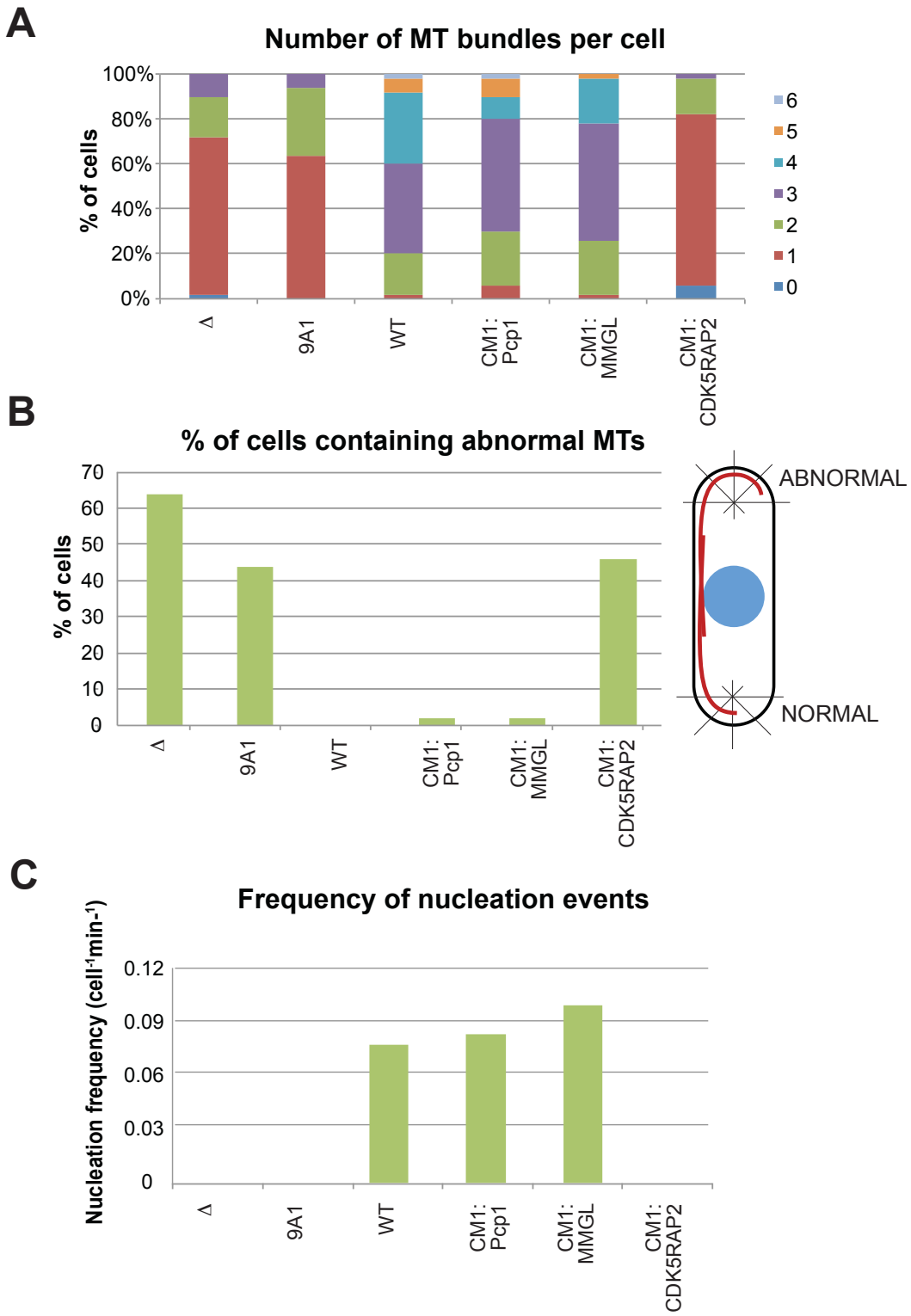

Figure 3.6. Quantification of MT arrays in *mto1(CM1)-GFP* cells. (A) Number of MT bundles per cell observed in Figure 3.5, n=50. (B) Number of abnormal MTs observed in Figure 3.5, n=50. MT was considered abnormal if it curved around more than 75% of the cell tip. (C) Quantification of the MT nucleation observed in movies of live cells co-expressing mCherry-α-tubulin and Mto1(CM1)-GFP, n=35. [Strains: KS2853, KS5335, KS6234, KS6235, KS6295, KS7096]

To quantify nucleation frequency in chimeric *mto1* mutants, I made movies of *nmt81*:mCherry-α-tubulin in *mto1(CM1)-GFP* cells and compared them to *mto1-GFP, mto1-9A1* and *mto1*Δ (Fig. 3.6 C). The frequency of MT nucleation *de novo* was scored for each mutant. The appearance of a new MT that did not originate from a MT breakage event or an existing bundle was taken as a nucleation event. Nucleation occurring along pre-existing MT bundles cannot be identified with confidence, because in most cases it is immediately followed by bundling, and therefore was excluded from the analysis. Occasionally, MTs shrink and become very short 'stubs' that are too small to be confidently identified as a MT. Re-growth events from such stubs were not counted as new nucleation events. In order to avoid scoring such re-growth events as nucleation *de novo,* the first four time points of each movie were rejected (because no information about possible stub formation prior to acquisition was available). *mto1(CM1:Pcp1)-GFP* and *mto1(CM1:MMGL)-GFP* cells showed *de novo* MT nucleation similar to wild-type cells, whereas *mto1*Δ*, mto1-9A1-GFP* and *mto1(CM1:CDK5RAP2)-GFP* showed virtually no nucleation. The MT nucleation frequency in *mto1(CM1:Pcp1)-GFP* and *mto1(CM1:MMGL)-GFP* cells was slightly higher than WT. This result further confirms that only CM1 regions of Pcp1 and MMGL can functionally substitute for the CM1 of Mto1.

3.2.1.2 Mto1(CM1)-GFP proteins interact with different amounts of the γ-TuC

To address why the CM1 region of CDK5RAP2 fails to rescue *mto1* function, I investigated the interaction of Mto1(CM1)-chimeric proteins with γ-TuC by co-immunoprecipitation followed by western blotting (Fig. 3.7 A). I hypothesised that the loss of Mto1 function in *mto1(CM1:CDK5RAP2)-GFP* background may be explained by the loss of Mto1-γ-TuC interaction, as it requires a functional CM1 domain to occur.

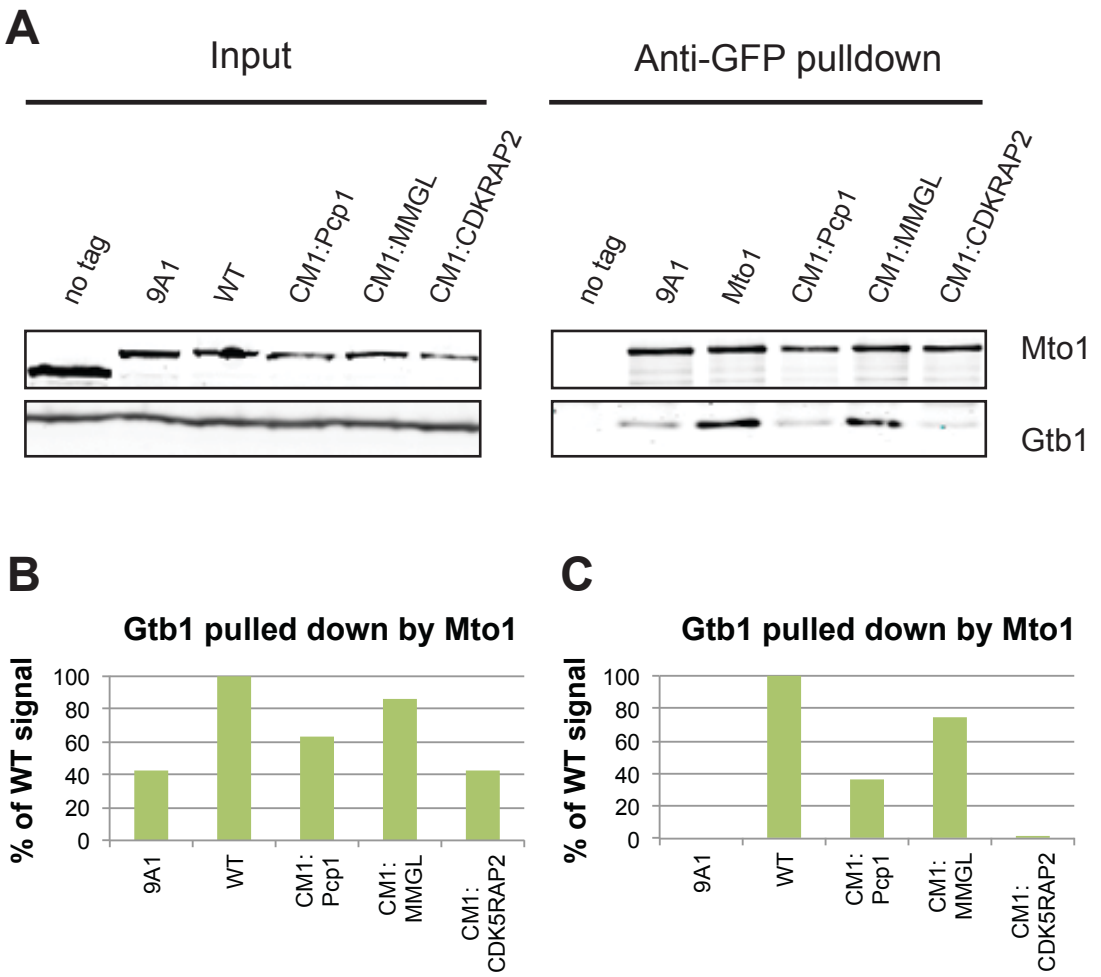

Figure 3.7. The efficiency of the Mto1-Gtb1 interaction is affected by the CM1 region substitution. (A) Mto1(CM1)-GFP immunoprecipitate different amounts of γ-tubulin. Total cell extracts expressing Mto1(CM1)-GFP were immunoprecipitated with anti-GFP antibody. Western blots were probed with anti-Mto1 and anti-Gtb1 antibodies. (B) Mto1(CM1)-GFP mutants pull down less Gtb1 than wild-type Mto1-GFP. Integrated intensities of IRDye800 were measured using Odyssey V3.0, and Gtb1 signal was normalised to Mto1-GFP and shown as percentage of wild-type signal. (C) The same data as in (B); after normalisation to Mto1-GFP signal, Gtb1 signal intentsity in 9A1 lane was used for background subtraction. Shown as percentage of wild-type signal. [Strains: KS516, KS819, KS2076, KS6060, KS6061, KS6237]

As expected, Mto1-GFP was able to co-immunoprecipitate γ-tubulin. Surprisingly, Mto1-9A1-GFP also pulled down γ-tubulin (43% of wild-type levels). This result differs from previous observations (Samejima et al., 2008), where no such interaction was found, and may be attributable to improved immunoprecipitation and western blotting conditions. Nevertheless, as *mto1-9A1-GFP* cells phenocopy *mto1*Δ, it is clear that the observed interaction between Mto1-9A1-GFP and the γ-TuC is not functional.

Mto1(CM1:CDK5RAP2)-GFP co-immunoprecipitated a similar amount of γ-tubulin as the non-functional Mto1-9A1-GFP (43% relative to wild-type, Fig 3.7 B). Both of these mutants lost their function *in vivo*, suggesting that the low amount of γ-tubulin they interact with is not sufficient to promote nucleation. Potentially, even though Mto1(CM1:CDK5RAP2)-GFP and Mto1-9A1-GFP are able to interact with the γ-TuC through the CM1, they are not able to activate it (for example, to induce conformational changes in the γ-TuC) (Lynch et al., 2013, unpublished). Alternatively, the observed interaction might be unspecific, and promoted by extensive Mto1 coiled-coil regions that can encourage protein aggregation (Sawin et al., 2004), possibly as an artefact of the altered immunoprecipitation protocol used in this study (this notion will be further investigated in Chapter 3.2.1.3). This hypothesis is supported by the fact that Mto1-9A1-GFP does not colocalise with the γ-TuC *in vivo* (Samejima et al., 2008). If that were the case, the signal intensity of γ-tubulin that co-immunoprecipitated with Mto1-9A1-GFP should be used as background signal. After background subtraction (Fig. 3.7 C), only 3% of γ-tubulin was co-immunoprecipitated by Mto1(CM1:CDK5RAP2)-GFP relative to Mto1-GFP.

Mto1(CM1:Pcp1)-GFP, Mto1(CM1:MMGL)-GFP and pulled down 63%, 85% and of the total γ-tubulin relative to Mto1-GFP, respectively, showing that introduction of heterologous CM1 regions somewhat impairs the γ-TuC-Mto1 interaction (Fig. 3.7 B). Subtraction of the signal intensity of γ-tubulin that co-immunoprecipitated with Mto1-9A1-GFP resulted in even lower numbers (36% and 75%, respectively, Fig. 3. 7 C).

3.2.1.3 Mto1(bonsai-CM1)-GFP aggregates colocalise with iSPB in *CM1:Pcp1* and *CM1:MMGL* background

I hypothesized that Mto1-9A1-GFP and Mto1(CM1:CDK5RAP2)-GFP interact with γ-tubulin non-specifically either directly in cells or, perhaps more likely, in protein extracts as an artefact of the immunoprecipitation procedure. The latter possibility is supported by the fact that Mto1-9A1-GFP does not colocalise with the γ-TuC *in vivo*, suggesting that no γ-TuC-Mto1-9A1-GFP interaction occurs *in vivo* (Samejima et al., 2008).

To understand the nature of the γ-TuC-Mto1-9A1-GFP interaction observed biochemically, as well as to examine the robustness of Mto1 functional rescue by the CM1 regions of Pcp1 and MMGL, I introduced the three heterologous CM1 regions into an *mto1* truncation background. An Mto1 truncation mutant, *mto1(131-*

549) dubbed *mto1[bonsai],* was used; in this mutant, the protein lacks a large proportion of its coiled-coils and all localisation regions, thus reducing the possibility of non-specific interactions in co-immunoprecipitation experiments.

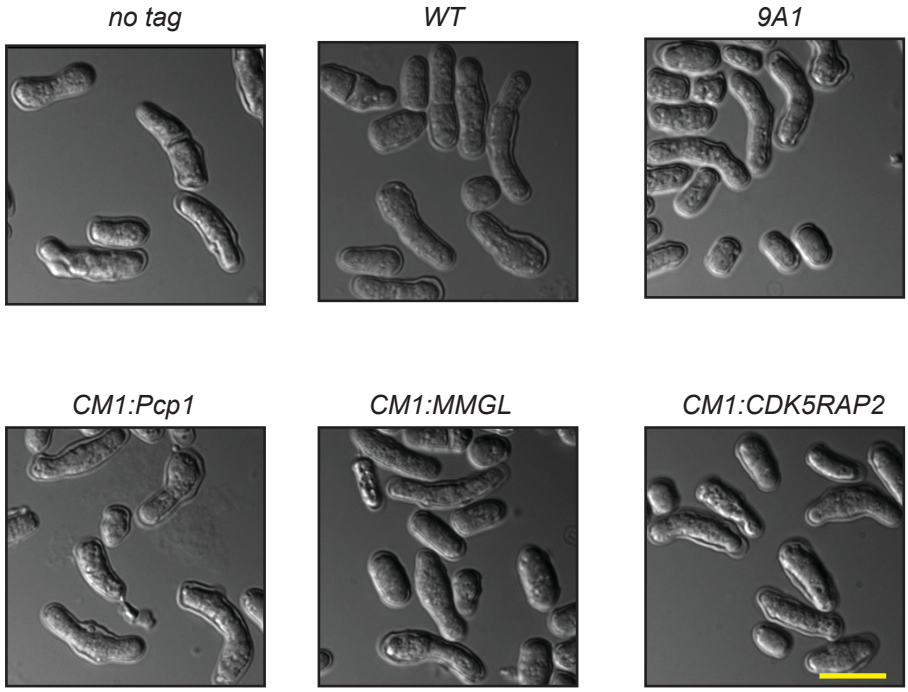

Figure 3.8. Cell morphology is abnormal in mto1(bonsai-CM1)-GFP mutants.
Cell morphology was examined after growing cells to stationary phase and re-introduction into fresh medium. *mto1-bonsai-GFP* cells (WT) showed normal, straight cell phenotype while untagged *mto1-bonsai* as well as *mto1(bonsai-CM1)-GFP* mutant cells showed abnormal, curved cell shape. Bar, 5 µm.
[Strains:KS516, KS6100, KS6339, KS6340, KS6342, KS6344]

Cell morphology of *mto1(bonsai-CM1)-GFP* mutants was assayed and compared to untagged and GFP-tagged *mto1-bonsai* cells (Fig. 3.8). Cells in *mto1-bonsai* background are somewhat bent due to the low expression levels of this truncation mutant, whereas *mto1-bonsai-GFP* cells exhibit near to wild-type cell morphology (E.M. Lynch, PhD thesis 2012). In contrast, all of the *mto1(bonsai-CM1)* mutants showed curved morphology, suggesting an impaired MT nucleation.

Live-cell imaging of *mto1(bonsai-CM1)-GFP* cells co-expressing *nmt81*:mCherry-α-tubulin revealed that Mto1 mutant proteins form large aggregates in the cytoplasm, which could affect MT nucleation in these cells and explain cell morphology defects (Fig. 3.9). *mto1(bonsai-CM1:Pcp1)-GFP* and *mto1(bonsai-CM1:MMGL)-GFP* cells contained fewer normal, and more abnormal MTs and MT nucleation frequencies in these cells were lower than in wild-type cells (Fig. 3.10 A-

C). The number of MT bundles in these cells was statistically different both from wild-type and *mto1(bonsai-9A1)-GFP* (Table 3.2). Consistent with previous results, the *mto1(bonsai-CM1:CDK5RAP2)-GFP* mutant phenocopied *mto1(bonsai-9A1)-GFP.*

Table 3.2. *mto1(bonsai-CM1)-GFP* cells are statistically different from both *mto1-GFP* and *mto1(bonsai-9A1)-GFP* cells. Wilcoxon rank-sum test was used for comparison between each mutant (Mann and Whitney, 1947). P values are shown.

	Δ	9A1	WT	CM1: Pcp1	CM1: MMGL
CM1: CDK5RAP2	0.6226	0.9968	3.34E-16	2.81E-13	3.89E-11
CM1:MMGL	1.74E-10	1.86E-10	8.66E-06	0.2536	
CM1:Pcp1	1.81E-12	1.57E-12	0.000509		
WT	1.85E-15	3.34E-16			
9A1	0.6723				

The γ-TuC localises at or near the inner face of the SPB throughout the cell cycle (Ding et al., 1997). In *mto1(bonsai-CM1)-GFP* mutants, nearly all cells contained at least one aggregate that was localised in the vicinity of the NE and the SPB (Fig 3.6A). To test the notion that Mto1(bonsai-CM1)-GFP aggregates bind to the SPBs, possibly through the interaction with the SPB-bound intranuclear γ-TuC, I generated strains co-expressing an RFP-tagged SPB marker, Cut12- tdTomato (Fig. 3.11) (Bridge et al., 1998). As expected, in *mto1-bonsai-GFP* and *mto1-bonsai-9A1-GFP* cells, where no aggregates were present, no colocalisation was observed. By contrast, in *mto1(bonsai-CM1:Pcp1)-GFP* and *mto1(bonsai-CM1:MMGL)-GFP* cells, GFP aggregates often colocalised with interphase SPBs (iSPB), but never with mitotic SPBs (mSPB). This was not observed in *mto1(bonsai-CM1:CDK5RAP2)-GFP* mutant, in which no colocalisation was detectable with either iSPB or mSPB. These observations are consistent with the notion that the SPB-localisation of Mto1(bonsai-CM1)-GFP aggregates is promoted by the interaction with the γ-TuC. Mto1 is only able to interact with the γ-TuC when in complex with Mto2 (Samejima et al., 2008), and the Mto1/2 complex disassembles in mitosis (L. M. Groocock, PhD Thesis 2010), thus, the aggregates can only interact with the γ-TuC in interphase.

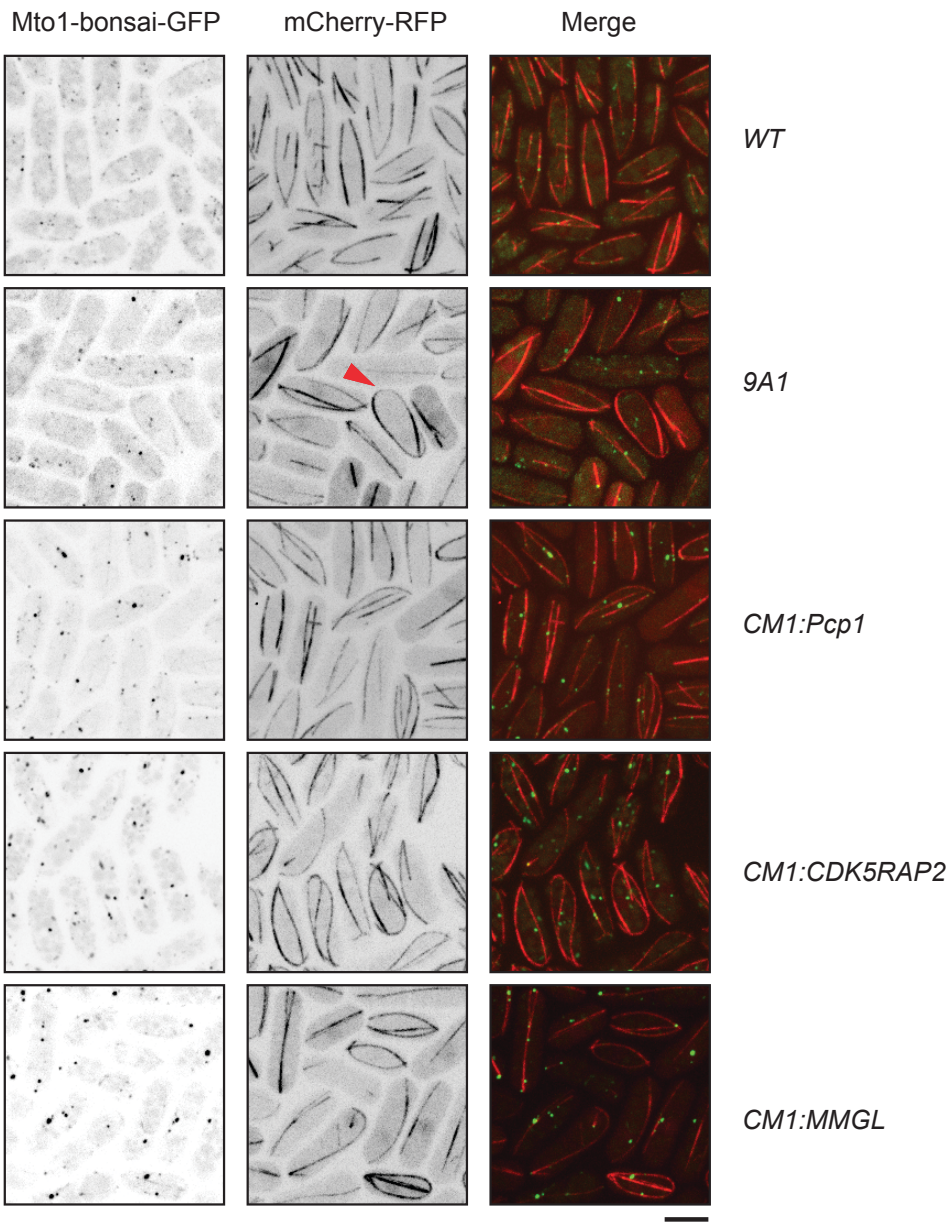

Figure 3.9. Cytoplasmic MT networks in *mto1(bonsai-CM1)-GFP* mutants.
Confocal images showing interphase MTs (mCherry-α-tubulin, red) in strains expressing Mto1(bonsai-CM1)-GFP (green). *mto1-bonsai-9A1-GFP* contains fewer MTs per cell than WT, and these MTs often curve around cell tips (red arrowhead). Neither of the CM1 mutants exhibits WT phenotype. Bar, 5 µm.
[Strains: KS6100, KS6339, KS6340, KS6342, KS6344]

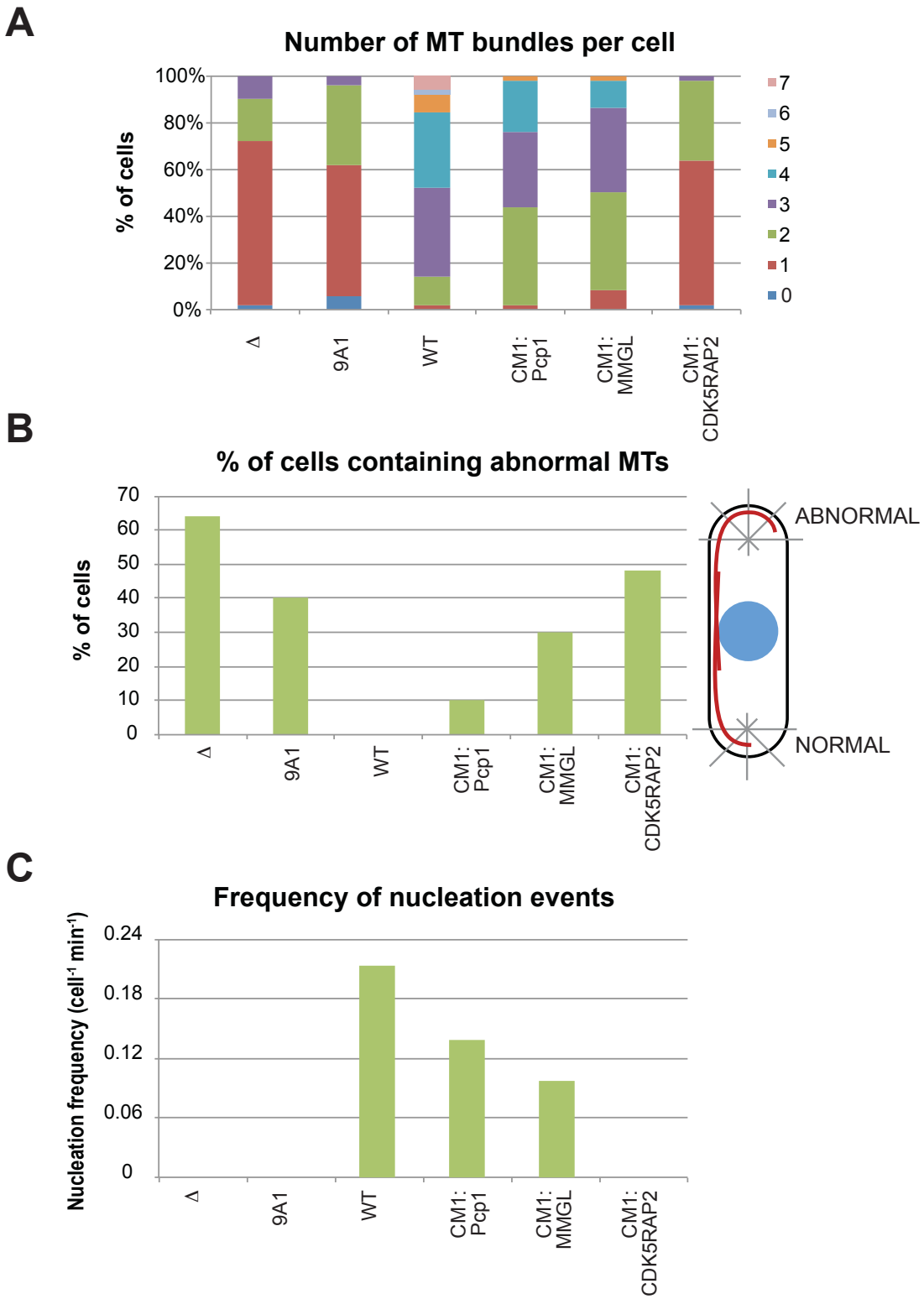

Figure 3.10. Quantification of MT arrays in *mto1(bonsai-CM1)-GFP* cells. (A) Number of MT bundles per cell observed in Figure 3.9, n=50. (B) Number of abnormal MTs observed in Figure 3.9, n=50. MT was considered abnormal if it curved around more than 75% of the cell tip. (C) Quantification of the MT nucleation observed in movies of live cells co-expressing mCherry-α-tubulin and Mto1(bonsai-CM1)-GFP, n=35. [Strains: KS5335, KS6100, KS6339, KS6340, KS6342, KS6344]

Also in agreement with this notion is the lack of the artefactual SPB localisation of the Mto1(bonsai-CM1:CDK5RAP2)-GFP, since the CM1 region of CDK5RAP2 did not rescue Mto1 function in the full-length protein context, and instead phenocopied *mto1-9A1-GFP* phenotype. As the γ-TuC is found at the nuclear face of the SPB throughout the cell cycle (Ding et al., 1997), it remains unclear how Mto1[bonsai] aggregates could get inside the nucleus to interact with the γ-TuC localised there. Possibly, a cryptic nuclear localisation signal was exposed due to partial protein misfolding. Alternatively, Mto1[bonsai] is able to get to the nucleus even in wild-type cells, but this is normally prevented by its binding to MT minus ends following MT nucleation.

To analyse the γ-TuC-Mto1(bonsai-CM1) interaction, I performed co-immunoprecipitation experiments as before (Fig. 3.12). As predicted, western blotting following immunoprecipitation revealed that both Mto1(bonsai-9A1)-GFP and Mto1(bonsai-CM1:CDK5RAP2)-GFP immunoprecipitated only a very small fraction of Gtb1 relative to Mto1-bonsai-GFP (5% and 7%, respectively). This also suggests that the interaction of full length Mto1-9A1-GFP and Mto1(CM1:CDK5RAP2)-GFP with the γ-TuC (compare to Fig 3.7 B and C) is indeed independent of the γ-TuC-CM1 interaction, and is most likely an artefact of co-immunoprecipitation procedure.

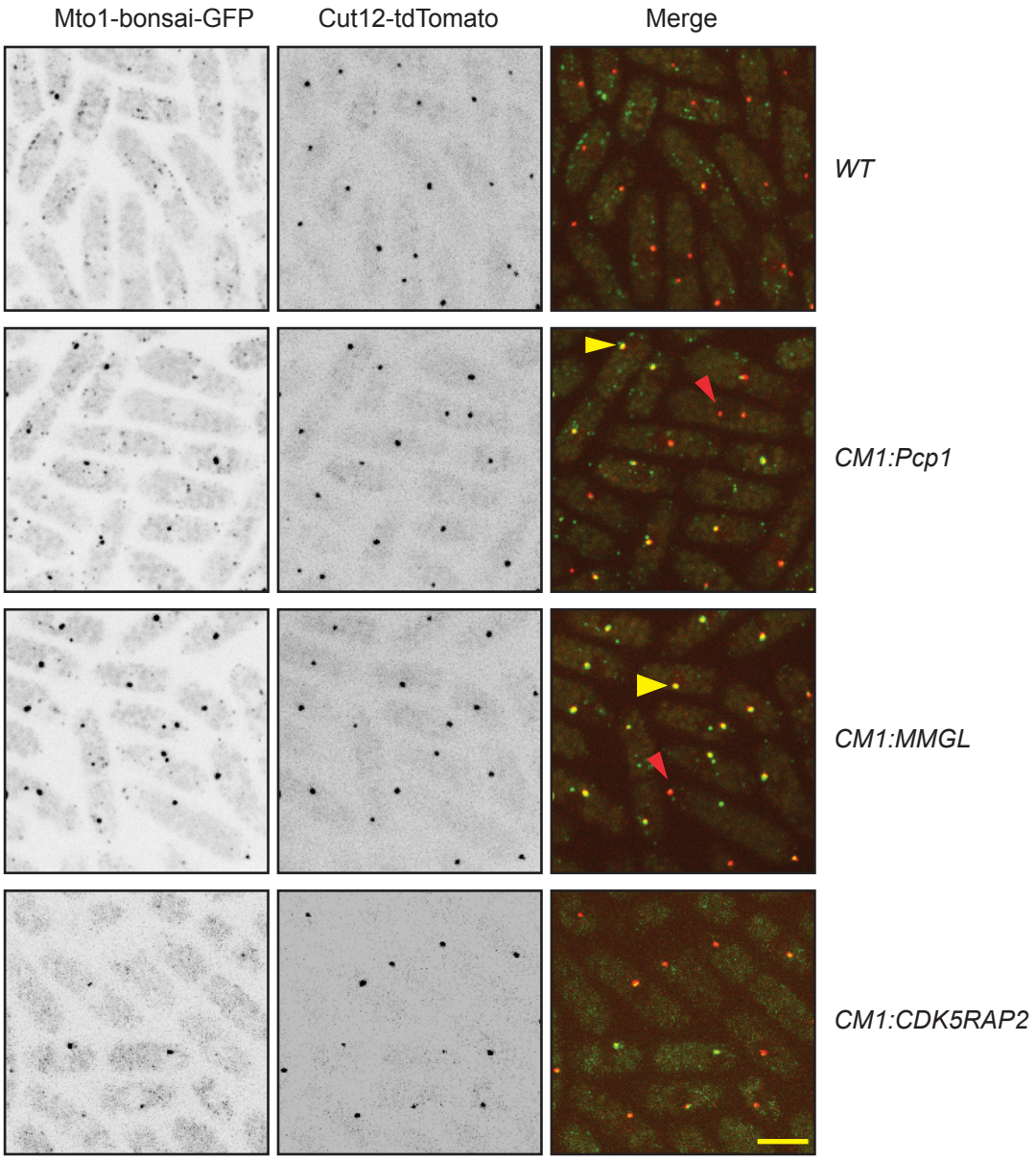

Figure 3.11. Functional Mto1(bonsai-CM1)-GFP mutants localise to iSPB but not to mSPB. Confocal images showing *mto1(bonsai-CM1)-GFP* cells co-expressing an SPB marker Cut12-tdTomato. In *mto1(bonsai-CM1)* background, Mto1(bonsai-CM1)-GFP mutant proteins form large aggregates, which in *CM1:Pcp1* and *CM1:MMGL* mutant cells colocalise with Cut12-RFP at interphase SPBs. Red arrow – no colocalisation at mitotic SPBs, yellow arrow – colocalisation at interphase SPB. Bar, 5 μm. [Strains: KS6346, KS6348, KS6350, KS6352]

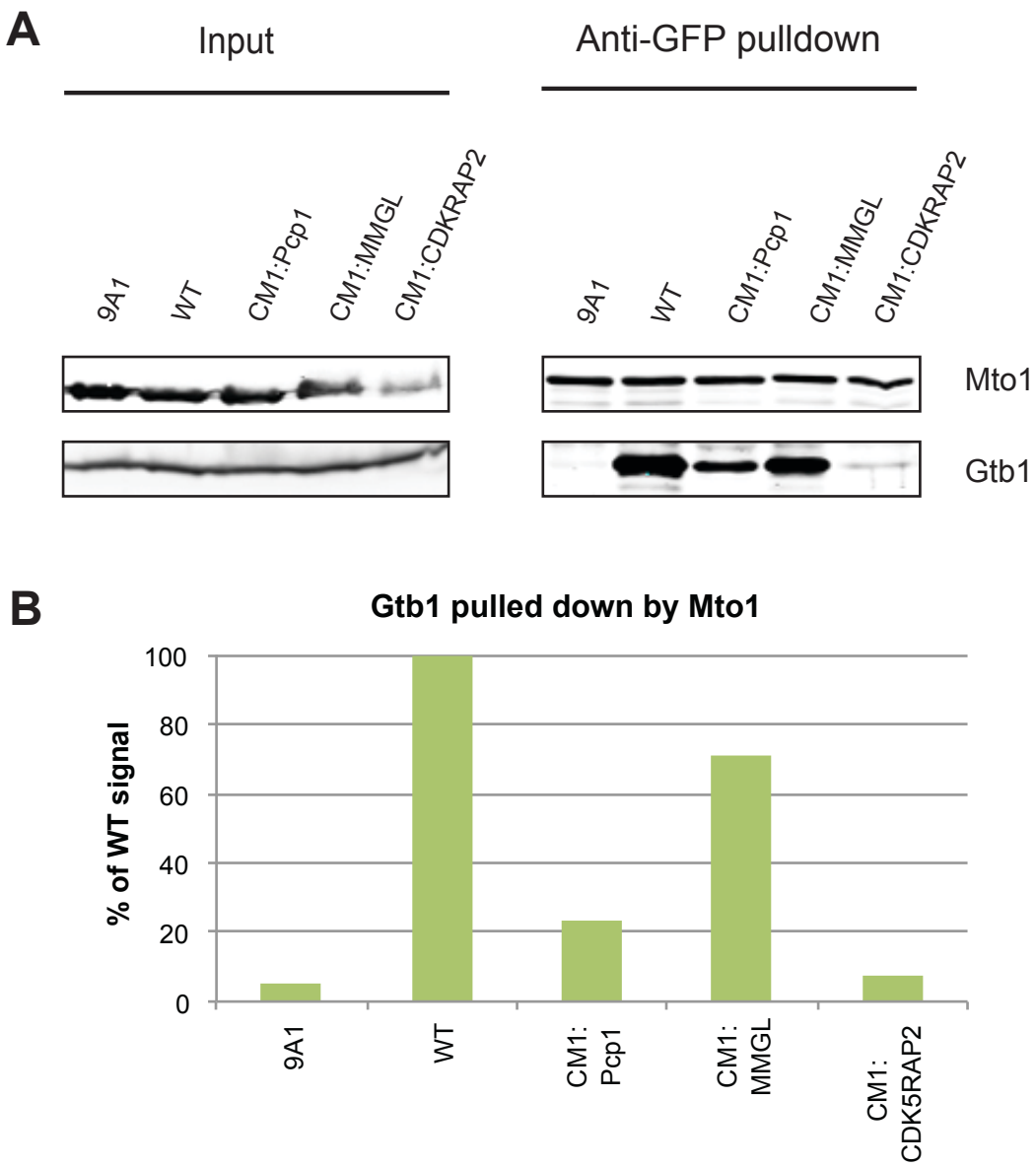

Figure 3.12. The various Mto1(bonsai-CM1)-GFP proteins mutants interact with the γ-TuC at different levels. (A) Mto1(bonsai-CM1)-GFP mutants immunoprecipitate different amounts of γ-tubulin. Total cell extracts expressing Mto1(bonsai-CM1)-GFP were immunoprecipitated with anti-GFP antibody. Western blots were probed against Mto1 and Gtb1. (B) Mto1(bonsai-CM1)-GFP mutants pull down less Gtb1 than wild-type Mto1-GFP. Integrated intensities of IRDye800 were measured using Odyssey V3.0, and Gtb1 signal was normalised to Mto1 and shown as proportion of wild-type signal. [Strains: KS5922, KS6080, KS6267, KS6269, KS6270]

3.2.2 Introduction of heterologous CM1 regions into Pcp1

3.2.2.1 Despite low expression levels, all three heterologous CM1 regions rescue Pcp1 function

As CM1 motif is a known γ-TuC-binding region, Pcp1 interaction with the γ-TuC is believed to occur through the CM1. A recent study showed that two point mutations within Pcp1 located in the CM1 and PACT regions of Pcp1 led to formation of a temperature-sensitive Pcp1 allele that failed to recruit the γ-TuC to mSPBs (Fong et al., 2010). The precise role of the CM1 region in Pcp1 function, however, was never deeply investigated. Prior to introduction of heterologous CM1 regions into Pcp1, I wanted to know what is the role of this motif in Pcp1. To address this, I generated a *pcp1-9A1* mutant, correspondent to *mto1-9A1* (Samejima et al., 2008), in which nine conserved amino acids within the CM1 were mutated to alanines.

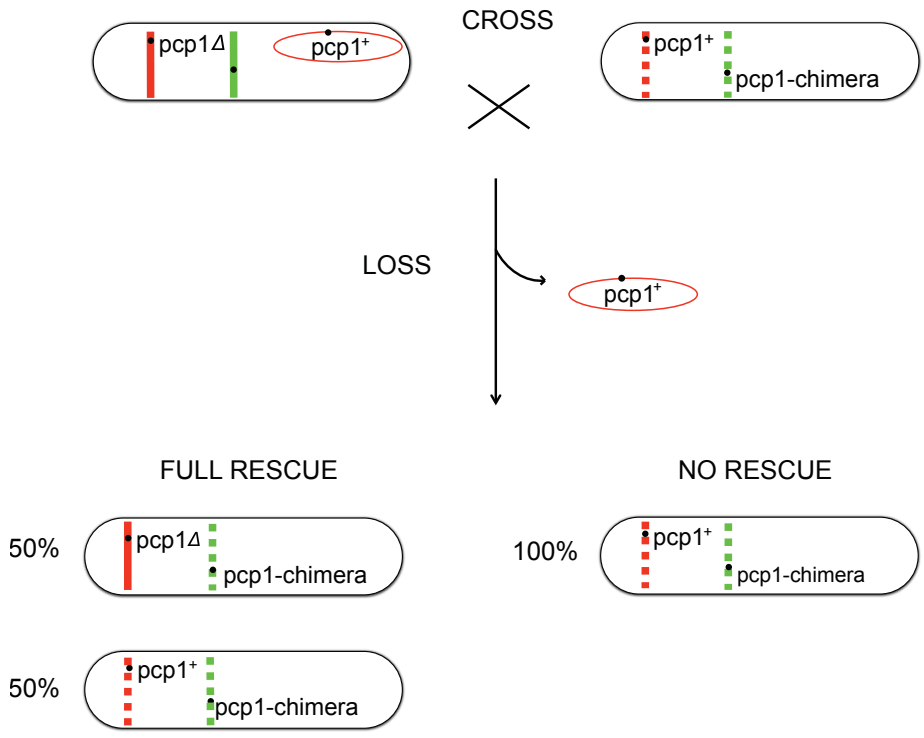

Figure 3.13. Cross and Loss assay. *pcp1*Δ strain *rescued* by a *pcp1*+ plasmid was crossed to a *pcp1*+ strain with *pcp1-chimera-GFP* integrated at *leu1*+ locus. The *pcp1*+ plasmid was lost in meiosis. If *pcp1-chimera-GFP* were not able to rescue *pcp1* function, only *pcp1*+ progeny would germinate whereas if the chimeric genes were able to fully rescue *pcp1* function, equal numbers of *pcp1*+ and *pcp1*Δ progeny should be observed.

pcp1 is an essential gene, rendering direct genetic manipulations at endogenous locus challenging. To circumvent this problem, I used a genetic assay, which we termed "Cross and Loss" (CaL) to introduce mutations into *pcp1* gene and to measure quantitatively how well such mutations rescue *pcp1* function (Fig. 3.13). I used a plasmid that contained *pcp1-GFP* gene with an intact 5'UTR containing promoter region but lacked 3'UTR (V. Miller, PhD Thesis 2008) to create a series of plasmids in which the *pcp1* CM1 region sequence was replaced by heterologous CM1 region sequences. Those plasmids contained also a sequence homologous to *S. pombe leu1* gene, which allowed their integration at *leu1* locus in *pcp1*$^+$ background. Thus, strains obtained by plasmid integration contained two copies of *pcp1* gene: one at *pcp1*$^+$ locus and one at *leu1*$^+$ locus (all *pcp1* mutants integrated at *leu1*$^+$ locus are henceforth collectively referred to as "*pcp1-chimera*" and wild-type *pcp1-GFP* integrated at *leu1*$^+$ locus as *pcp1-GFP:leu1*). Those strains were then crossed to a *pcp1*Δ strain rescued by a *pcp1*$^+$ plasmid that was subsequently lost in meiosis. As mentioned before, the CaL assay allowed me to assess the viability of *pcp1-chimera*, by scoring the ratio of the *pcp1-chimera* progeny that was either *pcp1*$^+$ or *pcp1*Δ. If the viability rescue by Pcp1-chimera were complete, the presence or absence of the *pcp1* gene at endogenous locus should not influence the viability, therefore the *pcp1*$^+$ to *pcp1*Δ ratio should be approximately 50%:50%, whereas if there were no rescue, the ratio should be 100%:0%, as only the *pcp1*$^+$ progeny would survive.

Table 3.3. Heterologous CM1 regions substitute for the Pcp1 CM1. Chi-square test was used for comparison with a theoretical proportion 50%:50% (Lydersen et al., 2009).

Mutant background	*pcp1*$^+$ progeny	*pcp1*Δ progeny	p value
WT:leu1	28	21	0.3173
9A1	26	0	<0.00001
CM1:Mto1	28	28	1.0000
CM1:CDK5RAP2	26	21	0.4658
CM1:MMGL	23	29	0.4054

For *pcp1-GFP:leu1* cells, a ratio close to 50%:50% was observed, while *pcp1-9A1-GFP* cells showed 100%:0% ratio (Table 3.3), showing that the Pcp1 CM1 region is essential for viability. I next used the CaL assay to address whether, and to what extent, heterologous CM1 regions could rescue Pcp1 CM1 function. In the CaL assay, CM1 regions of Mto1, MMGL and CDK5RAP2 fully substituted for the endogenous CM1 (Table 3.3).

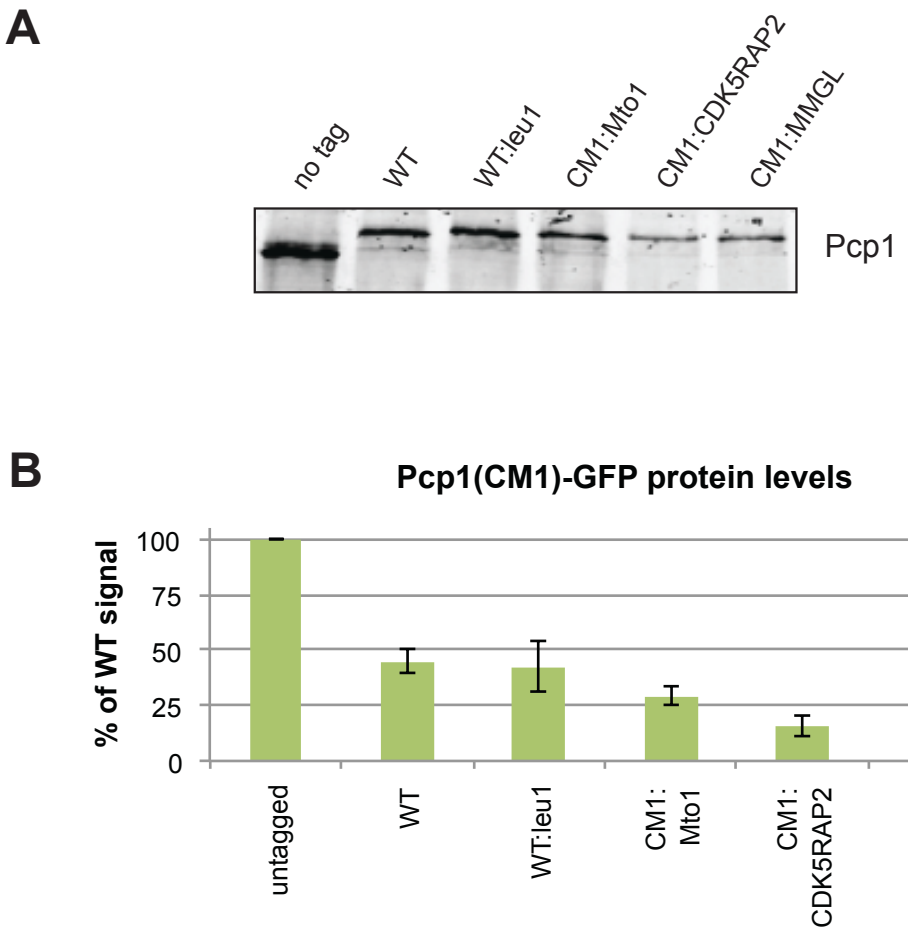

Figure 3.14. Pcp1(CM1)-GFP protein levels are lower relative to wild-type. (A) Anti-Pcp1 Western blot of total cell extracts expressing Pcp1(CM1)-GFP (B) Quantitation of Pcp1 expression levels in various *pcp1(CM1)-GFP* mutants. Integrated intensities of IRDye800 were measured using Odyssey V3.0, and Pcp1 signal was shown as proportion of wild-type signal. [Strains: KS516, KS1866, KS6361, KS6362, KS6383, KS6384]

Western blotting revealed that Pcp1-chimera-GFP levels are lower than wild-type (Fig. 3.14). Introduction of a GFP tag at the C-terminus of Pcp1 reduced steady state expression levels by half. Out of the three *pcp1(CM1)-GFP* mutants, Pcp1(CM1:MMGL)-GFP and Pcp1(CM1:CDK5RAP2)-GFP levels were the lowest (17% and 16% of wild-type, respectively). It is important to acknowledge that any phenotype observed for *pcp1(CM1)-GFP* mutants could be partially attributed to low protein expression levels as well as to specific CM1 region effects.

3.2.2.2 Cell cycle progression and mitosis timing is normal in *pcp1(CM1)-GFP* cells

To address how efficient the mitotic nucleation in *pcp1(CM1)-GFP* mutants is, I investigated mitosis timing and cell cycle progression in those cells. If mitotic nucleation were impaired, one would expect to observe mutant cells spend a longer time in mitosis and take longer to complete the cell cycle.

For mitosis timing, I made movies of *pcp1(CM1)-GFP* mitotic cells, and followed the distance between duplicated SPBs over time (Fig. 3.15 A). Despite low expression levels and heterologous CM1 regions introduced, all of the *pcp1(CM1)-GFP* mutants progressed through mitosis in timely fashion, i.e. identical to wild-type. In fact, the timing variation within genotypes was greater than between genotypes (compare Fig. 3.15 B, C and D). Consistent with this, mutant cell cycle progression was identical to the one of wild-type (Fig. 3.16), collectively showing that heterologous CM1 regions fully substituted for the CM1 region of Pcp1.

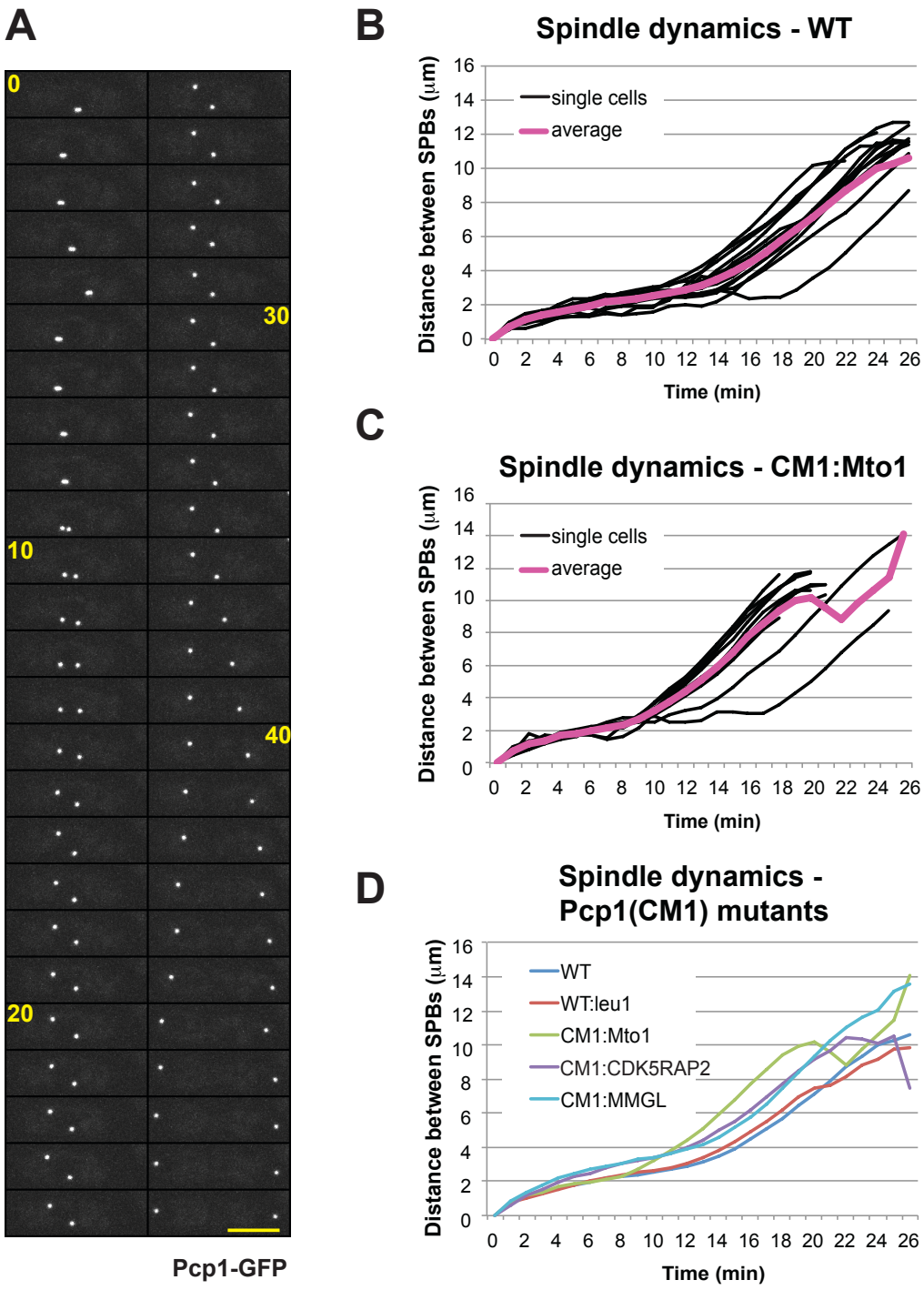

Figure 3.15. Mitosis timing is normal in *pcp1(CM1)-GFP* cells. SPBs separation dynamics in cells expressing Pcp1(CM1)-GFP. (A) An example of the SPB separation dynamics measurement method. Stills from a movie of Pcp1-GFP (1 min time interval); the distance between separated SPBs was measured for every timepoint. (B) and (C) Example plots of the SPB separation dynamics in wild-type and *pcp1(CM1:Mto1)-GFP* cells. The distance between separated SPBs for each mitotic cell was measured and plotted against time (black lines). Plots were aligned at the time of SPB separation (0 min), and the average SPB separation dynamics was calculated (magenta line). (C) Average SPB separation dynamics for each of the *pcp1(CM1)-GFP* mutants was plotted against time. Bar, 5 μm. [Strains (cells analysed): KS1866 (14), KS6521 (13), KS6523 (11), KS6525 (14), KS6529 (12)]

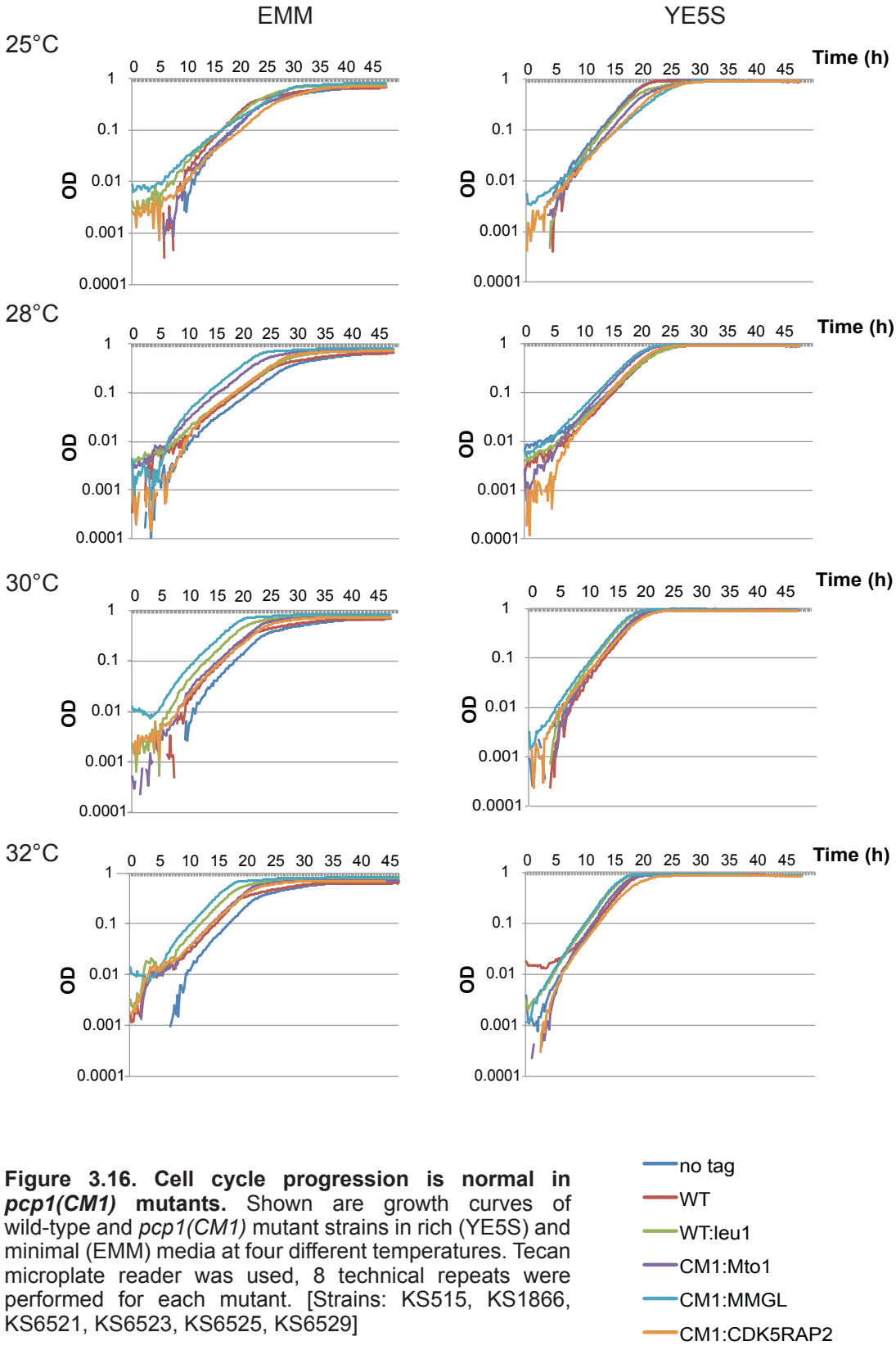

Figure 3.16. Cell cycle progression is normal in *pcp1(CM1)* mutants. Shown are growth curves of wild-type and *pcp1(CM1)* mutant strains in rich (YE5S) and minimal (EMM) media at four different temperatures. Tecan microplate reader was used, 8 technical repeats were performed for each mutant. [Strains: KS515, KS1866, KS6521, KS6523, KS6525, KS6529]

3.2.2.3 Introduction of heterologous CM1 regions into Pcp1 has no effect on cytoplasmic MT networks

I also wanted to determine whether introduction of heterologous CM1 has any effect on interphase MTs. One could imagine that, if the CM1 region had any specific role in cell-cycle regulation of MT nucleation, introduction of a heterologous CM1 region could potentially induce intranuclear nucleation in interphase, or somehow inhibit interphase cytoplasmic nucleation (for instance, by reducing the cytoplasmic pool of γ-tubulin).

In the CaL assay, *pcp1-chimera* genes were first introduced into *pcp1*$^{+}$ strains. Live-cell imaging revealed that in this background, Pcp1(CM1)-GFP proteins localisation was reminiscent of wild-type, with the exception of Pcp1-9A1-GFP, which localised to SPBs, but also formed occasional aggregates in the cytoplasm (Fig. 3.17 A). Previous work demonstrated that mildly over-expressed Pcp1-GFP exhibits a similar phenotype (Flory et al., 2002); this could explain the phenotype of Pcp1-9A1-GFP, which seemed to be slightly over-expressed, judged by the GFP signal intensity. However, imaging of *nmt81*:mCherry-α-tubulin showed that cytoplasmic MT networks were unaffected (Fig. 3.17). Importantly, live-cell imaging in this background allowed me to observe that *pcp1-9A1-GFP* does not posses a dominant-negative phenotype, as *pcp1*$^{+}$*pcp1-9A1-GFP* were indistinguishable from wild-type.

The lack of an interphase MT phenotype in *pcp1*$^{+}$*pcp1-chimera-GFP* cells could be explained by the presence of endogenous Pcp1 in these cells. In the final step of the CaL assay, the chimeric proteins are expressed in the absence of endogenous Pcp1. Live-cell imaging of these cells expressing *nmt81*:mCherry-α-tubulin was used to address the role of the Pcp1 CM1 in the interphase regulation of Pcp1 function (Fig. 3.18). In all of the *pcp1(CM1)-GFP* mutants, cytoplasmic MTs appeared to be unaffected, showing that the CM1 region plays no or negligible role in regulation of cytoplasmic nucleation MT nucleation.

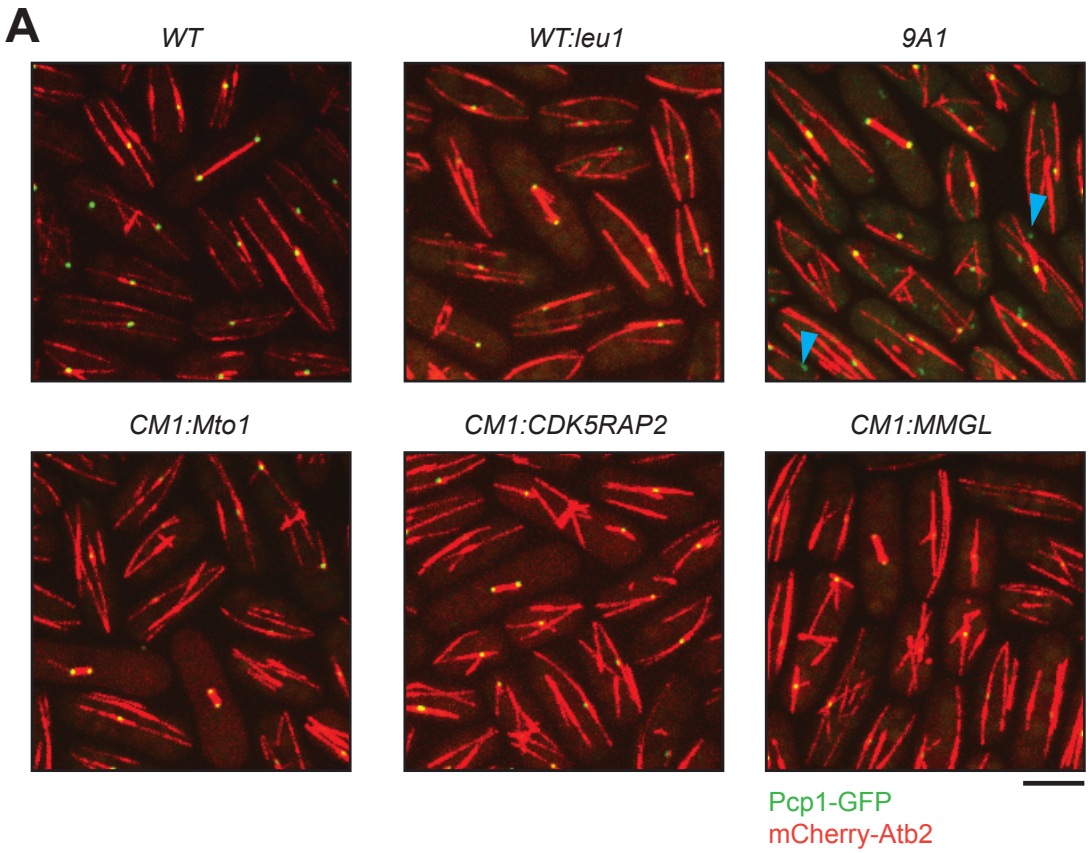

Figure 3.17. Cytoplasmic MT networks in *pcp1(CM1)-GFP* mutants in *pcp1*$^{+}$ background. (A) Confocal images showing interphase MTs (mCherry-α-tubulin, red) in strains expressing Pcp1(CM1)-GFP (green). Pcp1(CM1)-GFP localizes to interphase and mitotic SPBs. Pcp1-9A1-GFP, in addition to SPB localisation, forms cytoplasmic aggregates (blue arrowheads). (B) Number of MT bundles per cell observed in (A), n=50. Neither of the mutants is statistically different than WT. Bar, 5μm. [Strains: KS5201, KS6353, KS6355, KS6357, KS6364, KS6366]

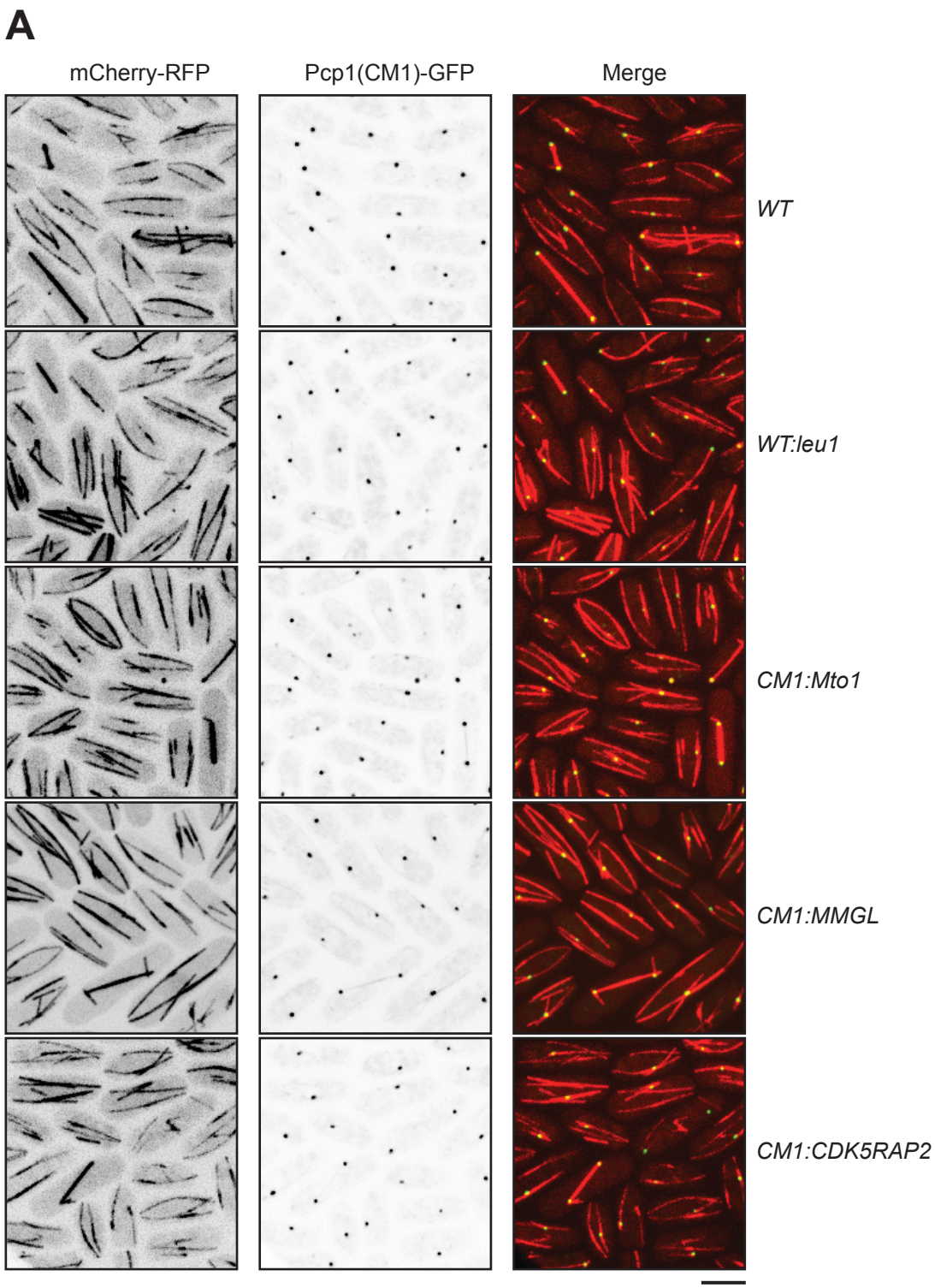
A
mCherry-RFP
Pcp1(CM1)-GFP
Merge
WT
WT:leu1
CM1:Mto1
CM1:MMGL
CM1:CDK5RAP2

B

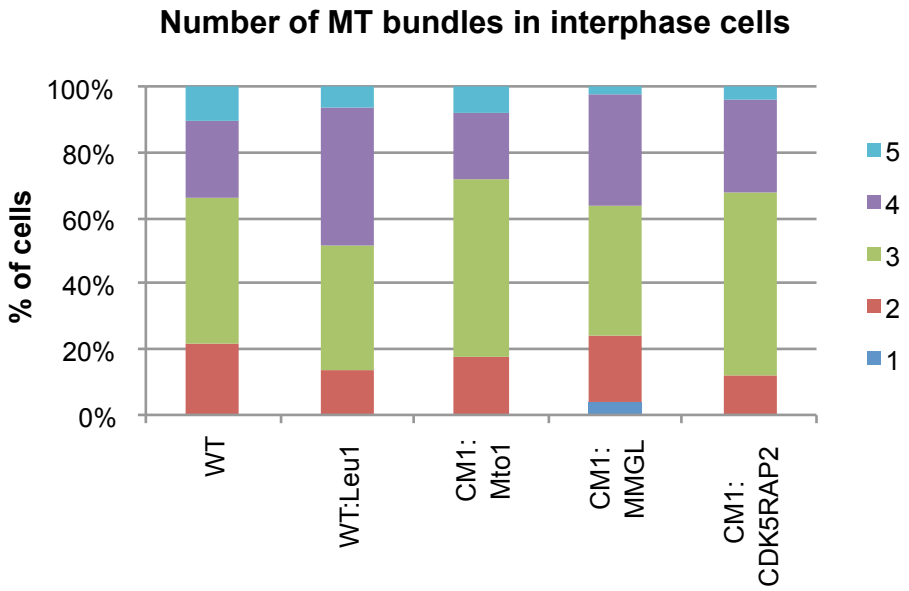

Figure 3.18. Introduction of heterologous CM1 regions into Pcp1 has no effect on cytoplasmic MT networks.
(A) Confocal images showing Pcp1(CM1)-GFP (green) in strains co-expressing mCherry-α-tubulin (red) to visualise MTs. Pcp1(CM1)-GFP localizes to interphase and mitotic SPBs.
(B) Number of MT bundles per cell observed in (A). Number of MT bundles in each cell was counted, n=50. Bar, 5 μm.
[Strains: KS5201, KS6361, KS6363, KS6383, KS6384]

3.3 Discussion

In this chapter, using genetic and biochemical approaches and live-cell imaging, I investigated the role of Pcp1 and Mto1 CM1 regions in differential regulation of MT nucleation in fission yeast as well as the functional conservation of the CM1 region from yeast to human.

3.3.1 The role of the CM1 region in cell-cycle regulation of MT nucleation

We hypothesised that the sequence differences between Mto1 and Pcp1 CM1 domains might contribute to the cytoplasm vs. nucleus (or mitosis vs. interphase) regulation of MT nucleation. This could be executed by either compartment- or cell cycle stage-specific γ-TuC modifications (Fig. 19 A and B). Alternatively, this

regulation could be achieved by differential modifications on one or both of the CM1 regions (Fig 19 C).

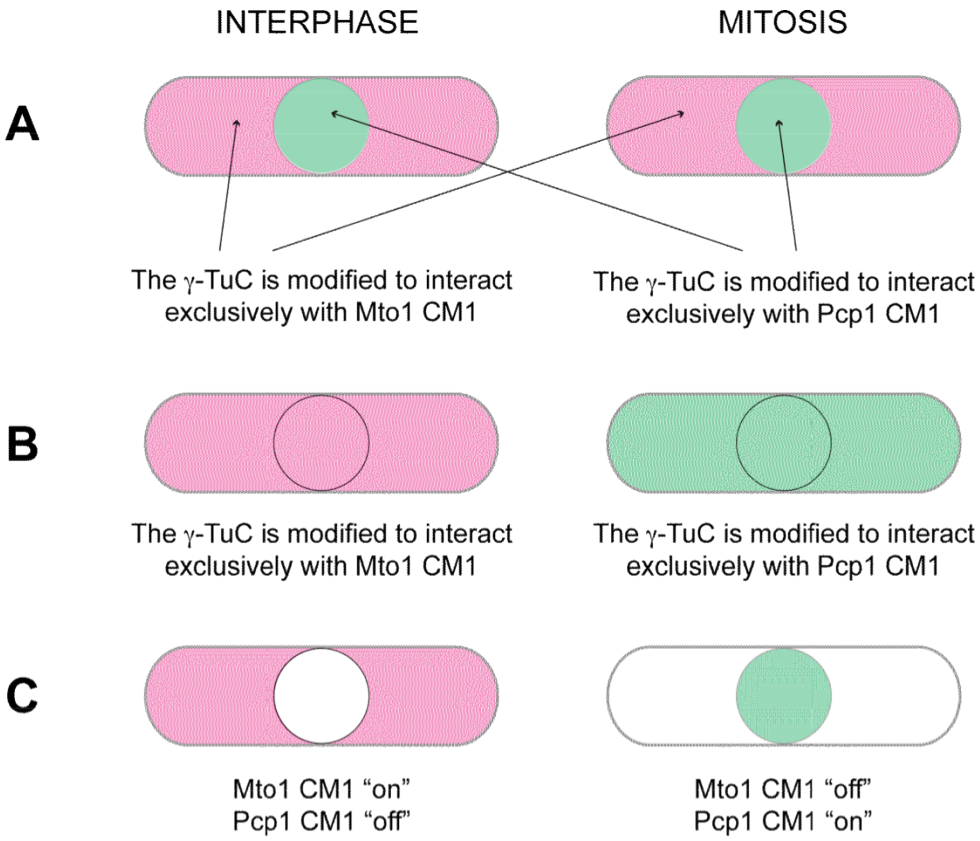

Figure 3.19. Models for cell cycle-regulation of MT nucleation. (A) Compartment-specific regulation of MT nucleation: cytoplasmic and intranuclear g-TuC pools are biochemically distinct. (B) Cell-cycle specific regulation of the g-TuC activity. In interphase, the g-TuC is able to interact exclusively with Mto1, while in mitosis it is only able to interact with Pcp1. (C) Cell-cycle specific post-translational modifications of Mto1 and Pcp1 CM1 regions allow the Mto1-g-TuC interaction to occur only in interphase and the Pcp1-g-TuC interaction to take place only in mitosis.

I showed that reciprocal domain swap did not have any measurable effect on cytoplasmic MT networks and nucleation frequency nor did it on the cell cycle or progression of mitosis. *mto1(CM1:Pcp1)-GFP* and *pcp1(CM1:Mto1)-GFP* cells were indistinguishable from their respective wild-type equivalents, suggesting that the sequence differences between Mto1 and Pcp1 CM1 regions play no role in differential regulation of MT nucleation. None of the three models depicted in Figure 3.19 proved to be correct. This result implicates that the CM1-interacting region of the γ-TuC is folded and modified in a uniform manner throughout the cell (contradictory to the model shown in Fig. 3.19 A). Different γ-TuC pools, cytoplasmic and nuclear, can interact with the same CM1 region, implying there are no major

structural differences in the γ-TuC CM1-interacting surface in different cell compartments. Moreover, this also shows that the CM1-binding motif of the γ-TuC is not modified in a cell cycle-dependent manner (in contradiction to the model shown in Fig. 3.19 B). Finally, this suggests that the two CM1 regions are not differentially modified during the cell cycle (contradictory to the model depicted in Fig. 3.19 C).

I also provided evidence that Pcp1 CM1 domain is essential for viability. Pcp1-9A1-GFP, in which nine consecutive residues within the CM1 were mutated to alanines (Fig. 3.2), did not rescue Pcp1 function. The lethality of this mutation is most likely due to disruption of the Pcp1-γ-TuC interaction and a subsequent failure to nucleate spindle MTs. Ideally, I would like to show the loss of this interaction in a co-immunoprecipitation experiment. However, as *pcp1-9A1-GFP* cells are not viable, the pull-down experiment would be possible only in *pcp1*$^{+}$ background. This would make data interpretation difficult, as there would be two copies of Pcp1 present in protein extracts: Pcp1-chimera-GFP and Pcp1. Presumably, even if an anti-GFP antibody were used for immunoprecipitation, both Pcp1 species would immunoprecipitate, as Pcp1 is likely to self-interact, similarly to Spc110 (Muller et al., 2005). More importantly, my attempts to perform anti-GFP immunoprecipitation experiments in *pcp1*Δ *pcp1-chimera-GFP* background were not successful, as the majority of Pcp1 pool was found in insoluble fraction of native protein extracts, most likely associated with SPB components (data not shown).

Notably, Pcp1-chimera proteins rescued Pcp1 function even when expressed at less than a fifth of wild-type levels. These results indicate that Pcp1 levels in cells are higher than required to ensure timely cell cycle progression.

In summary, evidence presented in this chapter shows that the CM1 region sequence differences have no apparent role in regulation of MT nucleation. In addition, they indicate that the CM1-interacting region of the γ-TuC is not differentially regulated.

3.3.2 Evolutionary conservation of the CM1 region

The MMGL CM1 region substituted for CM1 region of both Mto1 and Pcp1, while, somewhat surprisingly, the CDK5RAP2 CM1 region substituted only for the CM1 region of Pcp1. There could be several reasons for this. Firstly, the CDK5RAP2 CM1 might have misfolded in the Mto1 context; for proper folding, a

CM1 region might require specific forces exerted by its surroundings that facilitate its folding and “push it” in its proper position, and for the CDK5RAP2 CM1 these forces might be present in Pcp1 but not Mto1. In a recent report, however, the CDK5RAP2 CM1 region was shown to co-immunoprecipitate the γ-TuC from cell extracts (Choi et al., 2010). Thus, an alternative explanation is that the CDK5RAP2 CM1 region is able to fold independently of its surroundings, but fails to do so when placed within Mto1 due to some steric effects. Secondly, Pcp1 is likely to be a dimer (Muller et al., 2005), whereas Mto1 multimerizes in complex with Mto2 (Lynch PhD Thesis, 2012; Samejima et al., 2010). The CM1 might only be active when a protein adopts a certain oligomerisation state that could be different for Mto1 and Pcp1. This is, however, inconsistent with the full rescue of Mto1 and Pcp1 function in reciprocal domain swap experiment.

I showed that yeast and human CM1 were (with the exception of Mto1-CDK5RAP2 chimera) able to functionally interact with the yeast γ-TuC. In order to substitute for yeast CM1 domains, heterologous CM1 regions must have adopted fold similar to the endogenous CM1 region, thus indicating that the CM1 region is conserved through evolution. Moreover, evidence presented in this chapter indirectly implicates structural conservation of the γ-TuC itself. To achieve functional interaction with heterologous CM1 regions, the γ-TuC CM1-binding region folding must also, in addition to the CM1, be conserved.

Thus, results presented in this chapter provide an additional level of confidence in using *S. pombe* as a model organism in MT studies, as they show that the MT nucleation machinery is structurally and functionally conserved.

Chapter 4
Analysis of the role of Mto2 phosphorylation in regulation of Mto1/2 complex activity

4.1 Introduction

In fission yeast, the proteins Mto1 and Mto2 are required for all interphase MT nucleation. They associate together to form the Mto1/2 complex, which is required to localise the γ-TuC to prospective cytoplasmic MTOCs, such as MTs, the NE, SPBs, and eMTOCs, as well as to activate the γ-TuC to promote cytoplasmic MT nucleation Deletion of either *mto1*$^+$ or *mto2*$^+$ results in severe defects in cytoplasmic MT networks. In a variety of assays, *mto1*Δ cells are completely defective in cytoplasmic MT nucleation, while *mto2*Δ cells retain the ability to nucleate from SPBs and - to a much lesser extent – from eMTOCs, showing that Mto1-dependent nucleation from SPBs does not require the Mto1/2 complex formation (Janson et al., 2005; Lynch PhD Thesis, 2012; Samejima et al., 2005, 2008, 2010; Sawin et al., 2004; Venkatram et al., 2004, 2005).

Mto2 is a 397-amino acids protein that is predicted to be predominantly unstructured (Groocock PhD Thesis, 2010). It contains a short coiled-coil region towards its N-terminus and interacts with Mto1 and, independently of Mto1, with itself (Groocock PhD Thesis, 2010). In *mto1*Δ cells, differently-tagged versions of Mto2 can be co-immunoprecipitated; consistent with this, live-cell imaging has revealed that Mto2-GFP can form freely-diffusing cytoplasmic puncta in *mto1*Δ cells. This suggests that Mto2 can multimerise in the absence of Mto1. Recent work in the Sawin lab showed that bacterially expressed Mto2 may be either pentameric or exist as multiple species ranging from 4-mer to 6-mer. Dilution experiments with Mto2 expressed in insect cells demonstrated that Mto2 is in a dynamic equilibrium, confirming that Mto2 is multimeric to some extent. Previous work in the lab showed that Mto2 is phosphorylated in a cell cycle-regulated manner, hyperphosphorylated in mitosis, and hypophosphorylated in G1/S (Groocock PhD Thesis, 2010; Lynch PhD Thesis, 2012; Samejima et al., 2005; Venkatram et al., 2005).

Mto1 is a 1115-amino acids that contains several localisation and interaction domains. The N-terminal NE-localisation domain is followed a γ-TuC-binding Centrosomin Motif 1 (CM1) (Lynch PhD Thesis, 2012; Sawin et al., 2004; Zhang and Megraw, 2007). The Mto2-interaction domain is located in the central part of the

protein, followed by a MT localisation region and a C-terminal MASC domain that promotes Mto1 localisation to interphase and mitotic SPBs and eMTOCs (Samejima et al., 2008, 2010; Sawin et al., 2004). An *mto1* truncation mutant, *mto1(131-549)*, dubbed *mto1[bonsai]*, which lacks all of the localisation domains, is not able to localise the Mto1/2[bonsai] complex to any conventional MTOCs, yet it promotes a robust cytoplasmic MT nucleation in a spatially random manner. Biochemical analysis of the recombinant Mto1/2[bonsai] complex from insect cells showed that the complex is in a dynamic equilibrium, and that Mto1/2[bonsai] heterodimers associate to form multimers with a range of sizes. The largest of the multimers, at about 800kDa, would correspond to 9 copies of each Mto1[bonsai] and Mto2 within the complex. Because of the large molecular size of the complex *in vivo*, during interphase Mto1[bonsai]-GFP (or Mto2-GFP in *mto1[bonsai]* background) can be seen in the cytoplasm as freely diffusing GFP puncta. Detailed image analysis has revealed that actively nucleating Mto1/2[bonsai] complex consists of approximately 13 copies of both Mto1 and Mto2, matching the 13 copies of γ-tubulin molecules in a single γ-TuC and the symmetry of 13 protofilaments of a MT (Lynch PhD Thesis 2012). Dilution experiments with recombinant Mto1 from insect cells showed that, unlike Mto2, Mto1[bonsai] appears to be monodisperse.

Mto1/2 complex activity appears to be limited to interphase; the only cytoplasmic MTOCs active during cell division are mSPBs, from which Mto1 promotes astral MT formation, but even this occurs only during anaphase, when CDK activity would be expected to be low (Samejima et al., 2005, 2008; Venkatram et al., 2005). Live-cell imaging of Mto1[bonsai]-GFP revealed that the Mto1/2[bonsai]-GFP puncta are absent from mitotic cells, suggesting that the Mto1/2 complex is disassembled in mitosis (Lynch PhD Thesis, 2012). Moreover, co-immunoprecipitation experiments have shown that the Mto1-Mto2 interaction is lost in mitotic cells, coincident with Mto2 hyperphosphorylation (Groocock PhD Thesis, 2010). These observations have led to a hypothesis that the mitotic Mto2 phosphorylation disrupts the Mto1-Mto2 interaction, which leads to the Mto1/2 complex disassembly and abolition of Mto1/2-dependent MT nucleation during mitosis.

To test this hypothesis, a series of Mto2 phosphomutants was designed in which identified phosphorylated (or potentially phosphorylatable) residues of Mto2 were replaced by alanines (Groocock PhD Thesis, 2010); these mutants will be hereafter collectively referred to as *mto2[alanine],* and the mutant Mto1/2 complexes

as Mto1/2[A]. The residues were selected for mutations using a combination of mass-spectrometry, bioinformatics and *in vitro* data (Groocock PhD Thesis, 2010; Rosenberg PhD Thesis, 2007) (Table 4.1). If Mto2 phosphorylation were the main driver of Mto1/2 complex disassembly, one might expect the Mto1-Mto2 interaction and Mto1/2[bonsai]-GFP puncta to persist in mitosis in *mto2[alanine]* cells, while they would be disrupted in *mto2*$^{+}$ (wild-type) cells; in principle *mto2[alanine]* mutants might even be able to promote cytoplasmic MT nucleation in mitosis. Preliminary experiments further suggested that the Mto1-Mto2 interaction is maintained in *mto2[alanine]* cells in mitosis (I. Samejima, unpublished).

Table 4.1. Residues mutated in *mto2[alanine]* cells. Three *mto2[alanine]* mutants were designed with 6, 13, and 17 alanine substitutions in Mto2 sequence (dubbed *mto2-6A, mto2-13 A* and *mto2-17A,* respectively). The residues were selected for mutations if they had either a NetPhos prediction score greater than 0.9 or were conserved in fungal alignment or were identified in the mass spectrometry mapping *in vitro* or *in vivo* (Blom et al., 1999; Groocock PhD Thesis, 2010; Rosenberg PhD Thesis, 2007).

Residue	Sequsnce	*mto2-6A*	*mto2-13A*	*mto2-17A*	NetPhos Score	Identified in Rosenburg kinase assay	Conserved in fungal alignment	Identified in MS
T35	SRES**T**PRGS			Yes	0.996	Yes	Yes	
S39	TPRG**S**PWRA			Yes	0.994	Yes	Yes	
S81	NPLY**S**PSWP		Yes	Yes	0.926		Yes	Yes
S159	HNNL**S**PYRS	Yes	Yes	Yes	0.979	Yes		Yes
S176	PST**H**PHSP		Yes	Yes	0.930		Yes	Yes
S179	HSPH**S**PAPL		Yes	Yes	0.994		Yes	Yes
S220	LVNT**S**PSSV		Yes	Yes	0.964		Yes	
T264	LVRH**T**PPLN	Yes	Yes	Yes	0.169	Yes	Yes	
S271	LNYT**S**SVDS		Yes	Yes	0.955	Yes	Yes	
S276	SVDS**S**PQRM	Yes	Yes	Yes	0.985		Yes	
S282	QRMA**S**DSYG		Yes	Yes	0.982		Yes	Yes
T314	NVRT**T**LFSD		Yes	Yes	0.890		Yes	
T331	HTHS**T**PPSQ	Yes	Yes	Yes	0.578	Yes		Yes
S341	YSAA**S**HFRY		Yes	Yes	0.978		Yes	
S366	SLHP**S**PTSL	Yes	Yes	Yes	0.964	Yes		Yes
S382	PQRA**S**PASQ	Yes			0.992	Yes		
T394	SLQD**T**PSP-			Yes	0.772	Yes	Yes	
T396	QDTP**S**P---			Yes	0.325	Yes	Yes	

In this chapter, my aim was to elucidate the role of Mto2 phosphorylation in the regulation of the Mto1/2-promoted MT nucleation, and in particular, in the mitotic disassembly of the Mto1/2 complex. To do this, I used three *mto2[alanine]* mutants, in which Mto2 phosphorylatable residues were mutated to different extents. I found that Mto2 phosphorylation modulates the MT nucleation frequency in interphase by

controlling the Mto2 self-interaction and the affinity of the Mto1/2 complex to the γ-TuC. I showed that in *mto2[alanine]* cells, the formation of PAA is advanced, suggesting that that the post-mitotic re-assembly of the Mto1/2[A] complex is expedited in the absence of Mto2 phosphorylation. I also demonstrated that the mitotic disruption of the Mto1-Mto2 interaction is prevented in *mto2[alanine]* cells, showing that Mto2 phosphorylation disrupts the Mto1-Mto2 interaction. However, despite the maintenance of the Mto1-Mto2 interaction in mitosis, the Mto1/2[A] complexes disassemble upon mitotic entry, suggesting that additional regulation mechanisms are involved in the mitotic disassembly of the Mto1/2 complex. Indeed, the Mto2-Mto2 self-interaction is disrupted upon mitotic entry in *mto2[alanine]* cells. I showed that Mto2 is still phosphorylated in mitotic *mto2[alanine]* cells and hypothesised that this phosphorylation disrupts the Mto2-Mto2 self-interaction in mitosis. The role of this phosphorylation in mitotic disassembly of the Mto1/2 complex will be addressed in Chapter 5.

4.2 Results

4.2.1 Mto1-Mto2 is interaction is regulated in the cell cycle

Previous work in the lab revealed that Mto2 is a phosphoprotein (Groocock PhD Thesis, 2010). Its phosphorylation is regulated during the cell cycle and the protein is most phosphorylated in mitosis, coinciding with a loss of the Mto1-Mto2 interaction. Before analysing *mto2[alanine]* mutants mentioned in the introduction I wished to recapitulate previous results and follow the Mto2 phosphorylation throughout the cell cycle.

I wished to confirm that the Mto1-Mto2 interaction is lost in metaphase-arrested cells. To arrest cells in metaphase, I used an *nda3-KM311* cold-sensitive strain. *nda3-KM311* is a β-tubulin mutation, and at the restrictive temperatures *nda3-KM311* cells do not have any MTs and are not able to assemble the mitotic spindle, ultimately leading to spindle assembly checkpoint activation and early metaphase arrest (Hiraoka et al., 1984; Moreno et al., 1989; Toda et al., 1983). I used Mto1-TAPS to pull down Mto2 and examine the γ-TuC-Mto1/2 interaction. As shown before by Lynda Groocock, I found that Mto2 is hyperphosphorylated in metaphase arrest (Fig. 4.1, Input, lane 5), and the Mto1-Mto2 and Mto1-Gtb1

interactions were disrupted (Fig. 4.1, IgG pulldown, lane 5) (Groocock PhD Thesis, 2010; Samejima et al., 2008).

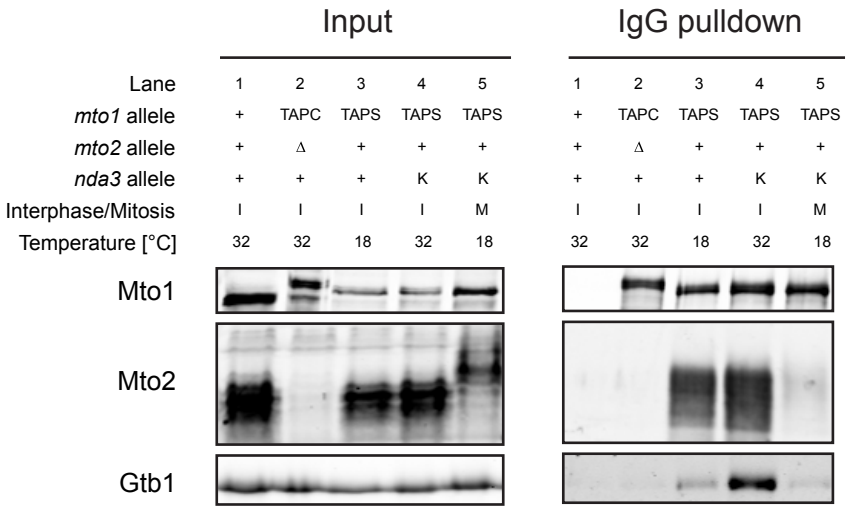

Figure 4.1. Mto1-Mto2 interaction is disrupted in metaphase-arrested cells. Mto1-Mto2 interaction and Mto1-Gtb1 interaction were analysed in interphase and mitosis. Extracts from asynchronous and metaphase-arrested cells were incubated with IgG-Dynabeads. Following pull-down, western blots were probed against Mto1, Mto2 and Gtb1. K, *nda3-KM311* allele. [Strains: KS516, KS6197, KS3472, KS3575]

During *nda3-KM311* arrest, cells were incubated at the restrictive temperature of 18ºC for 6 – 8 hours. To ensure that the growth conditions of the interphase and mitotic samples (grown at 32ºC and 18ºC, respectively) do not affect the result of the experiment, I also examined an *nda3*$^{+}$ strain grown at 18ºC (Fig. 4.1, lane 3). As expected, Mto2 phosphorylation as well as the Mto1-Mto2 interaction was not affected by growth conditions; however, unexpectedly, the Mto1-Gtb1 interaction was, and the amount of γ-tubulin pulled down by Mto1-TAPS from extracts grown in 18ºC was much lower than from extracts grown in 32ºC. The interaction between Mto1 and Gtb1 might be abolished in 18ºC due to a decrease in hydrophobic interactions between Mto1 and Gtb1, since hydrophobic interactions are known to weaken with decreasing temperature (Dias et al., 2010). It is known that the interaction between tubulin molecules within a MT is cold-sensitive; in fact, cold-induced depolymerisation of MTs is used in many tubulin purification procedures (Hyman et al., 1991); in addition, it has been shown that already at 10ºC, tubulin oligomers start to dissociate (Kravit et al., 1984). This suggests that the loss of interaction between the γ-TuC and Mto1-TAP in mitosis observed in Fig. 4.1, lane 5 might be an artefact of the experimental design and therefore this result should be

treated with caution. However, It is unlikely that the loss of Mto1-Gtb1 interaction in mitosis (lane 5) is only an effect of growth conditions, since it has been previously shown that the Mto1-Mto2 interaction is required for an efficient association of Mto1 with Gtb1. In *mto2*Δ and *mto1-334* cells, in which Mto2 is either absent or cannot interact with Mto1, Mto1 is not able to co-immunoprecipitate the γ-TuC (Samejima et al., 2008). Thus, the decrease in Gtb1 signal in *nda3-KM311* metaphase-arrested cells (for instance, in Fig. 4.1, lane 5) is most likely a combined effect of both growth conditions and the mitotic abolishment of the Mto1-Mto2 interaction. In addition, this result suggests that the Mto1-Gtb1 interaction is more labile than the Mto1-Mto2 interaction, which was not affected by growth temperature.

In an additional experiment, I examined Mto2 phosphorylation using the temperature-sensitive *cdc25-22* mutant (Fig 4.2 A-C) (Fantes, 1979; Thuriaux et al., 1980). In this mutant background, cells arrest in late G2 when grown at 36ºC (restrictive temperature); after release by shifting to 25ºC (permissive temperature), they progress synchronously through the cell cycle. I used Mto1-TAPS to pull down Mto2. Using *cdc25-22* block and release allowed me to avoid growing cells in cold medium and to examine the Mto1-Mto2 interaction in physiological growth conditions. This experiment was performed before (Groocock PhD Thesis, 2010), but I wanted to increase the time resolution and follow the cells through two subsequent mitoses. Following incubation at 36ºC, cells were released to 25ºC and harvested every 15 minutes. Cell cycle progression was monitored by septation index (Fig. 4.2 A), with septation beginning approximately 45 minutes after mitotic entry. Septation peaked at 60-90 minutes, indicating that mitosis started roughly 15 minutes after the release. As shown before by Lynda Groocock, when cells entered mitosis Mto2 became hyperphosphorylated (Fig. 4.2 B, Input). This coincided with a decrease of the Mto1-Mto2 interaction (Fig. 4.2 B, IgG pulldown; quantified in Fig. 4.2 C). In S phase, which in fission yeast occurs concurrently with septation (Mitchison and Nurse, 1985), Mto2 phosphorylation was reduced and faster-migrating Mto2 isoforms were detected; this coincided with an increase in the Mto1-Mto2 interaction strength. Following the first septation peak, cells entered second mitosis at 165 minutes. During the second mitosis, Mto2 hyperphosphorylation was not that prominent, and the Mto1-Mto2 interaction not as severely impaired as in the first mitosis. This was likely a result of a reduction in cell synchrony over time (less than 80% of cells septated simultaneously, as compared to more than 90% in the first mitosis).

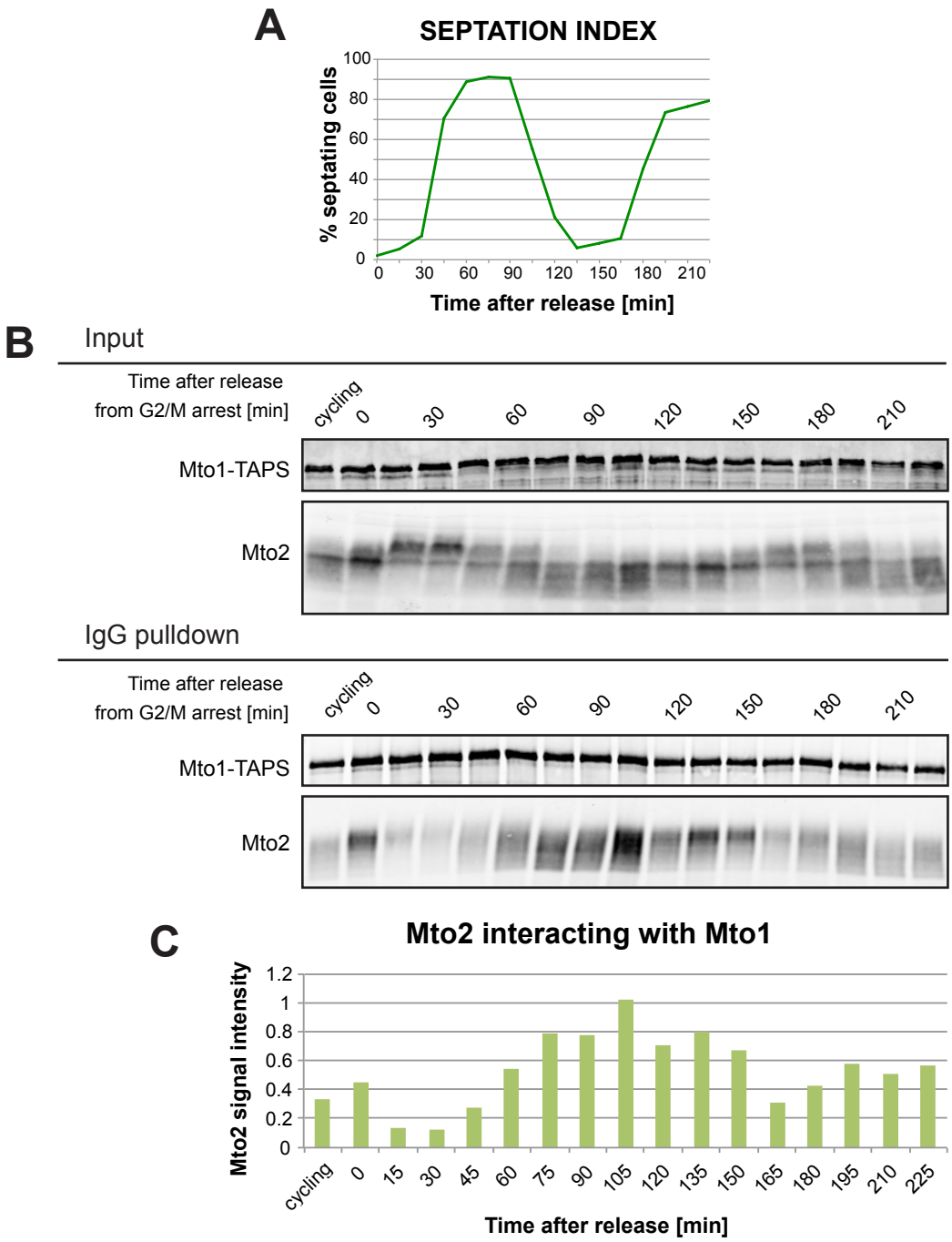

Figure 4.2. Mto1-Mto2 interaction is regulated in a cell cycle-dependent manner. Mto1-Mto2 interaction was examined throughout the cell cycle following the release from G2/M arrest.
(A) The septation index of cell samples taken every 15 minutes after release from *cdc25-22* block, based on fluorescent brightener staining.
(B) Extracts from samples from cycling and synchronous cultures were incubated with IgG-Dynabeads. Following pulldown, western blots were probed with anti-Mto1 and anti-Mto2. The slight unevenness of Mto1 signal is due to slight stretching of gel during werstern transfer.
(C) Mto1-Mto2 interaction is disrupted in mitosis following *cdc25-22* block and release. Integrated intensities of IRDye800 signal from (B) were measured using Odyssey V3.0, and Mto2 signal was normalised to Mto1. [Strain: KS6760]

Overall, these results confirm that Mto2 phosphorylation and the Mto1-Mto2 interaction are cell cycle-regulated.

4.2.2 MT depolymerisation does not affect Mto2 phosphorylation state

We hypothesised that mitotic hyperphosphorylation of Mto2 leads to the disassembly of the Mto1/2 complex. However, it might also be a result of an unspecific phosphorylation performed by a cytoplasmic kinase, which localisation is dependent on MTs and that gets released to the cytoplasm upon mitotic entry. That is, it might be a result of MT depolymerisation upon mitotic entry. An example of a kinase that becomes cytoplasmic upon mitotic entry is Pom1 kinase, which in interphase is delivered by MTs to cell tips. Previous studies have shown that Pom1 fails to localise to cell tips in the absence of MTs (Bähler and Pringle, 1998). At mitotic entry, when the constant delivery of polarity factors to the cell cortex is abolished with the disassembly of cytoplasmic MT arrays, Pom1 delocalises from cell tips and remains free in the cytoplasm until cytokinesis, when it localises to the division plane (Bähler and Pringle, 1998).

To test the notion that Mto2 phosphorylation is an indirect result of the MT depolymerisation upon mitotic entry, I analysed synchronous interphase cultures, in which MTs were disrupted using the drug MBC (Carbendazim). I used the temperature-sensitive mutant *cdc10-129*, which arrests cells in early G1 at 36ºC (restrictive temperature) (Nurse et al., 1976), and progresses synchronously through interphase after the release to 25ºC. This allowed monitoring of Mto2 phosphorylation from G1 until late G2; since mitotic entry is prevented in cells lacking MTs, cells were monitored only until the expected time of mitotic entry. In order to monitor cell cycle progression and to ensure complete absence of MTs, a strain expressing *nmt81:*GFP-α-tubulin was used. Typically, the *cdc10-129* arrest is performed under rich medium growth conditions (YE5S); however, the presence of the *nmt81* (no message in thiamine) promoter required cells to be grown in minimal medium, which unlike rich medium, does not contain thiamine. Thus, it was necessary to find a suitable experimental design to achieve complete G1 arrest, and to determine the exact time of mitotic entry after the release.

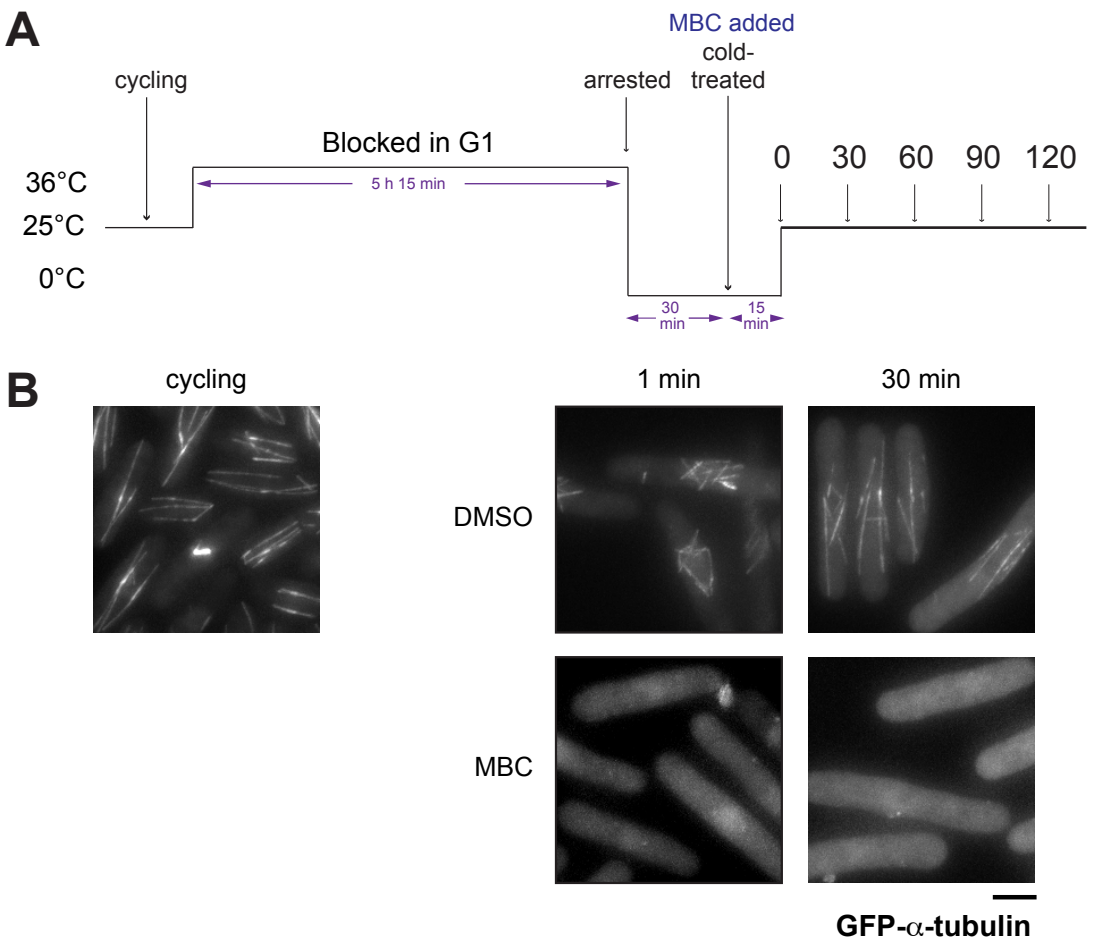

Figure 4.3. Absence of MTs does not affect Mto2 phosphorylation.
(A) Diagram of experimental design of *cdc10-129* block and release. *cdc10-129* cells were grown at the persimmisve temperature (25°C), arrested at 36°C for 5 h 15 min, then placed on ice slurry for 45 min. During incubation on ice, cells were treated with DMSO (control) or 50 μg/ml MBC, and then released to the permissive temperature. Samples were collected every 30 min after the release.
(B) GFP-α-tubulin images showing cycling and synchronised cells at 1 and 30 min. DMSO-treated samples showed MT regrowth from the NE after cold-depolymerisation (1 min) and normal MT networks (30 min). MBC-treated cells did not contain any MTs. Further time points are not shown, butthey were identical to 30 min.
(C) Extracts from samples from cycling and synchronous cultures were analysed by western blot probed with anti-Mto2. Percent of cells with mitotic spindle was scored , n=100.
Bar, 5μm. [Strain: KS349]

Imaging of GFP-α-tubulin revealed that cells reached maximal synchrony after 5 h and 15 minutes of incubation at the restrictive temperature, and mitosis occurred 2 h 30 minutes after the release to 25ºC (permissive temperature, not shown). To ensure complete MT disassembly following the G1 arrest, I combined treatment with MBC with cold-shock. Figure 4.3 A depicts the experimental design used. After the release, Mto2 phosphorylation was followed for 2 hours. Anti-Mto2 immunoblotting revealed that during interphase, after release from the G1 arrest, Mto2 phosphorylation was not any different in the presence vs. absence of MTs (Fig 4.3 C). This demonstrates that mitotic Mto2 phosphorylation is not an indirect result of the MT cytoskeleton rearrangements that occur upon mitotic entry.

4.2.3 Unlike wild-type Mto2, Mto2[alanine] mutants interact with Mto1 in both interphase *and* mitosis

Preliminary experiments performed in the Sawin laboratory suggested that the Mto1-Mto2 interaction is maintained in mitosis in *mto2[alanine]* mutants (I. Samejima, unpublished). This was initially performed in a tag affinity pulldown experiment using an *mto1* truncation *mto1[NE]* tagged with a TAPS tag. Mto1[NE] lacks a large proportion of its C-terminus (amino acids 550-1115), and therefore, is void of any C-terminal localisation domains and localises exclusively to the NE. The TAPS tag is described in detail in the following section (Section 4.2.4)

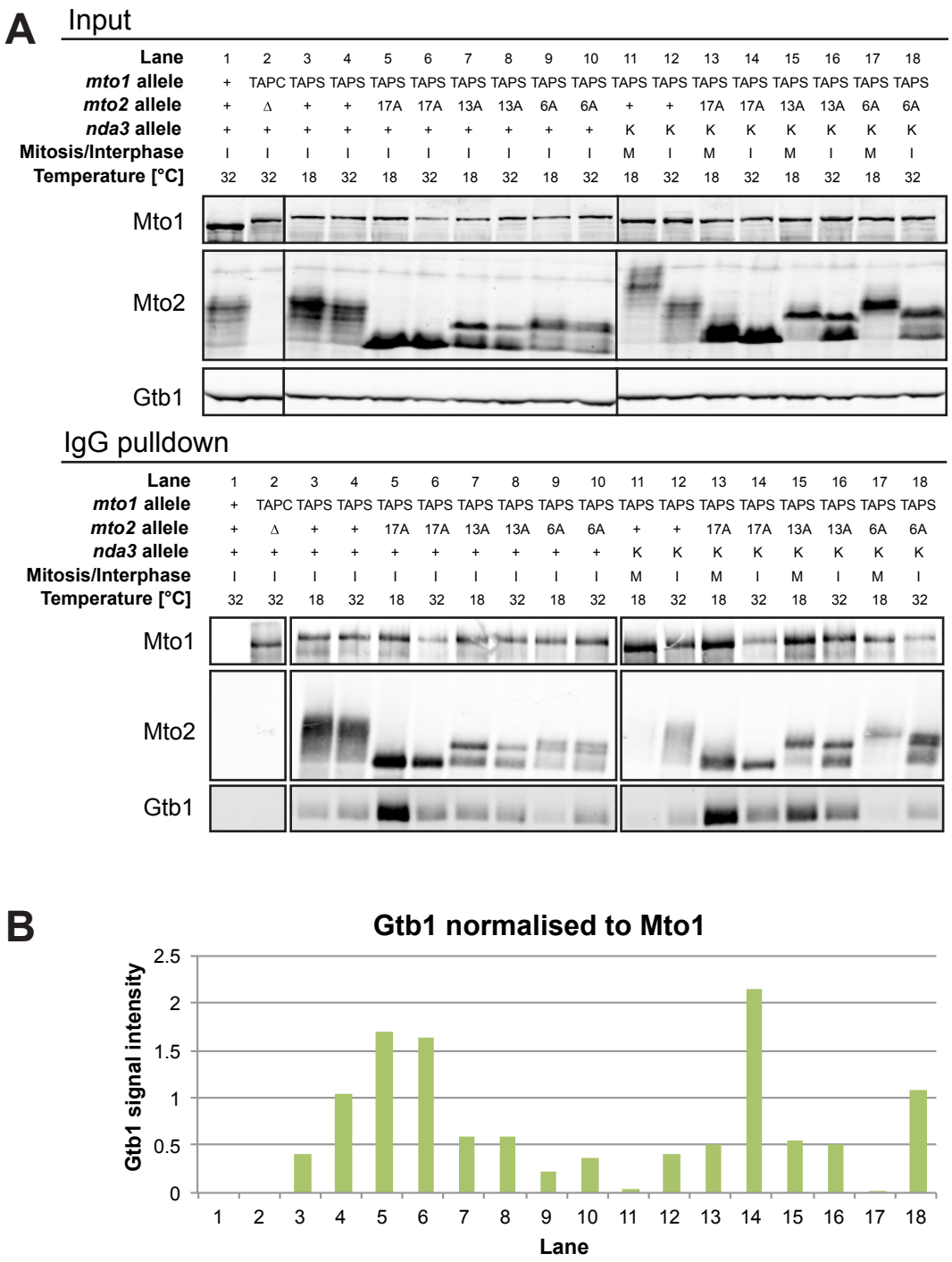

Figure 4.4. Unlike wild-type Mto2, Mto2-alanine mutants interact with Mto1-TAPS in mitosis.
(A) Extracts from asynchronous and metaphase-arrested cells were incubated with IgG-Dynabeads. Following pull-down, western blots were probed against Mto1, Mto2 and Gtb1. K, *nda3-KM311* allele.
(B) Integrated intensities of IRDye800 signal from IgG pulldown from (A) were measured using Odyssey V3.0, and Gtb1 signal was normalised to Mto1. Lanes 1 and 2 were used to define background, therefore, Gtb1 signal intesity equals zero.
[Strains: KS516, KS3524, KS3575, KS6197, KS6742, KS6743, KS6746, KS6747, KS6749, KS6751]

I wanted to examine the Mto1-Mto2[A] interaction in the context of full-length Mto1 (Fig. 4.4). Unlike Mto1[NE], full-length Mto1 localises to several cytoplasmic foci in interphase, which could affect the Mto2 phosphorylation and consequently the Mto1-Mto2 interaction (for example, specific localisation could bring the Mto1/2 complex in proximity to a kinase that could phosphorylate Mto2). To compare interphase and mitotic extracts, I again employed *nda3-KM311* arrest (Fig. 4.4 A, lanes 11-18); moreover, to fully take into account any effects of temperature on the Mto1-Gtb1 interaction (discussed in chapter 4.2.1) I also analysed *nda3*$^{+}$ strains grown at both 18ºC and 32ºC (Fig. 4.4 A, lanes 3-10). Anti-Mto2 western blotting revealed that Mto2[alanine] phosphorylation differed from wild-type, both in interphase and mitosis (Fig. 4.4 A; compare Input lanes: lane 11 and lanes 13, 15, 17; lane 12 and lanes 14, 16, 18), suggesting that at least some of the residues selected for mutation contributed to the mobility shift of wild-type Mto2. In all three *mto2[alanine]* mutants, Mto2 seemed to undergo mobility shifts in mitosis, which are likely to due to phosphorylation (Fig. 4.4 A; compare Input lanes: 13 and 14; 15 and 16, 17 and 18;). However, the mitotic mobility shift was much less prominent than in *mto2*$^{+}$ cells, especially in *mto2-17A* (see also Fig. 4.15 for phosphatase treatment on mitotic Mto2-17A). Pull down experiments revealed that all Mto2[alanine] mutant proteins could interact with Mto1 not only during interphase but also during mitosis (Fig. 4.4 A, IgG pulldown lanes 10 -18)). Moreover, quantification of the amount of γ-tubulin pulled down by Mto1/2[A] revealed that abolishing phosphorylation of Mto2 led to an increase in the amount of the co-precipitated γ-tubulin, which was particularly evident in *mto2-17A* cells. The amount of Mto2 pulled down by Mto1-TAPS in interphase was similar in *mto2*$^{+}$ and *mto2[alanine]* cells (data not shown).

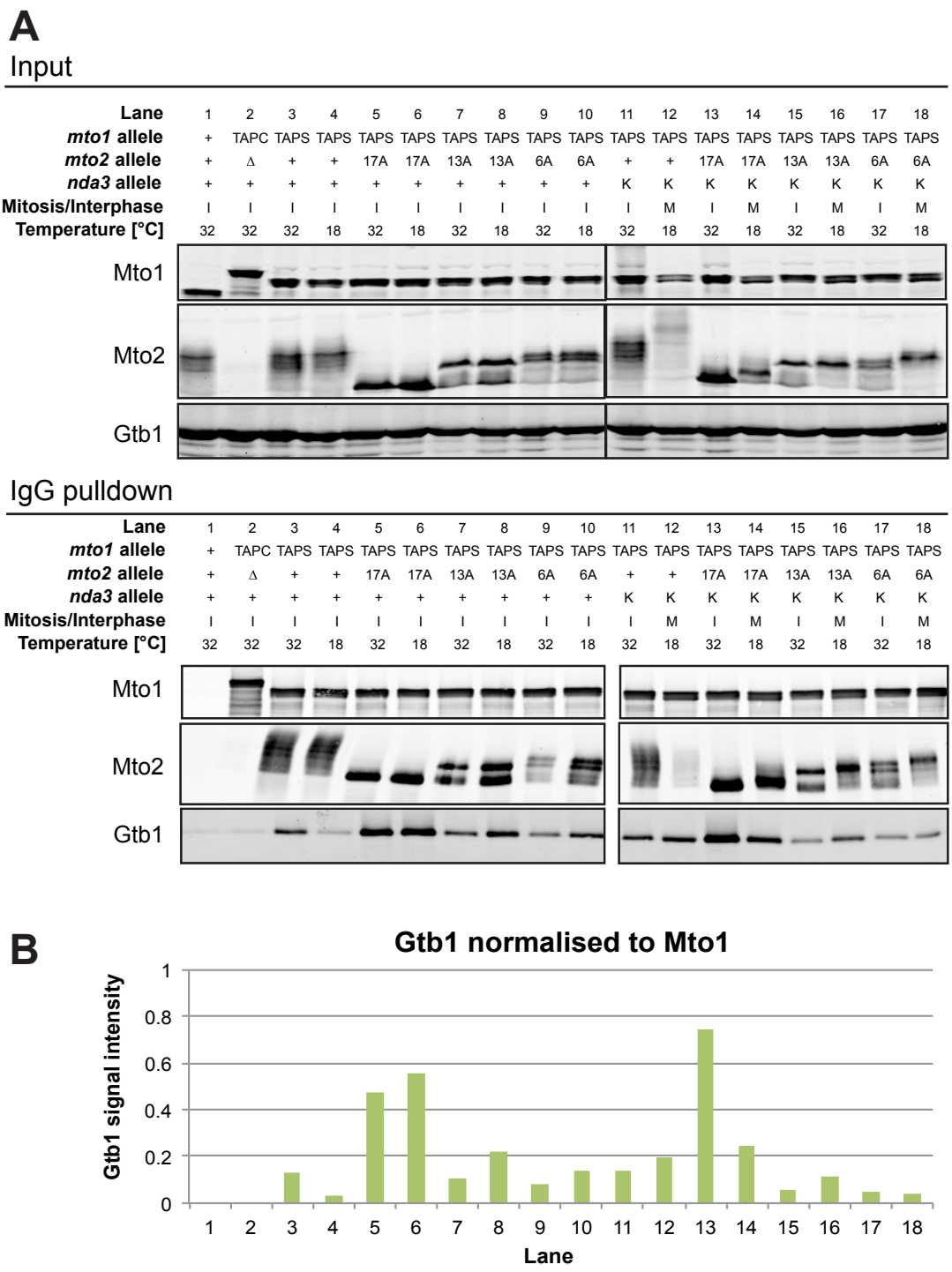

Figure 4.5. Unlike wild-type Mto2, Mto2-alanine mutants can interact with Mto1-NE-TAPS in mitosis.
(A) Extracts from asynchronous and metaphase-arrested cells were incubated with IgG-Dynabeads. Following pull-down, western blots were probed against Mto1, Mto2 and Gtb1. K, *nda3-KM311* allele.
(B) Integrated intensities of IRDye800 signal from IgG pulldown from (A) were measured using Odyssey V3.0, and Gtb1 signal was normalised to Mto1. Lanes 1 and 2 were used to define background, therefore, Gtb1 signal intesity equals zero.
[Strains: KS5607, KS6032, KS6193, KS6201, KS6388, KS6390, KS6397, KS6413, KS6474, KS6486]

Previous work in the lab suggested that Mto2[alanine] mutant proteins are able to interact with Mto1[NE] throughout the cell cycle. To recapitulate and extend these results I used Mto1[NE]-TAPS to pull down Mto2[alanine] proteins (Fig. 4.5). In these experiments, I also examined the interaction between the Mto1/2 complex and the γ-TuC. As before, I used extracts from asynchronous and metaphase-arrested cells (Fig. 4.5 A, lanes 11-18) as well as *nda3*$^{+}$ strains grown in the same growth conditions to account for the influence of growth temperature on the γ-TuC-Mto1/2 interaction (Fig. 4.5 A, lanes 3-10). As in the context of full-length *mto1*, Mto2 phosphorylation in *mto1[NE]* cells was decreased in *mto2[alanine]* cells as compared to *mto2*$^{+}$ cells in both interphase and mitosis (Fig. 4.5 A; compare lanes: lane 11 and lanes 13, 15, 17; lane 12 and lanes 14, 16, 18). As shown before by Itaru Samejima (unpublished), Mto1[NE]-TAPS pulled down Mto2[alanine] mutant proteins in interphase as well as in mitosis (Fig. 4.5 A, IgG pulldown, lanes 11-18). As in Mto1-TAPS pulldown, the amount of γ-tubulin pulled down by Mto1/2-17A complex was higher relative to wild-type (Fig. 4.5 B), while the amount of Mto2 pulled down by Mto1[NE]-TAPS in interphase did not change significantly (data not shown). Interestingly, the amount of γ-tubulin pulled down from extracts made of cultures grown in 18ºC increases with the increasing number of alanine substitutions in Mto2. This shows that introducing alanines into Mto2 sequence can overcome the effect that the growth temperature has on the γ-TuC-Mto1/2 interaction (compare γ-tubulin signal intensities in IgG pulldown lanes 4, 6, 8 and 10). This is consistent with the notion that abrogation of the γ-tubulin-Mto1 interaction in 18ºC is due to reduced hydrophobic interactions: alanine residues are less polar (more hydrophobic) than serine or threonine residues, and much less polar than a phosphate group. Thus, whether the residues are phosphorylated *in vivo* or not, the introduced mutations increase the overall hydrophobicity of Mto2.

Overall, these results demonstrate that mutating phosphoresidues within Mto2 to alanines abrogates the mitotic disruption of Mto1-Mto2 interaction. This suggests that the mitotic disruption of the Mto1-Mto2 interaction is due to Mto2 phosphorylation, and even a partial abolition of this phosphorylation (such as in *mto2-6A* cells) results in maintenance of the Mto1-Mto2 interaction throughout the cell cycle. In addition, these results imply that Mto2 phosphorylation regulates the interaction between the Mto1/2 and the γ-TuC, as abolition of Mto2 phosphorylation leads to more stable interaction of the Mto1/2 complex with the γ-TuC.

4.2.4 Mto2 phosphorylation is perturbed in *mto1[bonsai]-TAPC* cells

Next, I wished to determine if the Mto1-Mto2 interaction is maintained in *mto1[bonsai]* cells. In these cells, the Mto1/2[bonsai] complex does not localise to any conventional MTOCs and is observed as discrete puncta that stimulate spatially random nucleation. Therefore, any Mto2 phosphorylation observed in this background is completely independent of Mto1/2 localisation.

For pull-down experiments in *mto1[bonsai]* background, I used Mto1[bonsai] tagged with a TAPC tag, as opposed to a TAPS tag used previously. The two tags are very similar: they are both tandem affinity purification tags that contain two different affinity tags to ensure the purity of purified proteins, and they both consist of a double Z domain (Tasto et al., 2001), a synthetic Fc-region binding peptide derived from S domain of *Staphylococcus aureus* protein A, which is preceded by TEV protease cleavage site. The difference lies in the first affinity tag, which in the TAPS tag is an S-peptide from RNAse A (Brune et al., 2005; Kim and Raines, 1993), whereas in the TAPC tag is a calmodulin binding peptide (CBP).

As before, the Mto1-Mto2 and the Mto1-Gtb1 interactions were analysed in interphase and mitotic extracts of *nda3-KM311 mto2[alanine]* cells (Fig. 4.6). As expected, the interphase and mitotic Mto2 phosphorylation was decreased in *mto2[alanine]* cells as compared to *mto2*$^{+}$ cells (Fig. 4.6 A; compare Input lanes: lane 11 vs. 13, 15; lane 12 vs. 14, 16), with the exception of *mto2-6A*, where, unlike previously, Mto2 phosphorylation appeared to be reminiscent of wild-type (Fig. 4.6 A; compare Input lanes: 11 and 17; 12 and 18). Moreover, the Mto1[bonsai]-TAPC-Mto2-6A interaction was greatly decreased in mitosis, similarly to wild-type (Fig. 4.6 A; compare IgG pulldown lanes 12 and 18). More careful examination revealed that mitotic phosphorylation of wild-type Mto2 in *mto1[bonsai]-TAPC* cells was diminished when compared to other *mto1* backgrounds. In both *mto1-TAPS* and *mto1[NE]-TAPS* cells, mitotic Mto2 migrated slower than in *mto1[bonsai]-TAPC* (compare Fig. 4.6 and Fig. 4.4, Fig. 4.5). This change in the mitotic phosphorylation of Mto2 could be interpreted as a result of either using a smaller *mto1* truncation, or using a different affinity tag (TAPC vs. TAPS). As described below, the observed difference in phosphorylation was most likely due to a combination of these.

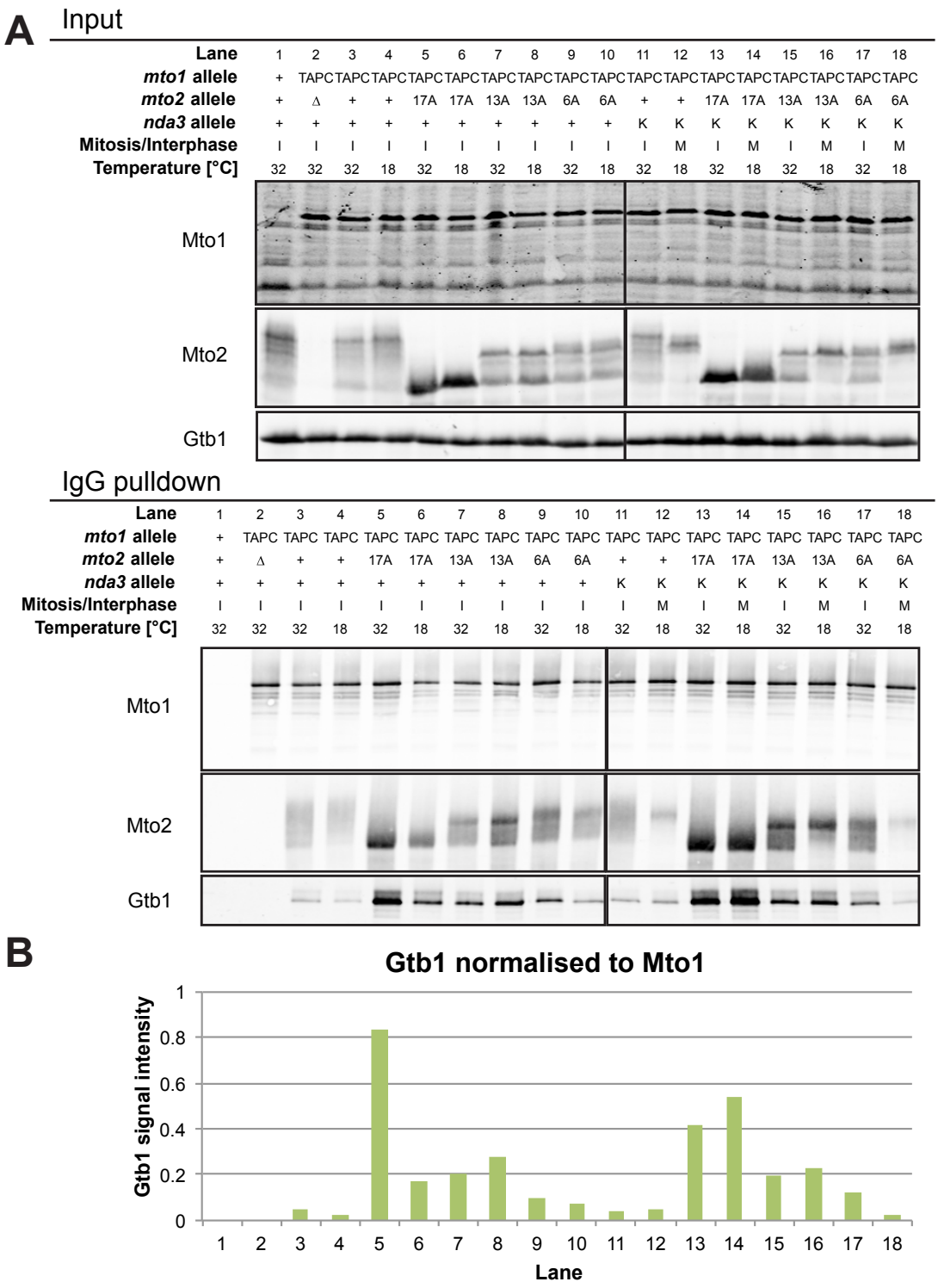

Figure 4.6. Mto2-alanine mutants interact with Mto1-bonsai-TAPC in mitosis, but wild-type Mto2 phosphorylation is perturbed.
(A) Extracts from asynchronous and metaphase-arrested cells were incubated with IgG-Dynabeads. Following pull-down, western blots were probed against Mto1, Mto2 and Gtb1. K, *nda3-KM311* allele.
(B) Integrated intensities of IRDye800 signal from IgG pulldown from (A) were measured using Odyssey V3.0, and Gtb1 signal was normalised to Mto1. Lanes 1 and 2 were used to define background, therefore, Gtb1 signal intesity equals zero. [Strains: KS6294, KS6626, KS6446, KS6447, KS6450, KS6451, KS6454, KS6455, KS6496, KS6498]

4.2.5 Mto2 phosphorylation is independent of Mto1

The observation that mitotic phosphorylation of wild-type Mto2 in *mto1[bonsai]-TAPC* cells is decreased in comparison to *mto1-TAPS* and *mto1[NE]-TAPS* cells suggested a hypothesis that Mto2 phosphorylation depends on Mto1. For example, Mto2 phosphorylation could depend on the localisation of the Mto1/2 to different MTOCs: thus in *mto1[NE]* or *mto1[bonsai]* cells, Mto2 phosphorylation could be less prominent than in wild-type cells. Mto1 could also provide a docking site for kinases that phosphorylate Mto2 and this docking site could be absent in *mto1[NE}* or *mto1[bonsai]* backgrounds. Alternatively, the change in Mto2 phosphorylation in *mto1[bonsai]* cells could be an artefact of the tag used.

To distinguish between these two possibilities, I directly compared the interphase and mitotic Mto2 phosphorylation in *mto1* backgrounds used in previous experiments, as well as in *mto1*Δ cells. An IgG pulldown using TAP-tagged Mto1 truncations used in previously described experiments was performed on extracts from asynchronous and metaphase-arrested cells, and analysed by western blot (Fig. 4.7 A). The only *mto1* mutant in which a perturbed Mto2 phosphorylation was observed was *mto1[bonsai]-TAPC*; in other mutant backgrounds, including *mto1*Δ*,* Mto2 phosphorylation was identical to wild-type (Fig. 4.7 A; compare Input lanes 4, 8, 12, and 16). The normal Mto2 phosphorylation in *mto1*Δ background shows that Mto2 phosphorylation does not depend on Mto1/2 complex formation, nor does it depend on localisation of Mto2 to any specific cytoplasmic foci.

This result also suggested that the altered Mto2 phosphorylation in *mto1[bonsai]-TAPC* cells is likely to be an artefact of using a TAPC tag. Therefore, I generated an *mto1[bonsai]-TAPS* strain, and examined Mto2 phosphorylation in this background (Fig. 4.7 B). Western blotting revealed that the mitotic Mto2 phosphorylation is normal in *mto1[bonsai]-TAPS* background, in contrast to *mto1[bonsai]-TAPC.* This tag-induced change occurred only in *mto1[bonsai]-TAPC,* but not *mto1[NE]-TAPC* cells, showing that altered Mto2 phosphorylation in *mto1[bonsai]-TAPC* cells is due to a combination of both the truncation and the tag. A possible explanation is that the CBP moiety, which is slightly bigger than the S-peptide, folds in a way that sterically hinders the interaction between a kinase and some of Mto2 phosphorylatable residues, which prevents phosphorylation. The altered Mto1 phosphorylation is not observed in *mto1[NE]-TAPC* cells, suggesting that the N-terminus of Mto1 somehow counteracts the effect the CPB has on Mto2

phosphorylation, possibly by physically occupying the space that the CPB moiety occupies in *mto1[bonsai]-TAPC* cells.

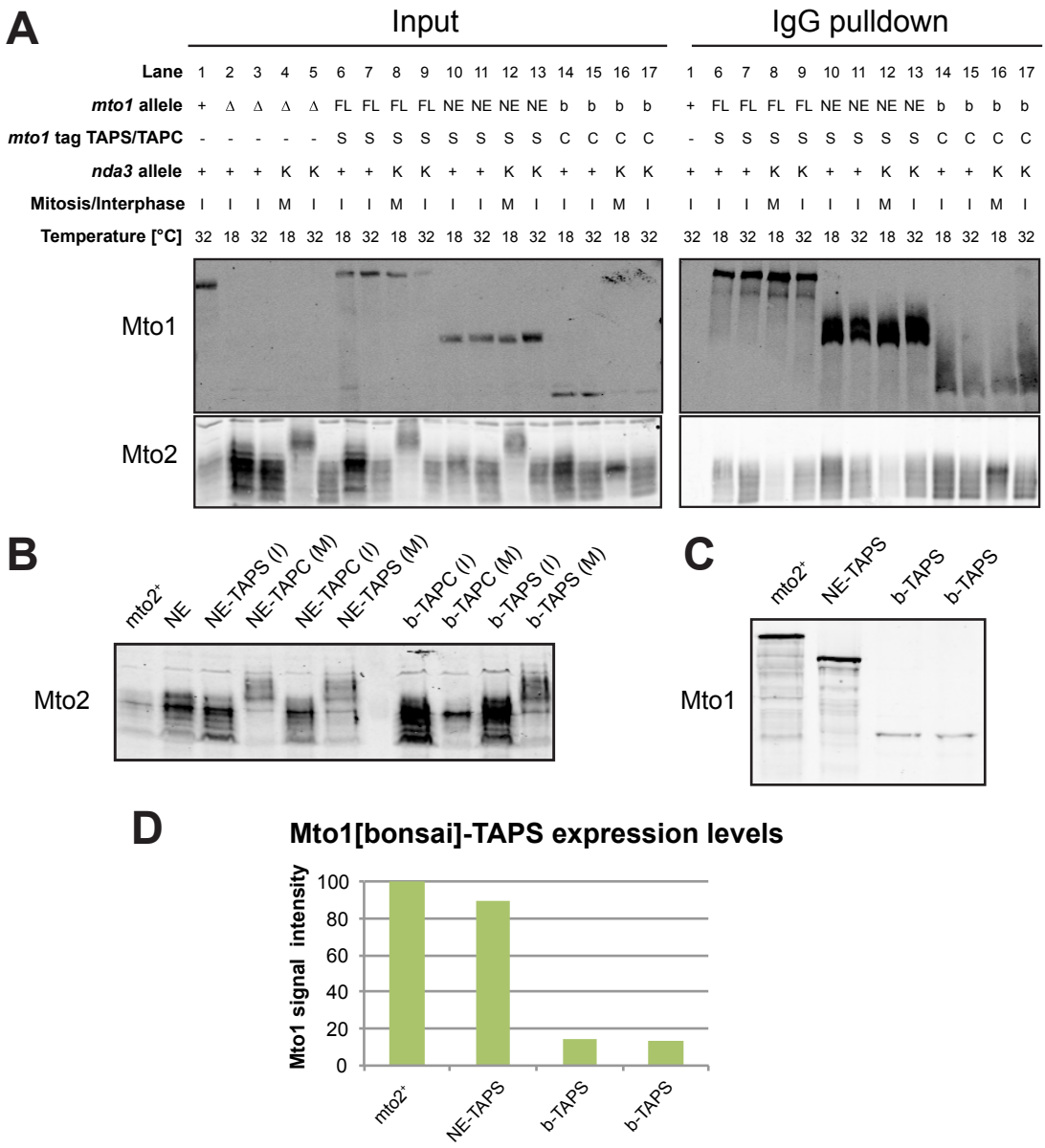

Figure 4.7. Mto2 phosphorylation is abnormal in *mto1[bonsai]-TAPC* background.
(A) Phosphorylation of Mto2 in different *mto1* backgrounds was examined. Extracts from asynchronous and metaphase-arrested cells were incubated with IgG-Dynabeads. Following pull-down, western blots were probed against Mto1 and Mto2. FL, Mto1; NE, Mto1[NE]; b, Mto1[bonsai]; C, TAPC tag; S, TAPS tag; K, *nda3-KM311* allele.
(B) Effects of C-terminal TAPS and TAPC tags on Mto2 phosphorylation were investigated in *mto1[NE]* and *mto1[bonsai]* backgrounds in asynchronous and metaphase-arrested cells.
(C) Anti-Mto1 western blot of whole cell extracts in various *mto1* mutants. Two different *mto1[bonsai]-TAPS* clones were analysed.
(D) Integrated intensities of IRDye800 signal from (C) were measured using Odyssey V3.0, and Mto1 signal was shown as proportion of wild-type signal.
[Strains: KS516, KS1158, KS1239, KS3524, KS3575, KS5607, KS6032, KS6175, KS6193, KS6454, KS6455, KS6828, KS6909, KS6910, KS6949]

As Mto2 phosphorylation is normal in *mto1[bonsai]-TAPS* cells, this mutant background appeared to be appropriate to examine the Mto1-Mto2 interaction in *mto2[alanine]* cells. However, quantification of Mto1[bonsai]-TAPS expression levels revealed that the protein is expressed only at less than 20% of wild-type levels (Fig. 4.7 C and D). As both Mto1 and Mto2 are low-abundance proteins, present at equal numbers of molecules per cell, a five-fold reduction in expression levels of one of the complex component could perturb the MT nucleation. Thus, I decided not to examine the Mto1-Mto2 interaction in *mto1[bonsai]-TAPS mto2[alanine]* background, despite the apparently normal Mto2 phosphorylation observed in these cells.

4.2.6 Human CDK1-Cyclin B phosphorylates wild-type, Mto2-6A and Mto2-13A *in vitro*

It was previously shown that in *mto1[1-800]-TAPS* cells, human CDK1-Cyclin B treatment on the partially purified Mto1/2 complex leads to hyperphosphorylation of wild-type Mto2 and the disruption of the Mto1-Mto2 interaction, suggesting that the Mto1/2 complex phosphorylation is directly responsible for its disassembly in mitosis (Groocock PhD Thesis, 2010). However, that experiment did not indicate whether phosphorylation of Mto2, Mto1 or both of the proteins disrupts the Mto1/2 complex. If Mto2 phosphorylation were sufficient to cause the Mto1/2 complex to dissociate, this dissociation should be abolished in *mto2[alanine]* cells.

To test this, I pulled down Mto1/2 complex from *mto2*$^{+}$ and *mto2[alanine]* cells in *mto1-TAPS* background and treated the pull-downs with human recombinant CDK1-Cyclin B. As expected based on results obtained by Lynda Groocock, upon kinase treatment wild-type Mto2 became phosphorylated, as demonstrated by the appearance of slower-migrating Mto2 isoforms similar to those observed in mitosis (Fig. 4.8, also compare to Fig. 4.1 A, lane 5). Comparison of untreated and kinase-treated Mto2-6A and Mto2-13A showed that the CDK1-Cyclin B complex phosphorylated both mutant proteins as demonstrated by Mto2 mobility shift. No change in electrophoretic mobility was observed for Mto2-17A in this assay, which was expected, as all but one of the identified Cdk1 sites were mutated to alanines in this mutant. However, the possibility that CDK1-Cyclin B phosphorylated Mto2-17A cannot be ruled out, as not every phosphorylation event results in a detectable SDS-PAGE mobility shift. Similarly, even though no Mto1 *in vitro* phosphorylation was

observed in this analysis, it cannot be ruled out it did occur without causing any mobility shift.

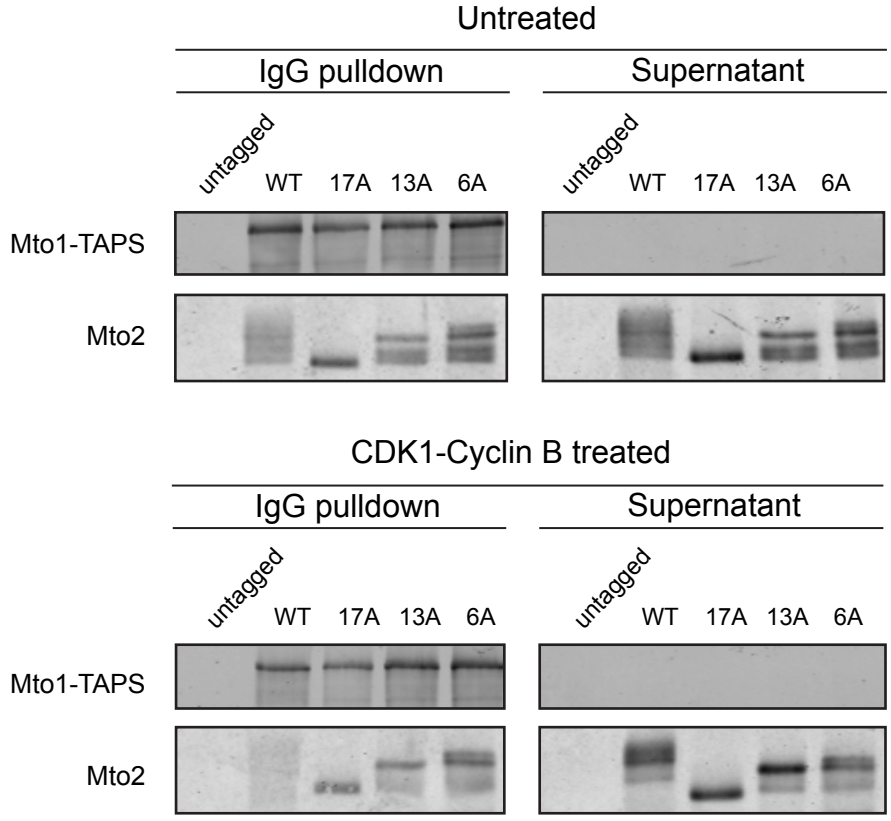

Figure 4.8. Human CDK1-Cyclin B phosphorylates purified Mto1/2-alanine complexes *in vitro*. Mto1/2-alanine complexes that had been purified using IgG-Dynabeads were incubated with 100 ng of CDK1-Cyclin B. Eluates and supernatants were analysed by western blot; membranes were probed against Mto1 and Mto2. [Strains: KS516, KS3575, KS6742, KS6746, KS6749]

Surprisingly, in both untreated and kinase-treated samples, wild-type Mto2 dissociated from Mto1-TAPS. This result is contradictory to what was observed by Lynda Groocock, where Mto2 dissociated from Mto1-TAPS only in kinase-treated extracts. This discrepancy might be an artefact of the experimental design I used; in experiments performed by Lynda Groocock the beads were incubated with the kinase for 30 minutes, whereas I increased the amount of protein used in the assay and extended the incubation time to 90 minutes; the prolonged incubation might have contributed to Mto2 dissociation from Mto1-TAPS. Thus, it is unclear whether the phosphorylated wild-type Mto2 as well as Mto2[A] proteins dissociated from Mto1-TAPS upon kinase treatment. To test that, a kinase treatment on partially

purified Mto1/2[A] complexes should be performed with varying incubation times to ensure that optimal conditions are used.

Overall, this analysis demonstrates that Cdk1 can phosphorylate wild-type Mto2, as well as Mto2-6A and Mto2-13A *in vitro*. It does not demonstrate whether this phosphorylation is sufficient to disrupt the Mto1-Mto2 interaction in either *mto2*$^{+}$ or *mto2[alanine]* cells.

4.2.7 MT nucleation is more efficient in *mto2[alanine]* cells compared to wild-type cells

Because my biochemical analysis demonstrated that Mto2 phosphorylation regulates the interaction between the Mto1/2 complex and the γ-TuC both in interphase and mitosis (see Fig. 4.5, IgG pulldown lanes 4, 6, 8 and 10), I wished to understand what role this phosphorylation may have in interphase cells. I used live-cell imaging of cells expressing GFP-α-tubulin to visualise interphase MT networks in *mto2[alanine]* cells (Fig. 4.9). I quantified the number of MT bundles per cell and the frequency of nucleation events for each mutant, using the method described in Section 3.2.1.1. All of the *mto2[alanine]* cells contained more MT bundles than *mto2*$^{+}$ cells (Fig. 4.9 B), and the difference was statistically significant (Table 4.2). However, they were not statistically different from each other. Furthermore, the MT nucleation frequency increased with increasing number of alanine substitutions (Fig 4.9 C). The MT nucleation frequency observed in *mto2[alanine]* cells was statistically different from the frequency observed in wild-type cells; moreover, the *mto2-6A* and *mto2-13A* were also different from *mt2-17A* (Table 4.3). The observation that *mto2[alanine]* mutants are similar in the respect of number of MT bundles but different in the respect of MT nucleation frequency is not surprising. In fission yeast, nascent MTs often get incorporated into pre-existing MT bundles soon after nucleation (Lynch PhD Thesis 2012), therefore, even a large increase in the MT nucleation frequency would result in a moderate increase of the number of MT bundles.

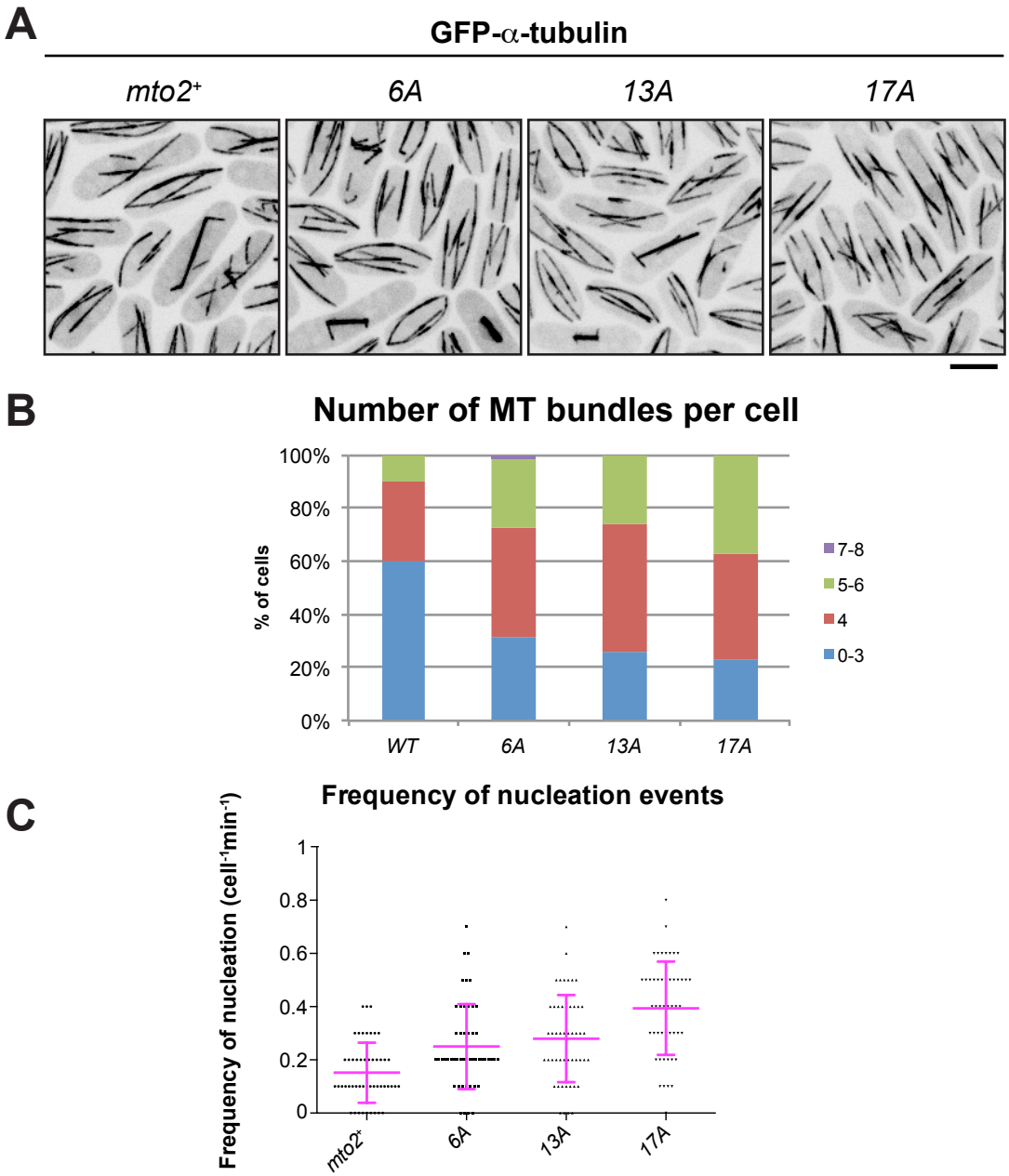

Figure 4.9. *mto2-alanine* cells contain more MT bundles and nucleate more MTs than wild-type.
(A) Interphase cells expressing GFP-α-tubulin. Interphase *mto2*$^{+}$ cells contained 3-5 MT bundles that extended along the long axis of the cell, while in *mto2-alanine* cells the number of MT bundles per cell was higher.
(B) Number of MT bundles per cell observed in (A), n=50. All three mutants were statisctically different from wild-type.
(C) Quantification of the MT nucleation observed in movies of live cells expressing GFP-α-tubulin, n=50. Magenta bars indicate the average number of nucleation events per cell and SEM.
Bar, 5 μm. [Strains: KS1235, KS6407, KS6512, KS6737]

Overall, this experiment shows that abolishing Mto2 phosphorylation leads to an increase in the number of MT bundles and MT nucleation events, therefore showing that Mto2 phosphorylation acts to negatively regulate the Mto1/2 complex MT nucleation activity during interphase.

Table 4.2. *mto2[alanine]* cells contain more MT bundles than wild-type cells. Wilcoxon rank-sum test was used for comparison between each mutant (Mann and Whitney, 1947). P values are shown.

	WT	6A	13A
17A	2.275E-07	0.1422	0.2016
13A	3.236E-05	0.7893	
6A	0.000204		

Table 4.3. MT nucleation frequency increases with increasing number of alanine substitutions in Mto2 sequence. Wilcoxon rank-sum test was used for comparison between each mutant (Mann and Whitney, 1947). P values are shown.

	WT	6A	13A
17A	1.892E-10	4.753E-05	0.001326
13A	4.971-05	0.266	
6A	0.001003		

4.2.8 Post-anaphase array formation is advanced in *mto2[alanine]* cells

As the Mto1-Mto2 interaction is maintained in mitosis in *mto2[alanine]* cells, I next wanted to investigate the mitotic MT phenotype in these cells. If the original hypothesis that led to generation of *mto2[alanine]* mutants were correct, the maintenance of the Mto1-Mto2 interaction throughout the cell cycle should prevent the Mto1/2 complex disassembly in mitosis. This could potentially lead to cytoplasmic *mitotic* MT nucleation, however the maintenance of intact Mto1/2 complexes in mitosis was not expected to result in formation of an interphase-like MT array in mitosis. Because the nuclear envelope does not break down during fission yeast mitosis, critical factors, such as MT bundling proteins or MT polymerases, must be imported to the nucleus to promote mitotic spindle formation. Therefore, even if the Mto1/2 complex persisted in mitosis, it might not be able to promote MT nucleation because of the lack of other proteins required for MT nucleation and persistence.

To observe potential MT nucleation events in mitosis, I imaged mitotic *mto2[alanine]* cells expressing GFP-α-tubulin. In wild-type *S. pombe* cells, upon commitment to mitosis, the cytoplasmic MT network breaks down, and the mitotic

spindle is formed between duplicated SPBs. The dynamics of the newly formed spindle consists of three phases: phase one, spindle formation; phase two, constant spindle length; and phase three, quick spindle elongation (Nabeshima et al., 1998). The separation of sister chromatids in anaphase A takes place at the end of phase two (Tatebe et al., 2001). Soon after, the spindle begins to elongate and astral MTs are nucleated from the cytoplasmic face of the SPB. The post-anaphase array (PAA) of MTs is nucleated from the eMTOCs at the end of phase three, concomitant with the arrival of the duplicated nuclei at the cell ends (Hagan and Hyams, 1988; Heitz et al., 2001). As expected, in *mto2*$^{+}$ cells, no cytoplasmic MTs were observed until late anaphase, when the spindle poles reached cell tips (Fig 4.10). In contrast, in *mto2[alanine]* mutants, the earliest eMTOCs-derived MTs were observed at much shorter spindle lengths. The premature PAA formation in *mto2[alanine]* cells could be explained by greatly reduced mitotic phosphorylation of Mto2 in these cells. According to this view, post-mitotic Mto2[alanine] dephosphorylation requires a lower number of phosphate groups to be removed, which presumably enables the expedited Mto1/2[A] complex re-assembly.

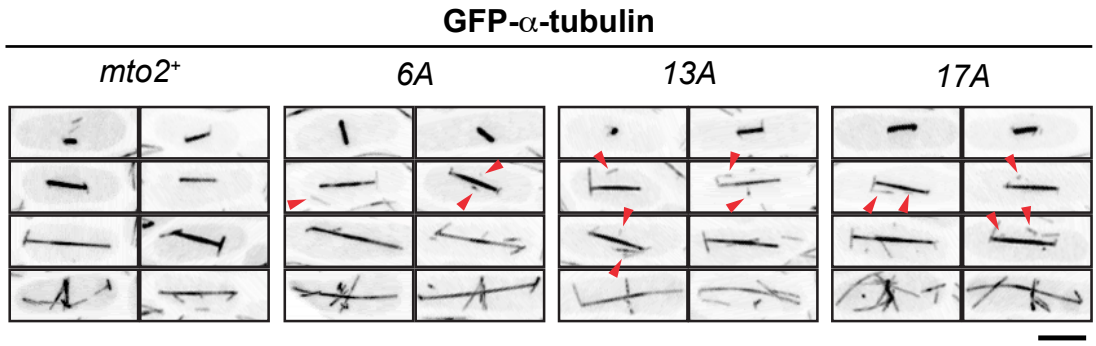

Figure 4.10. Post-anaphase array (PAA) formation is advanced in *mto2-alanine* cells. Confocal images showing mitotic cells expressing GFP-α-tubulin. Each frame represents a different cell. Arrowheads indicate prematurely nucleated PAA MTs.
Bar, 5 µm. [Strains: KS1235, KS6407, KS6512, KS6737]

However, no cytoplasmic MT nucleation in early metaphase *mto2[alanine]* cells was observed (Fig. 4.10 and data not shown). This suggests that, despite the maintenance of the specific Mto1-Mto2 interaction in mitosis, the Mto1/2 complex is either inactive or disassembled in metaphase.

4.2.9 The Mto1/2 complex size and intensity are comparable in wild-type and *mto2[alanine]* cells

Imaging of GFP-α-tubulin revealed that, relative to wild-type, the Mto1/2 complex is a better interphase MT nucleator in *mto2[alanine]* cells. This could be a result of an increased affinity of the Mto1/2 complex for the γ-TuC as well as a higher stability of the Mto1/2 complex in *mto2[alanine]* cells. I previously demonstrated (Section 4.2.3) that in *mto2[alanine]* cells, Mto1/2[A] complexes, in particular Mto1/2[17A], co-precipitate more γ-tubulin than in *mto2*$^{+}$ cells. However, the Mto1:Mto2 ratio did not change in *mto2[alanine]* cells relative to wild-type in those experiments (data not shown), presumably because the interaction was already 'saturated' in wild-type cells and no further increase in stoichiometry was possible. This does not rule out the possibility that the Mto1-Mto2 interaction is stronger in *mto2[alanine]* cells. Another interaction that contributes to the Mto1/2 complex formation and might be controlled by phosphorylation is the Mto2 self-interaction. Similarly to the Mto1-Mto2 interaction, an increase in the Mto2 self-interaction strength would also not be detected biochemically in pull down assays I performed. However, an increase in the affinities within the Mto1/2 complex (either the affinity of Mto2 to Mto1 or to itself, or both) could potentially result in an increase in the Mto1/2 complex size, which can be observed microscopically. Therefore, to examine the Mto1/2 complex *in vivo*, I imaged wild-type and *mto2[alanine]* cells expressing Mto1-GFP.

As expected, in *mto2*$^{+}$ cells Mto1-GFP localised to SPBs, the NE, along MTs and to eMTOCs during cytokinesis (Fig. 4.11 A). This was also true for *mto2[alanine]* cells; however, *mto1-GFP mto2-17A* cells, despite normal Mto1-GFP localisation patterns, exhibited polarity and cell separation defects, as demonstrated by the presence of branching and not fully separated cells. This phenotype is most likely an artefact of a combination of the C-terminal GFP tag on Mto1 as well as alanine substitutions in Mto2, since *mto2-17A mto1*$^{+}$ and *mto2-17A-GFP mto1*$^{+}$ cells exhibit normal cell morphologies (compare to Fig. 4.14 and data not shown).

The increase in strength of interactions within the Mto1/2[A] complex relative to wild-type Mto1/2 could lead to an increase in the size of Mto1/2[A] complexes observed by microscopy. Therefore, the size and intensity of Mto1-GFP puncta in *mto2[alanine]* mutants were analysed and compared to wild-type (Fig. 4.10 B). In all three mutants, Mto1-GFP puncta were of comparable size and intensity (less than

15% and less than 5% different than wild-type, respectively); these values should be analysed collectively as an increase in the amount of Mto1-GFP molecules within the Mto1/2 complex can lead either to an increase in size or in intensity. Statistical analysis demonstrated that there are differences between wild-type and phosphomutants, however they were not great and not consistent ($p<0.005$ was considered statistically significant); for example, in *mto2*-17A cells, Mto1-GFP puncta size was comparable to the wild-type puncta sizes, whereas Mto1-GFP punctum intensity was different than wild-type (Tables 4.4 and 4.5). These inconsistencies, along with not very low p values, suggested that the interactions within the Mto1/2 complex are not much stronger in *mto2[alanine]* background relative to wild-type. However, the increase in puncta size and intensity could have been difficult to precisely measure given their close proximity *in vivo*. Moreover, in *mto1-GFP* cells, the Mto1/2 complex localizes to various MTOCs including SPBs and eMTOCs (Fig. 4.11 B; note data points with punctum size or intensity much higher than other data points; those are most likely Mto1/2 complexes localised at SPBs or eMTOCs). The presence of those very large Mto1/2 puncta (localised to SPB or eMTOCs) could affect the analysis. Therefore, differences between wild-type and mutant Mto1/2 complexes could potentially be more evident in *mto1* truncation backgrounds, where the Mto1/2 complex does not localise or localises only to a subset of MTOCs and is visible as discrete puncta.

Table 4.4. Comparison of Mto1-GFP puncta size in *mto2*$^+$ and *mto2[alanine*] cells. Wilcoxon rank-sum test was used for comparison between each mutant (Mann and Whitney, 1947). P values are shown.

	WT	6A	13A
17A	0.3279	0.004629	0.01023
13A	0.08474	0.7985	
6A	0.04335		

Table 4.5. Comparison of Mto1-GFP puncta intensity in *mto2*$^+$ and *mto2[alanine*] cells. Wilcoxon rank-sum test was used for comparison between each mutant (Mann and Whitney, 1947). P values are shown.

	WT	6A	13A
17A	0.00417	0.001415	0.4556
13A	0.02386	0.01012	
6A	0.9754		

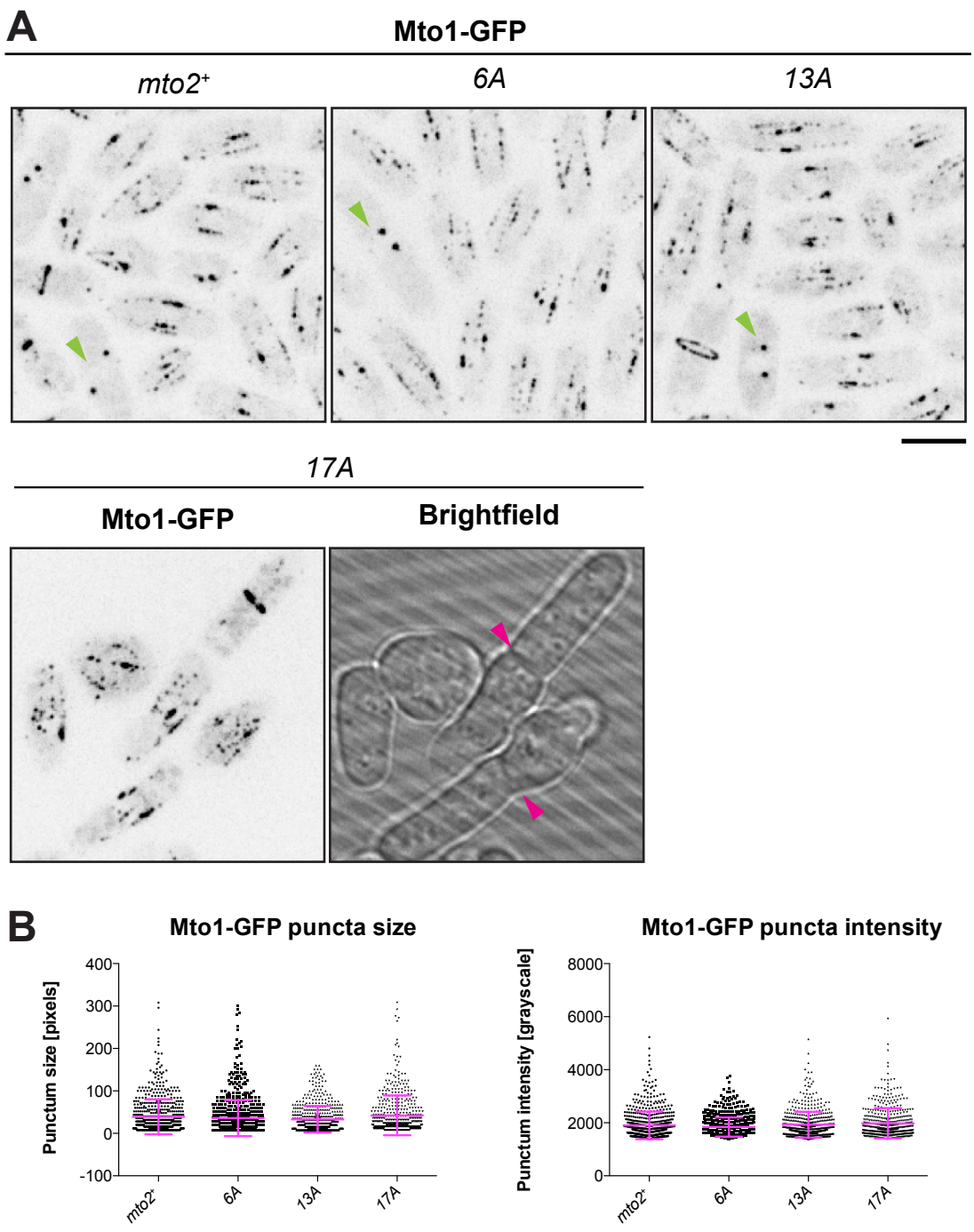

Figure 4.11. *mto1-GFP mto2-17A* cells show defects in cytokinesis.
(A) Confocal images of *mto2*$^{+}$ and *mto2-alanine* cells expressing Mto1-GFP. For *mto2-17A* cells, transmitted light images were also acquired to show morphology defects. Mto1-GFP localisation in *mto2-alanine* cells is reminiscent of wild-type. Early mitotic cells are indicated with green arrowheads. *mto1-GFP mto2-17A* cells exhibit cytokinesis defects and often fail to separate after cell division (magenta arrowheads).
(B) Size and intensity of puncta observed in (A) were quantified using Metamorph software. For each strain, puncta within a single imaging field were analysed. Magenta bars indicate the average puncta size or intensity and SEM.
Bar, 5 µm. [Strains (number of puncta analysed): KS819 (624), KS6422 (580), KS6426 (718), KS6510 (466)]

4.2.10 The Mto1/2 complex is disassembled in mitosis in wild-type and *mto2[alanine]* cells

Because imaging of GFP-α-tubulin in *mto2[alanine]* cells suggested the Mto1/2 complex is inactive or disassembled in early mitosis (see Section 4.2.8), I next wanted to image Mto1-GFP in *mto2*$^{+}$ and *mto2[alanine]* cells in order to examine the state of the mitotic Mto1/2 complex *in vivo*.

mto1-GFP mto2[alanine] mitotic cells exhibited wild-type Mto1-GFP localisation pattern, with Mto1-GFP localising exclusively to mSPBs (Fig. 4.11 A). The complete absence of cytoplasmic Mto1-GFP puncta from mitotic cells suggested that, despite maintaining the Mto1-Mto2 interaction, the multimeric Mto1/2 complex disassembles in mitosis. No mitotic cells are shown for the *mto2-17A* mutant, because its morphological defects (discussed in Section 4.2.9) made the imaging difficult, moreover, any mitotic phenotype could be an artefact of the observed polarity defects.

4.2.11 The Mto1/2[NE] complex size and intensity increase with increasing number of alanine substitutions in Mto2 sequence

Imaging of full-length Mto1-GFP in *mto2[alanine]* cells did not provide a compelling evidence for a stronger association within the Mto1/2 complex relative to wild-type cells. However, this might be due to a 'crowded' nature of MTOCs in *mto1-GFP* background and the presence of large Mto1/2 complex assemblies at SPBs and eMTOCs, which could have impeded the analysis. Therefore, I imaged Mto1[NE]-GFP in wild-type and *mto2[alanine]* backgrounds. In wild-type cells, Mto1 localisation to the NE depends on Mto2 – upon cold-treatment, Mto1 redistributes to the NE in *mto2*$^{+}$ but not in *mto2*Δ cells (Samejima et al., 2005). Mto1[NE] lacks majority of its localisation domains apart from the N-terminal NE localisation domain, therefore, in *mto1[NE]-GFP* cells, the Mto1/2 complex is observed as discrete puncta at the NE (Lynch PhD Thesis 2012). This localisation is lost upon mitotic entry (Groocock PhD Thesis, 2010).

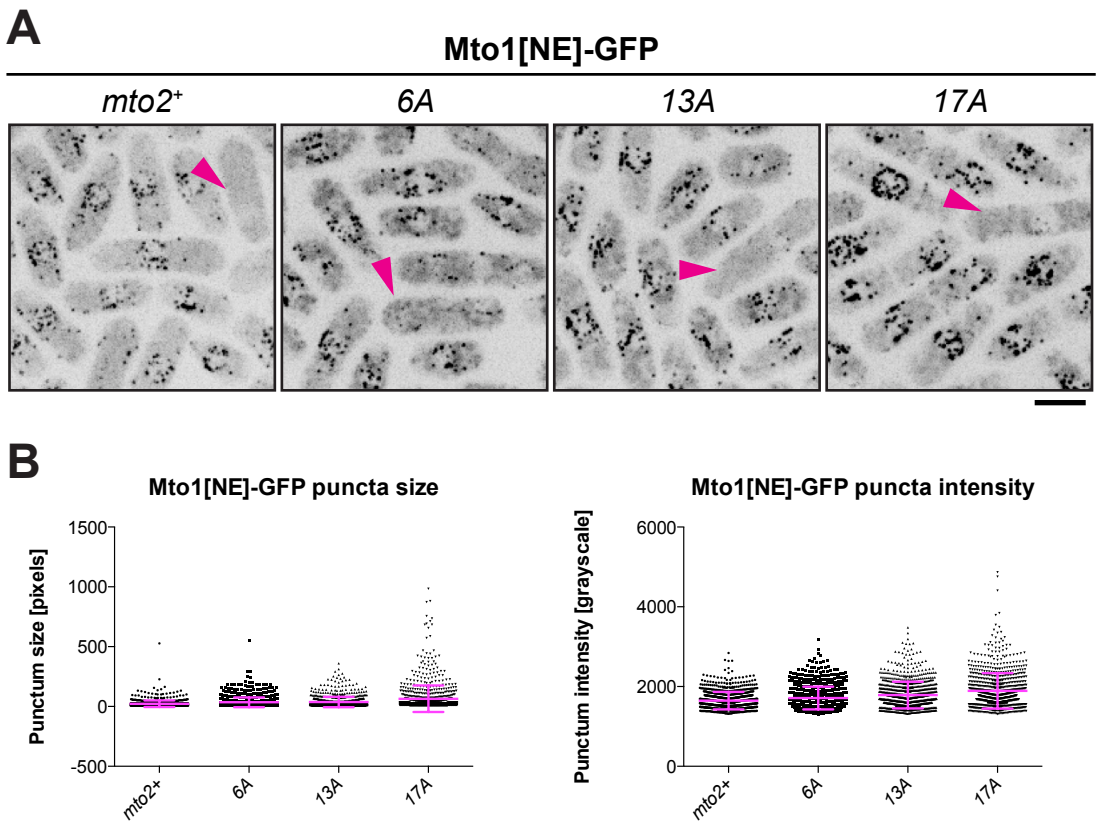

Figure 4.12. Localisation of Mto1-NE-GFP to the NE is disrupted in mitosis in mto2-alanine mutants.
(A) Confocal images of *mto2*$^{+}$ and *mto2-alanine* cells expressing Mto1[NE]-GFP. Interphase Mto1[NE]-GFP localisation in *mto2-alanine* cells resembles localisation in wild-type cells. In mitosis, Mto1[NE]-GFP delocalizes from the NE in wild-type and mutant cells (mitotic cells are indicated with magenta arrowheads).
(B) Size and intensity of puncta observed in (A) were quantified using Metamorph software. For each strain, puncta within a single imaging field were analysed. Magenta bars indicate the average puncta size or intensity and SEM.
Bar, 5 µm. [Strains (number of puncta analysed): KS5209 (903), KS6478 (924), KS6485 (997), KS6977 (934)]

As expected, in *mto1*$^{+}$ cells, Mto1[NE]-GFP was primarily visible as puncta localised to the NE and occasionally to MTs (Fig. 4.12 A), which is presumably a result of Mto1[NE]-GFP localisation to the minus end of MTs following nucleation. A similar localisation was observed in *mto2[alanine]* cells, however, in *mto2[alanine]* cells Mto1[NE]-GFP was clearly enriched at the NE compared to wild-type, suggesting that Mto2 phosphorylation might play a role in regulation of the interaction between the Mto1/2 complex and its, yet unidentified, nuclear receptor.

Quantitative analysis of Mto1[NE]-GFP puncta showed that increasing the number of alanine substitutions in Mto2 led to gradual increase in both punctum size

and intensity (Fig. 4.12 B). The size and intensity of Mto1[NE]-GFP puncta in *mto2[alanine]* cells were statistically different from wild-type. Moreover, the mutants were also statistically different from each other (Tables 4.6 and 4.7).

Overall, this experiment demonstrates that Mto2 phosphorylation plays a role in regulation of either the Mto2 self-affinity or its affinity to Mto1; abolition of Mto2 phosphorylation results in an increased size of Mto1/2[A] complexes i*n vivo*.

Table 4.6. Comparison of Mto1[NE]-GFP puncta size in *mto2*$^{+}$ and *mto2[alanine*] cells. Wilcoxon rank-sum test was used for comparison between each mutant (Mann and Whitney, 1947). P values are shown.

	WT	6A	13A
17A	2.2E-16	1.063E-08	3.076E-06
13A	2.2E-16	0.2793	
6A	2.023E-15		

Table 4.7. Comparison of Mto1[NE]-GFP puncta size in *mto2*$^{+}$ and *mto2[alanine*] cells. Wilcoxon rank-sum test was used for comparison between each mutant (Mann and Whitney, 1947). P values are shown.

	WT	6A	13A
17A	2.2E-16	2.2E-16	4.171E-06
13A	2.2E-16	1.274E-06	
6A	3.725E-05		

4.2.12 Localisation of Mto1[NE]-GFP to the NE is disrupted in mitosis in *mto2[alanine]* cells

In wild-type cells, Mto1[NE]-GFP delocalises from the NE upon mitotic entry (Groocock PhD Thesis, 2010). This can be explained by the fact that Mto1 localisation to the NE is dependent on Mto2, and the Mto1-Mto2 interaction is disrupted in mitosis. Because the Mto1-Mto2 interaction is maintained in mitosis in *mto2[alanine]* cells, I investigated the localisation of Mto1[NE]-GFP in these cells in mitosis (Figure 4.12 A). In all three *mto2[alanine]* mutants, Mto1[NE]-GFP puncta disassembled and were absent from the mitotic NE. This shows that maintaining the Mto1-Mto2 interaction is either not sufficient to prevent the mitotic disassembly of the Mto1/2 complex or to retain the NE localisation in mitosis. Presumably, the interaction with the NE receptor requires an intact multimeric Mto1/2 complex, thus, the disappearance of Mto1[NE]-GFP puncta leads to a loss of interaction between the Mto1/2 and the receptor. Alternatively, the interaction between the Mto1/2 and its NE receptor could be regulated in a cell cycle-dependent manner, i.e. the receptor is modified in mitosis to prevent the interaction with the Mto1/2.

4.2.13 The Mto1/2[bonsai] complex size and intensity increase with increasing number of alanine substitutions in Mto2 sequence

The smallest functional *mto1* truncation, *mto1(131-549)* lacks all localisation domains and is referred to as *mto1[bonsai]*, by analogy to other extensively truncated yet functional proteins (Ciferri et al., 2008; Lynch PhD Thesis, 2012; Widlund et al., 2011). In *mto1[bonsai]* cells, MT nucleation occurs in a spatially random manner throughout the cell. When tagged with GFP, Mto1[bonsai]-GFP is present throughout the cytoplasm in a form of discrete, quickly diffusing puncta that do not localise to any conventional MTOCs and promote all observed cytoplasmic nucleation in a spatially random manner.

I used live-cell imaging of Mto1[bonsai]-GFP to investigate characteristics of Mto1[bonsai]-GFP puncta observed in *mto2[alanine]* cells (Fig. 4.13 A). As shown before, Mto1[bonsai]-GFP in *mto2*$^{+}$ cells was visible as discrete puncta, often arranged in straight lines, indicating association with MTs. This was expected, as Mto1/2 was shown to often remain associated with the MT minus end following nucleation. The size and intensity of Mto1[bonsai]-GFP puncta increased slightly in *mto2-6A* and *mto2-13A* compared to wild-type, but both size and intensity of puncta greatly increased in *mto2-17A* cells, where Mto1[bonsai]-GFP formed large aggregates 2-3-fold bigger than wild-type puncta (Fig. 4.13 B). Mto2-17A is phosphorylated at a much lower level than wild-type Mto2, both in interphase and mitosis (see Figs. 4.4-4.6). As Mto2 phosphorylation regulates the Mto1-Mto2 interaction, and possibly Mto2 self-interaction, it is possible that the near-to-complete abolishment of Mto2 phosphorylation results in interaction between individual Mto1/2[bonsai] complexes, resulting in formation of aggregates. This could be prevented in other *mto1-GFP* and *mto1[NE]-GFP* backgrounds, where the Mto1/2 is localised to conventional MTOCs, which could potentially prevent individual complexes from aggregating. As in *mto1[NE]-GFP* cells, Mto1[bonsai]-GFP puncta observed in *mto2[alanine]* cells were statistically different from puncta observed in wild-type cells; the *mto2[alanine]* mutants were also statistically different from each other (Tables 4.8 and 4.9).

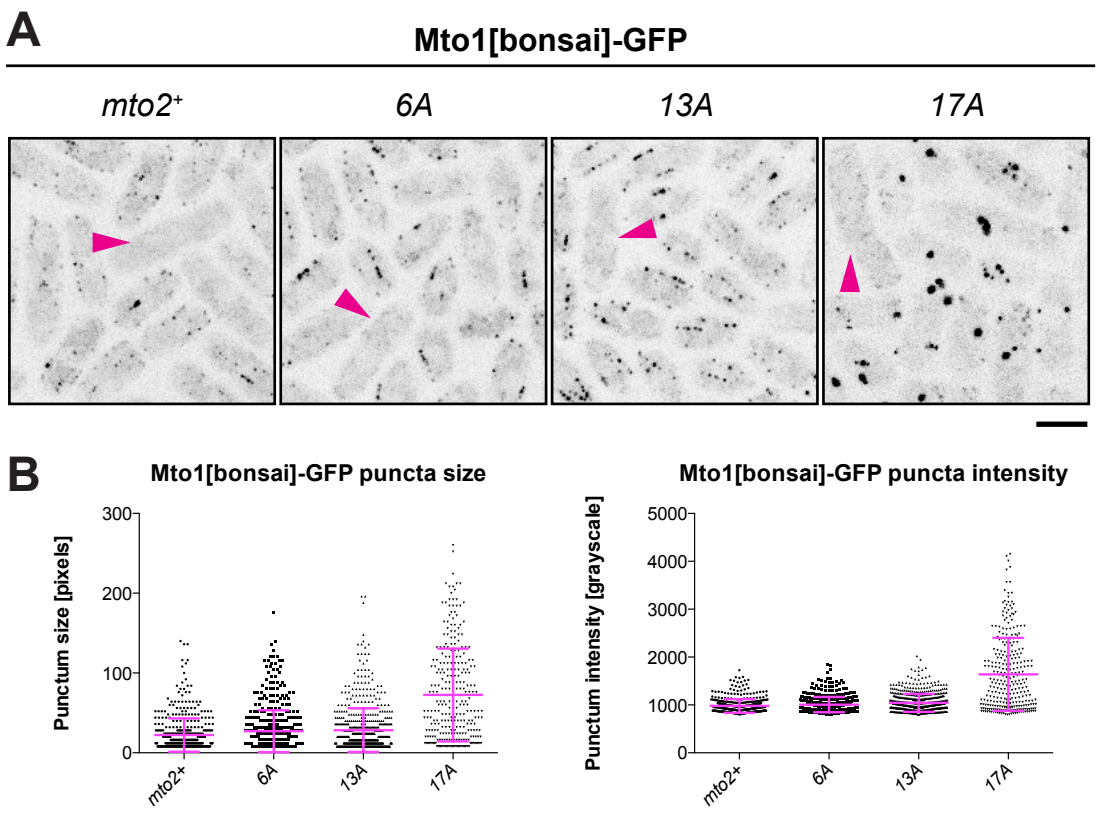

Figure 4.13. Mto1-bonsai-GFP puncta are disassembled in mitosis in wild-type and mto2-alanine cells.
(A) Confocal images of *mto2*$^{+}$ and *mto2-alanine* cells expressing Mto1[bonsai]-GFP. Interphase Mto1[bonsai]-GFP localisation in *mto2-alanine* cells resembles localisation in wild-type cells, with the exception of *mto2-17A* background, where Mto1[bonsai]-GFP forms large aggregates. In mitosis, Mto1[bonsai]-GFP puncta are disassembled in wild-type and mutant cells (mitotic cells are indicated with magenta arrowheads).
(B) Size and intensity of puncta observed in (A) were quantified using Metamorph software. For each strain, puncta within a single imaging field were analysed. Magenta bars indicate the average puncta size or intensity and SEM.
Bar, 5 µm. [Strains (number of puncta analysed): KS5922 (485), KS6434 (652), KS6440 (520), KS6600 (292)]

This experiment suggests that Mto2 phosphorylation negatively regulates either the Mto1-Mto2 or the Mto2-Mto2 interaction, and abolition of Mto2 phosphorylation leads to an increased size of Mto1/2[A] complexes i*n vivo*.

Table 4.8. Comparison of Mto1[bonsai]-GFP puncta size in *mto2*$^{+}$ and *mto2[alanine]* cells. Wilcoxon rank-sum test was used for comparison between each mutant (Mann and Whitney, 1947). P values are shown.

	WT	6A	13A
17A	2.2E-16	2.2E-16	2.2E-16
13A	5.115E-06	0.1994	
6A	0.001723		

Table 4.9. Comparison of Mto1[bonsai]-GFP puncta intensity in *mto2*$^{+}$ and *mto2[alanine*] cells. Wilcoxon rank-sum test was used for comparison between each mutant (Mann and Whitney, 1947). P values are shown.

	WT	6A	13A
17A	2.2E-16	2.2E-16	2.2E-16
13A	3.516E-10	7.947E-04	
6A	0.00236		

4.2.14 Mto1[bonsai]-GFP puncta disappear in mitosis in *mto2[alanine]* cells

Upon mitotic entry, Mto1[bonsai]-GFP puncta disassemble, and after anaphase they reassemble (Lynch PhD Thesis, 2012). I hypothesised that because the Mto1-Mto2 interaction is maintained in *mto2[alanine]* mutants, the Mto1/2[bonsai]-GFP puncta might be observed throughout the cell cycle in these cells. This was not observed in *mto1-GFP* or *mto1[NE]-GFP* backgrounds; however, in these background the Mto1/2 complex was localised to MTOCs, which potentially could facilitate its disassembly. I used live-cell imaging to observe Mto1[bonsai]-GFP in mitotic *mto2[alanine]* cells (Fig. 4.13 A).

Examination of mitotic cells revealed that the Mto1/2 complex disassemble in *mto2[alanine]* strains upon mitotic entry, as demonstrated by the disappearance of Mto1[bonsai]-GFP puncta. This showed that the complex is subject to cell cycle regulation in *mto2[alanine]* cells, despite the maintenance of the Mto1-Mto2 interaction in mitosis.

4.2.15 Mto2 self-interaction is regulated in the cell cycle

Mto2 multimerisation has been suggested to be the driving force of the Mto1/2 complex assembly, as it occurs independently of Mto1, both *in vitro* and *in vivo* (Lynch PhD Thesis 2012). *In vivo*, the role of Mto2 phosphorylation could therefore be to control not only the Mto1-Mto2 interaction but also the Mto2-Mto2 self-interaction.

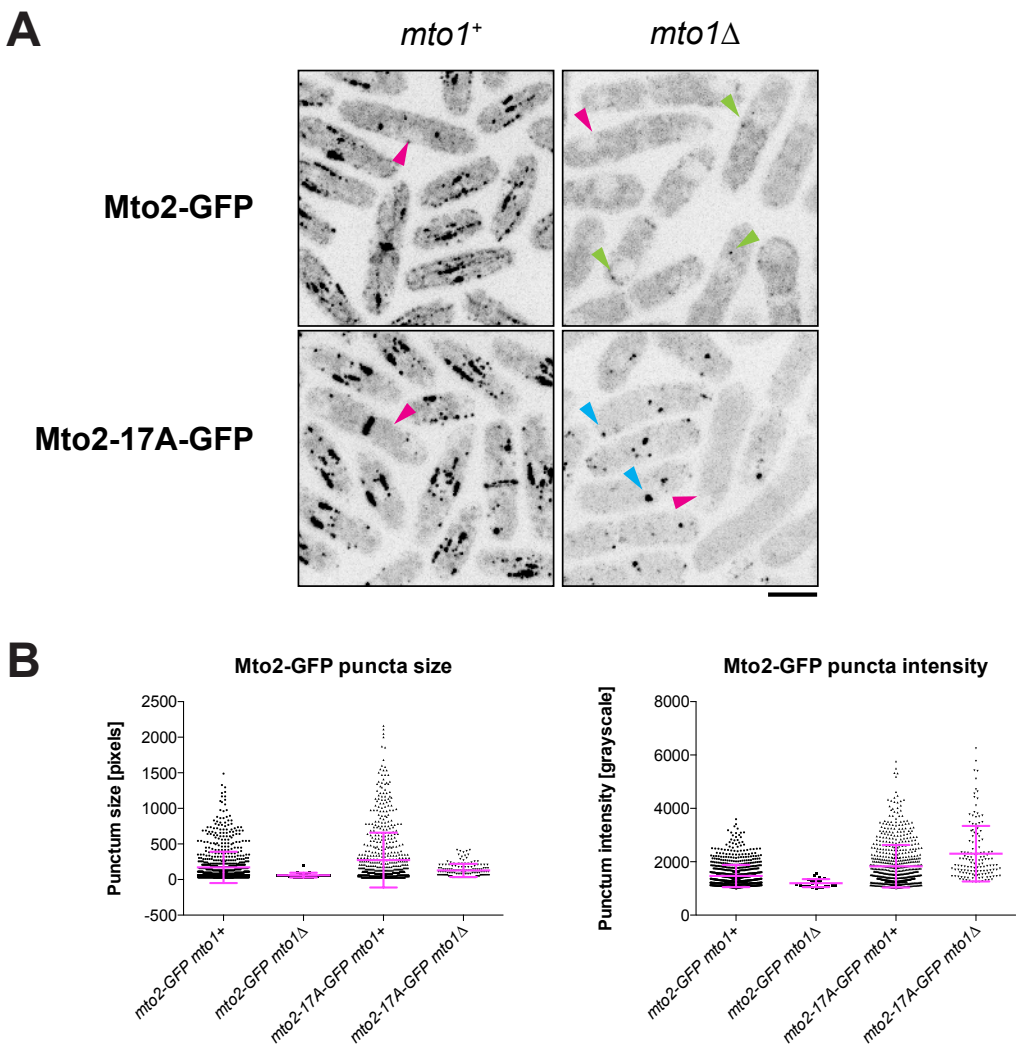

Figure 4.14. Mto2-17A-GFP forms puncta in the absence of Mto1 in a cell cycle-regulated manner.
(A) Mto2-GFP and Mto2-17A-GFP were imaged in *mto1*$^+$ and *mto1*Δ backgrounds. In *mto1*$^+$ background, both Mto2-GFP and Mto2-17A-GFP were observed on the NE, SPBs, MTs and eMTOCs. A small number of faint Mto2-GFP puncta (indicated with green arrowheads) was still observed in *mto2-GFP mto1*Δ cells. Mto2-17A-GFP in *mto1*Δ cells formed large puncta (blue arrowheads) that were absent from mitotic cells (mitotic cells are indicated with magenta arrowheads).
(B) Size and intensity of puncta observed in (A) were quantified using Metamorph software. For each strain, puncta within a single imaging field were analysed. Magenta bars indicate the average puncta size or intensity and SEM.
Bar, 5 μm. [Strains (number of puncta analysed): KS1459 (25), KS7081 (909), KS7099 (704), KS7158 (142)]

To investigate how the abolishment of *in vivo* Mto2 phosphorylation affects Mto2-Mto2 self-interaction, I used live cell imaging of Mto2-17A-GFP and Mto2-GFP (as a control) in *mto1*$^+$ and *mto1*Δ backgrounds (Figure 4.14). *mto2-17A* cells were specifically selected for imaging, because they were expected to exhibit a more evident phenotype than *mto2-13A* or *mto2-6A* cells. First, in tandem affinity tag

pulldown experiments, the Mto1/2 complex in *mto2-17A* cells pulled down more γ-tubulin than in *mto2*$^{+}$*, mto2-6A* and *mto2-13A* cells. Second, puncta formed by Mto1[NE]-GFP and Mto1[bonsai]-GFP in *mto2-17A* cells were much bigger than puncta formed in *mto2*$^{+}$*, mto2-6A* and *mto2-13A* cells.

As shown before, Mto2-GFP localised to the NE, along pre-existing MTs, to SBS and eMTOCs, reminiscent of Mto1-GFP (Fig. 4. 14 A). When imaged in *mto1*Δ background, rapidly diffusing Mto2-GFP puncta were observed, suggesting that Mto2-GFP can self-interact independently of Mto1. Mto2-17A-GFP imaged in *mto1*$^{+}$ cells exhibited mostly wild-type localisation pattern, showing slightly reduced MT localisation with simultaneous increased localisation in the vicinity of the NE. In *mto1*Δ cells, however, Mto2-17A-GFP, unlike wild-type Mto2-GFP, formed large aggregates (Fig. 4.14). This further supports the idea that Mto2 can self-interact in the absence of Mto1 and suggests that this interaction is negatively regulated by phosphorylation.

Mto2-GFP and Mto2-17A-GFP puncta size and intensity were measured (Fig. 4.14 B). Mto2-GFP puncta were smaller, less intense and abundant in *mto1*Δ cells compared to *mto1*$^{+}$ cells (Tables 4.10 and 4.11). This was also seen in Mto2-17A-GFP puncta, which were of comparable size but were more intense and much more abundant in *mto1*$^{+}$ cells than in *mto1*Δ*.* This shows that although Mto2 self-interaction occurs in the absence of *mto1* function in *mto2[alanine]* cells, the presence of Mto1 is needed to form a stable higher order structure. When Mto2-17A-GFP was compared to Mto2-GFP, an increase in both puncta size and intensity was observed, suggesting that Mto2 self-interaction is negatively regulated by Mto2 phosphorylation and this happens independently of Mto1 or Mto1/2 localisation to any conventional MTOCs.

Mto2-17A-GFP aggregates formed in *mto1*$^{+}$ cells resembled those formed by Mto1[bonsai]-GFP in *mto2-17A* cells (see Fig. 4.13). Presumably, in both cases they formed as a result of Mto2 self-interaction much stronger than in wild-type cells. In *mto1* and *mto1[NE]* cells, formation of such aggregates might be prevented by the presence of Mto1 molecules larger than in *mto1[bonsai]* cells (that is, the presence of the Mto1 N- or C-terminus), or by localisation of the Mto1/2 to conventional MTOCs (which might impose some structural limitations on the complex size or architecture).

In *mto1*Δ cells, Mto2-17A-GFP aggregates are absent from mitotic cells (Fig. 4.14 A). This result shows that Mto2 self-interaction is abolished in mitosis

independently of any interaction with Mto1. Therefore, in the wild-type Mto1/2 two interactions are disrupted: the Mto1-Mto2 interaction and the Mto2 self-interaction. In *mto2[alanine]* cells, the Mto1-Mto2 interaction is maintained throughout the cell cycle; the Mto2-Mto2 interaction is disrupted. Presumably, this mitotic disruption of Mto2-Mto2 self-interaction is what leads to the mitotic disassembly of the Mto1/2 complex.

Table 4.10. Comparison of Mto2-GFP and Mto2-17A-GFP puncta size in *mto1*$^+$ and *mto1*Δ cells. Wilcoxon rank-sum test was used for comparison between each mutant (Mann and Whitney, 1947). P values are shown.

	mto2-GFP	***mto2-GFP mto1*Δ**	***mto2-17A-GFP***
***mto2-17A-GFP mto1*Δ**	0.136	7.112E-05	0.496
mto2-17A-GFP	0.0002202	0.0006014	
***mto2-GFP mto1*Δ**	0.005636		

Table 4.11. Comparison of Mto2-GFP and Mto2-17A-GFP puncta intensity in *mto1*$^+$ and *mto1*Δ cells. Wilcoxon rank-sum test was used for comparison between each mutant (Mann and Whitney, 1947). P values are shown.

	mto2-GFP	***mto2-GFP mto1*Δ**	***mto2-17A-GFP***
***mto2-17A-GFP mto1*Δ**	2.2E-16	1.198-13	8.03E-12
mto2-17A-GFP	2.2E-16	1.225E-08	
***mto2-GFP mto1*Δ**	9.269E-05		

4.2.16 Lambda phosphatase treatment confirms that Mto2-17A is phosphorylated in mitosis

In the previous section (4.2.14) I showed that the Mto2-Mto2 self-interaction is disrupted in mitosis in *mto2-17A-GFP* cells independently of Mto1. Experiments presented in Section 4.2.3 suggested that Mto2-17A is phosphorylated in mitosis, as there was a small but detectable migration shift observed in mitotic vs. interphase extracts. If Mto2-17A were indeed phosphorylated in mitosis, this phosphorylation might be the driver for disruption of the Mto2-Mto2 self-interaction observed in *mto2-17A-GFP mto1*Δ cells.

To further confirm phosphorylation of Mto2-17A in mitosis, protein extracts from asynchronous and metaphase-arrested cells were incubated with active or heat-inactivated λ-phosphatase in the presence or absence of phosphatase inhibitors (Fig. 4.15, lanes 9-16). Extracts from *mto2*$^+$ cells were used as a control (Fig. 4.15 lanes 1-8). The phosphatase treatment on wild-type Mto2 confirmed it is

phosphorylated both in interphase and mitosis. When the interphase Mto2 extract was treated with phosphatase, nearly Mto2 isoforms collapsed to a single, fast migrating band (lane 2). This was not observed when heat-inactivated phosphatase was used, however, some Mto2 dephosphorylation did occur, possibly by the action of endogenous phosphatases present in extracts (lane 3); the dephosphorylation was also incomplete when active phosphatase was used in the presence of phosphatase inhibitors (lane 4). When the mitotic Mto2 extracts were treated with an active phosphatase, slower migrating Mto2 isoforms were converted into much faster migrating isoforms, although they did not collapse into a single band (lane 6). This may be due to using an insufficient amount of phosphatase in experiments. In *mto2-17A* extracts, both interphase and mitotic Mto2-17A changed migration velocity upon phosphatase treatment (lanes 10 and 14), although this was much more prominent in the mitotic extract (lane 14). The disappearance of slower migrating isoforms was also observed in samples treated with a heat-inactivated phosphatase (lane 15), where the dephosphorylation occurred presumably due to endogenous phosphatases activity. This result shows that Mto2-17A is phosphorylated in mitosis.

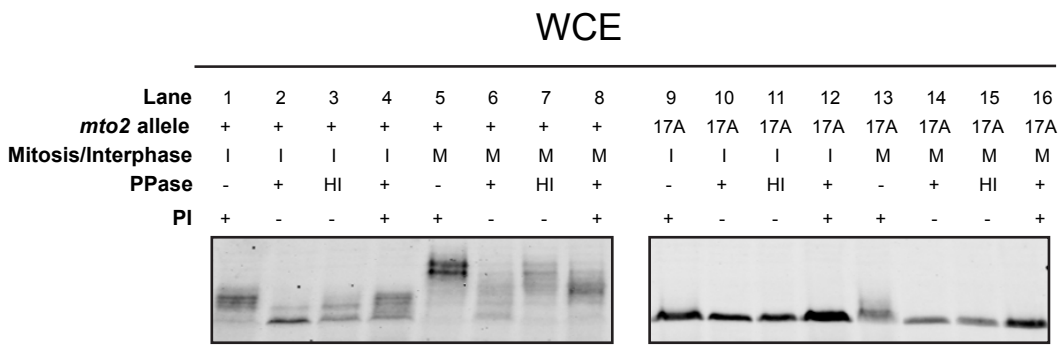

Figure 4.15. λ-protein phosphatase treatment on Mto2-17A confirms that Mto2-17A-GFP is phosphorylated in mitosis.
Total protein extract from asynchronous and metaphase-arrested *nda3-KM311* cells were incubated with active or heat-inactivated [HI] λ-PPase with or without PPase inhibitors [PI]. Western blots were probed with anti-Mto2 antibody. [Strains: KS3575, KS6742]

This result, collectively with results presented in previous chapters, suggested a hypothesis that in wild-type cells, Mto2 phosphorylation may lead to the Mto1/2 complex disassembly by disruption of both Mto1-Mto2 and Mto2-Mto2

interactions. In *mto2[alanine]* cells, the mitotic disruption of the Mto1-Mto2 interaction is abrogated. However, the mitotic disruption of the Mto2-Mto2 self-interaction still occurs. As Mto2 is phosphorylated in *mto2-17A* cells, I hypothesise that the phosphorylation of Mto2-17A leads to disruption of the Mto2 self-interaction and consequently – to the disassembly of the Mto1/2 complex. This will be further investigated in Chapter 5.

4.3 Discussion

Evidence presented in this chapter elucidates many roles of Mto2 phosphorylation in cell cycle regulation of the Mto1/2 complex and MT nucleation in fission yeast. Using a combination of biochemical assays and live-cell imaging, I demonstrated that Mto2 phosphorylation regulates the Mto1/2 complex MT nucleation activity in interphase and contributes to its disassembly in mitosis. The interphase regulation is achieved by regulation of interactions within the Mto1/2 complex as well as by regulation of the interaction between the Mto1/2 and the γ-TuC. In mitosis, Mto2 phosphorylation leads to the disruption of the Mto1-Mto2 interaction, and potentially, the Mto2 self-interaction. The role of Mto2 phosphorylation in the regulation of the Mto2-Mto2 self-interaction will be investigated in Chapter 5.

4.3.1 Mto2 phosphorylation acts as a dial to fine-tune cytoplasmic MT nucleation levels in interphase

In the research presented in this chapter, several independent observations suggest that Mto2 phosphorylation negatively regulates the Mto1-Mto2 interaction and the Mto2 self-interaction *in vivo.*

First, the amount of wild-type Mto2 co-precipitated by Mto1-TAPS increased in G1/S, when Mto2 is hypophosphorylated, suggesting that the Mto1-Mto2 interaction is stronger when Mto2 is hypophosphorylated. Importantly, abolition of Mto2 phosphorylation in *mto2[alanine]* mutants, in which various numbers of phosphorylatable residues within Mto2 were replaced with alanine to prevent phosphorylation, led to maintenance of the Mto1-Mto2 interaction in mitosis (discussed in more detail in the following section), suggesting that Mto2 phosphorylation leads to disruption of this interaction in wild-type cells.

Second, live-cell imaging of GFP-tagged *mto1*, *mto1[NE]* and *mto1[bonsai]* in *mto2[alanine]* cells demonstrated that abolition of Mto2 phosphorylation results in formation of bigger Mto1/2[A] complexes. The size and/or the intensity of Mto1-GFP, Mto1[NE]-GFP and Mto1[bonsai]-GFP puncta increased with the increasing number of alanine substitutions in Mto2 sequence, suggesting that the Mto1/2 complex size is regulated by Mto2 phosphorylation. The Mto1/2[A] complex size increase was especially evident in *mto2-17A mto1[bonsai]* cells where Mto1/2 complex aggregates were 2-3 times bigger than complexes observed in *mto2*$^{+}$ cells. The increase in puncta size and intensity could be a result of an increased affinity of Mto2 to Mto1, or to itself or a combination of both.

Third, imaging of Mto2-GFP (as a control) and Mto2-17A-GFP in the absence of Mto1 showed that Mto2 phosphorylation negatively regulates the Mto2 self-interaction independently of Mto1. Puncta formed by Mto2-17A-GFP in *mto1*Δ cells were bigger and more abundant than those of Mto2-GFP in *mto1*Δ. The increase in puncta size and intensity suggests that Mto2 self-affinity increased in *mto2-17A* cells as compared to *mto2*$^{+}$. Similar puncta were observed in *mto2-17A mto1[bonsai]* cells, but not in *mto1*$^{+}$ or *mto1[NE]* cells, suggesting that the presence of Mto1 or Mto1[NE] prevented formation of large aggregates in *mto2-17A* cells. This could potentially be achieved by localising the Mto1/2 complex to conventional MTOCs, which might impose some structural limitations on the complex size. The observation that Mto2-17A in *mto1[bonsai]* and *mto1*Δ cells forms similarly sized puncta suggests that the observed increase in size of Mto1/2[A] complexes with an increasing number of alanine substitutions is due to increasing Mto2 self-affinity rather than increasing affinity of Mto2 to Mto1.

Overall, these observations suggest that the Mto1-Mto2 and the Mto2-Mto2 interactions are regulated by Mto2 phosphorylation by two different mechanisms (Fig. 4.16). *In vivo,* the Mto1-Mto2 interaction is controlled by a switch-like mechanism; the abolition of Mto2 phosphorylation leads to maintenance of the Mto1-Mto2 interaction in mitosis. By contrast, the Mto2-Mto2 self-interaction appears to be controlled by a dial-like mechanism, in which Mto2 phosphorylation regulates the steady-state multimerisation state of Mto2. The less phosphorylated Mto2 is, the more stable the Mto2 self-interaction is, leading to formation of stable higher-order Mto2 assembles. This is in agreement with *in vitro* data that shows that Mto2, unlike Mto1[bonsai], is in a dynamic equilibrium between Mto2 multimers of various sizes (Lynch PhD Thesis, 2012).

It would be interesting to see how Mto2-6A-GFP and Mto2-13A-GFP proteins behave in the absence of Mto1. Based on presented data, I predict the puncta size and intensity would increase with increasing number of alanine substitutions.

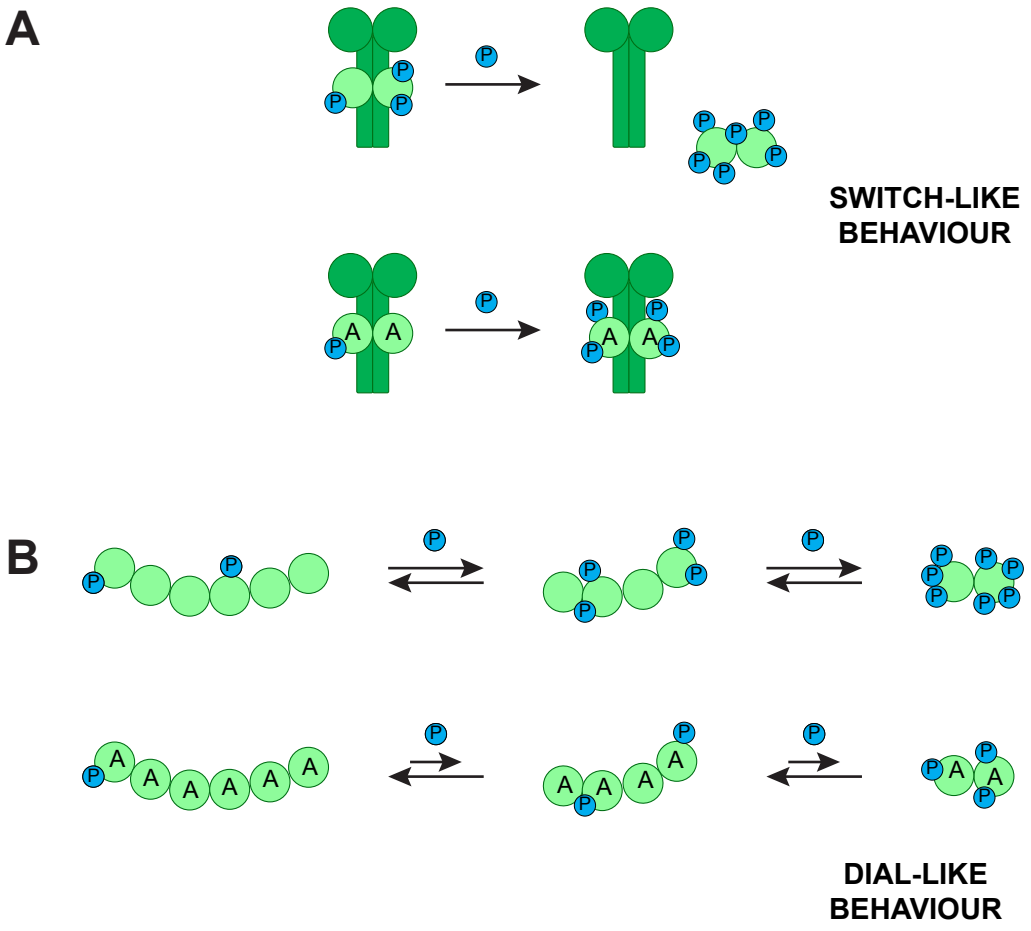

Figure 4.16. Mto2 phosphorylation regulates Mto1-Mto2 interaction and Mto2-Mto2 self-interaction *in vivo*.
(A) The interaction between Mto1 and Mto2 is regulated by phosphorylation in a switch-like manner. In wild-type cells, phosphorylation of Mto2 leads to abolition of the Mto1-Mto2 interaction. In *mto2[alanine]* cells, even partial abolition of Mto2 phosphorylation abrogates the Mto1-Mto2 interaction disruption.
(B) Mto2 self interaction is regulated by phosphorylation by a dial-like mechanism. In cells, Mto2 exist in a form of a mixture of oligomers in a dynamic equilibrium. Phosphorylation decreases Mto2 self-affinity shifting the equilibrium toward smaller oligomers. In *mto2[alanine]* cells, this equilibrium is shifted towards higher-order Mto2 assemblies.
Mto1 is shown in dark green and Mto2 in light green. A, Mto2-alanine.

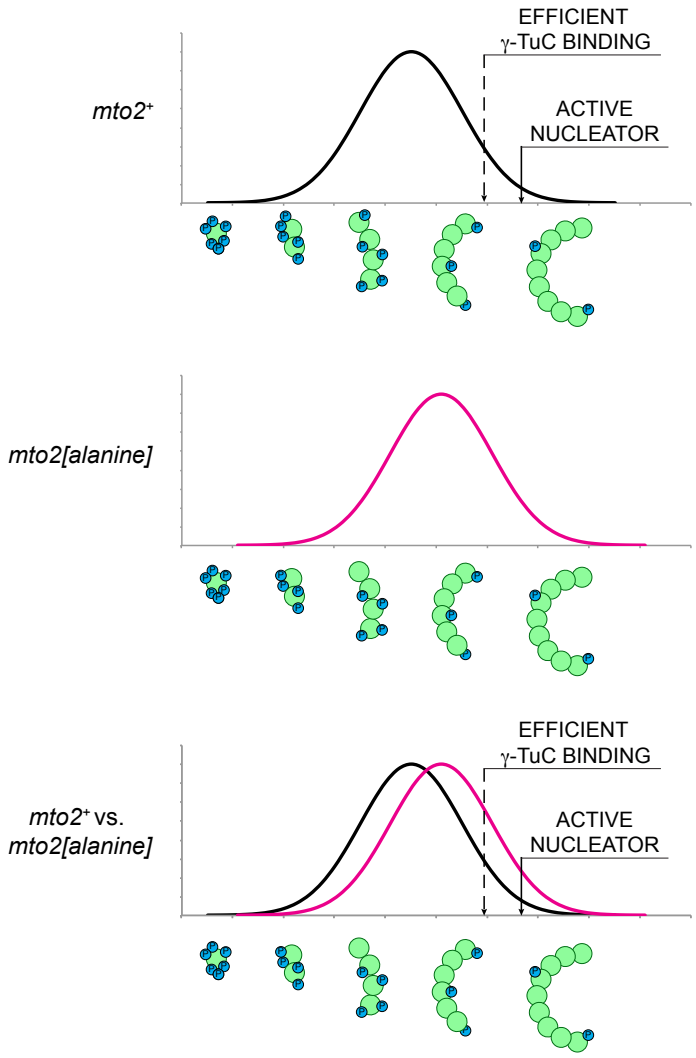

Figure 4.17. Model of how Mto1/2 complexes in *mto2[alanine]* cells are better MT nucleators.
Mto1 is not shown for simplicity. Wild-type (*mto2*$^+$) Mto1/2 complex exists in a dynamic equilibrium between complexes with various degrees of multimerisation. Potentially, only after reaching a critical size it is able to bind the γ-TuC and promote MT nucleation. Since Mto2 self-interaction is negatively regulated by phosphorylation, abolition of Mto2 phosphorylation results in shifting the equilibrium towards higher-order assemblies (*mto2[alanine]*). Therefore, higher proportion of the total Mto1/2 pool reaches the critical size required for γ-TuC binding and MT nucleation, leading to an increased amount of Gtb1 interacting with the Mto1/2 and an increased MT nucleation frequency in *mto2[alanine]* cells.

I also showed that in the Mto1/2[A] complex is a better MT nucleator than the Mto1/2 complex in wild-type cells. GFP-α-tubulin imaging revealed that *mto2[alanine]* cells contained more MT bundles and nucleated MTs more frequently than wild-type cells. This increase in nucleation frequency might be explained by a stronger the interaction between the Mto1/2 complex and the γ-TuC in *mto2[alanine]* cells compared to *mto2*$^+$ observed biochemically. In pulldown experiments,

Mto1/2[A] complexes co-precipitated more γ-tubulin than wild-type Mto1/2 complex, showing that Mto2 phosphorylation regulates the γ-TuC-Mto1/2 interaction. This regulation might be direct – whereby the Mto2-γ-TuC interaction surface is phosphorylated to reduce the affinity of Mto2 to the γ-TuC, or indirect – whereby the phosphorylation of Mto2 decreases the size of the multimeric Mto1/2 complex, and because only Mto1/2 complexes above certain size are able to stably bind the γ-TuC, it also decreases the frequency of nucleation events. This is in agreement with *in vivo* and *in vitro* biochemical data showing that the Mto1/2 complex exists as a mixture of Mto1/2 multimers in a dynamic equilibrium (Lynch PhD Thesis 2012). Size exclusion chromatography of Mto1/2[bonsai] from insect cells showed that the complex eluted as a very broad peak containing complexes of sizes ranging from 75 kDa to 800 kDa (Lynch PhD Thesis, 2012). Potentially, abolition of Mto2 phosphorylation shifts the equilibrium towards higher-order structures, which allows for more efficient γ-TuC binding and more frequent MT nucleation (Fig.4.17).

I also provided evidence that the PAA formation is advanced in *mto2[alanine]* cells. In *mto2[alanine]* cells, live-cell imaging of GFP-α-tubulin showed that eMTOC-derived MTs were observed at shorter spindle lengths as compared to *mto2*$^{+}$cells. This could be explained by the lower level of mitotic phosphorylation of Mto2[alanine] mutant proteins. After anaphase, the Mto1/2 complex reassembles and localises to the eMTOC to facilitate the PAA formation (Samejima et al., 2005, 2008). In *mto2[alanine]* cells, Mto2 mitotic phosphorylation is much less prominent than in *mto2*$^{+}$ cells, therefore requiring removal of a lower number of phosphate groups in order to achieve an interphase Mto2 phosphorylation state. This presumably enables the advanced Mto1/2[A] complex re-assembly, either because a lower phosphatase activity is sufficient to remove phosphate groups (therefore, the dephosphorylation is initiated earlier in the cell cycle) or because the removal of phosphate groups is completed in a shorter time (therefore, the dephosphorylation is initiated at the same cell cycle stage, but completed earlier) (Fig. 4.18).

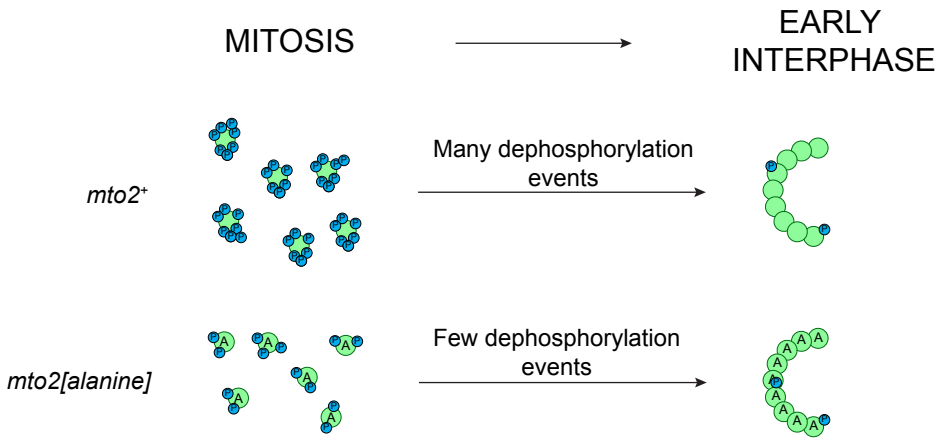

Figure 4.18. Post-mitotic re-assembly of the Mto1/2 complex is advanced in *mto2[alanine]* cells resulting in premature PAA formation.
In mitosis, Mto2 is hyperphosphorylated and the Mto2-Mto2 interaction is disrupted in wild-type (*mto2*$^+$) cells. Upon mitotic exit, hyperphosphorylated Mto2 needs to be dephosphorylated in order to be able to interact with Mto1 and itself. In *mto2[alanine]* cells, Mto2[alanine] is phosphorylated to a lesser extent than wild-type Mto2; therefore, the removal of phosphate groups can be achieved earlier in the cell cycle.

These findings collectively suggest a model in which Mto2 phosphorylation modulates Mto1/2-dependent MT nucleation throughout interphase (Fig 4.19). According to the model presented in Fig 4.17, Mto2 phosphorylation could regulate the multimeric state of the Mto1/2 complex. When Mto2 is highly phosphorylated, the equilibrium shifts towards smaller multimers, leading to a decreased cytoplasmic nucleation. When Mto2 is hypophosphorylated, the equilibrium shifts towards higher-order multimers, leading to an increased MT nucleation frequency. This mechanism could be also used to control the nucleation frequency from a specific MTOC, where differently localised kinases or phosphatases could control the Mto1/2-promoted nucleation by locally phosphorylating or dephosphorylation Mto2 at various MTOCs. This, however, seems to be unlikely, given that the interphase Mto2 phosphorylation state observed biochemically does not change in different *mto1* backgrounds (*mto1*Δ*, mto1*$^+$*, mto1[NE], mto1[bonsai]*) in which the Mto1/2 complex localises differently.

Overall, in this chapter I provided evidence that Mto2 phosphorylation negatively regulates the Mto1/2 complex MT nucleation activity in interphase. This is achieved by regulating the interaction of the Mto1/2 complex with the γ-TuC as well as by regulation of interactions within the Mto1/2 complex (that is, the Mto1-Mto2 interaction and the Mto2 self-interaction).

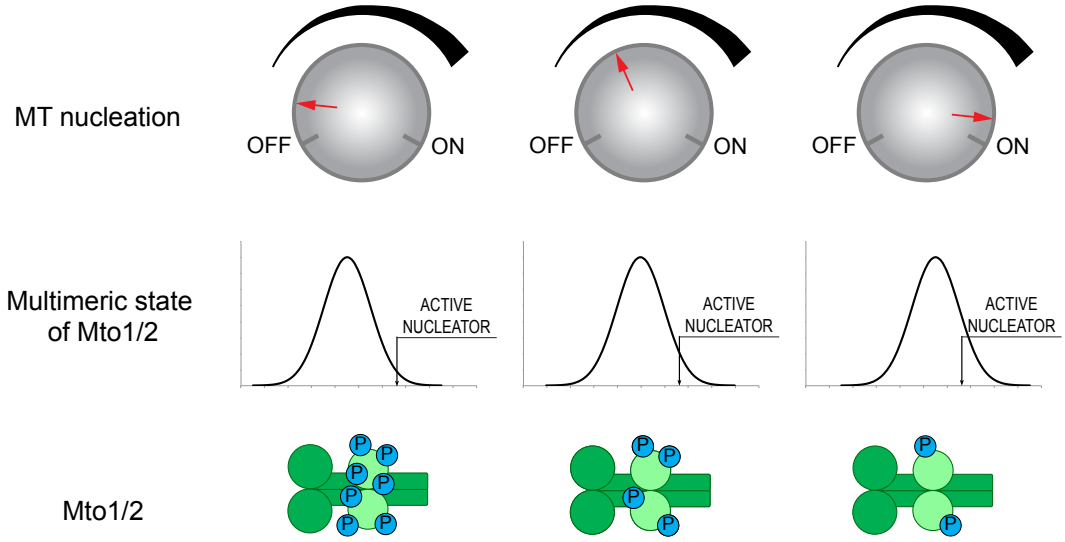

Figure 4.19. Mto2 phosphorylation negatively regulates interphase MT nucleation.
The Mto1/2 complex exists in as a mixture of multimers of various sizes, and only multimers above certain size can promote MT nucleation. Dephosphorylation of Mto2 shifts the equilibrium towards bigger multimers, therefore, more of the total Mto1/2 complexes can promote MT nucleation. This leads to an increased MT nucleation frequency.
Mto1 is shown in dark green and Mto2 in light green.

4.3.2 Mto2 phosphorylation plays a role in regulation of the interaction between the Mto1/2 complex and its NE receptor

Imaging of *mto2[alanine]* cells suggested that Mto2 phosphorylation modulates Mto1/2 complex localisation to the NE during interphase. Mto1[NE]-GFP was enriched at the NE in *mto2[alanine]* cells as compared to wild-type. Similarly, Mto2-17A-GFP was enriched at the NE when compared to Mto2-GFP. Mto2 phosphorylation can contribute to the Mto1/2 localisation to the NE in at least two ways. First, the NE enrichment might be a result of a direct regulation, whereby the lack of Mto2 phosphorylation strengthens the interaction between Mto2 and its NE receptor. This is, however, unlikely, as Mto2 does not localise to the NE in the absence of Mto1. The second, perhaps more plausible explanation is that the NE enrichment might be an indirect effect of increased stability of the Mto1/2 complex, leading to a more stable interaction with the NE receptor. Possibly, the interaction with the NE receptor of the Mto1/2 complex might only occur when higher-order assemblies of the Mto1/2 complex are formed. According to the model presented in

Fig. 4.17, in *mto2[alanine]* cells higher-order Mto1/2 multimers are more abundant than in wild-type cells, which could lead to an increased NE localisation.

It was recently suggested that the enhanced Mto1/2 localisation to the NE in *mto1[NE]* cells is a result of abolishment of competition for the Mto1/2 complex between the NE and higher affinity (or more numerous) other MTOC sites, such as SPBs or the MT lattice (Lynch PhD Thesis 2012). The NE was hypothesised to contain either lower affinity receptors of the Mto1/2 complex, or a smaller number of those. Since abolishment of Mto2 phosphorylation leads to an increased NE localisation, it seems more plausible that there are many lower affinity sites at the NE rather than fewer sites of higher affinity. This is in agreement with the observation that simultaneous overexpression of Mto1[NE]-GFP and Mto2 leads to a complete NE decoration by the Mto1/2 (Groocock PhD Thesis, 2010), suggesting that Mto1/2 receptors are abundant at the NE.

4.3.3 Mto2 phosphorylation acts as a switch to abolish cytoplasmic MT nucleation in mitosis

My main objective in this chapter was to elucidate the role of Mto2 phosphorylation in the abolishment of non-SPB cytoplasmic nucleation in mitosis. We hypothesised that the mitotic phosphorylation of Mto2 leads to the Mto1/2 complex disassembly by disruption of the Mto1-Mto2 interaction.

I confirmed at least part of this hypothesis, by showing that in *mto2[alanine]* cells, unlike wild-type cells, the interaction between the Mto1 and Mto2[alanine] proteins is maintained in mitosis. Mutating as few as six phosphorylatable residues to alanines allowed for maintenance of the Mto1-Mto2 interaction throughout the cell cycle, even though the abolishment of mitotic phosphorylation was not complete. This shows that Mto1-Mto2 interaction is regulated by a switch-like mechanism (Fig. 4.16).

However, imaging of Mto1[NE]-GFP and Mto1[bonsai]-GFP revealed that the Mto1/2[A] complex disassembles in mitosis, despite the maintenance of the Mto1-Mto2 interaction. This suggested that the Mto1/2 complex disruption in mitosis is due to disruption of the Mto2-Mto2 interaction, as well as the Mto1-Mto2 interaction.

Indeed, imaging of Mto2-17A-GFP in *mto1*Δ cells showed that Mto2-17A-GFP forms aggregates that disassemble upon mitotic entry, confirming that the

Mto2 self-interaction is disrupted in mitosis independently of Mto1. Comparison of Mto2-GFP and Mto2-17A-GFP in interphase *mto1*Δ cells demonstrated that the size of GFP puncta dramatically increased in *mto2-17A-GFP* cells, providing evidence that phosphorylation regulates Mto2 self-affinity. Phosphatase treatment on mitotic protein extracts confirmed that Mto2-17A is phosphorylated in mitosis. Since I showed that phosphorylation regulates Mto2 self-interaction in interphase, it appears plausible that the Mto2-Mto2 self-interaction is also regulated by phosphorylation in mitosis.

Collectively, those observations suggested a model in which Mto2 phosphorylation contributes to Mto1/2 complex disassembly in two independent ways: by the disruption of the Mto1-Mto2 interaction, and by disruption of Mto2 self-interaction (Fig. 4.20).

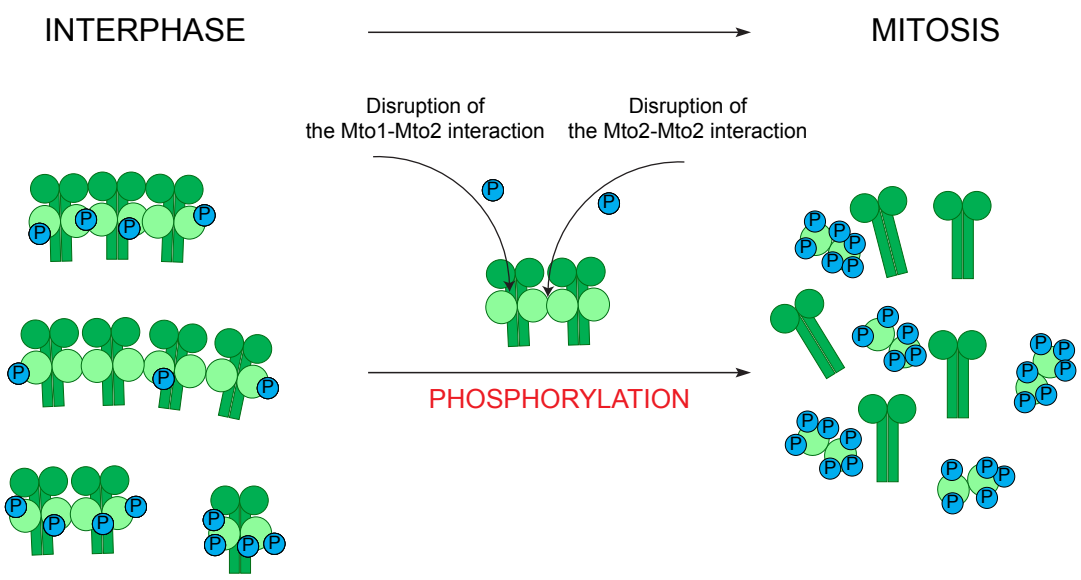

Figure 4.20. Model of the Mto1/2 complex disruption upon mitotic entry.
In interphase, the Mto1/2 complex multimerises to different extents, depending on the phosphorylation state of Mto2. Upon mitotic entry, both the Mto1-Mto2 interaction and the Mto2 self-interaction are disrupted by phosphorylation, leading to the disassembly of Mto1/2 multimers.
Mto1 is shown in dark green and Mto2 in light green.

I hypothesised that the Mto1/2 complex disruption at mitotic entry is a result of Mto2 phosphorylation resulting in abolishment of not only the Mto1-Mto2 interaction, but also the Mto2 self-interaction. This hypothesis will be investigated in

the following chapter, where I will aim to identify and mutate crucial mitosis-specific phosphorylation sites (beyond those mutated in Mto2-17A). I will do that by comparing interphase and mitotic protein extracts, with the hope to generate Mto2 phosphomutants in which both the Mto1-Mto2 interaction and the Mto2-Mto2 self-interaction would persist in mitosis.

Chapter 5
Identification and mutagenesis of mitosis-specific phosphorylation sites in Mto2-17A

5.1 Introduction

The results presented in Chapter 4 elucidated the many roles that Mto2 phosphorylation plays in regulation of MT nucleation in both interphase and mitosis. I showed that in *mto2-17A* cells, unlike in wild-type cells, the Mto1-Mto2 interaction is maintained in mitosis. However, both in *mto2*$^{+}$ and *mto2-17A* cells the Mto2 self-interaction is lost in mitosis, presumably leading to the Mto1/2 complex mitotic disassembly. Because phosphatase treatment of Mto2-17A showed that the protein is phosphorylated upon mitotic entry, I hypothesised that mitotic phosphorylation of Mto2-17A may lead to disruption of the Mto2 self-interaction. In this chapter I attempted to test this hypothesis by generating a "completely non-phosphorylatable" Mto2 phosphovariant.

In order to identify mitosis-specific phosphorylation sites, I used the SILAC technique (Stable Isotope Labelling of Amino acids in Cell culture), which allowed me to distinguish between phosphopeptides originating from asynchronous and metaphase-arrested cultures. SILAC is a quantitative proteomics method that was developed in Matthias Mann's group (Ong et al., 2003, 2002) and involves growing cells in either conventional growth medium (leading to "light" protein synthesis) or in growth medium in which some amino acids were replaced by their (non-radioactive) isotopically-labelled counterparts (leading to "heavy" protein synthesis). Lysine and arginine are commonly used for labelling of heavy samples in SILAC, because trypsin, the protease most commonly used to generate peptides, cleaves after these two basic amino acids. Thus, heavy labelling of solely arginine and lysine ensures that all tryptic peptides are labelled with at least one heavy amino acid. Since introducing the method in 2002, SILAC has been used successfully used in many contexts, including mapping protein-protein interactions and phosphorylation sites, quantifying protein translation or and identifying interphase- and mitosis-specific MAPs (Microtubule Associated Proteins) (Gruhler et al., 2005; Guerrero et al., 2006; Schwanhäusser et al., 2009; Syred et al., 2013). Research performed in the Sawin lab has developed a methodology allowing to use SILAC in fission yeast (Bicho et al., 2010).

In SILAC, light and heavy cultures are grown separately and then mixed in 1:1 ratio. The sample processing can be performed on the mixed sample or on separate samples that are then mixed prior to the MS analysis (Fig. 5.1). Peptides originating from heavy and light samples are distinguishable in the MS spectra due to the higher molecular mass observed in heavy-labelled peptides. For example, all peptides from the heavy sample containing $^{13}C_6{}^{15}N_2$-lysine will be shifted 8 Da relative to the same peptides from the light-labelled sample, while peptide containing $^{13}C_6$-arginine will be shifted 6 Da relative to its light counterpart.

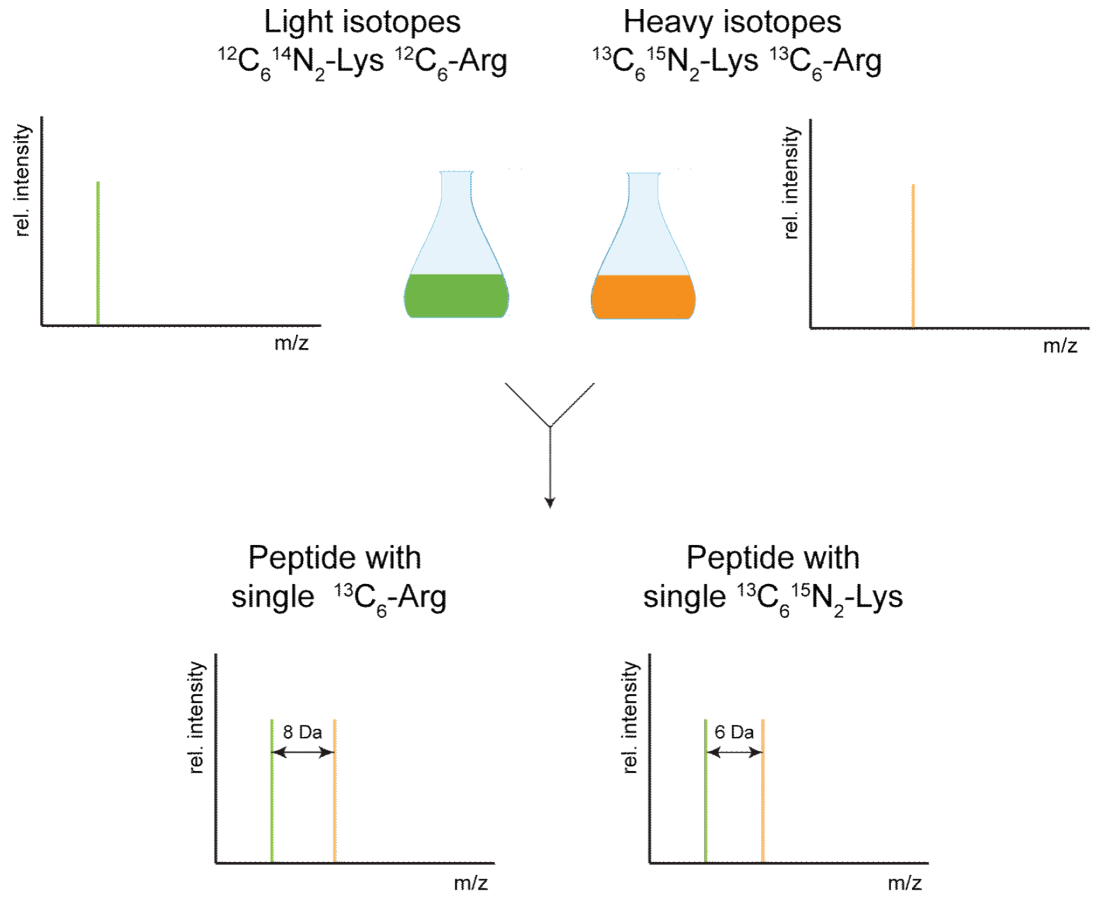

Figure 5.1. SILAC experimental set-up.
In SILAC experiments, two cultures are grown separately in the presence of either light arginine and lysine (green) or heavy lysine and arginine (orange). The cultures are then mixed in 1:1 ratio and the resulting mixture is processed for MS analysis. Peptides originating from two different cultures can be distinguished in the MS spectra due to different molecular masses resulting in m/z shifts. For example, if a heavy peptide contains one molecule of lysine, it will be 8 Da heavier than its light counterpart.

In this chapter, my aim was first, to identify mitosis-specific phosphorylation sites using SILAC, second, to generate completely non-phosphorylatable Mto2 phosphomutants (if this is possible), and third, to analyse the phenotype of such

mutants. To this end, I identified a number of phosphosites in Mto2-17A and used a novel method based on quantification of *unmodified* peptides to identify candidate mitosis-specific phosphorylation sites. I generated a series of *mto2* phosphovariants and identified one of them, *mto2-NT2*, as being essentially completely non-phosphorylatable. Preliminary analysis suggests that Mto2-NT2 is similar to Mto2-17A; however, further analysis will be needed to confirm this.

5.2 Results

5.2.1 Optimisation of SILAC methodology for large-scale immunoprecipitation

During a SILAC experiment heavy and light cultures are mixed and analysed by MS (Fig. 5.1). Because heavy labelled amino acids are considerably expensive, especially for large-scale experiments, I wished to optimise immunoprecipitation conditions to ensure the most cost-effective immunoprecipitation procedure is used.

First, I compared two different types of beads that could be used for immunoprecipitation: anti-GFP coupled Protein G-Dynabeads and GFP-Trap magnetic beads. Dynabeads are routinely used in the Sawin lab for immunoprecipitation, and the preparation of beads for a GFP-immunoprecipitation requires binding of anti-GFP antibodies to the commercially available Protein G-Dynabeads. GFP-Trap beads are commercially available magnetic beads coupled to a GFP-binding protein (GBP) (Rothbauer et al., 2008). The advantage of using GFP-Trap is that the GBP is only 13 kDa, as compared to 55 kDa IgG heavy chain and 25 kDa light chain, and the presence of a smaller protein should interfere less with the MS result. I performed pull-downs using varying amount of both anti-GFP Dynabeads and GFP-Trap (Fig. 5.2 A and B). Anti-Mto2 immunoblotting revealed that anti-GFP Dynabeads immunoprecipitated more of Mto2-GFP relative to GFP-Trap beads. The optimal volume of anti-GFP Dynabeads was between 10 and 20 μL of beads per 1 mL of extract. Given that Dynabeads are much cheaper than GFP-Trap magnetic beads, and that they were easier to handle (that is, separated from the solution quicker than GFP-Trap beads), I decided to use them in all further experiments.

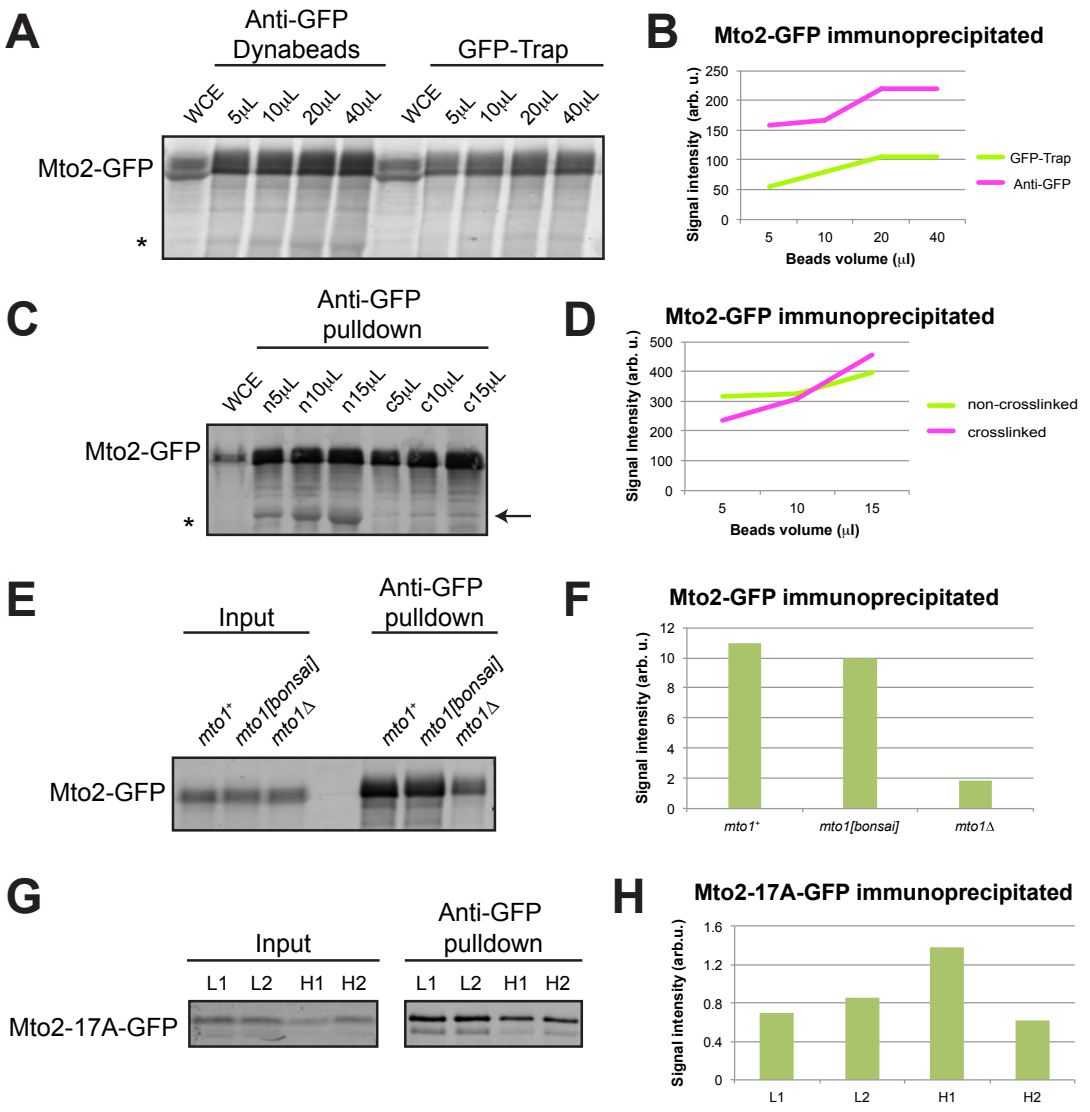

Figure 5.2. Optimisation of immunoprecipitation procedure for SILAC.
(A) Anti-GFP-coupled Protein G-Dynabeads show a better immuprecipitation efficiency than commercial GFP-Trap beads. Extracts were incubated with indicated volumes of anti-GFP-Protein G-Dynabeads or GFP-Trap bead suspension. Following imuprecipitation, western blots were probed against Mto2. *- IgG detected by secondary antibody. **(B)** Quantification of (A). Integrated intensities of IRDye800 were measured using Odyssey V3.0. **(C)** DMP-crosslinked anti-GFP Protein G-Dynabeads immuprecipitate Mto2-GFP as well as non-crosslinked beads. Extracts were incubated with indicated volumes of crosslinked and non-crosslinked anti-GFP-Protein G-Dynabeads. Following imuprecipitation, western blots were probed against Mto2. *- IgG detected by secondary antibody. Note the absence of IgG in the crosslinked fractions. **(D)** Quantification of (C). Integrated intensities of IRDye800 were measured using Odyssey V3.0.
(E) Mto2-GFP immunoprecipitation efficiency is lower in *mto1*Δ cells. Extracts were incubated with anti-GFP-Protein G-Dynabeads. Following imuprecipitation, western blots were probed against Mto2. **(F)** Quantification of (E). Integrated intensities of IRDye800 were measured using Odyssey V3.0. Mto2 signal was normalised to Input.
(G) Mto2-17A-GFP co-immunoprecipitation efficiency is comparable for cells grown in heavy and light medium. Extracts were incubated with anti-GFP-Protein G-Dynabeads. Following imuprecipitation, western blots were probed against Mto2. **(H)** Quantification of (G). Integrated intensities of IRDye800 were measured using Odyssey V3.0. Mto2-17A-GFP signal was normalised to Input.
[Strains: KS7081, KS7093]

Second, when comparing anti-GFP Dynabeads to GFP-Trap I noticed that a significant amount of IgG was observed on western blots of the immunoprecipitates (also by Ponceau S staining, not shown). This raised a possibility that during the MS analysis following large-scale pulldown, the IgG, and not Mto2-17A-GFP, would be the main protein identified in Mto2-17A-GFP samples. An easy way to overcome this problem is to crosslink the anti-GFP antibody to Dynabeads. One of the standard crosslinking reagents is DMP (dimethyl pimelimidate), which irreversibly crosslinks amino groups. The disadvantage of crosslinking is that some of the antibody paratopes (antigen-binding sites) might be lost during crosslinking; this, however, was not expected to largely influence the immunoprecipitation efficiency, because the anti-GFP used in all the experiments is polyclonal, therefore a range of paratopes should be observed. Nevertheless, to ensure the best immunoprecipitation conditions I compared immunoprecipitation efficiency when using crosslinked and non-crosslinked anti-GFP Dynabeads (Fig. 5.2 C and D). Because the previous experiment indicated that the optimal beads/extract ratio is approximately 10 to 20 μL of beads per 1 mL of extract, I tested different beads/extract ratios to better determine the exact volume of beads needed. Crosslinked beads showed comparable immunoprecipitation efficiency to non-crosslinked beads. Moreover, no IgG was observed in samples immunoprecipitated with crosslinked beads. Therefore, 15 μl of DMP-crosslinked anti-GFP Dynabeads per 1 mL of protein extracts was used in further experiments.

Third, both in interphase and mitosis, a large fraction of Mto2 can be found in large subcellular structures, such as the SPB, or the NE. During the preparation of native protein extracts, these structures are often found in the pellet, potentially with Mto2 still bound to them. The pellet is rejected during extract preparation, which could result in loosing a large fraction of cellular Mto2. In *mto1[bonsai]* and *mto1*Δ cells, the Mto1/2 complex does not localise to any of the aforementioned structures (Lynch et al., 2013). I wanted to know whether changing the *mto1* background would increase the pool of available Mto2. Therefore, I tested Mto2-GFP immunoprecipitation efficiency in *mto1*$^{+}$*, mto1[bonsai]* and *mto1*Δ cells (Fig. 5.2 E and F). Mto2-GFP immunoprecipitation efficiency was comparable in *mto1*$^{+}$ and *mto1[bonsai]* cells but much lower in *mto1*Δ cells. This experiment, even though it was designed for optimisation purposes, implied that during immunoprecipitation in *mto1*$^{+}$ cells, one molecule of anti-GFP antibody immunoprecipitates not just one molecule of Mto2-GFP, but rather a multimer of Mto1/2. In *mto1*Δ cells, Mto2 can

self-interact, but forms smaller multimers than in *mto1*$^{+}$ cells, which results in lower amounts of Mto2-GFP pulled down (see also Section 4.2.15). Because the highest immunoprecipitation efficiency was observed in *mto1*$^{+}$ cells, this strain background was used in further experiments.

Finally, to ensure that the isotopic effect does not have effect on immunoprecipitation efficiency, I compared heavy and light extracts containing Mto2-17A-GFP (Fig. 5.2 G). Two biological replicas were analysed for heavy and light culture. The immunoprecipitation appeared to be slightly more efficient in the heavy culture; however, the protein concentration in both of the heavy cultures was lower than in light culture (WCE), which could also affect the immunoprecipitation efficiency. When pulldown signal was normalised to WCE, the immunoprecipitation efficiency was comparable in both samples (Fig. 5.3 H).

In summary, I showed that for the large-scale purification of Mto2-17A-GFP from yeast native protein extracts I should use 15 μL of DMP-crosslinked anti-GFP Dynabeads per 1 mL of extract. The immunoprecipitation should be performed in *mto1*$^{+}$ background, which ensures the highest immunoprecipitation efficiency.

5.2.2 Design of Mto2 phosphomutants

5.2.2.1 Identification of mitotic phosphorylation sites in Mto2-17A-GFP using SILAC

In order to identify mitosis-specific phosphorylation events occurring on Mto2-17A-GFP, I compared interphase and mitotic samples containing Mto2-17A-GFP purified from fission yeast cells. *nda3-KM311* allele was used to arrest cells in metaphase (Hiraoka et al., 1984; Moreno et al., 1989; Toda et al., 1983). Anti-GFP immunoprecipitation was then performed and proteins were resolved on 10% SDS-PAGE and Coomassie stained (Fig. 5.3 A). Mto2-17A-GFP bands were excised, trypsin-digested and Stage-Tip purified (Rappsilber et al., 2003), and then Juan Zhou from the Rappsilber group carried out the MS analysis.

A

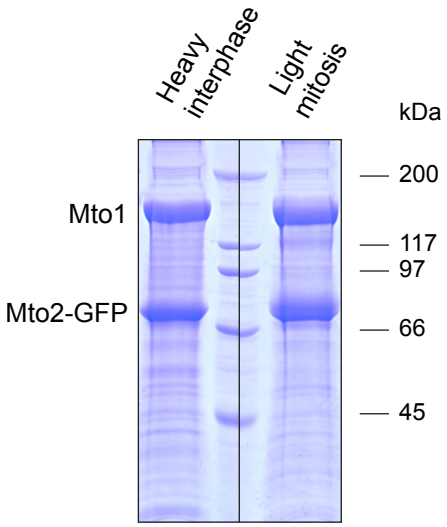

B

```
1   MSEHNYQSDR EVAEDPFLNY EASANQLSSN SRESAPRGAP WRAGMRSASL MTEPLEDSMY
61  SDNNYLDNGV SFTKDENPLY APSWPSLADA NVNSMKSNNA IQEHKAAKFV SEKSLEKVST
121 ADNNLVLQEL ENLRERLNQV ELQLSERPSS YLGYHNNLAP YRSPNSYPSL LPSTHAPHAP
181 APLSTMQTAL MRLRTYHPSP IILKPVEQAV NHAITLVNTA PSSVVDALCR SLAELCLGLV
241 QEAIDASILS QQESSNSLDL VRHAPPLNYT ASVDSAPQRM AADSYGRPSL HLNDPFPSVD
301 LQSNELSHHN VRTALFSDDS RFHSKIHTHS APPSQMYSAA AHFRYRSDPS TRHVSNSTNK
361 SSLHPAPTSL RVAHPIIPQR ASPASQSFPS LQDAPAP
```

Figure 5.3. Mto2-17A phosphorylation sites identified by mass spectrometry analysis.
(A) Mto2-17A-GFP was immunoprecipitated from native extracts and analysed on 10% SDS-PAGE. The gel was stained with Coomassie. Mto1 co-immunoprecipitated with Mto2-17A-GFP both in interphase and mitosis.
(B) Mto2-17A sequence. Peptide coverage (cumulative from all experiments) is shown in green, phosphorylated residues identified are indicated in **red** (if identified only in a light-only mitotic run) or **blue** (if identified in at least one of the SILAC experiments).
[Strain: KS 7093]

Both in interphase and mitosis, Mto1 was efficiently co-immunoprecipitated by Mto2, and Coomassie staining indicated approximately 1:1 stoichiometry of the complex. Mto1 protein samples were also analysed by MS, and results are presented in Appendix 1.

In total, four independent MS runs were performed: the first run involved analysis of only the light mitotic sample, and in the other three runs, both heavy and light samples were analysed (Table 5.1). Because of the fault of the spectrometer, one of the three SILAC experiments provided qualitative, but not quantitative data. This means that quantitative data was only obtained from two out of four experiments.

Table 5.1. Experimental design of four MS runs summarised.

Experiment	Light culture	Heavy culture	Quantitative?
0	MITOSIS	-	NO
1	MITOSIS	INTERPHASE	YES
2	INTERPHASE	MITOSIS	NO
3	INTERPHASE	MITOSIS	YES

Because of the large amount of proteins used (estimated by Coomassie staining to be more than 2 μg in each sample in each experiment), nearly the entire Mto2 sequence was covered by identified peptides (Fig. 5.3 B).

A large number of phosphorylation sites were identified in the four MS runs (Table 5.2). Mto2-17A contains many phosphorylatable residues (while there are over 100 potentially phosphorylatable residues in wild-type Mto2, there are still 89 serines, threonines or tyrosines within Mto2-17A sequence), which means that vast majority of peptides obtained by trypsin digest had more than one phosphorylatable residue. This renders data interpretation more difficult, because from the MS data it is not always possible to determine which of the residues was phosphorylated. This is because commonly used MS/MS fragmentation methods (including the one used in this study) often result in a neutral loss of phosphate or phosphoric acid, thus reducing sequence information (Molina et al., 2007).

Table 5.2. Phosphorylation sites identified during MS analysis of Mto2-17A-GFP. Residues in the same row were present on the same monophosphorylated peptide. Therefore, it is possible that not all of the indicated residues were phosphorylated *in vivo*, but the determination, which were or were not, was impossible due to the limitations mentioned above.

Experiment	Residues identified
0	S2, S23, S28,S29, S31 S114 S145, S149, S150 S266, Y269, T270 T328, S330 S347 S357, T359, S361 S382, S385, S387
1	S94, S114 S114, S119, T120 S307 S328, S330 S355, S557, T358
2	S2, S114, S119, T120 Y269, T270, S272 S307 S355, S357, T359 S382, S385, S387
3	S2, S8 S114, S119, T120 S145, S149, S150 S166 T368, S369 S382, S385

In my SILAC experiments, the majority of phosphopeptides were detected in both interphase and mitotic samples, but with distinct Mitosis/Interphase ratios (that is: heavy-to-light or light-to-heavy, depending on the experiment). The H/L ratio is calculated by Maxquant software and is based on the signal intensity of MS peaks detected by the mass spectrometer. The software is able to calculate the H/L ratio only for identical peptides, and it does not account for the fact that the same peptide can exist as many different species (for example: singly phosphorylated, doubly phosphorylated, with methionines oxidised, etc.). This could potentially lead to a loss of quantitative information; for instance if interphase a given peptide was phosphorylated in 1% and in mitosis it would be a mixture of monophosphorylated and dephosphorylated peptides, the quantitation based on solely monophosphorylated peptides in interphase and mitosis would not reflect the real situation observed in cells. For this reason, I decided to perform a manual analysis of MS data to ensure no quantitative information is lost or misinterpreted.

5.2.2.2 Quantification of phosphopeptides and their corresponding unmodified peptides

Manual quantification of H/L ratios involves analysis of MS spectra. During HPLC/MS2 analysis, peptides are separated by HPLC and then analysed by MS. In the spectrometer, peptides are first ionised in an *ioniser*, then a *mass detector* sorts the ions by their m/z ratio. Next, a *detector* measures the value of an indicator quality, which allows for quantification of abundance of each peptide (ion) present. Thus analysed ion is then fragmented and subsequently the ion fragments produced from the peptides are analysed which gives sequence information. The relative amount of each peptide can be measured by integrating the intensity under the elution peak (using data generated by the detector). In high-resolution spectra, one peptide gives rise to more than one MS peak. Each peptide creates what is called an isotope envelope, a result of the fact that atoms building amino acids exist as a mixture of various isotopes, that is, atoms that have the same number of protons but varying number of neutrons (Fig. 5.4 A). In the isotope envelope, the first peak is referred to as monoisotopic peak, because it corresponds to a peptide composed only of principal (i.e. most abundant) isotopes of each element. In proteomics, principal isotopes happen to be the lightest, but it is not always the case (for example, the lightest isotope of iron is ^{54}Fe, while the most abundant is ^{56}Fe). The most commonly occurring non-principal isotope is ^{13}C, which makes up more than 1% of all natural carbon on Earth. This means, that one in every hundred of carbon atoms is ^{13}C, not ^{12}C, and this can be observed by MS, because incorporation of a heavy atom into some of the peptides results in formation of a mixture of peptides with the same amino acid sequence but masses varying by 1 Da. The bigger the analysed molecule (peptide) is, the more carbon atoms it contains, and the more likely it is that some of the molecules will contain heavy carbon atoms. Therefore, to quantify the abundance of each peptide, elution volumes of every single isotope variant of any given peptide should be analysed. This was done for all the phosphopeptides identified in SILAC runs two and four (see Table 5.1), as well as their unmodified counterparts.

Thus obtained data can be quantified in three different ways (Fig. 5.4 B).

In the first method, the abundance of monophosphorylated peptides in both samples is compared (monophosphorylated peptides are the only form of phosphopeptides easily detectable in MS analysis). If a monophosphorylated peptide were much more abundant in the mitotic sample, the most straightforward

interpretation would be that the modification is mitosis-specific (or mitosis-enriched, if the relative difference in abundance is less extreme). This method, however, has its limitations: it is known that peptides bearing more than one phosphate groups (multiple phosphorylated peptides, MPPs) have a much lower ionisation efficiency than unmodified peptides, and thus are very rarely detected by spectrometers (Thingholm et al., 2009). In Mto2, the vast majority of predicted tryptic peptides could theoretically become MPPs, as they all contain multiple phosphorylatable residues. If MPPs were abundant in the analysed sample, a method based on quantifying solely the monophosphorylated peptides could give false negative results (i.e. ignore phosphorylation events that give rise to undetectable MPPs).

The second method is to compare the abundance of monophosphorylated peptides relative to their total pool, which includes also their unmodified counterparts. In both samples, any given peptide can exist as either unmodified or modified (that is, monophosphorylated, multiply phosphorylated, with methionines oxidised etc.). For instance, if 1% of the total pool of the peptide is monophosphorylated in interphase, and 50% of the peptide is monophosphorylated in mitosis, one can conclude that the modification is mitosis-specific. However, this method, similarly to the first one, does not take into consideration the pool of MPPs and therefore can give false negative results. Furthermore, this method is based on the incorrect assumption that ionisation efficiencies of unmodified peptides and their modified cognate peptides are comparable. Because peptide ionisation efficiency depends largely on its basicity, phosphopeptides, containing an acidic phosphate group, have much lower ionisation efficiencies relative to their unmodified counterparts.

The third method is based on quantification of unmodified peptides. Any *in vivo* modification occurring in mitosis would decrease the M/I ratio of the unmodified peptide, by altering the molecular mass (that is, the m/z) and by changing the retention time. The extent of this decrease is correlated with the degree of the modification. Therefore, if 50% of the total pool of a given peptide were phosphorylated in mitosis (giving rise to both monophosphorylated peptides and MPPs), a 50% decrease in the amount of this peptide would be observed in the mitotic sample relative to the interphase sample. This method is the only of the three that accounts for the existence of MPPs, and indeed any modification that is not recognised (or not recognisable) by the mass spectrometer, since the decrease in the signal intensity would be observed regardless whether the peptide was mono- or

multiply- phosphorylated. The limitation of this method is, however, that the decrease in unmodified peptide abundance could be a result of any modification, not only phosphorylation. Therefore, this method cannot truly be said to “quantify phosphopeptides” even though it may be of considerable value when abundance of MPPs is high.

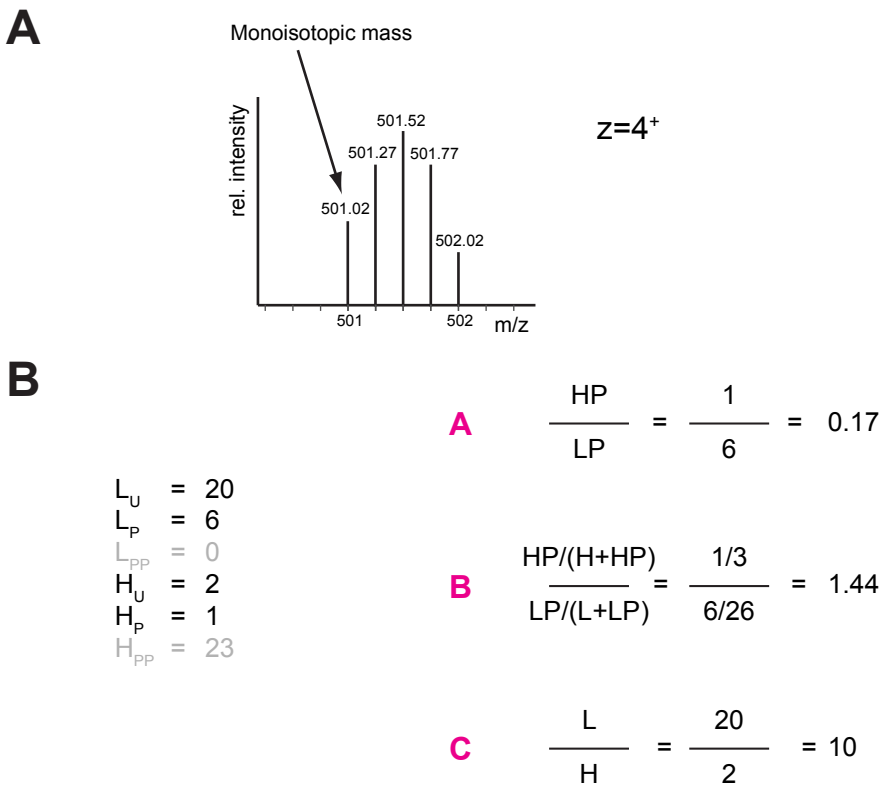

Figure 5.4. Methods to quantify abundance of phosphorylation in the heavy sample realtive to the light sample.
(A) A schematic representation of an isotopic envelope observed by high-resolution mass spectrometers. The charge of the peptide can be inferred from the distances between isotope peaks. In this example, $z=4^+$, because the distance between peaks equals 0.25.
(B) An example of calculations using three different methods of quantitation. L_U/H_U, abundance of the light/heavy unmodified peptide; L_P/H_P, abundance of the light/heavy monophosphorylated peptide; L_{PP}/H_{PP}, abundance of the light/heavy multiply phosphorylated peptide (including all peptides phosphorylated on more than one residue). L_{PP} and H_{PP} peptides would not be detected in the mass spectrometer. Three different quantitation methods give contradictory results.
In method (A), intensities of only the phosphorylated peptides are compared and show that the phosphorylation is enriched 6 times in the light sample. In method (B), the peak intensity of the phosphorylated peptide is ‘normalised’ to the total intensity of this peptide (a sum of phosphorylated and unmodified peptide intensities). This method suggests that the phosphorylation is slightly more abundant in the heavy sample. In method C, abundance of unmodified peptides are compared. The 10 fold decrease in the abundance of unmodified peptide suggests that 90% of this peptide is phosphorylated in the heavy sample.

I used all three methods to quantify the abundance of monophosphorylated and unmodified peptides in interphase and mitotic samples of Mto2-17A-GFP (an example of MS, and MS/MS spectra used during quantitation are shown in Fig. 5.5). The third SILAC experiment resulted in the best quality MS data, because a longer (than in the first SILAC run) time of HPLC gradient was used, which allowed identification of more peptides. Moreover, a different mass spectrometer was used in the third run, which additionally improved the data quality. Therefore, data obtained during the last experiment was used in all further analyses. To obtain M/I ratios (Table 5.3), I first integrated the elution peak areas for all isotopic peaks of any given peptide. I then normalised the obtained values to correct for uneven loading of heavy and light samples, by multiplying them by a constant value calculated by MaxQuant software (see below). Finally, I used these normalised values to calculate M/I ratio using the three different methods described above.

Table 5.3. Three quantification methods give different results.

M/I ratio / Residue	**Method A** (phosphopeptides only)	**Method B** (both unmodified and phosphopeptides)	**Method C** (unmodified peptides only)**
S2, S8	0.04	0.28	6.48
S114, S119, T120	30.49	na	na
S145, S148, S149	1.08	4.09	3.8
S166	1.01	1.29	1.27
T368, S369	2.55	na	na
S382, S385	8.75	na	na
S382, S385*	1.5	3.47	2.33

* - the same residues were detected to be phosphorylated twice, on two different peptides, one of which was a result of miscleavage; ** - for unmodified peptides I/M (not M/I) ratio is shown, to better show the relative abundance of the modified peptides.

The normalisation step was required, because in my experiments the heavy and light samples were not mixed at the beginning of the experiment. The cultures were processed for MS analysis (resolved on 10% SDS-PAGE gel, Coomassie stained, excised, digested with trypsin and purified using Stage-Tip) separately, and combined by Juan Zhou prior to injection, and this resulted in a H/L ratio different than 1:1 in the analysed mixture. MaxQuant calculates the normalisation constant by ordering all the identified peptides (modified and unmodified) by increasing H/L ratio and finding the median. The median is then used for normalisation. This method is prone to errors when the sample size is small, as it was in this case (only one protein with 397 amino-acid residues was analysed). Furthermore, if there were a lot of phosphorylation events in the heavy mitotic sample, heavy MMPs would not

be detected resulting in a skewed distribution, with many peptides with very low M/I ratios. Indeed, this was observed (Fig. 5.6 A); when M/I ratios for all of unmodified Mto2 peptides were plotted against their peptide rank, the curve was shifted towards low M/I ratios. The same trend was observed in the Experiment 1; he curve was skewed towards low M/I ratios (that is, low L/H ratios, because the labels were swapped in that experiment, data not shown). This was, however, not observed for Mto1 isolated from the same sample (data not shown). This is consistent with the interpretation that Mto2-17A-GFP is heavily modified in mitosis. Alternatively, some other modification occurs in mitosis. This, is however, unlikely, as no other modifications were detected by MS. Moreover, I showed in Chapter 4, that significant fraction of Mto2-17A is phosphorylated in mitosis (as demonstrated by presence of slower-migrating Mto2-17A isoforms that change into faster-migrating isoform upon phosphatase treatment).

The observation that the normalisation is likely to be incorrect further suggested that none of the quantitation method presented above is ideal. In a sense, this should be obvious from first principles: in the absence of comprehensive identification and measurement of all modified forms of all peptides, any quantification method will involve some unproven assumptions. Nonetheless, out of the three methods, the one based solely on unmodified peptides seemed to be the most suited for identifying mitosis-specific phosphorylation of Mto2. First, because it accounted for presence of MPPs. Second, because it would likely give the lowest false-negative rate. The limitation, as mentioned before, is that this method would likely give higher false-positive rate than the other two methods, because it does not provide any information about the type of modification that decreased the pool of a given unmodified peptide (the modification could be not only phosphorylation, but also virtually any other modification that changes the peptide's m/z or retention time). Nevertheless, in the Mto2-17A case, MS and western blot analyses confirmed the fact that Mto2-17A is indeed phosphorylated in mitosis, supporting the notion that the third quantification method would be the most appropriate in Mto2-17A analysis. Values shown in Table 5.3 were calculated only for the peptides detected to be phosphorylated; however, it could not be ruled out that in mitosis some of the Mto2-17A peptides were present exclusively as MPPs when phosphorylated (i.e. not present as monophosphorylated) and thus, were never detected as phosphopeptides (as MPPs are not detectable). Hence, I decided to use non-normalised data for *unmodified peptides* to obtain information about which peptides

could have potentially been phosphorylated in mitosis, by looking at which of the unmodified peptides became less abundant in mitosis.

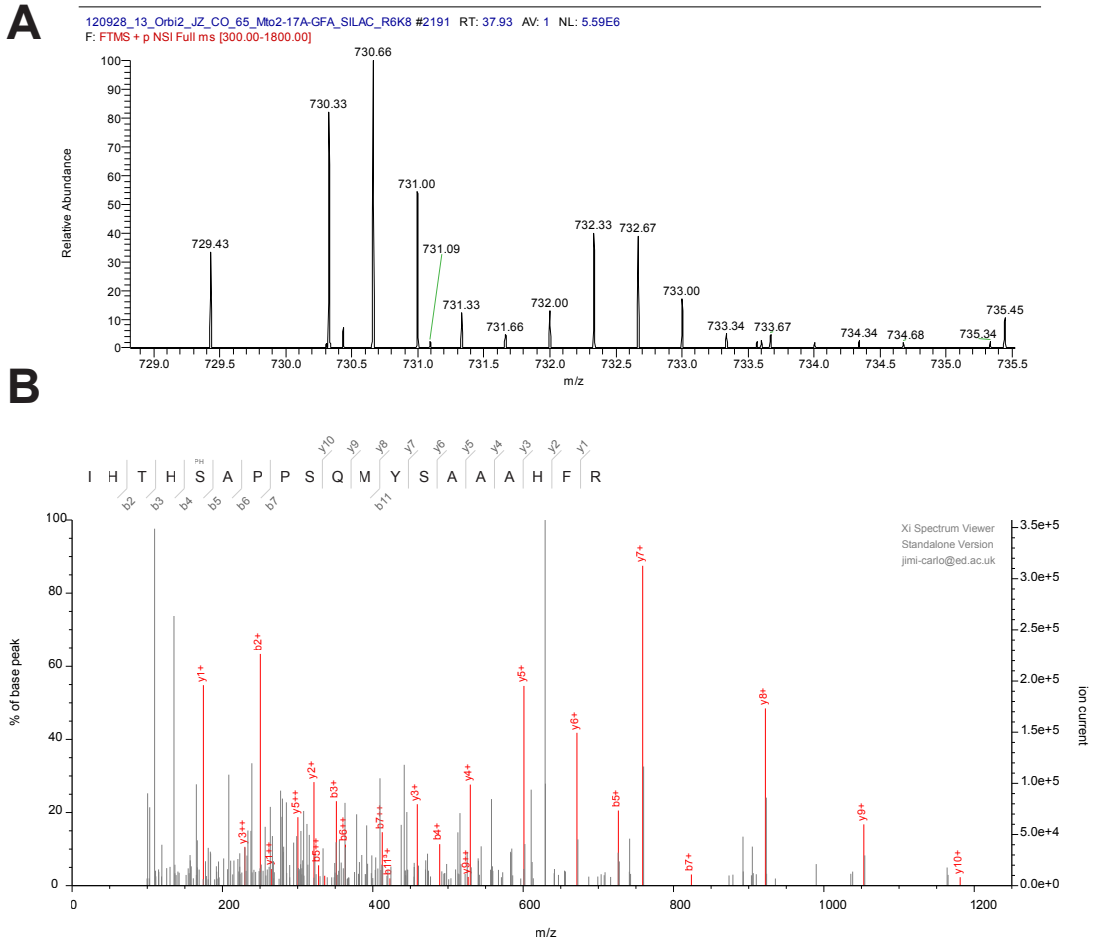

Figure 5.5. Manual quantification of phosphopeptides abundance.
(A) An example of a MS spectrum of a phosphopeptide IHTHSphSAPPSQMYSAAAHFR. Raw data was analysed using XCalibur MS spectrum viewer to visualise precursor ion peaks. Isotope envelopes corresponding to both light (monoisotopic peak m/z=730.33) and heavy (monoisotopic peak m/z=732.33) phosphorylated peptide are shown.
(B) An example of a MS/MS spectrum of the same phosphopeptide (light). Raw data was analysed using XiSPEC MS/MS spectrum viewer to visualise identified ions. y and b ions are indicated in red.

To do that, I used *unmodified peptide* data generated by MaxQuant, which assigns H/L ratios for all identified peptides. Because of the small sample size, the same Mto2-17A-GFP peptides were often detected multiple times, and different H/L ratios were assigned to them each time. I averaged the H/L ratios for each peptide, and used this average value for further analysis. Because the mitotic sample was heavy in this experiment, the H/L ratio is also the M/I ratio. The M/I ratio for every

identified peptide was plotted against the position of the peptide within the protein (Fig 5.6 B). This showed that some of the Mto2-17A-GFP unmodified peptides had very low M/I ratios, the lowest below 0.1, suggesting that they underwent modifications, most likely phosphorylation, in mitosis. Recently, a similar method of quantification was used to follow CDC27 and APC5 modifications occurring in HeLa cells upon MT-drug nocodazole treatment (Singh et al., 2009).

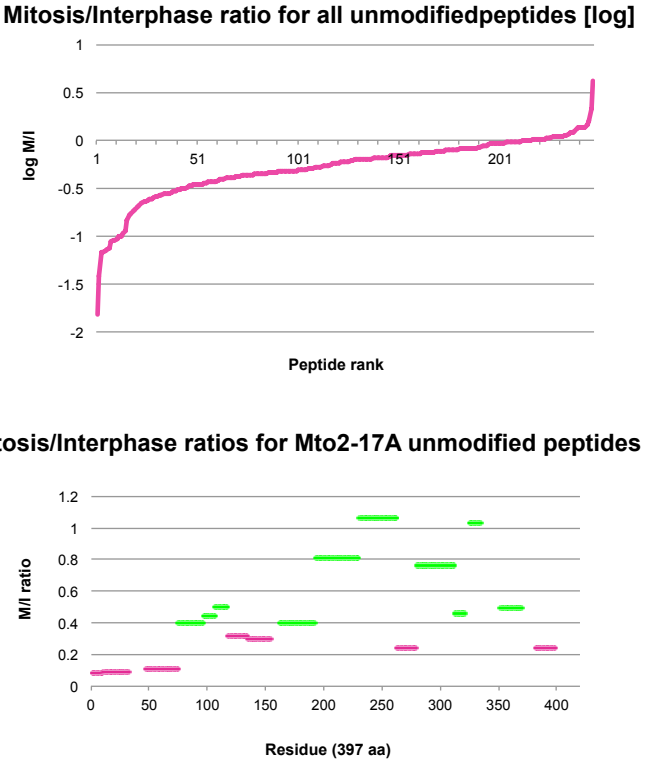

Figure 5.6. Quantification of SILAC data based on unmodified peptides.
(A) All unmodified Mto2 peptides were ordered according to their M/I ratio and plotted from the lowest M/I ratio to the highest.
(B) Relative peptide abundance of Mto2-17A-GFP peptides. Non-normalised Mitosis:Interphase (H/L) ratios were plotted for each identified peptide. If the normalisation were performed, it would result only in a relative change of the scale on the Y axis; the differences between particular peptides would be the same. Peptides are drawn to scale and ordered according to their position along the protein (X-axis). Residues within peptides with a M/I ratio lower that 0.4 were subsequently selected for mutagenesis (magenta).

5.2.2.3 Design of Mto2 phosphomutants

The information obtained by analysis of unmodified peptides appeared to be the most reliable, as it accounted for the existence of MPPs, and thus was used to design Mto2 phosphomutants. Peptides with an M/I ratio lower than 0.4 were

selected for mutagenesis (Fig. 5.6 B). Each of those peptides contained many (4-9) phosphorylatable residues, out of which some, but not all, were identified as being phosphorylated in previous experiments (MS runs 0-3, Table 5.2). I designed 5 phosphomutants, each containing 4-7 alanine substitutions (Table 5.4).

Table 5.4. Mto2 phosphomutants design based on unmodified peptide data. Five phosphomutants in which additional alanine substitutions were introduced into Mto2-17A sequence were designed based on MS data. Magenta, residues selected for mutations based on unmodified peptides quantitation, *in vivo* phosphorylation confirmed. Green, residues selected for mutations based on unmodified peptides quantitation, phosphorylation not confirmed. Blue, selected for mutation based on data for phosphorylated peptides.

Mutant name	Relevant peptide(s)	M/I ratio	Residues mutated	How were they chosen ?	Total no. of mutated residues
N-terminal 1 (NT1)	1-MSEHNYQSDREVAED PFLNYEASANQLSSNSR-32	0.09	S2, S8, S23, S28, S29, S31	All	23
N-terminal 2 (NT2)	47-SASLMTEPIEDSMYSD NNYLDNGVSFTK-74	0.11	S47, S49, T52, S58, S62, S72, T74	Tyr residues rejected	24
Flanking coiled-coil (FCC)	109-FVSEKSLEK-117 118-VSTADNNLVLQELENLR-134 137-LNQVELQLSERPS SYLGYHNNLAPYR-162	0.5 0.32 0.31	S114, S118, T120, S145, S149, S150	S114 included	23
C-terminal 1 (CT1)	236-HAPPLNYTASVDSAPQR-286	0.24	Y269, T270, S272, S275	All	21
C-terminal 2 (CT2)	381-ASPASQSFPSIQDAPAPR-397 *	0.25	S382, S385, S387, S390	All	21

*- The arginine residue comes from a linker between Mto2-17A and GFP tag.

In Mto2-NT1, all six phosphorylatable residues were mutated to alanines. All of these residues were detected to be phosphorylated *in vivo*. In Mto2-NT2 seven (out of nine phosphorylatable) residues were mutated. The two remaining residues, which were tyrosines, were not mutated, as previous experiments performed by Lynda Groocock suggested Mto2 is not phosphorylated on tyrosine residues (Groocock PhD Thesis, 2010). In the context of the above discussion on how to quantify phosphopeptides, it is important to note that none of the residues mutated in Mto2-NT2 was ever directly identified by me to be phosphorylated in Mto2-17A. In Mto2-FCC, six residues were mutated to alanine, using data from three different peptides. Two of the unmodified peptides had a M/I ratio less than 0.4. The third unmodified peptide had a slightly higher M/I ratio, but its phosphorylated cognate was identified as highly abundant in mitosis during the same MS run (see Table 5.3), and therefore was also selected for mutation. Both Mto2-CT1 and Mto2-CT2

contained four alanine substitutions, and all of the mutated sites had been identified as phosphosites in previous MS analyses.

5.2.3 Analysis of Mto2 phosphomutants

5.2.3.1 Mto2-NT2 is not hyperphosphorylated in mitosis

The five new Mto2 phosphovariants were designed in the existing Mto2-17A context in order to try to abolish the remaining mitotic phosphorylation observed in Mto2-17A. The constructs were synthesised by GeneART [Germany] and integrated at the *mto2*$^{+}$ locus, as the sole copy of Mto2. To investigate the mitotic phosphorylation of these Mto2 phosphovariants, I used the *nda3-KM311* mutation to arrest cells in mitosis and then analysed protein extracts from interphase and mitosis-arrested cells (Fig. 5.7) (Hiraoka et al., 1984; Moreno et al., 1989; Toda et al., 1983). As seen previously, in *mto2*$^{+}$ and *mto2-17A* cells, a change in Mto2 mobility was observed in mitotic vs. interphase extracts. The same was seen in Mto2-NT1, Mto2-FCC, Mto2-CT1 and Mto2-CT2 extracts, although, as expected, the mobility change in Mto2-17A was relatively small compared to that of wild-type Mto2. The mitotic mobility of four of the variants, Mto2-NT1, Mto2- FCC, Mto2-CT1 and Mto2-CT2, was not significantly different from that of their parent mutant, Mto2-17A. Strikingly, the fifth variant, Mto2-NT2 did not undergo any mobility shift in mitotic sample, suggesting that mitotic phosphorylation is significantly blocked in this strain. Because the other four phosphomutants appeared to exhibit the same mitotic phosphorylation levels as Mto2-17A, only Mto2-NT2 was selected for further analysis (see below).

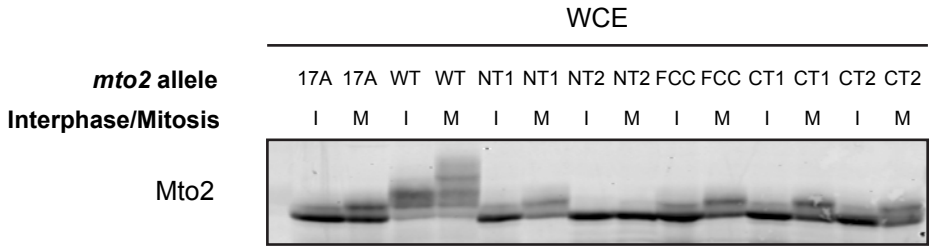

Figure 5.7. Mitotic phosphorylation of Mto2-NT2 is almost completely abolished in mitosis relative to Mto2-17A.
Extracts from interphase and metaphase-arrested cells were analysed by western blot probed against Mto2.
[Strains: KS1740, KS6415, KS7221, KS7223, KS7225, KS7227, KS7229]

It is particularly noteworthy in this experiment that the only phosphomutant yielding an obvious decrease in mitotic phosphorylation contained mutations at residues for which no direct evidence for phosphorylation was available. This supports the idea that quantification of unmodified peptides can provide crucial information in this type of MS analysis. It is also important to note that, despite the lack of mobility shift observed in this mutant, it is nevertheless possible that some mitotic phosphorylation does occur on Mto2-NT2, as not all of phosphorylation events result in mobility shift, and not all of the MS detected phosphosites were mutated in this variant. To ensure Mto2-NT2 is not phosphorylated, a SILAC experiment should be performed comparing Mto2-17A and Mto2-NT2 phosphorylation in mitosis.

At the same time, it is also possible that one of the sites mutated in Mto2-NT2 was a "priming site", and therefore abolishing phosphorylation on this residue led to abolition of phosphorylation on other residues. A similar phenomenon is observed for budding yeast Sic1 protein. Sic1 multisite phosphorylation targets Sic1 for degradation, which allows for the initiation of S phase (Kõivomägi et al., 2011; Nash et al., 2001). Sic1 is phosphorylated by Cdk1, and the interaction between Sic1 and Cdk1 is mediated by Cks1, the phosphoadaptor unit of Cdk1. Cks1 binds exclusively to phosphorylated residues (Arvai et al., 1995), therefore Cdk1-Cks1 complex requires phosphorylation to occur in order to bind to Sic1.

5.2.3.2 Mto1[NE]-GFP puncta disappear from the NE in *mto2-NT2* cells

To characterise *mto2-NT2* cells, I first looked at Mto1[NE]-GFP localisation to the NE. As described in Section 4.2.12, during interphase Mto1[NE]-GFP localises to the NE as discrete puncta, and this localisation is lost (in wild-type cells) upon mitotic entry, coinciding with the Mto1/2 complex disassembly (Groocock PhD Thesis, 2010; Lynch PhD Thesis, 2012). This is also observed in *mto2-alanine* mutants, including *mto2-17A* (see Section 4.2.12). If the Mto1/2 complex persisted through mitosis in *mto2-NT2* cells, it could potentially retain the ability to localise to the NE in mitosis. To test this, I imaged cells expressing mCherry-α-tubulin together with Mto1[NE]-GFP (Fig. 5.8 A). As expected, in *mto2*$^{+}$ and *mto2-17A* cells, Mto1[NE]-GFP delocalised from the NE when cells entered mitosis and re-localised to the NE after mitotic spindle disassembly. Interestingly, the same behaviour was also observed in *mto2-NT2* cells: Mto1[NE]-GFP delocalised from the NE upon

mitotic entry and was present as diffuse cytoplasmic signal until late anaphase. This shows that the formation of the Mto1/2 complex and its localisation to the NE and is cell cycle regulated in *mto2-NT2* cells.

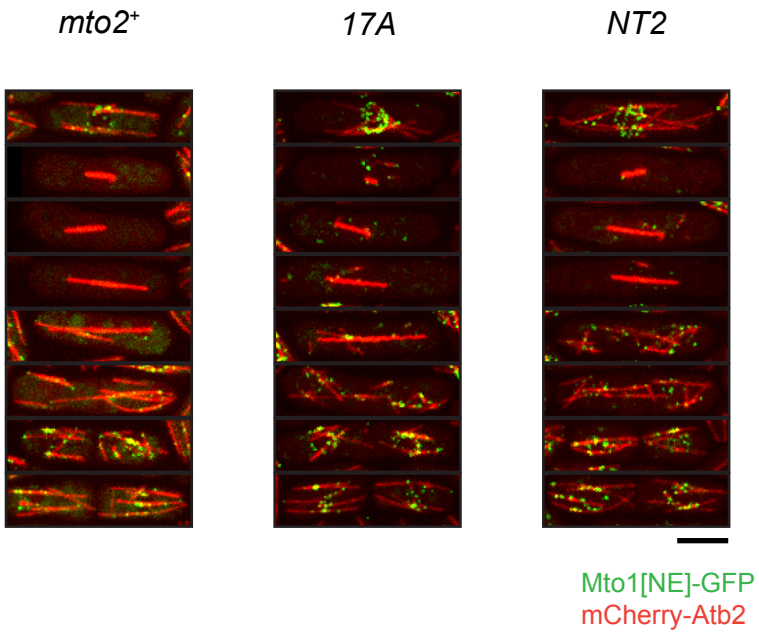

Figure 5.8. Mto1[NE]-GFP delocalises from the NE upon mitotic entry in *mto2*$^+$, *mto2-17A* and *mto2-NT2* cells.
Confocal images showing mitotic *mto2*$^+$, *mto2-17A* and *mto2-NT2* cells co-expressing Mto1[NE]-GFP and mCherry-α-tubulin. Images were taken from different cells exhibiting different spindle lengths.
Bar, 5 μm. [Strains: KS6677, KS7282, KS7284]

5.2.3.3 *mto2-NT2* and *mto2-17A* cells nucleate more MTs than wild-type cells in *mto1[NE]-GFP* background

I showed in the Chapter 4 that Mto2 phosphorylation state regulates interphase MT nucleation levels. Because Mto2-NT2 appears not to be phosphorylated, I investigated interphase MT networks in this mutant. I used Mto1[NE]-GFP background rather than full length Mto1-GFP, as *mto1-GFP mto2-17A* cells exhibited polarity and separation defects (see Section 4.2.9), and I predicted these effects would be similar or even more severe in *mto1-GFP mto2-NT2* cells. I imaged mCherry-α-tubulin and Mto1[NE]-GFP in interphase *mto2-NT2* and *mto2-17A* cells and in control *mto2*$^+$ cells, and I counted the number of MT bundles per cell (Fig. 5.9). As expected (based on data presented in Chapter 4), *mto2-17A* cells contained more interphase MT bundles than WT cells; this increase

in MT bundle was also observed for *mto2-NT2* cells. Both mutants were statistically different from wild-type, but not from each other (Table 5.5).

Table 5.5. *mto2-NT2 mto1[NE]-GFP* and *mto2-NT2 mto1[NE]-GFP* cells contain more MT bundles than *mto2*$^{+}$ *mto1[NE]-GFP* cells. Wilcoxon rank-sum test was used for comparison between each mutant (Mann and Whitney, 1947). P values are shown.

	WT	17A
NT2	0.000877	0.8332
17A	0.0001821	

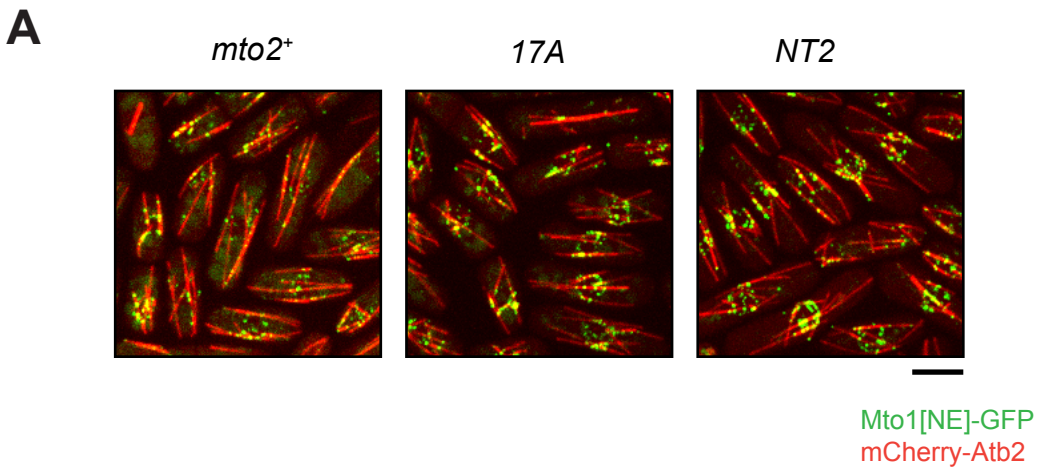

Figure 5.9. Microscopy analysis of Mto1[NE]-GFP in *mto2-17A* and *mto2-NT2* interphase cells.
A) Mto1[NE]-GFP is enriched at the NE relative to WT and Mto2-17A. Confocal images showing Mto1[NE]-GFP (green) in strains co-expressing mCherry-α-tubulin (red) to visualise MTs.
B) Number of MT bundles per cell observed in (A). Number of MT bundles in each cell was counted, n=50. Both mutants were statistically different from wild-type.
Bar, 5 μm. [Straiins: KS6677, KS7282, KS7284]

In Section 4.2.11 I showed that Mto1[NE]-GFP was enriched at the NE in *mto2-alanine* cells relative to wild-type cells. This was also observed in *mto2-NT2* cells, where Mto1[NE]-GFP localisation to the NE was more evident than in wild-type cells, but comparable to *mto2-17A* cells (Fig. 5.9 A). This further suggests that Mto2 phosphorylation may regulate the interaction between the Mto1/2 complex and its NE receptor. How this can be achieved was discussed in Sections 4.2.11 and 4.3.2.

5.2.3.4 Mto1[bonsai]-GFP aggregate formation in *mto2-17A* and *mto2-NT2* cells impairs interphase MT networks

I also wished to analyse interphase MT networks in *mto2-NT2 mto1[bonsai]-GFP* cells by imaging mCherry-α-tubulin. In Section 4.2.13 I showed that the numbers of MT bundles in *mto1*$^+$ *mto2-alanine* cells are statistically different from those in *mto2*$^+$ cells. *mto2-6A*, *mto2-13A* and *mto2-17A* cells, despite having different MT nucleation frequencies, contained similar numbers of MT bundles. This lack of differences between the three mutants might stem from the fact that nascent MTs are very quickly incorporated into MT bundles (Lynch PhD Thesis, 2012), maintaining a steady-state number of MT bundles. In *mto1[bonsai]-GFP* cells, the number of MT bundles is higher than in *mto1*$^+$ cells, which potentially could allow observing subtle differences between different *mto2-alanine* mutants (Lynch PhD Thesis, 2012). Therefore, in addition to co-imaging mCherry-α-tubulin and Mto1[bonsai]-GFP in *mto2-NT2* cells, I also included into the analysis *mto2-alanine* cells, in hope that in this *mto1* background the differences between mutants would become more evident.

First, I looked at Mto1[bonsai]-GFP localisation in wild-type and mutant cells co-expressing mCherry-α-tubulin (Fig. 5.10 A). As shown before ((Lynch et al., 2013), Section 4.2.13), in *mto2*$^+$*, mto2-6A* and *mto2-13A* cells, Mto1[bonsai]-GFP was seen in the cytoplasm as discrete puncta localised to the minus ends of MTs and along MT bundles (presumably also to the minus ends of MTs incorporated into bundles and not to the MT lattice as the Mto1 MT-localisation signals are removed in *mto1[bonsai]-GFP cells*). In both *mto2-17A* and *mto2-NT2* cells, Mto1[bonsai]-GFP formed large aggregates, several times bigger than those observed in wild-type cells (Fig. 5.10 C) .

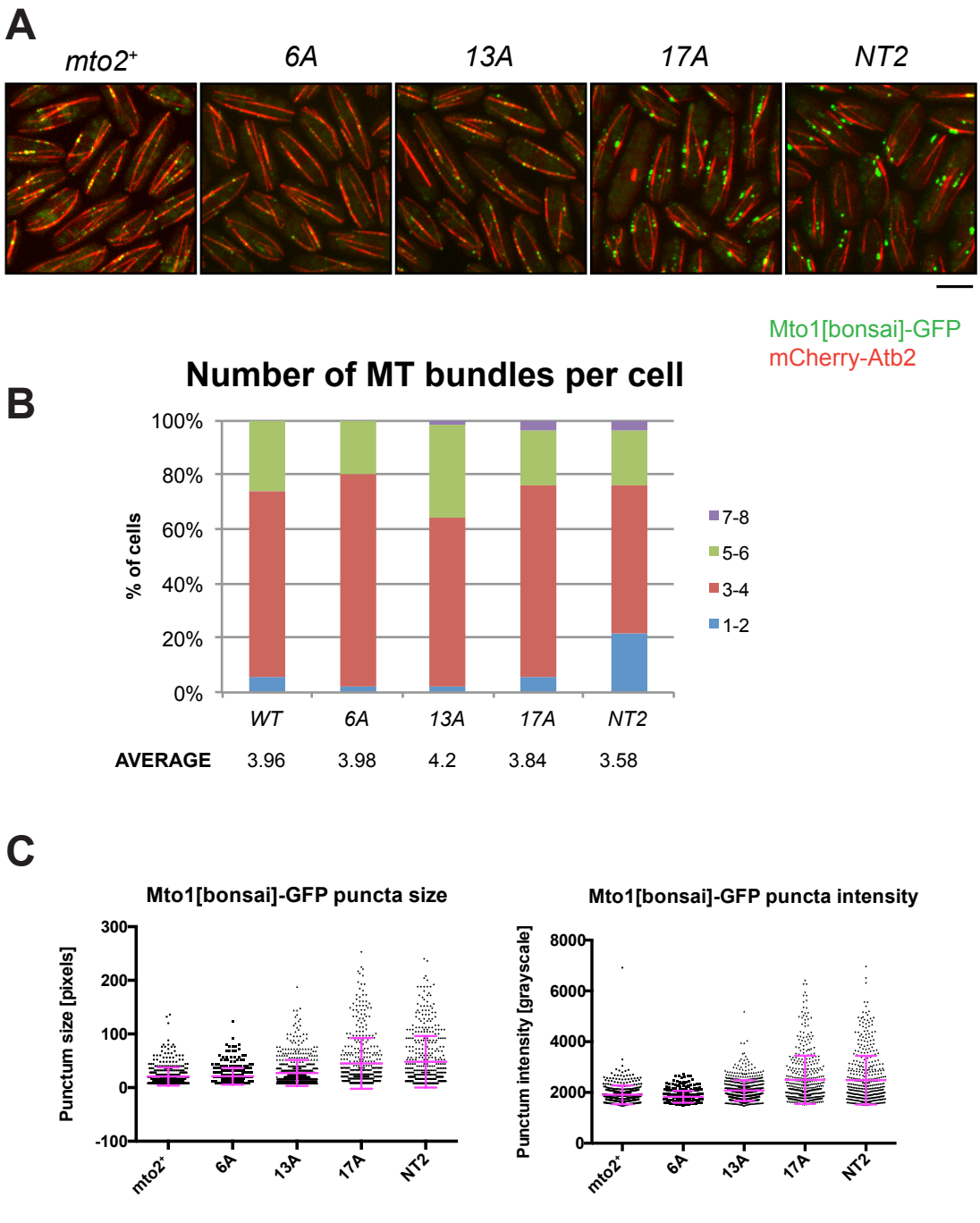

Figure 5.10. Microscopy analysis of Mto1[bonsai]-GFP in *mto2-alanine* and *mto2-NT2* interphase cells.
(A) Mto1[bonsai]-GFP forms aggregates in *mto2-17A* and *mto2-NT2* cells. Confocal images showing Mto1[bonsai]-GFP (green) in strains co-expressing mCherry-α-tubulin (red) to visualise MTs.
(B) Number of MT bundles per cell observed in (A). Number of MT bundles in each cell was counted, n=50.
(C) Size and intensity of puncta observed in (A) were quantified using Metamorph software. For each strain, puncta within a single imaging field were analysed. Magenta bars indicate the average puncta size or intensity and SEM.
Bar, 5 μm. [Strains (number of puncta analysed): KS6678 (477), KS7241 (402), KS7246 (691), KS7249 (468), KS7260 (421)]

Second, I quantified the number of MT bundles in all analysed mutants. *mto2-6A* and *mto2-13A* cells seemed to contain slightly more MT bundles than wild-type cells, whereas *mto2-17A* and *mto2-NT2* cells contained slightly fewer MTs per cell (Fig. 5.10 B). Statistical analysis showed that the only phosphomutant statistically different from wild-type was *mto2-NT2* (Table 5.6), but it contained less, not more, MT bundles (on average 3.58 vs. 3.96). It was also statistically different from *mto2-6A* and *mto2-13A.* The lack of differences between wild-type and *mto2-alanine* cells might seem to contradict the previous conclusion from Chapter 4 that Mto2 phosphorylation negatively regulates interphase MT nucleation levels. Nevertheless, in *mto1[bonsai]-GFP* cells the number of MT bundles is already much higher than in *mto1-GFP* cells (Lynch PhD Thesis, 2012); possibly, because of external limitations, such as limited α-, β- and γ-tubulin pools, no further increase in MT bundle number is possible. Moreover, given that the Mto1[bonsai]-GFP forms aggregates in both *mto2-17A* and *mto2-NT2* cells, the decrease in MT bundle numbers observed in those cells is most likely a result of Mto1[bonsai]-GFP aggregation. Possibly, the aggregates are too big to efficiently promote nucleation; alternatively, they can promote nucleation but they are not abundant enough to nucleate enough of MTs. It would be interesting to see if those aggregates attract comparable amounts of γ-TuC components.

Table 5.6. *mto2-NT2 mto1[bonsai]-GFP* and *mto2-17A mto1[bonsai]-GFP* cells contain fewer MT bundles than *mto2*$^{+}$ *mto1[bonsai]-GFP* cells. Wilcoxon rank-sum test was used for comparison between each mutant (Mann and Whitney, 1947). P values are shown.

	WT	6A	13A	17A
NT2	0.04994	0.01655	0.003744	0.2205
17A	0.3299	0.1334	0.3763	
13A	0.2202	0.2731		
6A	0.76			

5.2.3.5 Analysis of Mto1[bonsai]-GFP puncta in *mto2-NT2* mitotic cells

The main purpose of generating *mto2-NT2* and other Mto2 phosphovariants was to elucidate the role of Mto2 phosphorylation in mitotic disassembly of the Mto1/2 complex. If Mto2 phosphorylation were the sole mechanism disrupting both the Mto1-Mto2 and the Mto2-Mto2 interactions upon mitotic entry, generation of a completely non-phosphorylatable *mto2* mutant would result in the Mto1/2 complex persisting in mitosis. Possibly, some limited MT nucleation would also be observed;

this, however, is not likely, as there are several other factors involved in MT formation that are also cell cycle-regulated. Because fission yeast undergo closed mitosis, several factors needed for MT nucleation and maintenance are imported into the nucleus upon mitotic entry. Such factors include Alp7/Alp14 (TACC/TOG) complex, involved in MT array remodelling (Sato et al., 2009; Zheng et al., 2006), or tubulin itself (Hayashi et al., 2012; Leo et al., 2012). Results presented in Section 5.2.3.2, in which the Mto1[NE]-GFP signal became diffused in mitotic cells, suggested that the Mto1/2 complex likely disassembles in *mto2-NT2 mto1[NE]-GFP*. Perhaps a better tool to investigate the Mto1/2 complex assembly and disassembly is Mto1[bonsai]-GFP, because it forms cytoplasmic puncta that, unlike Mto1[NE]-GFP puncta, do not localise anywhere in the cytoplasm (Lynch PhD Thesis, 2012). Thus, in *mto1[bonsai[-GFP* cells any regulation of the Mto1/2 complex formation can be expected to be completely independent of its localisation.

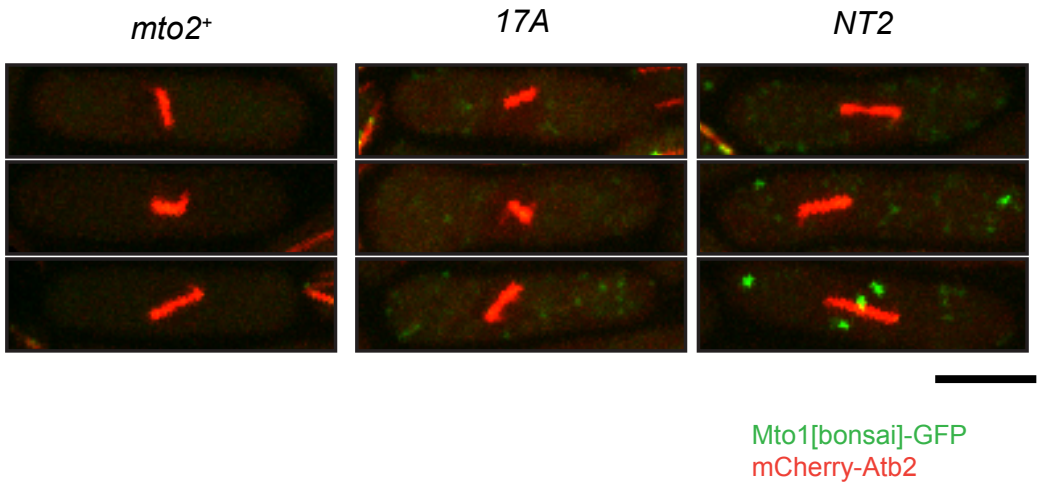

Figure 5.11. Mto1[bonsai]-GFP puncta in early mitosis in *mto2+*, *mto2-17A* and *mto2-NT2* cells.
Confocal images of mitotic cells expressing Mto1[bonsai]-GFP (green) in strains co-expressing mCherry-α-tubulin (red) to visualise MTs. Three different cells are shown. Bar, 5μm. [Strains: KS6678, KS7249, KS7260]

To investigate the behaviour of Mto1[bonsai]-GFP puncta I imaged *mto2+*, *mto2-17A* and *mto2-NT2* cells co-expressing Mto1[bonsai]-GFP and mCherry-α-tubulin to visualise MTs (Fig. 5.11). I imaged asynchronous cultures and looked for cells with short spindles, indicating early mitosis. In wild-type cells, no Mto1[bonsai]-GFP puncta were observed in such cells. In some of both *mto2-17A* and *mto2-NT2*

cells, Mto1[bonsai]-GFP puncta were occasionally observed. However, cells with short spindles can be either in metaphase or anaphase A. Therefore, it was impossible to conclude whether the puncta were observed in metaphase. In future, a similar experiment should be performed with the use of a marker allowing distinguishing between metaphase and early-anaphase cells.

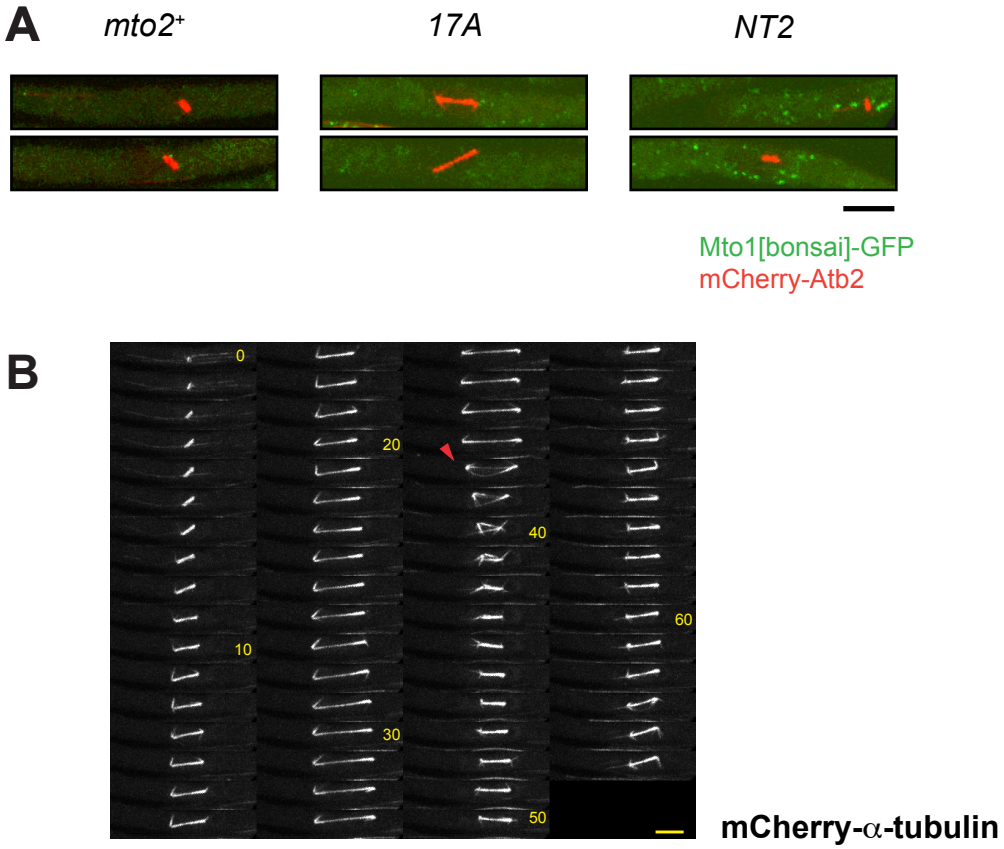

Figure 5.12. Mto1[bonsai]-GFP puncta in mitotic cells in *mto2⁺ cdc25-22, mto2-17A cdc25-22* and *mto2-NT2 cdc25-22* cells.
(A) Confocal images of mitotic cells expressing Mto1[bonsai]-GFP (green) and mCherry-α-tubulin (red) to visualise MTs. Two cells are shown for each mutant.
(B) Stills from a movie of mCherry-α-tubulin in *mto2⁺ cdc25-22* cells (1 min time interval); at t=38 min the spindle collapses (arrowhead).
Cells are not shown whole as often they were larger than the imaging field.
Bar, 5μm. [Strains: KS7268, KS7270, KS7272]

To analyse Mto1[bonsai]-GFP puncta in a larger number of metaphase *mto2-NT2* cells I decided to employ a *cdc25-22* arrest (Fantes, 1979; Thuriaux et al.,

1980). This allele allows arresting cells in late G2, and subsequent release into mitosis. Cells were arrested at the restrictive temperature of 36ºC and then released to 25ºC, and imaged 50 minutes after release. As expected, in *mto2*$^{+}$ cells, no Mto1[bonsai]GFP puncta were observed in cells with short spindles (Fig. 5.12 A). This was also seen in *mto2-17A* cells. By contrast, Mto1[bonsai]-GFP puncta were seen in some of *mto2-NT2* cells with short spindles. As cells arrested in G2 remain their ability to grow, *cdc25-22* arrested cells are 3-4 times longer than *cdc25*$^{+}$ cells; which could lead to a formation of a longer mitotic spindle (Gay et al., 2012). To determine the exact spindle length at metaphase in *cdc25-22* cells (phase 2 during spindle elongation, discussed in Section 4.2.8) (Nabeshima et al., 1998), I followed four *mto2*$^{+}$ *mCherry-*α*-tubulin* mitotic cells for more than an hour (Fig. 5.12 B). During the course of the experiment, the mitotic spindle collapsed in all four observed cells, suggesting they were under stress. This suggested that the observed Mto1[bonsai]-GFP phenotypes might not be physiological. There are further limitations of this experiment: because cells continue to grow during the arrest, they reach bigger sizes which could potentially affect their MT cytoskeleton, which could in turn influence the Mto1/2 complex formation and stability as availability of the γ-TuC components.

Another way to enrich for mitotic cells is to use the *nda3-KM311* allele to arrest cells in early metaphase (Hiraoka et al., 1984; Moreno et al., 1989; Toda et al., 1983). Cells were grown at the restrictive temperature of 18ºC to enrich for mitotic cells; at the restrictive temperature *nda3-KM311* cells contain no MTs and therefore they arrest in early metaphase, because they are not able to assemble the mitotic spindle. After 4h (approximately half of the culture should be arrested after this time), cells were processed for imaging. As the preparation of a microscope slide takes place at room temperature and takes about 5 minutes (Snaith et al., 2010), imaging started 5 minutes after the release. Surprisingly, *nda3-KM311* cells did not release from the arrest under imaging conditions used (data not shown). After approximately a minute of imaging, MTs depolymerised and cells re-arrested, regardless of the imaging temperature (25-30ºC was tested). This suggests other strategies to visualise the mitotic state of Mto1/2 should be used.

5.3 Discussion

In this chapter my main aim was to generate a completely non-phosphorylatable Mto2 phosphomutant and use it to investigate the role of Mto2 phosphorylation in the regulation of the Mto2 self-interaction. I used SILAC to identify cell cycle-regulated phosphorylation sites on the existing mutant Mto2-17A, and a novel quantification method to uncover which of the identified phosphorylation sites are mitosis-specific. I generated five Mto2 phosphovariants, and analysed one of them, Mto2-NT2, as western blotting suggested that Mto2-NT2 was not phosphorylated in mitosis.

Analysis of interphase *mto2-NT2* cells suggested, that they are overall very similar to *mto2-17A*. Interphase *mto2-NT2* and *mto2-17A* cells contained comparable numbers of MT bundles, both in *mto1[NE]-GFP* and *mto1[bonsai]-GFP* backgrounds. In *mto1[NE]-GFP* cells, *mto2-NT2* and *mto2-17A* contained more MT bundles than wild-type cells. This supports the hypothesis discussed in Chapter 4, that Mto2 phosphorylation negatively regulates interphase MT nucleation, and is consistent with results presented in Section 4.2.7, where an increasing number of alanine substitutions in Mto2 resulted in an increase in cytoplasmic MT nucleation levels. Somewhat surprisingly, this increase was not observed in *mto1[bonsai]-GFP* cells where increasing the number of alanine substitutions did not lead to an increased number of cytoplasmic MT bundles. The number of bundles slightly increased in *mto2-6A* and *mto2-13A* relative to wild-type cells, and then dropped in *mto2-17A* and *mto2-NT2*. The difference between observations in *mto1*$^{+}$ cells (Section 4.2.7) and *mto1[bonsai]-GFP* cells could be explained by two independent reasons. The first possible reason stems from the fact that *mto1[bonsai]-GFP* cells contain more MTs than *mto1*$^{+}$ cells; therefore, perhaps *mto1[bonsai]-GFP* cells already have the maximal possible number of MTs, and formation and maintenance of any further MTs is not possible, for example because there is not enough of further tubulin available, or all MT polymerases and stabilising enzymes, such as fission yeast homologue of XMAP215, Dis1, are already bound to existing MTs (Roque et al., 2010; Wade, 2009). The second possible reason is that Mto1[bonsai]-GFP puncta size increases with an increasing number of alanine substitutions, and reaches sizes substantially bigger than wild-type in both *mto2-17A* and *mto2-NT2* cells. This could impair the MT nucleation; presumably, above a certain size the complex becomes a less efficient nucleator. This explanation is supported by the

fact that an increase in MT bundles number is observed in *mto1[NE]-GFP* cells, where no aggregation occurs.

mto2-17A and *mto2-NT2* cells are also similar during mitosis. I attempted to analyse the Mto1/2 complex formation in mitosis in four ways. First, I looked at the Mto1/2 complex localisation to the NE in *mto1[NE]-GFP* cells. In *mto2*$^{+}$ cells, Mto1[NE]-GFP delocalises from the NE upon mitotic entry (Groocock PhD Thesis, 2010). This was also observed in *mto2-17A* (consistent with results presented in Section 4.2.12) and *mto2-NT2* cells. Upon delocalisation, the Mto1[NE]-GFP signal became diffuse, suggesting that in all of these different *mto2* backgrounds, the Mto1/2 complex disassembles (i.e. no freely diffusing puncta were observed). The delocalisation from the NE can be a result of the Mto1/2 complex disassembly (if only a fully multimerised complex could interact with the NE receptor), or can be a result of a disruption of the interaction between the NE and the Mto1/2. This is discussed in more detail in Sections 4.2.12 and 4.3.2. The other three ways involved looking at Mto1[bonsai]-GFP puncta in various genetic backgrounds. Second, I looked at Mto1[bonsai]-GFP puncta in mitotic cells from asynchronous cultures. Mto1[bonsai]-GFP puncta seemed to appear in some *mto2-17A* and *mto2-NT2* cells with short spindles, however, it was difficult to determine if these occur in metaphase or early anaphase cells, therefore the experiment was non-conclusive. Third, I looked at Mto1[bonsai]-GFP puncta in mitotic cells in *cdc25-22* arrested cells. Some Mto1[bonsai]-GFP puncta were observed in *mto2-17A* and *mto2-NT2* cells, although a time-course experiment suggested that cells were under high stress conditions, hence any observations should be treated with caution. Furthermore, *cdc25-22* arrested cells are much longer than *cdc25*$^{+}$ cells, which also makes data interpretation difficult. Finally, I also attempted to use *nda3-KM311* arrest to enrich for mitotic cells. However, in the imaging conditions used (Snaith et al., 2010), cells did not release from the arrest. Thus, none of the experiments performed definitely showed whether the Mto1[bonsai]-GFP puncta persist in mitosis.

More experiments are needed to generate more definitive conclusions. First, Mto2-NT2-GFP should be imaged in the presence and absence of Mto1, as was done for Mto2-17A-GFP in Section 4.2.15. Imaging of Mto2-NT2-GFP in *mto1*Δ cells would allow observing whether the Mto2 self-interaction is still regulated in cell-cycle dependent manner in *mto2-NT2-GFP* cells. Second, Mto1[bonsai]-GFP in *mto2-NT2* cells should be co-imaged with a marker, that would allow to distinguish between

metaphase and anaphase cells. Such a marker could be Cdc13, fission yeast Cyclin B, which is rapidly degraded during metaphase-to-anaphase transition (Decottignies et al., 2001; Tatebe et al., 2001).

Third, the *nda3-KM311* arrest should be re-attempted, but possibly using different imaging conditions. Current work in the lab (S. Ashraf, K. Sawin, unpublished) showed that a "closed" imaging system (that is, a sealed microscope slide) along with the use of GFP laser triggers a stress response in cells. This potentially could explain why *nda3-KM311* cells re-arrested during imaging. A solution for that is the use of a different imaging system that would allow imaging in more physiological conditions. Sanju Ashraf's work in the Sawin lab showed that use of an YFP tag in combination with an "open" imaging system (in which cells have access to oxygen and nutrients) allows for imaging of proteins of interest without triggering the stress response. Therefore, imaging of Mto1[bonsai]-YFP in *nda3-KM311* arrested and subsequently released into mitosis cells in an "open" system could potentially be an ideal experiment to look at Mto1/2 complex in mitosis in *mto2-NT2* cells.

Chapter 6
Structure-function mutagenesis of Mto2 conserved regions to reveal Mto2 domains important for its function

6.1 Introduction

In Chapters 4 and 5 I demonstrated that Mto2 phosphorylation regulates Mto1-Mto2 and Mto2-Mto2 interactions. Phosphorylation may regulate protein-protein interactions by two non-exclusive mechanisms. First, phosphorylation could occur directly at the interaction interface, thus changing the polar properties of a modified region. Second, phosphorylation could occur at a residue not directly involved in establishing the interaction and induce conformational changes that disrupt the interaction. Currently, no data on the Mto1/2 complex structure is available (such as EM or crystallographic data); therefore, it is unknown which Mto2 regions are important for the Mto1-Mto2 and Mto2-Mto2 interactions. A truncation analysis previously performed in the Sawin lab (Groocock PhD Thesis, 2010) showed that removing the first 88 amino acids of Mto2 did not influence the interaction between Mto1 and Mto2 and Mto2-Mto2 self-interaction. Cells expressing *nmt81*:HFG-Mto2(89-397) (HFG tag is made of His_6, FLAG and GFP) had reduced number of MT bundles when compared to wild-type cells. However, *nmt81*:HFG-Mto2(89-397) localised similarly to wild-type Mto2-GFP (MTs, eMTOCs, SPBs), suggesting that the Mto1/2 complex is intact in these cells. Cells expressing further N-terminal and C-terminal truncations tagged with HFG tag (Mto2(181-397) and Mto2(1-320)) exhibited *mto2*Δ MT arrays, yet mutant proteins still localised to SPBs and other MTOCs;. Thus, at least a fraction of the total protein pool was stable and able to interact with Mto1 to promote localisation to MTOCs. *In vitro* MBP pull down assays employing bacterially expressed MBP-Mto2 truncations used as a bait, and full length Mto2 tagged with NusA was used to analyse Mto2 self-interaction. The assay showed that Mto2(89-397)-MBP is able to interact with Mto2-NusA, but removal of additional amino acids at either terminus abolishes the interaction with Mto2-NusA (summarised in Table 6.1).

Table 6.1. Summary of Mto2 truncation analysis. For *in vitro* pull down assays Mto2 truncations were tagged with MBP, and full length Mto2-NusA was used as a bait. For *in vivo* analysis, Mto2 truncations were tagged with *nmt81:*HFG tag (His_6 FLAG GFP) and then the protein localisation was examined by microscopy. MT arrays were analysed in *mto2-HFG* cells by imaging GFP-α-tubulin (Groocock PhD Thesis, 2010).

Truncation	Pulls down Mto2-NusA *in vitro*?	Localisation in cells	MT arrays in cells
Mto2(89-397) [N1]	Yes	Slightly reduced compared to WT MTs, eMTOCs, SPB	Reduced MT number compared to WT
Mto2(181-397) [N2]	No	Strong at SPBs, faint eMTOCs, iMTOCs	Phenocopies *mto2*Δ cells
Mto2(1-320) [C1]	No	Faint at SPBs, very faint at eMTOCs, iMTOCs	Phenocopies *mto2*Δ cells
Mto2(1-258) [C2]	No	n.a.	n.a.

Another way to perform interaction mapping is a technique termed alanine scanning mutagenesis (Cunningham and Wells, 1989; Morrison and Weiss, 2001). This method involves mutating specific amino acids in a protein of interest, to probe how sidechains of individual amino acids (or of clusters of amino acids) contribute to the properties of the protein and to interactions between proteins. Protein residues that are in direct contact mediate non-covalent interactions between proteins via hydrogen bonds, salt bridges, dipole-dipole interactions or hydrophobic interactions. Substitution of a given amino acid with alanine is particularly useful in looking for protein-protein interactions. First, all the atoms beyond the β-carbon are removed in the sidechain. Second, alanine sidechain (a methyl group) is neither polar nor hydrophobic, thereby eliminating all types of interactions listed above. This technique was successfully applied to address many biological questions, including CD4 binding to HIV-gp120 (Ashkenazi et al., 1990) or the enzymatic activity of protein kinases (Gibbs and Zoller, 1991). Recently, a systematic study investigated the role of charged amino acids at the surface of an epithelial sodium channel. Alanine scanning focused on charged residues of channel proteins showed their importance in the channel behaviour (Edelheit et al., 2011).

In this chapter, I aimed to identify regions of Mto2 important for Mto1-Mto2 and Mto2-Mto2 interaction. I used “charged-to-alanine” scanning, which involved mutating stretches of charged amino acids within Mto2 sequence to alanines. I showed that there are two regions of Mto2 required for Mto1-Mto2 interaction: the predicted α-helical coiled-coil region located in the N-terminal part of the protein and

a region highly conserved in (fungal) Mto2 homologues, located in the C-terminal part of Mto2. It remains to be uncovered whether these regions are directly involved in Mto1-Mto2 binding. I also showed, that a region at Mto2 N-terminus plays a role in the interaction between the Mto1/2 complex and the γ-TuC.

Imaging and part of biochemical experiments were first performed by Christian C. Wiggam, an undergraduate student that I supervised. However, all the experiments presented below were performed by me.

6.2 Results

6.2.1 Design of *mto2* alanine-scanning (*mto2-asc*) mutants

Mto2 is a relatively unstructured protein, with several regions predicted to be disordered (Fig. 6.1 A). GlobPlot software predicted that residues 117-147 form a coiled-coil structure, while the residues 184-259 are likely to form a globular domain (Fig. 6.1 A) (Linding, 2003). As mentioned in the introduction, in the absence of any structural information about Mto2, "charged-to-alanine" scanning was applied to perform Mto2 interaction mapping. Clusters of charged amino acids selected from Mto2 primary sequence were mutated to alanine. Twelve mutant constructs were generated, encompassing ten distinct clusters of charged amino acids (Fig. 6.1 B). Residues were selected for mutations if they were conserved in fungal homologues of Mto2. DNA constructs purchased from GENEART were integrated in *mto1[bonsai]-GFP mCherry-α-tubulin* strains, which allowed for subsequent biochemical and cytological analysis. These mutants will be henceforth referred to as *mto2-asc* (for alanine-scanning).

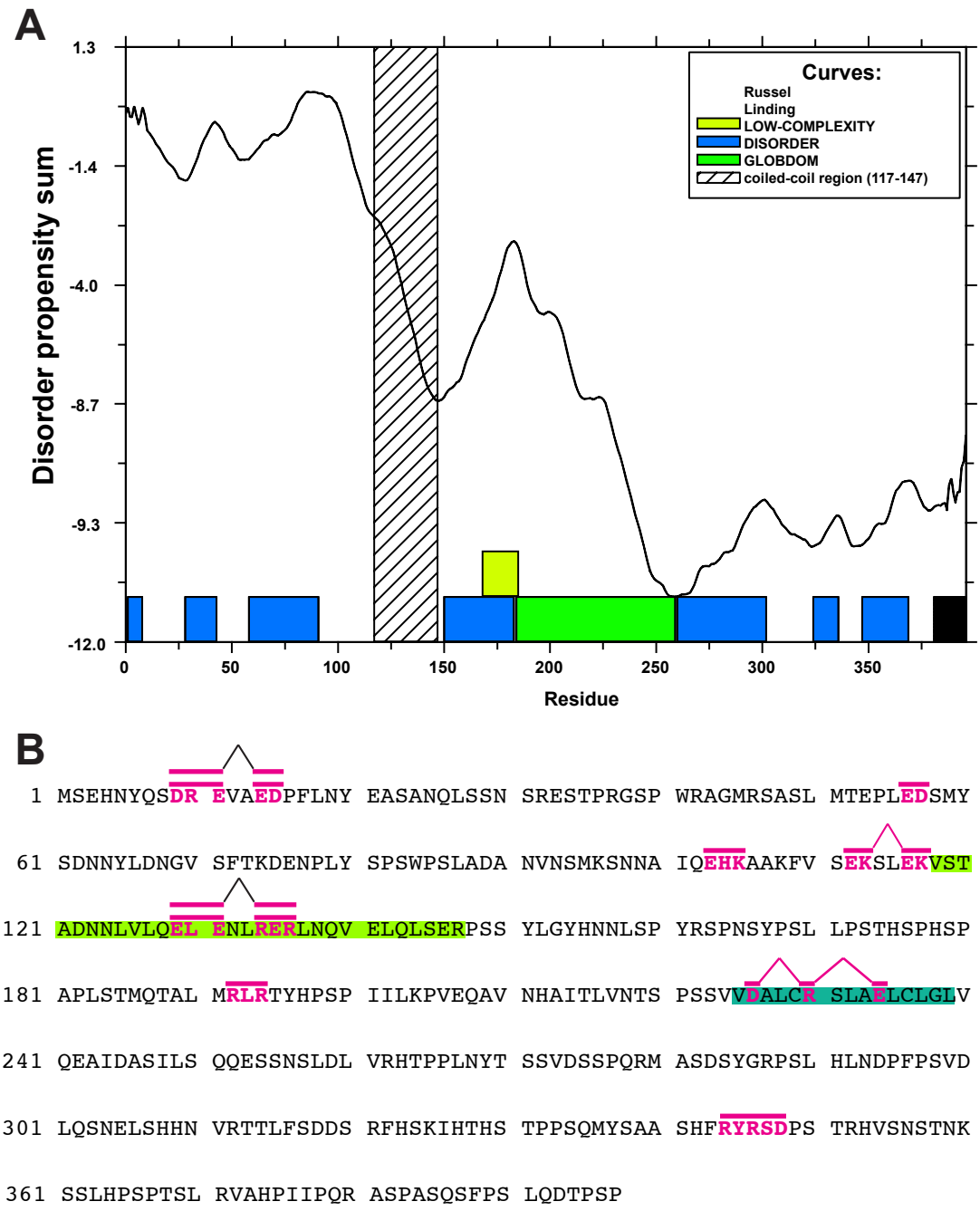

Figure 6.1. Design of *mto2-asc* mutants.
(A) Mto2 secondary structure prediction. Mto2 secondary structure was predicted using GlobPlot (www.globplot.embl.de). Residues 117-147 are predicted to have coiled-coil structure, while residues 184-259 are predicted to form a globular domain. The black line represents propensities of given residues to be in either an ordered or disordered region, based on Russel/Lindeing set of propensities for amino acids (Linding a et al., 2003). The positive slope indicates that a given region is disordered while the negative slope indicates that a region is structured.
(B) Mto2 primary sequence is shown. Mutated charged residues are indicated in magenta. Magenta bars connected by black lines indicate constructs that have a combination of two mutations. Magenta bars joined by magenta lines represent mutations made in a single construct, where the mutated residues were not adjacent to each other. The predicted α-helical coiled-coil region is indicated in green, the highly conserved is indicated in teal.

6.2.2 Mutations in three regions of Mto2 affect interphase MT networks

In order to address whether MT arrays are normal in *mto2-asc* cells, live-cell imaging of mCherry-α-tubulin was used to directly compare MT networks in *mto2*$^{+}$ and *mto2-asc* mutant strains (Fig 6.2). As shown before (Lynch et al., 2013)., *mto1[bonsai]-GFP mCherry-α-tubulin* cells expressing wild-type Mto2 showed normal MT arrays, and Mto1[bonsai]-GFP puncta were observed in the cytoplasm and along MTs. By contrast, *mto2*Δ cells contained very few MTs and no Mto1[bonsai]-GFP puncta. Mto1[bonsai]-GFP puncta were abundant in all mutants apart from *mto2*-129ELE, *mto2*-129ELE2RER, *mto2*-134RER and *mto2*-226D3R3E, in which puncta could occasionally be observed, mostly in post-mitotic cells.

To obtain more quantitative information, the percentage of abnormal MT bundles was also counted for each mutant (Fig. 6.3 A) A characteristic of impaired *mto2* function is the shape of MT bundles: in wild-type (*mto2*$^{+}$) cells, MT bundles extend along the long axis of the cell and terminate at cell tips, whereas in *mto2*Δ (as well as *mto1*Δ) they often curve abnormally around cell ends (Samejima et al., 2008; Sawin et al., 2004; Venkatram et al., 2004; Zimmerman and Chang, 2005). The number of MT bundles per cell was also counted for each mutant, and compared to that of *mto2*$^{+}$ and *mto2*Δ (Fig. 6.3 B).

Quantification of MT bundles showed that five *mto2-asc* mutants (*mto2*-009DRE, *mto2*-056ED, *mto2*-103HK, *mto2*-112EK2EK and *mto2*-344RYRSD) had wild-type MT bundles number per cell ($p>0.01$ in Wilcoxon rank-sum test, Table 6.2), they also contained either a small number or no abnormal MTs, as defined in Fig. 6.3 A.

Three mutants (*mto2*-009DRE2ED, *mto2*-014ED and *mto2*-192RLR) showed an intermediate phenotype with a visible decrease in MT number per cell ($p>10E-06$ when compared to wild-type) and occasional aberrant MTs. All three mutants are very similar to one another ($p>0.5$ when compared pairwise).

The third group of mutants, including *mto2*-129ELE, *mto2*-129ELE2RER, *mto2*-134RER and *mto2*-226D3R3E, showed the most severe phenotype ($p<10E-07$ when compared to wild-type), with greatly reduced number of MTs bundles and many aberrant MTs. This phenotype highlights the important of two Mto2 regions – the coiled-coil region (mutated in *mto2*-129ELE, *mto2*-129ELE2RER and *mto2*-134RER cells) and the “conserved” region (mutated in *mto2*-226D3R3E).

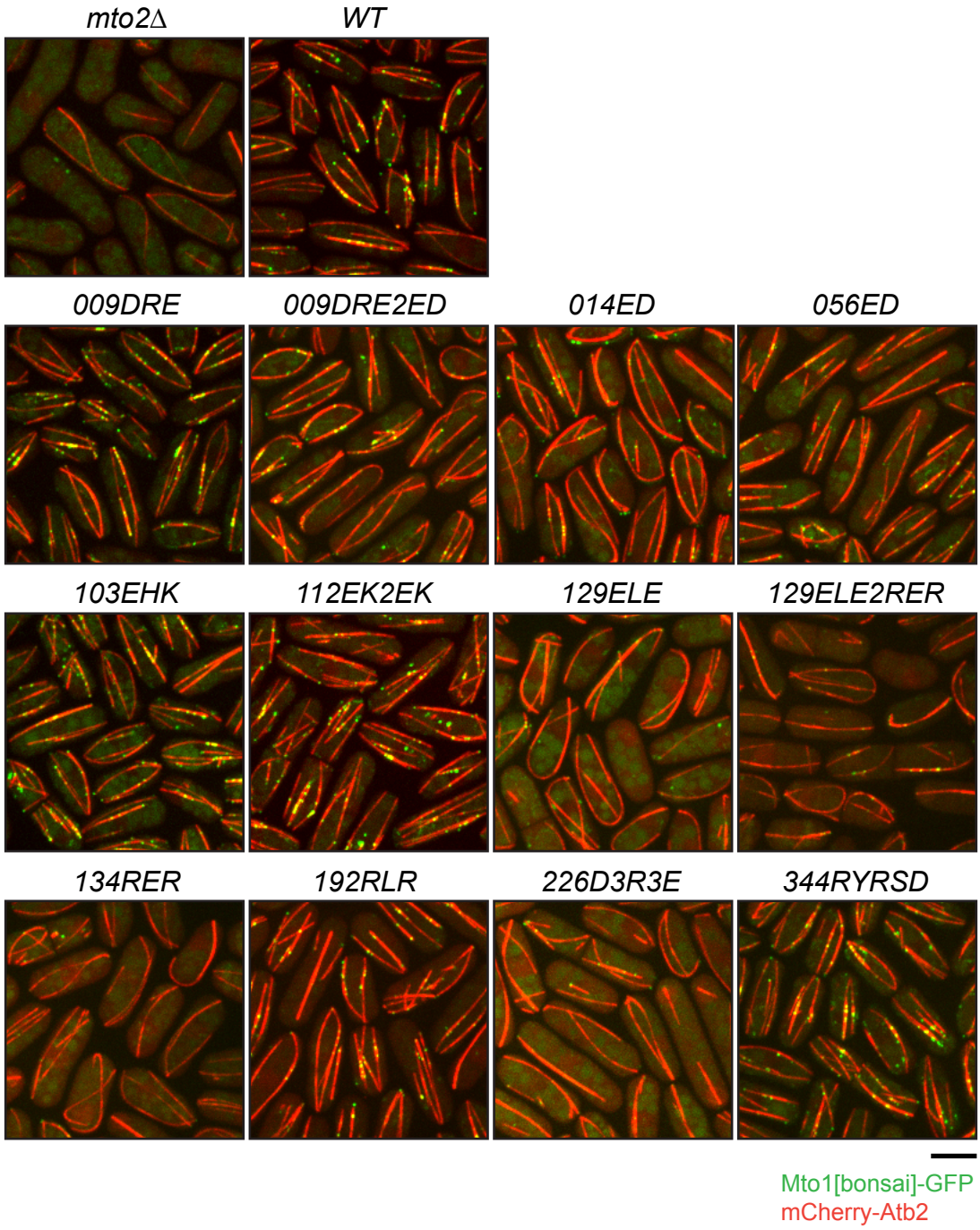

Figure 6.2. Cytoplasmic MT networks in *mto2-asc mto1[bonsai]-GFP* cells. Interphase MTs (mCherry-α-tubulin, red) in strains expressing Mto1[bonsai]-GFP (green). Bar, 5μm. [Strains: KS6678, KS6928, KS7057, KS7059, KS7061, KS7063, KS7065, KS7069, KS7071, KS7073, KS7075, KS7077, KS7079]

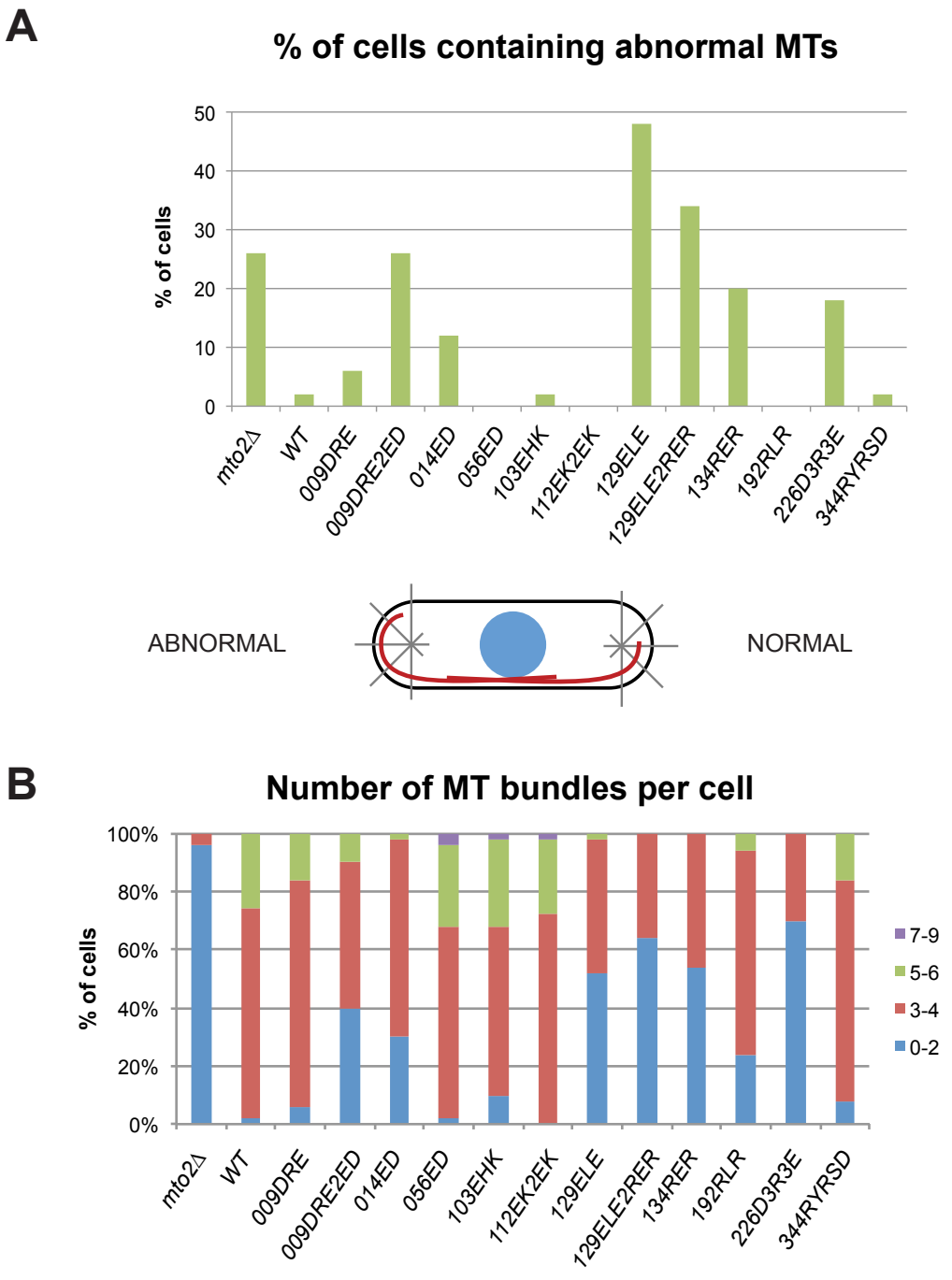

Figure 6.3. Quantitative analysis of MT bundles in *mto2-asc* cells.
(A) Number of abnormal MTs observed in Figure 6.2, n=50. MT was considered abnormal if it curved around more than 75% of the cell tip.
(B) Number of MT bundles per cell observed in Figure 6.2, n=50.

Somewhat surprisingly, even mutants with the most severe MT phenotypes were statistically different from *mto2*Δ cells. In *mto2*Δ cells, the majority of cells contained just one microtubule, and more than 20% of cells had no microtubules at all. By contrast, the most severe of the mutants (*mto2*-129ELE, *mto2*-129ELE2RER, *mto2*-134RER and *mto2*-226D3R3E) contained one to three MTs, with majority of cells containing two microtubules. Almost complete absence of Mto1[bonsai]-GFP puncta suggests that the multimeric Mto1/2 complex does not form efficiently in these mutants. However, MTs seem to be more stable than in *mto2*Δ cells. Potentially, these multimerisation-incompetent mutant forms of Mto2 are somehow stabilising MTs, for instance by binding to MT lattice or to the γ-TuC at minus ends of existing MTs. It has been suggested that the Mto2-GFP can transiently bind to MTs in the absence of Mto1 (Lynch PhD Thesis, 2012). In future experiments, it would be interesting to compare *mto2-asc* mutants to *mto1-334* mutant, in which Mto2 exists, but is not able to bind Mto1, therefore possibly mimicking the situation observed in some of the *mto2-asc* strains (Samejima et al., 2008).

6.2.3 Mutations in three Mto2 regions affect Mto1-Mto2 and Mto1/2-γ-TuC interactions

To determine how *mto2-asc* mutations affect Mto2 interactions with Mto1 and the γ-tubulin complex, I performed an anti-GFP immunoprecipitation (i.e. pulling down the Mto1[bonsai]-GFP in these cells), followed by western blotting for Mto1, Mto2, and γ-tubulin (Fig. 6.4). Analysis of immunoprecipitation "inputs" on anti-Mto2 western blots revealed that Mto2-asc proteins are expressed at wild-type levels (Fig. 6.4 A, Input; compare lane 1 with lanes 3-15). In some of the mutants, the phosphorylation state of Mto2 appeared to be affected (*mto2*-014ED, *mto2*-056ED, *mto2*-192RLR; Input, lanes 6, 7 and 13), with faster migrating (presumably hypophosphorylated) isoforms of Mto2 more abundant than in wild-type cells and most other mutants. This suggests that the mutated residues might play a role in binding of interphase kinases to Mto2. Their role in kinase docking might be direct (i.e., they might be a part of an interaction surface to which the kinase binds) or indirect (i.e., they might affect Mto2 folding or multimerisation state which in turn affects the kinase binding). As Mto1[bonsai]-GFP puncta are observed in these mutants, and two of them exhibit wild-type MT arrays, it seems unlikely that the

general folding or multimerisation state of Mto2 is affected; therefore the notion that the kinase binding site is affected directly seems to be more plausible.

As expected, both wild-type Mto2 and Gtb1 (γ-tubulin) were co-immunoprecipitated with Mto1[bonsai]-GFP (Fig. 6.4 A, Anti-GFP pulldown, lane 3), whereas no Mto2 or Gtb1 were co-immunoprecipitated in *mto2*Δ cells (Fig. 6.4 A, Anti-GFP pulldown, lane 3; Fig. 6.4 B and C). Mto2 and Gtb1 were also efficiently co-immunoprecipitated by Mto1[bonsai]-GFP in *mto2*-009DRE, *mto2*-056ED, *mto2*-103HK, *mto2*-112EK2EK and 344RYRSD cells (Anti-GFP pulldown, lanes 4, 7, 8, 9 and 15, quantified in Fig.6.4 B and C), which is in agreement with the observation that these five mutants exhibited wild-type MT arrays (see also Fig.6.2 and 6.3).

In the four mutants that exhibited "*mto2*Δ-like" MT networks (*mto2*-129ELE, *mto2*-129ELE2RER, *mto2*-134RER and *mto2*-226D3R3E, Anti-GFP pulldown lanes 10-12 and 14) neither Mto2 nor Gtb1 was efficiently co-immunoprecipitated with Mto1[bonsai]-GFP, which may provide a mechanistic explanation for the observed MT phenotype. This again highlights a critical role the coiled-coil and the "highly conserved" region of Mto2 play in its activity.

Interestingly, in two mutants (*mto2*-009DRE2ED and *mto2*-014ED, Anti-GFP pulldown lanes 5 and 6) wild-type amounts of Mto2, but no Gtb1, co-immunoprecipitated with Mto1[bonsai]-GFP. The amount of Gtb1 detected by western blotting was comparable to signal intensity in *mto2*Δ lane (compare Anti-GFP pulldown lanes 2, 5 and 6), therefore was near to background levels, as Mto1[bonsai]-GFP is not able to immunoprecipitate Gtb1 in the absence of Mto2 (Lynch et al., 2013). This appears to be in contradiction with microscopy data, which shows that *mto2*-009DRE2ED and *mto2*-014ED cells exhibit "intermediate" MT phenotype (Fig. 6.2 and 6.3), and will be discussed in more detail in Section 6.3.

Another interesting mutant is the *mto2*-192RLR construct (Anti-GFP pulldown lane 13). In this mutant, the amount of Mto2 co-immunoprecipitated with Mto1[bonsai]-GFP is greatly decreased when compared to wild-type, and is comparable to what is seen in *mto2*Δ-like mutants. Nevertheless, this mutant is able to efficiently bind the γ-TuC. This observation is in agreement with microscopy data, which shows that this mutant has an "intermediate" phenotype (Fig. 6.2 and 6.3) implying that the cytoplasmic MT nucleation is impaired but not abolished.

.

Table 6.2. Statistical analysis of MT bundles number in *mto2-asc* cells when compared to *mto2*$^{+}$ and *mto2*Δ cells. Wilcoxon rank-sum test was used (Mann and Whitney, 1947). P values are shown. p<0.01 was considered statistically significant. Highlighting colours indicate mutants with wild-type-like MT arrays (green), *mto2*Δ-like arrays (red), or intermediate arrays (yellow). Average number of MT bundles per cell is shown for each strain.

mto2-asc Mutant	No. of bundles	WT	mto2Δ	009 DRE	009 DRE2ED	014 ED	056 ED	103 EHK	112 EK2EK	129 ELE	129 ELE2RER	134 RER	192 RLR	226 D3R3E
WT	**3.96**													
mto2Δ	**1.06**	2.2E-16												
009 DRE	**3.68**	0.3783	2.2 E-16											
009 DRE2ED	**2.96**	2.234 E-04	1.665 E-12	0.00243										
014 ED	**2.92**	3.969 E-06	8.575 E-15	6.222 E-05	0.911									
056 ED	**4.16**	0.3119	2.2 E-16	0.04746	1.158 E-05	6.596 E-08								
103 EHK	**4.02**	0.5049	2.2 E-16	0.1032	6.488 E-05	1.473 E-06	0.8046							
112 EK2EK	**4.24**	0.05424	2.2 E-16	0.00241 4	3.105 E-07	1.077 E-10	0.4582	0.3815						
129 ELE	**2.4**	1.57 E-08	2.0 E-08	1.948 E-07	0.03093	0.0185 8	5.852 E-10	8.113 E-09	4.236 E-12					
129 ELE2RER	**2.22**	1.313 E-10	8.703 E-08	1.552 E-09	0.002794	5.361 E-04	7.445 E-12	1.457 E-10	7.701 E-14	0.4156				
134 RER	**2.3**	2.134 E-10	6.613 E-09	2.869 E-09	0.01091	0.0032 29	8.358 E-12	2.739 E-10	3.201 E-14	0.7717	0.5218			
192 RLR	**3**	2.623 E-05	1.94 E-14	3.394 E-04	0.86	0.6918	5.799 E-07	9.335 E-06	1.465 E-09	0.0102	2.894 E-04	0.001 423		
226 D3R3E	**2.24**	4.238 E-12	1.677 E-09	5.977 E-11	0.001721	9.358 E-05	3.668 E-13	1.506 E-11	4.468 E-15	0.4064	0.9061	0.476 8	4.457 E-05	
344 RYRSD	**2.62**	0.2115	2.2 E-16	0.6972	0.006207	2.981 E-04	0.02077	0.05379	8.133 E-04	8.021 E-07	6.486 E-09	1.546 E-08	0.00141 7	2.784E-10

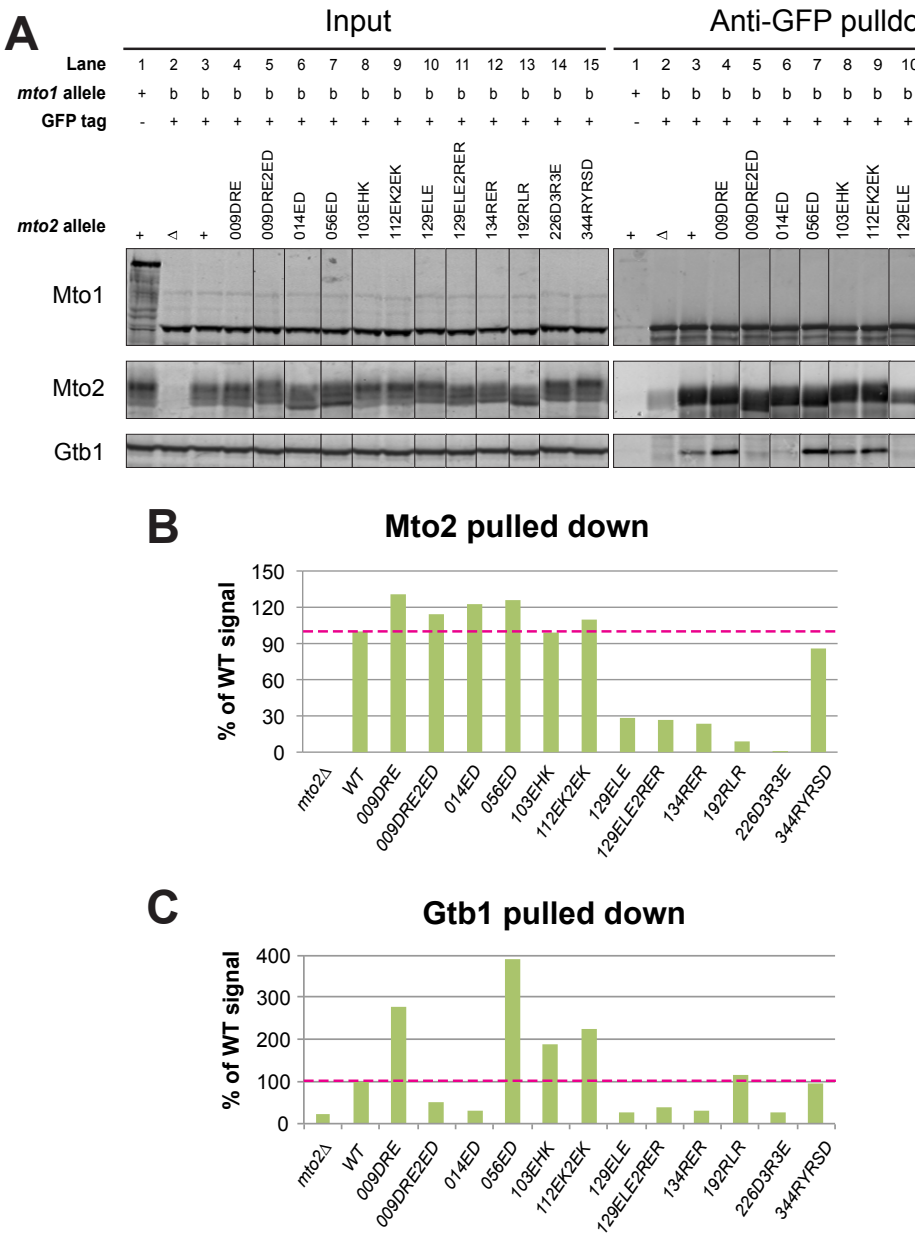

Figure 6.4. Mto1-Mto2 and Mto1/2-Gtb1 interactions are impaired in *mto2-asc* mutants.

(A) Total cell extracts from *mto2-asc* cells expressing Mto1[bonsa immunoprecipitated with anti-GFP antibody. Western blots were probed again and Gtb1. Because samples were loaded in an undesired order, the image was order samples with an increasing number of mutated residue . b, *mto1[bonsai]-*

(B) Quantificaton of Mto2 co-immunoprecipitated by Mto1[bonsai]-GFP in *m* Integrated intensities of IRDye800 were measured using Odyssey V3.0, and M normalised to Mto1[bonsai]-GFP and shown as percentage of wild-type sig mto2Δ lane was used for background subtraction. Magenta line indicates wild-t

(C) Quantificaton of Mto2 immunoprecipitated by Mto1[bonsai]-GFP in *m* Quantification was performed as in (B). Signal in *mto1*$^{+}$ lane was used fo subtraction. Magenta line indicates wild-type levels.

[Strains: KS516, KS6678, KS6928, KS7057, KS7059, KS7061, KS7063, KS7 KS7071, KS7073, KS7075, KS7077, KS7079]

6.3 Discussion

In this chapter I used “charged-to-alanine” mutagenesis to identify Mto2 regions important for protein-protein interactions. I analysed *mto2-asc* mutants biochemically and microscopically, and identified two regions that are important for the Mto1-Mto2 interaction, and one that is important for the interaction between the Mto1/2 complex and the γ-TuC.

All *mto2-asc* mutant proteins were expressed at wild-type levels, and exhibited several phosphoisoforms. Observation that mutant Mto2 proteins are efficiently phosphorylated in cells suggests that the protein folding is not affected, as misfolded protein would not allow for kinase binding. Presumably, there are several interphase kinases that bind to and phosphorylate Mto2. If Mto2 phosphorylation is largely unaffected, this suggests that kinases were able to bind to Mto2; therefore, the protein folding is likely to be similar to wild-type (even in nucleation-deficient mutants).

Three of the mutant proteins showed slightly reduced phosphorylation when compared to wild-type (*mto2*-014ED, *mto2*-056ED, *mto2*-192RLR). This might indicate that kinase docking sites were affected in these mutants. Alternatively, protein folding could be affected, which consequently could lead to impaired kinase binding; this, however, appears to be less likely, as in all these mutants Mto1[bonsai]-GFP puncta are formed suggesting that the protein is correctly folded.

Five of the analysed *mto2-asc* mutants (*mto2*-009DRE, *mto2*-056ED, *mto2*-103HK, *mto2*-112EK2EK and *mto2*-344RYRSD) exhibited wild-type MT arrays; they also efficiently interacted with both Mto1[bonsai]-GFP and Gtb1 (in some cases, the interaction with Gtb1 was much stronger than in wild-type). This suggests that none of the mutated residues plays an important role in Mto2 folding or binding to other proteins.

In two of the analysed mutants (*mto2*-009DRE2ED, *mto2*-014ED) Mto1[bonsai]-GFP failed to efficiently interact with Gtb1, while still being able to interact with Mto2. However, as these mutants contain more MTs that *mto2*Δ-like cells, I predict that nucleation, most likely impaired, occurs in these cells. This implies that there must be a physical interaction between the Mto1/2 complex and the γ-TuC, because MT nucleation would not take place if the Mto1/2-γ-TuC interaction were abolished. Most likely, the western blot Gtb1 signal was too weak to be detected. During data acquisition, near to maximal LiCOR laser power had to be

used in order to obtain detectable Gtb1 signal, suggesting that the Gtb1 quantities were low. Therefore, most likely these mutants do interact with the Gtb1, just at levels much lower than wild-type, which allows them to maintain low levels of MT nucleation. This suggests that the N-terminus of Mto2 is involved in the interaction with the γ-TuC, independently of the interaction with Mto1. In both of these mutants, Mto1[bonsai]-GFP puncta were seen by microscopy, confirming that the Mto1-Mto2 interaction occurs *in vivo* (the puncta are not formed in the absence of Mto1-Mto2 interaction). Because *mto2*-009DRE exhibits wild-type MT phenotype, and pulls down wild-type amounts of Gtb1, it is likely that the phenotype observed in *mto2*-009DRE2ED is due to mutation of residues 14E and 15D only. This indicates that residues 14E and 15D are important for efficient γ-TuC binding by the Mto1/2 complex.

mto2-192RLR mutant also exhibited 'intermediate' MT arrays; however, in this mutant background, Mto2-192RLR did not co-immunoprecipitate efficiently with Mto1[bonsai[-GFP, while Gtb1 did. Potentially, mutations in this region might influence the strength of the Mto1-Mto2 interaction, either directly (if they are a part of Mto1-Mto2 interaction interface), or indirectly (by affecting folding of the neighbouring crucial regions, namely the coiled-coil or the "conserved" region). If that were the case, Mto1-Mto2 could interact to form a complex, but the interaction would be more labile resulting in a weaker Mto2 signal detected immunochemically.

Finally, four *mto2-asc* mutants (*mto2*-129ELE, *mto2*-129ELE2RER, *mto2*-134RER and *mto2*-226D3R3E) showed severely impaired MT networks; in these cells, neither Mto2 nor Gtb1 co-immunoprecipitated with Mto1[bonsai]-GFP. Mto1[bonsai]-GFP puncta were almost completely absent from these cells, showing that multimeric Mto1/2 complex was not formed. This identified two regions of Mto2 required for Mto1/2 complex formation: the central α-helical coiled coil and the highly conserved C-terminal region that lies within the predicted globular domain of Mto2 (Fig. 6.1 A). Interestingly, the two regions identified by mutagenesis lie within the only two regions of Mto2 that are predicted to be structured.

Previous work indicated that Mto2 oligomerises *in vitro* and *in vivo*, and this oligomerisation is the driver of the Mto1/2 complex formation (Lynch PhD Thesis, 2012). Hydrodynamic analysis suggested that endogenous Mto1/2 complex isolated from fission yeast extract may be heterotetrameric (Groocock PhD Thesis, 2010), while *in vitro* analysis of Mto1/2[bonsai] complex expressed in insect cells suggested it may form a dimer (Lynch PhD Thesis, 2012). These core subunits,

whether dimers or tetramers, could associate into larger complexes to form the multimeric Mto1/2 complex.

Mto2 multimerisation requires Mto2 to have at least two self-interaction surfaces; in addition, Mto2 also has to contain an Mto1-binding interface. The loss of Mto1-Mto2 interaction in *mto2*-129ELE, *mto2*-129ELE2RER, *mto2*-134RER and *mto2*-226D3R3E cells can be a result of direct abolition the Mto1-Mto2 interaction. Alternatively, loss of the Mto1-Mto2 interaction could be indirect, and be a result of abolition of the Mto2-Mto2 interaction. In agreement with the hypothesis that these two regions are important for Mto2 oligomerisation, preliminary experiments using bacterially expressed Mto2 fragments showed that fragments containing either Mto2 coiled-coil region or Mto2 conserved region are able to dimerise *in vitro* (H. Thakur, unpublished). Potentially, the loss of the Mto2 self-interaction might result in the loss of Mto1-Mto2 interaction. If Mto1 were able to interact with dimeric (but not monomeric) Mto2, abolishing Mto2 dimerisation would result in the loss of Mto1-Mto2 interaction, despite the Mto1-Mto2 interaction interface still being present in the protein. For example, the Mto1 interaction surface could be created upon Mto2 dimerisation or multimerisation (such that one molecule of Mto1 would bind "between" two molecules of Mto2). Alternatively, Mto2 dimerisation or multimerisation could induce conformational changes in Mto2 structure that would expose Mto1-binding surface.

More experiments should be done to further understand the role of identified regions in Mto2 protein-protein interactions. Mto1[bonsai]-GFP mCherry-α-tubulin movies should be acquired and MT nucleation frequency scored for each mutant. This would give an idea of the Mto1/2 complex MT nucleation capacity in these mutants. Perhaps, a better negative control for imaging could be *mto1-334[bonsai]-GFP mto2*$^{+}$ or *mto1(131-500)-GFP mto2*$^{+}$ strains, where Mto2 is present in cells, but not able to form the multimeric Mto1/2 complex, because Mto1 lacks the Mto2 binding domain (Lynch et al., 2013; Samejima et al., 2008).

Moreover, the anti-GFP co-immunoprecipitation should be repeated, and more Gtb1 used, which might allow me to address to what extent Gtb1 binding is affected in *mto2-asc* mutants, particularly in 009DRE2ED and 014ED mutants, as the experiment presented above was performed close to LiCOR detection limit.

To analyse the Mto2-Mto2 self-interaction in *mto2-asc* cells *in vivo*, a strain expressing two differently tagged Mto2 mutant copies should be made. This can be

done by creating a diploid strain, or by integrating an additional copy of *mto2* gene at a different than genomic locus. Another way to analyse the role of identified regions in protein-protein interaction is using insect cell expression system to produce mutant forms of Mto2. Mto2 purified from insect cells exists as a mixture of multimers of different sizes in a dynamic equilibrium (Lynch PhD Thesis, 2012). It would be interesting to know how mutations in the α-helical coiled-coil region or the conserved C-terminal region affect Mto2 the multimerisation state of Mto2. As the Mto1[bonsai]-GFP puncta formation is abolished in these mutants, I predict that they would not be able to multimerise efficiently. This would also allow addressing whether these non-multimeric Mto2 isoforms are able to interact with Mto1 (that is, whether Mto2 has to be multimeric to be able to interact with Mto1). Truncation analysis performed by Lynda Groocock suggested that abolishment of Mto2-Mto2 self-interaction does not completely abolish the Mto1-Mto2 interaction. This was, for instance, observed in Mto2-N2 mutant, which could not pull down Mto2-NusA *in vitro,* but when tagged with GFP, was able to localise to SPBs, eMTOCs and iMTOCs, which is mediated by Mto1. However, in the analysis performed by Lynda Groocock GFP-tagged proteins were expressed under *nmt81* promoter, and could have been overexpressed, which could have affected the observed phenotype.

Ultimately, the EM and crystal structures of the Mto1/2 complex as well as both proteins separately would provide information about the exact interaction surfaces within the complex.

Appendix 1. Identification of phosphorylation sites in Mto1

Introduction

In fission yeast, the Mto1/2 complex is required for all non-SPB cytoplasmic nucleation. In previous Chapters, I focused mainly on the Mto2 protein and its role in regulation of the complex performance throughout the cell cycle. However, it is also possible, that Mto1 is regulated in a cell cycle regulated manner.

Mto1 is a relatively large coil-coiled protein of 1115 amino acids (Sawin et al., 2004; Venkatram et al., 2004), containing a γ-TuC-binding CM1 region (Sawin et al., 2004; Zhang and Megraw, 2007) (Fig. 3.1). It promotes cytoplasmic MT nucleation from several cytoplasmic MTOCs, by localising the γ-TuC to distinct foci within the cell, such as MTs, the NE, the outer face of the SPB and eMTOCs (Sawin et al., 2004; Venkatram et al., 2004). It does so using multiple localisation domains: the NE-localisation domain is located at the N-terminus, the C-terminus promotes localisation to interphase and mitotic SPBs, MTs and to eMTOCs (Samejima et al., 2008, 2010; Sawin et al., 2004). The CM1 region is located towards the N-terminus and is followed by more centrally located Mto2-binding region. All of these interactions can be potentially regulated by PTMs, such as phosphorylation. Mto1 phosphorylation has been reported previously, but the significance of it remains to be studied (Wilson-Grady et al., 2008).

During Mto2-17A-GFP immunoprecipitation from interphase and mitotic extracts, stoichiometric amounts of Mto1 in interphase and mitosis were co-immunoprecipitated. These were subjected to SILAC analysis to identify interphase- or mitosis-specific phosphorylation sites in Mto1. In this appendix I showed that Mto1 is phosphorylated both in interphase and mitosis. The biological roles of detected phosphorylation events are unknown and further analysis is required.

Mto1 is phosphorylated both in interphase and mitosis

To identify interphase- or mitosis-specific phosphorylation events occurring on Mto2-17A-GFP, I compared interphase and mitotic samples containing Mto1 that co-purified with Mto2-17A-GFP from fission yeast cells. *nda3-KM311* allele was used to arrest cells in metaphase (Hiraoka et al., 1984; Moreno et al., 1989; Toda et al., 1983). Anti-GFP immunoprecipitation was performed and proteins were resolved

on 10% SDS-PAGE and Coomassie stained (see Fig. 5.3 A). Mto1 was stoichiometrically co-immunoprecipitated by Mto2-17A-GFP from both in interphase and mitotic extracts. Analysis of Mto2 phosphorylation is presented in Chapter 4. Mto1 bands were excised, subjected to in-gel trypsin digest followed by Stage-Tip purification (Rappsilber et al., 2003), and then Juan Zhou from the Rappsilber group carried out the MS analysis.

Table A1.1. Experimental design MS runs summarised.

Experiment	Light culture	Heavy culture	Quantitative?
1	MITOSIS	INTERPHASE	YES
2	INTERPHASE	MITOSIS	YES

Two independent MS runs were performed (Table A1.1) and a number of phosphorylation sites were identified (Table A1.2). The majority of phosphopeptides were detected in both samples, but with distinct Mitosis/Interphase ratios (that is: heavy-to-light or light-to-heavy, depending on the experiment). The M/I ratios shown in Table A1.2 were calculated by Maxquant software, based on the signal intensity of MS peaks detected by the mass spectrometer. Because the MS analysis of Mto1 phosphorylation was not the main purpose of this study, the abundance of phosphorylated and unmodified peptides was not quantified manually, as described in Chapter 5 for Mto2-17A-GFP peptides. Instead, normalised values generated by MaxQuant were used to obtain M/I ratios. If a ratio higher than one is obtained using Method A, it means that the phosphopeptides was more abundant in the mitotic sample. If a score greater than one is obtained by method C, it means that the unmodified peptide is less abundant, and therefore, that modified peptides are more abundant in the mitotic sample.

Table A1.2. Quantification of phosphorylated and unmodified peptides detected during SILAC analysis of Mto1. Quantification performed is identical to the one used in Chapter 5 (see Section 5.2.2.2). Method A uses H/L ratio for phosphopeptides only, while Method C for unmodified peptides only. Method B was not used. In Method C, the I/M (not M/I) ratio is shown, to better show the relative abundance of the modified peptides. n.a., not assigned. -, not detected.

M/I ratio / Peptide	Experiment 1			Experiment 2		
	Residue	Method A	Method C	Residue	Method A	Method C
32-IL**S**PRKEGSR-42	S35	1.39	n.a	S35	-	-
216-ISDILIPA**S**AMK-227	S224	4.20	0.71	S224	4.55	1.33
215-KISDILIPA**S**AMK-227	S224	1.33	1.30	S224	n.a.	2
321-IKPDQSFNISTPSP APSNLITIQSR-346	One of: S327, S331, T332	0.91	1.70	-	-	-
874-NI**S**G**SSS**PSER-884	S876	n.a.	0.86	One of: S878 - S880	5.26	n.a.
997-LLGAGSTS**S** IPN**S**PR-1011	S1009	0.59	2.44	S1005, S1009	1.16	n.a.
995-VKLLGAGSTSS IPN**S**PR-1011	S1009	2.67	1.82	-	-	-
1025-IVPA**S**PDK SAVQR-1037	S1029	0.90	n.a.	S1029	5.55	8
1024-KIVPA**S**PDK SAVQR-1037	-	-	-	S1029	3.45	10.4

13 phosphorylation sites were detected in total. Residues S1005 and S1009 were shown to be phosphorylated previously, while the remaining 11 identified sites are novel (Table A1.3) (Wilson-Grady et al., 2008). Out of all the detected sites, majority does not appear to be either interphase- or mitosis-specific, especially when Method C is used for quantification. The only modification enriched in mitosis is serine 1029 phosphorylation.

Table A1.3. Mto1 phosphorylation sites detected in previously published studies. (Wilson-Grady et al., 2008)

Peptide 1	Residue 1	Residue 2
79-LHQNATAPTS**S**TPLQ**S**PDESVNK-91	S89	S94
79-LHQNATAPTS**S**TPLQSPDESVNK-91	S94	-
997-LLGAGSTS**S**IPN**S**PR-1011	S1005	S1009
997-LLGAGSTSSIPN**S**PR-1011	S1009	-

Potentially, differential phosphorylation of Mto1 might play a role in controlling the Mto1/2 complex (and therefore, the γ-TuC) localisation to distinct cytoplasmic MTOCs in interphase. Kinases and phosphatases localised to particular

MTOCs could influence the MT nucleation patterns by regulating the Mto1/2 complex localisation.

Serine 1029, found within the minimal consensus sequence of Cdk1, S/T-P (Nigg, 1993), lies within a region required for the Mto1-Myp2 interaction, which promotes Mto1 localisation to eMTOCs following cytokinesis (Samejima et al., 2010). Myp2, unconventional myosin II, associates with the contractile actomyosin ring during anaphase B (Wu et al., 2003). Perhaps, mitotic phosphorylation of S1029 residue might regulate the Mto1-Myp2 to interaction and prevent premature association between the Myp2 and Mto1 in the cytoplasm during earlier stages of mitosis, only allowing for the Mto1-Myp2 interaction to occur once Myp2 is localised to the contractile actomyosin ring and Mto1 is dephosphorylated. It would be interesting to see if the Mto1-Myp2 interaction is found in metaphase-arrested cells, and whether the Mto1-S1029A phosphomutant has any defects, such as pre-mature PAA formation, or nucleation of PAA MTs from sites different than eMTOCs.

Importantly, in this analysis only a subset of the total Mto1 pool was analysed, as only Mto2-bound Mto1 was co-immunoprecipitated. It is possible that free Mto1 (that is, Mto1 not bound to Mto2) displays a different phosphorylation than Mto2-bound Mto1. In order to fully analyse the differences between interphase and mitotic Mto1 phosphorylation, an anti-Mto1 immunoprecipitation experiment should be followed by SILAC. Potentially, an interesting experiment would be SILAC comparing free and Mto2-bound Mto1, which could suggest what phosphorylation events on Mto1 might be important for the regulation of Mto1-Mto2 interaction.

Appendix 2. $^{13}C_6{}^{15}N_4$-arginine conversion to other amino acids

Introduction

SILAC, a method developed in Matthias Mann's group (Ong et al., 2003, 2002), involves growing cells in either conventional "light" growth medium or in "heavy" growth medium in which some amino acids were replaced by their isotopically-labelled counterparts. Two different growth conditions allow for quantitative analysis, because heavy and light peptides can be distinguished in the MS spectra due to the higher molecular mass observed in heavy-labelled peptides (see also Section 5.1 and Fig. 5.1). Typically, heavy lysine and arginine are used for sample labelling in SILAC, because trypsin cleavage occurs after these two basic residues. Therefore, at least one heavy amino acid (either arginine or lysine) is present in each peptide after trypsin digestion.

Research performed in the Sawin lab provided a SILAC methodology suitable for fission yeast, allowing to use $^{13}C_6$-lysine and $^{13}C_6$-arginine (Bicho et al., 2010). However, there are other heavy labelled amino acids available, such as $^{13}C_6{}^{15}N_2$-lysine and $^{13}C_6{}^{15}N_4$-arginine. The advantage of using amino acids with higher number of heavy atoms is that the greater the difference in m/z between heavy vs. light peptides, the more separated these peptides are on a MS spectrum, making the quantification easier. For example, for a doubly charged peptide ($z=2^+$) containing one arginine residue, the m/z difference between heavy and light peptide will be 3 ($\Delta m/z=6/2$), if the heavy arginine is $^{13}C_6$-arginine, containing six more neutrons than its light counterpart. If the $^{13}C_6{}^{15}N_4$-arginine is used, the m/z difference will equal 5 ($\Delta m/z=10/2$), because $^{13}C_6{}^{15}N_4$-arginine contains 10 more neutrons than the light arginine.

During MS analysis presented in Chapter 5 I initially attempted to use $^{13}C_6{}^{15}N_4$-arginine and $^{13}C_6{}^{15}N_2$-lysine to label heavy, mitotic sample. However, MS analysis of the heavy-labelled samples revealed that $^{13}C_6{}^{15}N_4$-arginine is converted into other amino acids in yeast. I showed that the heavy-labelled carbon atoms do not get transferred into other amino acids, but the heavy nitrogen atoms do. We hypothesised that this occurs via Nitric Oxide Synthase (NOS) activity, and I attempted to find a gene encoding the fission yeast NOS. However, deletion of neither of the two candidate genes abolished the arginine conversion. More experiments should be performed to find the mechanism of $^{13}C_6{}^{15}N_4$-arginine

conversion in fission yeast and whether this occurs due to NOS activity as well as to find fission yeast NOS.

$^{13}C_6{}^{15}N_4$-arginine is converted into other amino acids

An Mto2-17A-GFP purified by anti-GFP immunoprecipitation from interphase culture grown in a heavy medium containing $^{13}C_6{}^{15}N_4$-arginine and $^{13}C_6{}^{15}N_2$-lysine resolved on 10% SDS-PAGE and Coomassie stained. The Mto2-17A-GFP band was excised, and in-gel trypsin digest followed by Stage-Tip purification was performed (Rappsilber et al., 2003). Resulting peptides were eluted from the Stage-Tip and Juan Zhou from the Rappsilber group carried out the MS analysis.

Surprisingly, an extensive conversion of labelled arginine into other amino acids was observed (Fig. A2.1). In this experiment, a genetic background was used that does not allow for a transfer of arginine carbon atoms into other amino acids, which suggested that the transfer of heavy nitrogen atoms caused the conversion (Bicho et al., 2010). To further confirm that the conversion is a result of transferring ^{15}N atoms onto other amino acids, different types of media were tested containing differently labelled arginine and lysine (Table A2.1). MS analysis of cell extracts confirmed that the arginine conversion occurred only when heavy-labelled nitrogen atoms were present in the arginine molecule. MS spectra showed that the arginine conversion results in formation of peptides that had a lower than expected m/z ratios, with the monoisotopic peak 3 Da lower than expected (Fig. A2.1). This suggests that some pool of arginine exchanges heavy labelled nitrogen atoms to unlabelled, resulting in formation of arginine molecules with only one nitrogen atom labelled. Potentially, the non-exchangeable nitrogen atom could form the α-amino group, while the exchangeable atoms could form the guanidinium group. Spectra showed also the presence of peptides that had a higher than expected m/z ratios, suggesting that some of the heavy nitrogen atoms removed from arginine molecules are built into other amino acids.

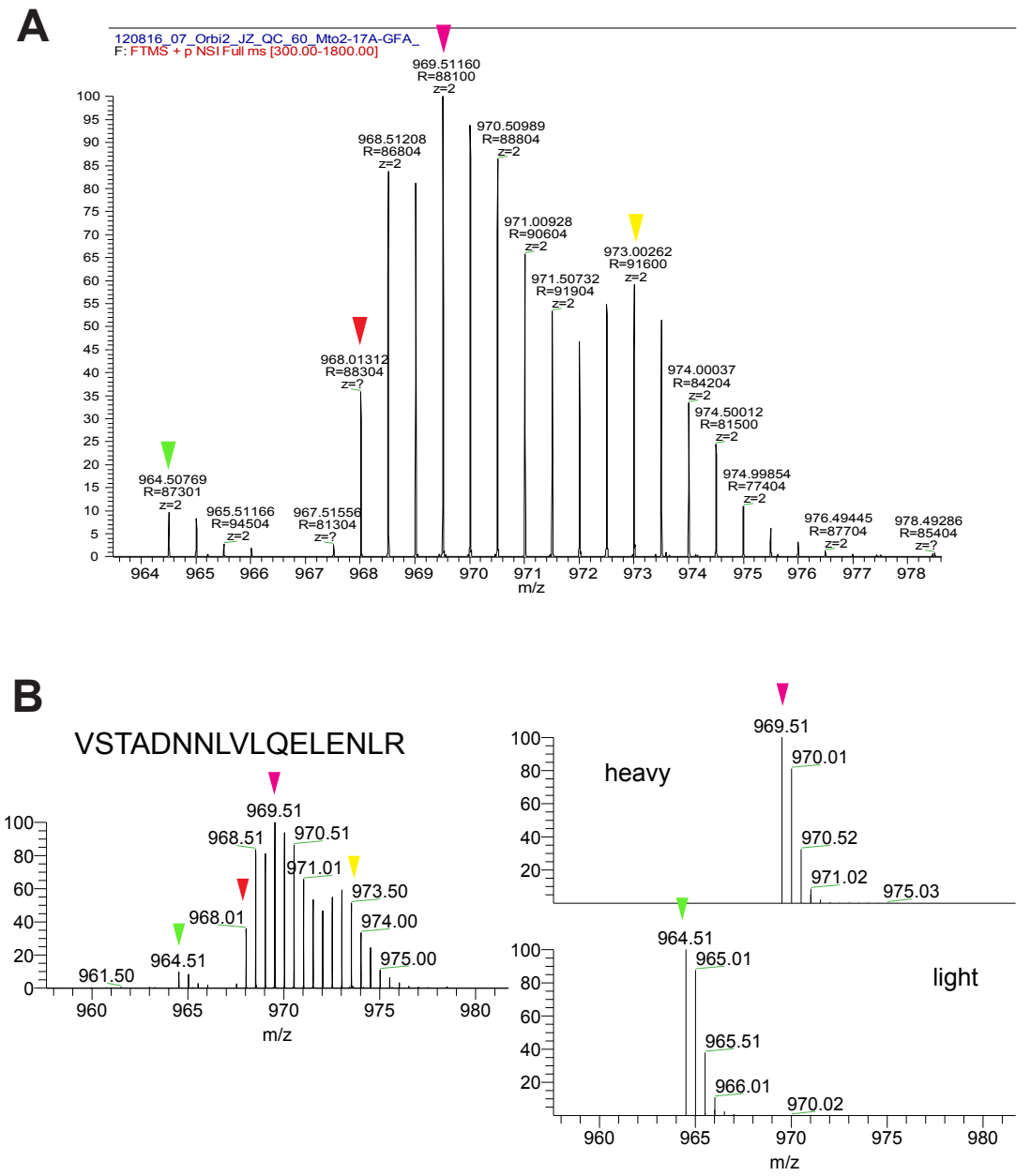

Figure A2.1. Arginine conversion.
(A) An example of a MS spectrum of a phosphopeptide VSTADNNLVLQELENLR. Raw data was analysed using XCalibur MS spectrum viewer to visualise precursor ion peaks. Isotope envelopes corresponding to both light (monoisotopic peak m/z=964.51, grean arrowhead) and heavy (monoisotopic peak m/z=969.51, magenta arrowhead) phosphorylated peptide are shown. Several other peaks are visible, with m/z higher (yellow arrowhead) and lower (red arrowhead) than the m/z of the heavy peptide.
(B) The same MS spectrum presented diffeerently. Here, the light and the heavy signal was extracted (right panel). All the peaks in the left panel that are not shown in the right panel originate from peptides that incorporated either not completely labeled arginine or other heavy labelled amino acids.

Table A2.1. Heavy-labelled amino acid conversion in fission yeast. [Strains: KS5042, KS7093]

Arginine	Lysine	Conversion?
light	light	no
light	$^{13}C_6{}^{15}N_2$	no
$^{13}C_6{}^{15}N_4$	light	yes
$^{13}C_6{}^{15}N_4$	$^{13}C_6{}^{15}N_2$	yes
$^{13}C_6$	$^{13}C_6$	no

Nitric Oxide Synthase (NOS) catalyses synthesis of nitric oxide (NO), a messenger molecule that plays important roles in many physiological processes (Tuteja et al., 2004). The substrate for this reaction is L-arginine (Fig. A2.2). Although the fission yeast NOS has never been identified, NO was shown to be a signalling molecule in *S. pombe*. Moreover, production of NO is inhibited in yeast extracts following treatment with a NOS inhibitor, L-NAME (Kig and Temizkan, 2009).

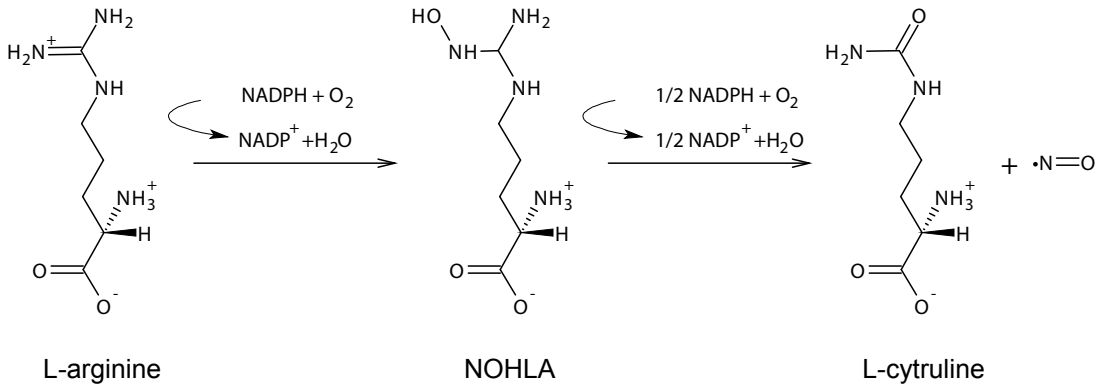

Figure A2.2. Nitric Oxide Synthase-catalysed reaction of NO synthesis from L-arginine. NO is made by NOS in two subsequent oxidation reactions. During the first oxigenation reaction, N^{ω}-hydroxy-L-arginine (NOHLA) is formed that is subsequently oxidised to L-citruline.

We hypothesized that the observed arginine conversion is a result of fission yeast NOS activity. To investigate if the arginine conversion was tested when the growth medium was supplemented with different concentrations of L-NAME (12 μM – 200 mM range was tested, data not shown). L-NAME presence in the growth media did not affect the conversion even at concentrations that were inhibiting growth (cells grew poorly at 120 mM and did not exit the lag phase at 200 mM). However, the fact that L-NAME did not inhibit arginine conversion does not rule out a possibility that the fission yeast NOS is responsible for this conversion. L-NAME

was never used in fission yeast and might not have been able to cross the cell wall. Moreover, to become an active inhibitor of NOS, L-NAME has to be hydrolysed by cellular esterases, a process that has never been shown to occur in yeast (Pfeiffer et al., 1996). Most likely, the hydrolysis step occurs *in vivo*, as the NO synthesis is inhibited by L-NAME in yeast extracts (Kig and Temizkan, 2009). Therefore, it is more likely that the first step (L-NAME import through the cell wall) might either not occur or not be sufficient to block the NO synthesis. In budding yeast, inhibition of NO synthesis was achieved by transient (1 h) incubation in growth medium with very high (200 mM) L-NAME concentration (Almeida et al., 2007).

Another way to address the hypothesis that the fission yeast NOS is responsible for the arginine conversion is to test whether the conversion occurs in the absence of NOS activity. To identify the fission yeast NOS, candidate genes were selected for analysis, and deletion strains were obtained from Bioneer fission yeast deletion strains collection. One of the NOS cofactors is flavin adenine dinucleotide (FAD), therefore two uncharacterised open reading frames (SPAC1783.01 and SPBC12C2.03c in the fission yeast genome) that contain FAD-binding regions were chosen for analysis. However, both individual and concurrent deletion of SPAC1783.01 and SPBC12C2.03c open reading frames did not prevent $^{13}C_6{}^{15}N_4$-arginine conversion. This suggests that the deleted genes do not encode for the fission yeast NOS or that it is not the (or the only) factor responsible for the conversion. Potentially, another fission yeast gene *ccr1* (SPBC29A10.01) could be the fission yeast NOS. Like human NOS, it contains several cofactor-binding regions and is able to bind FAD, NADPH and FMN, which is characteristic for NO synthases (Wang et al., 1997).

None of the performed experiments confirmed or disproved the hypothesis that the fission yeast NOS might be responsible for arginine conversion. Another method to address whether NO is made from heavy labelled arginine is to directly analyse the produced NO and show whether the nitrogen atom is ^{15}N or ^{14}N. The most commonly used method to measure NO concentration in a variety of biological samples is the Griess reaction (Fig. A2.3) (Sun et al., 2003). In this reaction, NO is converted to a nitrite ion that then reacts with sulphonamide and later with an azo dye. Resulting product is pink, and the test can be used both qualitatively and quantitatively. An experiment that would address $^{13}C_6{}^{15}N_4$-arginine is converted to NO would involve treating yeast extracts with the Griess reagent and then analysing the resulting reaction product by MS. A product that incorporated a heavy NO

molecule would have molecular mass one Da higher than a product that incorporated a light NO molecule. Appropriate controls would be yeast extracts made of cells grown in light media, as well as extracts of yeast grown in heavy media treated with L-NAME during extract preparation. Another reagent that could be used in a similar way (a chemical reaction followed by MS), is DAF-FM, a fluorescent dye used for NO detection (Mur et al., 2011).

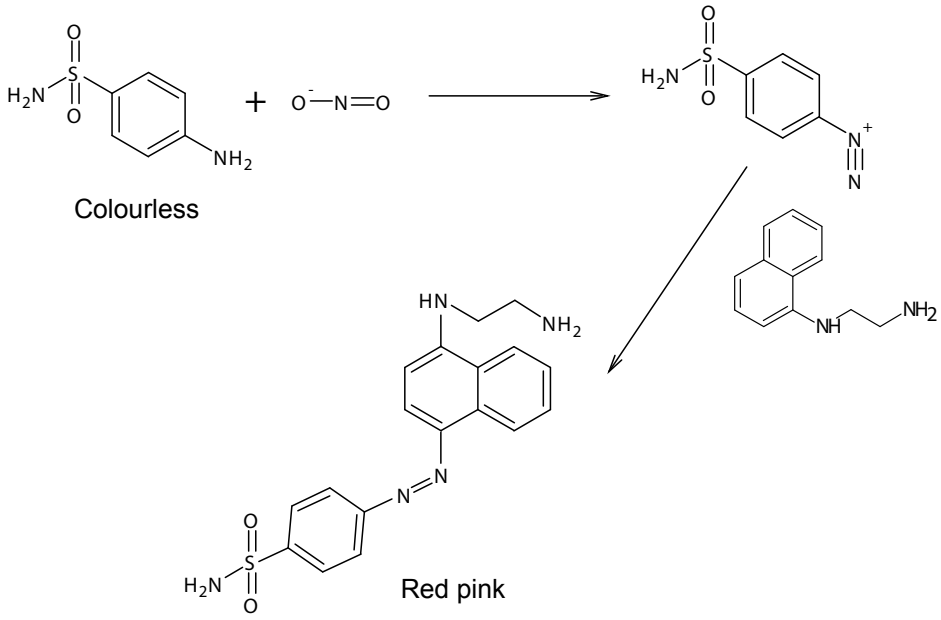

Figure A2.3. Griess test used to detect nitrite ions.
Nitrate ions are stable products of NO breakdown. In Griess reaction, the nitrite ion reacts with sulphonamide (shown) or sulfanilic acid to form a diazonium salt that later reacts with an azo dye. The second reaction gives a pink product.

The NOS hypothesis does not explain, however, why $^{13}C_6{}^{15}N_4$-arginine loses 3 heavy atoms (as shown in Fig A2.1). NOS activity should only remove one heavy nitrogen atom from the arginine molecule, leading to formation of citruline (Fig A2.2). It is known that arginine gets metabolised to ornithine by the action of two arginases Aru1 and Car1 (Fig. A2.4) (Davis, 1986). Ornithine can be reverted back into arginine in a 3-step enzymatic reaction catalysed by Arg3, Arg7 and Arg12 proteins. If a heavy arginine were converted to ornithine and then back to arginine, three of its heavy atoms would be replaced by light atoms, giving $^{13}C_5{}^{15}N_2$-arginine, which would be 3 Da lighter than $^{13}C_6{}^{15}N_4$-arginine. This is consistent with the observed loss of 3 Da in arginine-containing peptides (Fig. A2.1). To test the hypothesis that

this enzymatic pathway leads to $^{13}C_6{}^{15}N_4$-arginine conversion to other amino-acids, potential arginine conversion should be examined in *aru1*Δ *car1*Δ background.

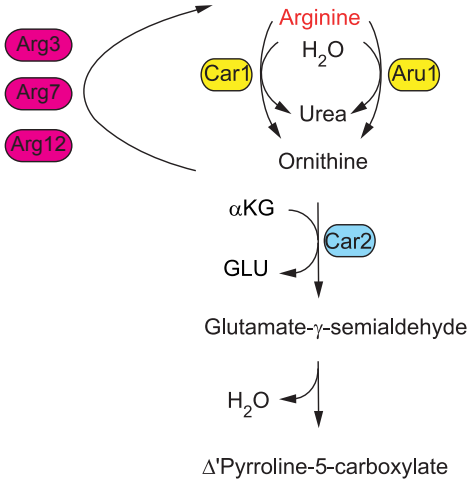

Figure A2.4. Argnine metabolism in yeast.
Metabolic pathways leading to conversion of arginine into other amino acids (adapted from Bicho et. al., 2010). In a first step, arginine is converted into ornithine by arginases encoded by genes aru1 and car1. Ornithine can be reverted back into arginine into arginine in a series of enxymatic reactions performed by Arg3, Arg7 and Arg12 proteins.

Appendix 3. Generation of anti-Pcp1 antibodies

During the course of this study, antibodies against Pcp1 were generated. Pcp1 was split into two equal fragments, Pcp1(1-604) and Pcp1(605-1208), and tagged with C-terminal His_6 tag by Gateway recombination (Busso et al., 2005) to allow purification and decrease protein solubility. The aim of the low protein solubility was to induce inclusion body formation in bacteria that would facilitate purification. Both Pcp1 fragments were then expressed, inclusion bodies were purified and the solubilised protein was purified on His-Bind Fractogel, and resolved on an SDS-PAGE gel. A band containing the protein was excised, lyophilised and ground to a fine powder, which was later used to immunise sheep. Two animals were used for each Pcp1 truncation (Table A3.1).

Table A3.1. Generation of anti-Pcp1 antibodies.

Pcp1 truncation	Animal
1-604	S188D
	S189D
605-1208	S191D
	S193D

The third and fourth bleed sera were tested against Pcp1 (Fig. A3.1). Each serum was tested against untagged and GFP-tagged Pcp1; the recognition of two bands of different molecular weights provided confirmation that the antibodies do not detect an unknown protein of a similar molecular weight to Pcp1. Western blot analysis revealed that sera from animals immunised with C-terminal part of Pcp1 (s191D, s193D) give a good signal to noise ratio, particularly at 1:1000 dilution. The antibody against Pcp1 N-terminus in the s188D serum did recognise Pcp1, however, the signal was fainter than in the case of s191D or s193D. Serum s189D gave a very high background signal, and Pcp1 bands were hardly visible.

The same was observed during the analysis of fourth bleed, however, s189D serum was not analysed given the high background signal observed in third bleed serum.

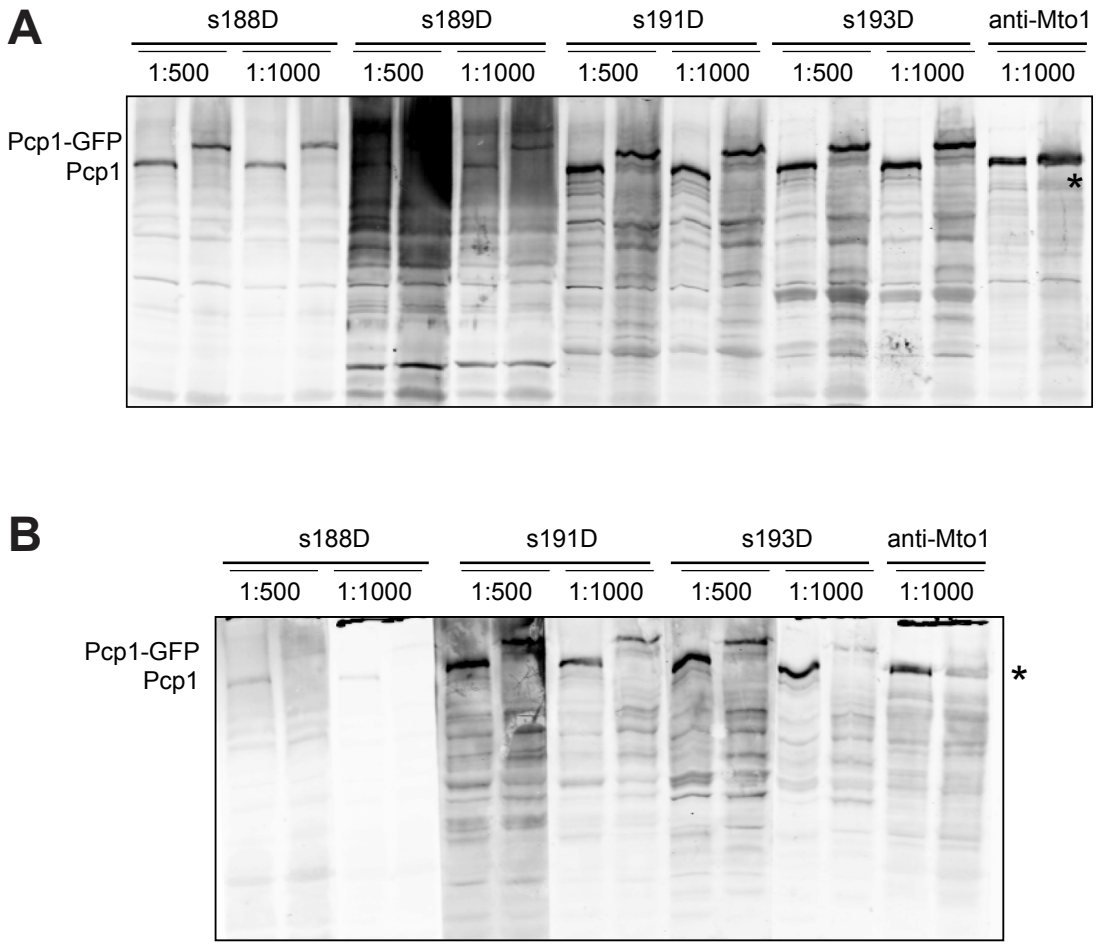

Figure A3.1. Testing of anti-Pcp1 antibodies
(A) Third bleed testing. Extracts from cells expressing untagged and GFP-tagged Pcp1 were analysed by western blot. Four anti-Pcp1 antibodies were tested at 1:500 and 1:1000 dilutions. Anto-Mto1 antibody was used as a control.
(B) Fourth bleed testing. Extracts from cells expressing untagged and GFP-tagged Pcp1 were analysed by western blot. Three anti-Pcp1 antibodies were tested at 1:500 and 1:1000 dilutions. Anto-Mto1 antibody was used as a control.
*- Mto1 detection was used to control western blotting conditions.

References

Aldaz, H., Rice, L.M., Stearns, T., and Agard, D. a (2005). Insights into microtubule nucleation from the crystal structure of human gamma-tubulin. Nature *435*, 523–527.

Almeida, B., Buttner, S., Ohlmeier, S., Silva, A., Mesquita, A., Sampaio-Marques, B., Osório, N.S., Kollau, A., Mayer, B., Leão, C., et al. (2007). NO-mediated apoptosis in yeast. J. Cell Sci. *120*, 3279–3288.

Alvarado-Kristensson, M., Rodríguez, M.J., Silió, V., Valpuesta, J.M., and Carrera, A.C. (2009). SADB phosphorylation of gamma-tubulin regulates centrosome duplication. Nat. Cell Biol. *11*, 1081–1092.

Ambrose, C., and Wasteneys, G.O. (2011). Cell edges accumulate gamma tubulin complex components and nucleate microtubules following cytokinesis in Arabidopsis thaliana. PLoS One *6*, e27423.

Anders, A., and Sawin, K.E. (2011). Microtubule stabilization in vivo by nucleation-incompetent γ-tubulin complex. J. Cell Sci. *124*, 1207–1213.

Anders, A., Lourenço, P.C.C., and Sawin, K.E. (2006). Noncore components of the fission yeast gamma-tubulin complex. Mol. Biol. Cell *17*, 5075–5093.

Andersen, J.S., Wilkinson, C.J., Mayor, T., Mortensen, P., Nigg, E.A., and Mann, M. (2003). Proteomic characterization of the human centrosome by protein correlation profiling. Nature *426*, 570–574.

Arnal, I., Karsenti, E., and Hyman, a a (2000). Structural transitions at microtubule ends correlate with their dynamic properties in Xenopus egg extracts. J. Cell Biol. *149*, 767–774.

Arvai, A.S., Bourne, Y., Hickey, M.J., and Tainer, J.A. (1995). Crystal structure of the human cell cycle protein CksHs1: single domain fold with similarity to kinase N-lobe domain. J. Mol. Biol. *249*, 835–842.

Ashkenazi, a, Presta, L.G., Marsters, S. a, Camerato, T.R., Rosenthal, K. a, Fendly, B.M., and Capon, D.J. (1990). Mapping the CD4 binding site for human immunodeficiency virus by alanine-scanning mutagenesis. Proc. Natl. Acad. Sci. U. S. A. *87*, 7150–7154.

Avidor-Reiss, T., and Gopalakrishnan, J. (2013). Building a centriole. Curr. Opin. Cell Biol. *25*, 72–77.

Baas, P.W. (2013). Microtubule stability in the axon: new answers to an old mystery. Neuron *78*, 3–5.

Bähler, J., and Pringle, J.R. (1998). Pom1p, a fission yeast protein kinase that provides positional information for both polarized growth and cytokinesis. Genes Dev. *12*, 1356–1370.

Bähler, J., Wu, J.Q., Longtine, M.S., Shah, N.G., McKenzie, a, Steever, a B., Wach, a, Philippsen, P., and Pringle, J.R. (1998). Heterologous modules for efficient and versatile PCR-based gene targeting in Schizosaccharomyces pombe. Yeast *14*, 943–951.

Bartolini, F., and Gundersen, G.G. (2006). Generation of noncentrosomal microtubule arrays. J. Cell Sci. *119*, 4155–4163.

Bettencourt-Dias, M., and Glover, D.M. (2007). Centrosome biogenesis and function: centrosomics brings new understanding. Nat. Rev. Mol. Cell Biol. *8*, 451–463.

Bicho, C.C., Alves, F.D.L., Chen, Z.A., Rappsilber, J., Sawin, K.E., and de Lima Alves, F. (2010). A genetic engineering solution to the “arginine conversion problem” in stable isotope labeling by amino acids in cell culture (SILAC). Mol. Cell. Proteomics *9*, 1567–1577.

Blom, N., Gammeltoft, S., and Brunak, S. (1999). Sequence and structure-based prediction of eukaryotic protein phosphorylation sites. J. Mol. Biol. *294*, 1351–1362.

Bond, J., Roberts, E., Springell, K., Lizarraga, S.B., Lizarraga, S., Scott, S., Higgins, J., Hampshire, D.J., Morrison, E.E., Leal, G.F., et al. (2005). A centrosomal mechanism involving CDK5RAP2 and CENPJ controls brain size. Nat. Genet. *37*, 353–355.

Bridge, a. J., Morphew, M., Bartlett, R., and Hagan, I.M. (1998). The fission yeast SPB component Cut12 links bipolar spindle formation to mitotic control. Genes Dev. *12*, 927–942.

Brune, C., Munchel, S.E., Fischer, N., Podtelejnikov, A. V, and Weis, K. (2005). Yeast poly(A)-binding protein Pab1 shuttles between the nucleus and the cytoplasm and functions in mRNA export. RNA *11*, 517–531.

Bugnard, E., Zaal, K.J.M., and Ralston, E. (2005). Reorganization of microtubule nucleation during muscle differentiation. Cell Motil. Cytoskeleton *60*, 1–13.

Burkhardt, J.K. (1998). The role of microtubule-based motor proteins in maintaining the structure and function of the Golgi complex. Biochim. Biophys. Acta *1404*, 113–126.

Burns, R.G. (1991). Alpha-, beta-, and gamma-tubulins: sequence comparisons and structural constraints. Cell Motil. Cytoskeleton *20*, 181–189.

Busso, D., Delagoutte-Busso, B., and Moras, D. (2005). Construction of a set Gateway-based destination vectors for high-throughput cloning and expression screening in Escherichia coli. Anal. Biochem. *343*, 313–321.

Cala, O., Remy, M.-H., Guillet, V., Merdes, A., Mourey, L., Milon, A., and Czaplicki, G. (2013). Virtual and biophysical screening targeting the γ-tubulin complex--a new target for the inhibition of microtubule nucleation. PLoS One *8*, e63908.

Caplow, M., Ruhlen, R.L., and Shanks, J. (1994). The free energy for hydrolysis of a microtubule-bound nucleotide triphosphate is near zero: all of the free energy for hydrolysis is stored in the microtubule lattice. J. Cell Biol. *127*, 779–788.

Caviston, J.P., and Holzbaur, E.L.F. (2006). Microtubule motors at the intersection of trafficking and transport. Trends Cell Biol. *16*, 530–537.

Ching, Y.P., Qi, Z., and Wang, J.H. (2000). Cloning of three novel neuronal Cdk5 activator binding proteins. Gene *242*, 285–294.

Choi, Y.-K., Liu, P., Sze, S.K., Dai, C., and Qi, R.Z. (2010). CDK5RAP2 stimulates microtubule nucleation by the gamma-tubulin ring complex. J. Cell Biol. *191*, 1089–1095.

Chrétien, D., and Wade, R.H. (1991). New data on the microtubule surface lattice. Biol. Cell *71*, 161–174.

Ciferri, C., Pasqualato, S., Screpanti, E., Varetti, G., Santaguida, S., Dos Reis, G., Maiolica, A., Polka, J., De Luca, J.G., De Wulf, P., et al. (2008). Implications for kinetochore-microtubule attachment from the structure of an engineered Ndc80 complex. Cell *133*, 427–439.

Cunningham, B.C., and Wells, J.A. (1989). High-resolution epitope mapping of hGH-receptor interactions by alanine-scanning mutagenesis. Science *244*, 1081–1085.

Daga, R.R., and Chang, F. (2005). Dynamic positioning of the fission yeast cell division plane. Proc. Natl. Acad. Sci. U. S. A. *102*, 8228–8232.

Davis, R.H. (1986). Compartmental and regulatory mechanisms in the arginine pathways of Neurospora crassa and Saccharomyces cerevisiae. Microbiol. Rev. *50*, 280–313.

Decottignies, a, Zarzov, P., and Nurse, P. (2001). In vivo localisation of fission yeast cyclin-dependent kinase cdc2p and cyclin B cdc13p during mitosis and meiosis. J. Cell Sci. *114*, 2627–2640.

Delattre, M., and Gönczy, P. (2004). The arithmetic of centrosome biogenesis. J. Cell Sci. *117*, 1619–1630.

Desai, a, and Mitchison, T.J. (1997). Microtubule polymerization dynamics. Annu. Rev. Cell Dev. Biol. *13*, 83–117.

Dhani, D.K., Goult, B.T., George, G.M., Rogerson, D.T., Bitton, D.A., Miller, C.J., Schwabe, J.W.R., and Tanaka, K. (2013). Mzt1/Tam4, a fission yeast MOZART1 homologue, is an essential component of the γ-tubulin complex and directly interacts with GCP3Alp6. Mol. Biol. Cell.

Dias, C.L., Ala-Nissila, T., Wong-ekkabut, J., Vattulainen, I., Grant, M., and Karttunen, M. (2010). The hydrophobic effect and its role in cold denaturation. Cryobiology *60*, 91–99.

Dimitrov, A., Quesnoit, M., Moutel, S., Cantaloube, I., Poüs, C., and Perez, F. (2008). Detection of GTP-tubulin conformation in vivo reveals a role for GTP remnants in microtubule rescues. Science *322*, 1353–1356.

Ding, R., West, R.R., Morphew, D.M., Oakley, B.R., and McIntosh, J.R. (1997). The spindle pole body of Schizosaccharomyces pombe enters and leaves the nuclear envelope as the cell cycle proceeds. Mol. Biol. Cell *8*, 1461–1479.

Dobbelaere, J., Josué, F., Suijkerbuijk, S., Baum, B., Tapon, N., and Raff, J. (2008). A genome-wide RNAi screen to dissect centriole duplication and centrosome maturation in Drosophila. PLoS Biol. *6*, e224.

Van Driessche, B., Tafforeau, L., Hentges, P., Carr, A.M., and Vandenhaute, J. (2005). Additional vectors for PCR-based gene tagging in Saccharomyces cerevisiae and Schizosaccharomyces pombe using nourseothricin resistance. Yeast *22*, 1061–1068.

Edelheit, O., Hanukoglu, I., Dascal, N., and Hanukoglu, A. (2011). Identification of the roles of conserved charged residues in the extracellular domain of an epithelial sodium channel (ENaC) subunit by alanine mutagenesis. AJP Ren. Physiol. *300*, F887–F897.

Efimov, A., Kharitonov, A., Efimova, N., Loncarek, J., Miller, P.M., Andreyeva, N., Gleeson, P., Galjart, N., Maia, A.R.R., McLeod, I.X., et al. (2007). Asymmetric CLASP-dependent nucleation of noncentrosomal microtubules at the trans-Golgi network. Dev. Cell *12*, 917–930.

Ehrhardt, D.W. (2008). Straighten up and fly right: microtubule dynamics and organization of non-centrosomal arrays in higher plants. Curr. Opin. Cell Biol. *20*, 107–116.

Erickson, H.P. (2000). Gamma-tubulin nucleation: template or protofilament? Nat. Cell Biol. *2*, E93–6.

Erickson, H.P., and Stoffler, D. (1996). Protofilaments and rings, two conformations of the tubulin family conserved from bacterial FtsZ to alpha/beta and gamma tubulin. J. Cell Biol. *135*, 5–8.

Erlemann, S., Neuner, A., Gombos, L., Gibeaux, R., Antony, C., and Schiebel, E. (2012). An extended γ-tubulin ring functions as a stable platform in microtubule nucleation. J. Cell Biol. *197*, 59–74.

Evans, L., Mitchison, T., and Kirschner, M. (1985). Influence of the centrosome on the structure of nucleated microtubules. J. Cell Biol. *100*, 1185–1191.

Fantes, P. (1979). Epistatic gene interactions in the control of division in fission yeast. Nature *279*, 428–430.

Feierbach, B., and Chang, F. (2001). Cytokinesis and the contractile ring in fission yeast. Curr. Opin. Microbiol. *4*, 713–719.

Ferenz, N.P., Gable, A., and Wadsworth, P. (2010). Mitotic functions of kinesin-5. Semin. Cell Dev. Biol. *21*, 255–259.

Fishel, E. a, and Dixit, R. (2013). Role of nucleation in cortical microtubule array organization: variations on a theme. Plant J. *75*, 270–277.

Flory, M.R., Moser, M.J., Monnat, R.J., and Davis, T.N. (2000). Identification of a human centrosomal calmodulin-binding protein that shares homology with pericentrin. Proc. Natl. Acad. Sci. U. S. A. *97*, 5919–5923.

Flory, M.R., Morphew, M., Joseph, J.D., Means, A.R., and Davis, T.N. (2002). Pcp1p, an Spc110p-related calmodulin target at the centrosome of the fission yeast Schizosaccharomyces pombe. Cell Growth Differ. *13*, 47–58.

Fong, C.S., Sato, M., and Toda, T. (2010). Fission yeast Pcp1 links polo kinase-mediated mitotic entry to gamma-tubulin-dependent spindle formation. EMBO J. *29*, 120–130.

Fong, K.-W., Choi, Y.-K., Rattner, J.B., and Qi, R.Z. (2008). CDK5RAP2 is a pericentriolar protein that functions in centrosomal attachment of the gamma-tubulin ring complex. Mol. Biol. Cell *19*, 115–125.

Fujita, A., Vardy, L., Garcia, M.A., and Toda, T. (2002). A fourth component of the fission yeast gamma-tubulin complex, Alp16, is required for cytoplasmic microtubule integrity and becomes indispensable when gamma-tubulin function is compromised. Mol. Biol. Cell *13*, 2360–2373.

Funaya, C., Samarasinghe, S., Pruggnaller, S., Ohta, M., Connolly, Y., Müller, J., Murakami, H., Grallert, A., Yamamoto, M., Smith, D., et al. (2012). Transient structure associated with the spindle pole body directs meiotic microtubule reorganization in S. pombe. Curr. Biol. *22*, 562–574.

Fygenson DK, Flyvbjerg, H., Sneppen, K., Libchaber, A., and Leibler, S. (1995). Spontaneous nucleation of microtubules. Phys. Rev. E. Stat. Phys. Plasmas. Fluids. Relat. Interdiscip. Topics *51*, 5058–5063.

Gadde, S., and Heald, R. (2004). Mechanisms and molecules of the mitotic spindle. Curr. Biol. *14*, R797–805.

García-Osta, A., Cuadrado-Tejedor, M., García-Barroso, C., Oyarzábal, J., and Franco, R. (2012). Phosphodiesterases as therapeutic targets for Alzheimer's disease. ACS Chem. Neurosci. *3*, 832–844.

Gardner, M.K., Charlebois, B.D., Jánosi, I.M., Howard, J., Hunt, A.J., and Odde, D.J. (2011). Rapid microtubule self-assembly kinetics. Cell *146*, 582–592.

Gardner, M.K., Zanic, M., and Howard, J. (2013). Microtubule catastrophe and rescue. Curr. Opin. Cell Biol. *25*, 14–22.

Gay, G., Courtheoux, T., Reyes, C., Tournier, S., and Gachet, Y. (2012). A stochastic model of kinetochore-microtubule attachment accurately describes fission yeast chromosome segregation. J. Cell Biol. *196*, 757–774.

Geiser, J.R., Sundberg, H.A., Chang, B.H., Muller, E.G., and Davis, T.N. (1993). The essential mitotic target of calmodulin is the 110-kilodalton component of the spindle pole body in Saccharomyces cerevisiae. Mol. Cell. Biol. *13*, 7913–7924.

Gibbs, C.S., and Zoller, M.J. (1991). Identification of electrostatic interactions that determine the phosphorylation site specificity of the cAMP-dependent protein kinase. Biochemistry *30*, 5329–5334.

Gibney, J., and Zheng, J.Q. (2003). Cytoskeletal dynamics underlying collateral membrane protrusions induced by neurotrophins in cultured Xenopus embryonic neurons. J. Neurobiol. *54*, 393–405.

Gillingham, a K., and Munro, S. (2000). The PACT domain, a conserved centrosomal targeting motif in the coiled-coil proteins AKAP450 and pericentrin. EMBO Rep. *1*, 524–529.

Goshima, G., and Kimura, A. (2010). New look inside the spindle: microtubule-dependent microtubule generation within the spindle. Curr. Opin. Cell Biol. *22*, 44–49.

Graser, S., Stierhof, Y.-D., and Nigg, E.A. (2007). Cep68 and Cep215 (Cdk5rap2) are required for centrosome cohesion. J. Cell Sci. *120*, 4321–4331.

Groocock PhD Thesis, L.M. (2010). PhD Thesis.

Gruhler, A., Olsen, J. V, Mohammed, S., Mortensen, P., Faergeman, N.J., Mann, M., and Jensen, O.N. (2005). Quantitative phosphoproteomics applied to the yeast pheromone signaling pathway. Mol. Cell. Proteomics *4*, 310–327.

Guerrero, C., Tagwerker, C., Kaiser, P., and Huang, L. (2006). An integrated mass spectrometry-based proteomic approach: quantitative analysis of tandem affinity-purified in vivo cross-linked protein complexes (QTAX) to decipher the 26 S proteasome-interacting network. Mol. Cell. Proteomics *5*, 366–378.

Guillet, V., Knibiehler, M., Gregory-Pauron, L., Remy, M.-H., Chemin, C., Raynaud-Messina, B., Bon, C., Kollman, J.M., Agard, D.A., Merdes, A., et al. (2011). Crystal structure of γ-tubulin complex protein GCP4 provides insight into microtubule nucleation. Nat. Struct. Mol. Biol. *18*, 915–919.

Gunawardane, R.N., Martin, O.C., and Zheng, Y. (2003). Characterization of a new gammaTuRC subunit with WD repeats. Mol. Biol. Cell *14*, 1017–1026.

Hagan, I.M. (1998). The fission yeast microtubule cytoskeleton. J. Cell Sci. *111 (Pt 1*, 1603–1612.

Hagan, I., and Yanagida, M. (1997). Evidence for cell cycle-specific, spindle pole body-mediated, nuclear positioning in the fission yeast Schizosaccharomyces pombe. J. Cell Sci. *110 (Pt 1*, 1851–1866.

Hagan, I.M., and Hyams, J.S. (1988). The use of cell division cycle mutants to investigate the control of microtubule distribution in the fission yeast Schizosaccharomyces pombe. J. Cell Sci. *89 (Pt 3)*, 343–357.

Haren, L., Remy, M.-H., Bazin, I., Callebaut, I., Wright, M., and Merdes, A. (2006). NEDD1-dependent recruitment of the gamma-tubulin ring complex to the centrosome is necessary for centriole duplication and spindle assembly. J. Cell Biol. *172*, 505–515.

Haren, L., Stearns, T., and Lüders, J. (2009). Plk1-dependent recruitment of gamma-tubulin complexes to mitotic centrosomes involves multiple PCM components. PLoS One *4*, e5976.

Hartley, J.L., Temple, G.F., and Brasch, M.A. (2000). DNA cloning using in vitro site-specific recombination. Genome Res. *10*, 1788–1795.

Hayashi, H., Kimura, K., and Kimura, A. (2012). Localized accumulation of tubulin during semi-open mitosis in the Caenorhabditis elegans embryo. Mol. Biol. Cell *23*, 1688–1699.

Hegemann, B., Hutchins, J.R. a, Hudecz, O., Novatchkova, M., Rameseder, J., Sykora, M.M., Liu, S., Mazanek, M., Lénárt, P., Hériché, J.-K., et al. (2011). Systematic phosphorylation analysis of human mitotic protein complexes. Sci. Signal. *4*, rs12.

Heitz, M.J., Petersen, J., Valovin, S., and Hagan, I.M. (2001). MTOC formation during mitotic exit in fission yeast. J. Cell Sci. *114*, 4521–4532.

Hentges, P., Van Driessche, B., Tafforeau, L., Vandenhaute, J., and Carr, A.M. (2005). Three novel antibiotic marker cassettes for gene disruption and marker switching in Schizosaccharomyces pombe. Yeast *2 i2*, 1013–1019.

Hiraoka, Y., Toda, T., and Yanagida, M. (1984). The NDA3 gene of fission yeast encodes beta-tubulin: a cold-sensitive nda3 mutation reversibly blocks spindle formation and chromosome movement in mitosis. Cell *39*, 349–358.

Höög, J.L., Schwartz, C., Noon, A.T., O'Toole, E.T., Mastronarde, D.N., McIntosh, J.R., and Antony, C. (2007). Organization of interphase microtubules in fission yeast analyzed by electron tomography. Dev. Cell *12*, 349–361.

Horio, T., Uzawa, S., Jung, M.K., Oakley, B.R., And, K.T., and Yanagida, M. (1991). The fission yeast y-tubulin is essential for mitosis and is localized at microtubule organizing centers. J. Cell Sci. *2*.

Hutchins, J.R.A., Toyoda, Y., Hegemann, B., Poser, I., Hériché, J.-K., Sykora, M.M., Augsburg, M., Hudecz, O., Buschhorn, B.A., Bulkescher, J., et al. (2010).

Systematic analysis of human protein complexes identifies chromosome segregation proteins. Science *328*, 593–599.

Hyman, a, Drechsel, D., Kellogg, D., Salser, S., Sawin, K., Steffen, P., Wordeman, L., and Mitchison, T. (1991). Preparation of modified tubulins. Methods Enzymol. *196*, 478–485.

Hyman, a a, Salser, S., Drechsel, D.N., Unwin, N., and Mitchison, T.J. (1992). Role of GTP hydrolysis in microtubule dynamics: information from a slowly hydrolyzable analogue, GMPCPP. Mol. Biol. Cell *3*, 1155–1167.

Izumi, N., Fumoto, K., Izumi, S., and Kikuchi, A. (2008). GSK-3beta regulates proper mitotic spindle formation in cooperation with a component of the gamma-tubulin ring complex, GCP5. J. Biol. Chem. *283*, 12981–12991.

Janski, N., Masoud, K., Batzenschlager, M., Herzog, E., Evrard, J.-L., Houlné, G., Bourge, M., Chabouté, M.-E., and Schmit, A.-C. (2012). The GCP3-interacting proteins GIP1 and GIP2 are required for γ-tubulin complex protein localization, spindle integrity, and chromosomal stability. Plant Cell *24*, 1171–1187.

Janson, M.E., Setty, T.G., Paoletti, A., and Tran, P.T. (2005). Efficient formation of bipolar microtubule bundles requires microtubule-bound gamma-tubulin complexes. J. Cell Biol. *169*, 297–308.

Janson, M.E., Loughlin, R., Loïodice, I., Fu, C., Brunner, D., Nédélec, F.J., and Tran, P.T. (2007). Crosslinkers and motors organize dynamic microtubules to form stable bipolar arrays in fission yeast. Cell *128*, 357–368.

Jaspersen, S.L., and Ghosh, S. (2012). Nuclear envelope insertion of spindle pole bodies and nuclear pore complexes. Nucleus *3*, 226–236.

Jaspersen, S.L., and Winey, M. (2004). The budding yeast spindle pole body: structure, duplication, and function. Annu. Rev. Cell Dev. Biol. *20*, 1–28.

Jiang, K., and Akhmanova, A. (2011). Microtubule tip-interacting proteins: a view from both ends. Curr. Opin. Cell Biol. *23*, 94–101.

Kamasaki, T., O'Toole, E., Kita, S., Osumi, M., Usukura, J., McIntosh, J.R., and Goshima, G. (2013). Augmin-dependent microtubule nucleation at microtubule walls in the spindle. J. Cell Biol. *202*, 25–33.

Keating, T.J., and Borisy, G.G. (2000). Immunostructural evidence for the template mechanism of microtubule nucleation. Nat. Cell Biol. *2*, 352–357.

Keck, J.M., Jones, M.H., Wong, C.C.L., Binkley, J., Chen, D., Jaspersen, S.L., Holinger, E.P., Xu, T., Niepel, M., Rout, M.P., et al. (2011). A cell cycle phosphoproteome of the yeast centrosome. Science *332*, 1557–1561.

Kettenbach, A.N., Schweppe, D.K., Faherty, B.K., Pechenick, D., Pletnev, A. a, and Gerber, S. a (2011). Quantitative phosphoproteomics identifies substrates and

functional modules of Aurora and Polo-like kinase activities in mitotic cells. Sci. Signal. *4*, rs5.

Khodjakov, A., and Rieder, C.L. (1999). The sudden recruitment of gamma-tubulin to the centrosome at the onset of mitosis and its dynamic exchange throughout the cell cycle, do not require microtubules. J. Cell Biol. *146*, 585–596.

Khodjakov, a, Cole, R.W., Oakley, B.R., and Rieder, C.L. (2000). Centrosome-independent mitotic spindle formation in vertebrates. Curr. Biol. *10*, 59–67.

Kig, C., and Temizkan, G. (2009). Nitric oxide as a signaling molecule in the fission yeast Schizosaccharomyces pombe. Protoplasma *238*, 59–66.

Kikkawa, M. (2013). Big steps toward understanding dynein. J. Cell Biol. *202*, 15–23.

Kim, J.S., and Raines, R.T. (1993). Ribonuclease S-peptide as a carrier in fusion proteins. Protein Sci. *2*, 348–356.

Kim, H.-K., Kang, J.-G., Yumura, S., Walsh, C.J., Cho, J.W., and Lee, J. (2005). De novo formation of basal bodies in Naegleria gruberi: regulation by phosphorylation. J. Cell Biol. *169*, 719–724.

Kim, S., Cho, H., Lee, D., and Webster, M.J. (2012). Association between SNPs and gene expression in multiple regions of the human brain. Transl. Psychiatry *2*, e113.

Kline-Smith, S.L., and Walczak, C.E. (2004). Mitotic spindle assembly and chromosome segregation: refocusing on microtubule dynamics. Mol. Cell *15*, 317–327.

Knop, M., and Schiebel, E. (1997). Spc98p and Spc97p of the yeast gamma-tubulin complex mediate binding to the spindle pole body via their interaction with Spc110p. EMBO J. *16*, 6985–6995.

Knop, M., and Schiebel, E. (1998). Receptors determine the cellular localization of a gamma-tubulin complex and thereby the site of microtubule formation. EMBO J. *17*, 3952–3967.

Knop, M., Pereira, G., and Schiebel, E. (1999). Microtubule organization by the budding yeast spindle pole body. Biol. Cell *91*, 291–304.

Kõivomägi, M., Valk, E., Venta, R., Iofik, A., Lepiku, M., Balog, E.R.M., Rubin, S.M., Morgan, D.O., and Loog, M. (2011). Cascades of multisite phosphorylation control Sic1 destruction at the onset of S phase. Nature *480*, 128–131.

Kollman, J.M., Polka, J.K., Zelter, A., Davis, T.N., and Agard, D. a (2010). Microtubule nucleating gamma-TuSC assembles structures with 13-fold microtubule-like symmetry. Nature *466*, 879–882.

Kollman, J.M., Merdes, A., Mourey, L., and Agard, D. a (2011). Microtubule nucleation by γ-tubulin complexes. Nat. Rev. Mol. Cell Biol. *12*, 709–721.

Kravit, N.G., Regula, C.S., and Berlin, R.D. (1984). A reevaluation of the structure of purified tubulin in solution: evidence for the prevalence of oligomers over dimers at room temperature. J. Cell Biol. *99*, 188–198.

Kumar, N., Goldminz, A.M., Kim, N., and Gottlieb, A.B. (2013). Phosphodiesterase 4-targeted treatments for autoimmune diseases. BMC Med. *11*, 96.

Landy, A. (1989). Dynamic, structural, and regulatory aspects of lambda site-specific recombination. Annu. Rev. Biochem. *58*, 913–949.

Langford, G.M. (1980). Arrangement of subunits in microtubules with 14 profilaments. J. Cell Biol. *87*, 521–526.

Lee, K., and Rhee, K. (2011). PLK1 phosphorylation of pericentrin initiates centrosome maturation at the onset of mitosis. J. Cell Biol. *195*, 1093–1101.

Leo, M., Santino, D., Tikhonenko, I., Magidson, V., Khodjakov, A., and Koonce, M.P. (2012). Rules of engagement: centrosome-nuclear connections in a closed mitotic system. Biol. Open *1*, 1111–1117.

Li, R., and Gundersen, G.G. (2008). Beyond polymer polarity: how the cytoskeleton builds a polarized cell. Nat. Rev. Mol. Cell Biol. *9*, 860–873.

Li, H., DeRosier, D.J., Nicholson, W. V, Nogales, E., and Downing, K.H. (2002). Microtubule structure at 8 A resolution. Structure *10*, 1317–1328.

Lin, T., Gombos, L., Neuner, A., Sebastian, D., Olsen, J. V, Hrle, A., Benda, C., and Schiebel, E. (2011). Phosphorylation of the yeast γ-tubulin Tub4 regulates microtubule function. PLoS One *6*, e19700.

Linding, R. (2003). GlobPlot: exploring protein sequences for globularity and disorder. Nucleic Acids Res. *31*, 3701–3708.

Löwe, J., Li, H., Downing, K.H., and Nogales, E. (2001). Refined structure of alpha beta-tubulin at 3.5 A resolution. J. Mol. Biol. *313*, 1045–1057.

Lüders, J., Patel, U.K., and Stearns, T. (2006). GCP-WD is a gamma-tubulin targeting factor required for centrosomal and chromatin-mediated microtubule nucleation. Nat. Cell Biol. *8*, 137–147.

Luduena, R.F., and Woodward, D.O. (1973). Isolation and partial characterization of alpha and beta-tubulin from outer doublets of sea-urchin sperm and microtubules of chick-embryo brain. Proc. Natl. Acad. Sci. U. S. A. *70*, 3594–3598.

Ludueńa, R.F., Shooter, E.M., and Wilson, L. (1977). Structure of the tubulin dimer. J. Biol. Chem. *252*, 7006–7014.

Lydersen, S., Fagerland, M.W., and Laake, P. (2009). Recommended tests for association in 2 x 2 tables. Stat. Med. *28*, 1159–1175.

Lynch, E.M., Groocock, L.M., Borek, W.E., and Sawin, K.E. (2013). Activation of the gamma-tubulin complex by the Mto1 / 2 complex. Revis.

Lynch PhD Thesis, E.M. (2012). PhD Thesis.

Mandelkow, E.M., Schultheiss, R., Rapp, R., Müller, M., and Mandelkow, E. (1986). On the surface lattice of microtubules: helix starts, protofilament number, seam, and handedness. J. Cell Biol. *102*, 1067–1073.

Mann, H.B., and Whitney, D.R. (1947). On a Test of Whether one of Two Random Variables is Stochastically Larger than the Other. Ann. Math. Stat. *18*, 50–60.

Masuda, H., Mori, R., Yukawa, M., and Toda, T. (2013). Fission yeast MOZART1/Mzt1 is an essential γ-tubulin complex component required for complex recruitment to the MTOC, but not its assembly. Mol. Biol. Cell.

Matsuyama, A., Shirai, A., Yashiroda, Y., Kamata, A., Horinouchi, S., and Yoshida, M. (2004). pDUAL, a multipurpose, multicopy vector capable of chromosomal integration in fission yeast. Yeast *21*, 1289–1305.

McEwen, B., and Edelstein, S.J. (1980). Evidence for a mixed lattice in microtubules reassembled in vitro. J. Mol. Biol. *139*, 123–145.

McIntosh, J.R., and O'Toole, E.T. (1999). Life cycles of yeast spindle pole bodies: getting microtubules into a closed nucleus. Biol. Cell *91*, 305–312.

Megraw, T.L., Li, K., Kao, L.R., and Kaufman, T.C. (1999). The centrosomin protein is required for centrosome assembly and function during cleavage in Drosophila. Development *126*, 2829–2839.

Michalski, J.M., Golden, G., Ikari, J., and Rennard, S.I. (2012). PDE4: a novel target in the treatment of chronic obstructive pulmonary disease. Clin. Pharmacol. Ther. *91*, 134–142.

Mitchison, J.M., and Nurse, P. (1985). Growth in cell length in the fission yeast Schizosaccharomyces pombe. J. Cell Sci. *75*, 357–376.

Mitchison, T., and Kirschner, M. (1984a). Dynamic instability of microtubule growth. Nature *312*, 237–242.

Mitchison, T., and Kirschner, M. (1984b). Microtubule assembly nucleated by isolated centrosomes. Nature *312*, 232–237.

Molina, H., Horn, D.M., Tang, N., Mathivanan, S., and Pandey, A. (2007). Global proteomic profiling of phosphopeptides using electron transfer dissociation tandem mass spectrometry. *104*, 2199–2204.

Moreno, S., Hayles, J., and Nurse, P. (1989). Regulation of p34cdc2 protein kinase during mitosis. Cell *58*, 361–372.

Moritz, M., Braunfeld, M.B., Guénebaut, V., Heuser, J., and Agard, D. a (2000). Structure of the gamma-tubulin ring complex: a template for microtubule nucleation. Nat. Cell Biol. *2*, 365–370.

Morrison, K.L., and Weiss, G. a (2001). Combinatorial alanine-scanning. Curr. Opin. Chem. Biol. *5*, 302–307.

Muller, E.G.D., Snydsman, B.E., Novik, I., Hailey, D.W., Gestaut, D.R., Niemann, C.A., O'Toole, E.T., Giddings, T.H., Sundin, B.A., and Davis, T.N. (2005). The organization of the core proteins of the yeast spindle pole body. Mol. Biol. Cell *16*, 3341–3352.

Mur, L. a J., Mandon, J., Cristescu, S.M., Harren, F.J.M., and Prats, E. (2011). Methods of nitric oxide detection in plants: a commentary. Plant Sci. *181*, 509–519.

Murata, T., and Hasebe, M. (2007). Microtubule-dependent microtubule nucleation in plant cells. J. Plant Res. *120*, 73–78.

Murata, T., Sonobe, S., Baskin, T.I., Hyodo, S., Hasezawa, S., Nagata, T., Horio, T., and Hasebe, M. (2005). Microtubule-dependent microtubule nucleation based on recruitment of gamma-tubulin in higher plants. Nat. Cell Biol. *7*, 961–968.

Nabeshima, K., Nakagawa, T., Straight, A.F., Murray, A., Chikashige, Y., Yamashita, Y.M., Hiraoka, Y., and Yanagida, M. (1998). Dynamics of centromeres during metaphase-anaphase transition in fission yeast: Dis1 is implicated in force balance in metaphase bipolar spindle. Mol. Biol. Cell *9*, 3211–3225.

Nakamura, M., Yagi, N., Kato, T., Fujita, S., Kawashima, N., Ehrhardt, D.W., and Hashimoto, T. (2012). Arabidopsis GCP3-interacting protein 1/MOZART 1 is an integral component of the γ-tubulin-containing microtubule nucleating complex. Plant J. *71*, 216–225.

Nash, P., Tang, X., Orlicky, S., Chen, Q., Gertler, F.B., Mendenhall, M.D., Sicheri, F., Pawson, T., and Tyers, M. (2001). Multisite phosphorylation of a CDK inhibitor sets a threshold for the onset of DNA replication. Nature *414*, 514–521.

Nigg, E.A. (1993). Cellular substrates of p34(cdc2) and its companion cyclin-dependent kinases. Trends Cell Biol. *3*, 296–301.

Nogales, E., Wolf, S.G., and Downing, K.H. (1998). Structure of the alpha beta tubulin dimer by electron crystallography. Nature *391*, 199–203.

Nogales, E., Whittaker, M., Milligan, R.A., and Downing, K.H. (1999). High-resolution model of the microtubule. Cell *96*, 79–88.

Nurse, P., Thuriaux, P., and Nasmyth, K. (1976). Genetic control of the cell division cycle in the fission yeast Schizosaccharomyces pombe. Mol. Gen. Genet. *146*, 167–178.

Oakley, C.E., and Oakley, B.R. (1989). Identification of gamma-tubulin, a new member of the tubulin superfamily encoded by mipA gene of Aspergillus nidulans. Nature *338*, 662–664.

Oegema, K., Wiese, C., Martin, O.C., Milligan, R.A., Iwamatsu, A., Mitchison, T.J., and Zheng, Y. (1999). Characterization of two related Drosophila gamma-tubulin complexes that differ in their ability to nucleate microtubules. J. Cell Biol. *144*, 721–733.

Ong, S., Kratchmarova, I., and Mann, M. (2003). Properties of 13C-substituted arginine in stable isotope labeling by amino acids in cell culture (SILAC). J. Proteome Res. *2*, 173–181.

Ong, S.-E., Blagoev, B., Kratchmarova, I., Kristensen, D.B., Steen, H., Pandey, A., and Mann, M. (2002). Stable isotope labeling by amino acids in cell culture, SILAC, as a simple and accurate approach to expression proteomics. Mol. Cell. Proteomics *1*, 376–386.

Oriolo, A.S., Wald, F.A., Canessa, G., and Salas, P.J.I. (2007). GCP6 binds to intermediate filaments: a novel function of keratins in the organization of microtubules in epithelial cells. Mol. Biol. Cell *18*, 781–794.

Overlack, N., Kilic, D., Bauss, K., Märker, T., Kremer, H., van Wijk, E., and Wolfrum, U. (2011). Direct interaction of the Usher syndrome 1G protein SANS and myomegalin in the retina. Biochim. Biophys. Acta *1813*, 1883–1892.

Pardo, M., and Nurse, P. (2003). Equatorial retention of the contractile actin ring by microtubules during cytokinesis. Science *300*, 1569–1574.

Pereira, G., Knop, M., and Schiebel, E. (1998). Spc98p directs the yeast gamma-tubulin complex into the nucleus and is subject to cell cycle-dependent phosphorylation on the nuclear side of the spindle pole body. Mol. Biol. Cell *9*, 775–793.

Petry, S., Groen, A.C., Ishihara, K., Mitchison, T.J., and Vale, R.D. (2013). Branching microtubule nucleation in Xenopus egg extracts mediated by augmin and TPX2. Cell *152*, 768–777.

Pfeiffer, S., Leopold, E., Schmidt, K., Brunner, F., and Mayer, B. (1996). Inhibition of nitric oxide synthesis by NG-nitro-L-arginine methyl ester (L-NAME): requirement for bioactivation to the free acid, NG-nitro-L-arginine. Br. J. Pharmacol. *118*, 1433–1440.

Piel, M., and Tran, P.T. (2009). Cell shape and cell division in fission yeast. Curr. Biol. *19*, R823–7.

Pierre, P., Scheel, J., Rickard, J.E., and Kreis, T.E. (1992). CLIP-170 links endocytic vesicles to microtubules. Cell *70*, 887–900.

Prokop, A. (2013). The intricate relationship between microtubules and their associated motor proteins during axon growth and maintenance. Neural Dev. *8*, 17.

Rajagopalan, S., Bimbo, A., Balasubramanian, M.K., and Oliferenko, S. (2004). A Potential Tension-Sensing Mechanism that Ensures Timely Anaphase Onset upon Metaphase Spindle Orientation. Curr. Biol. *14*, 69–74.

Rappsilber, J., Ishihama, Y., and Mann, M. (2003). Stop and go extraction tips for matrix-assisted laser desorption/ionization, nanoelectrospray, and LC/MS sample pretreatment in proteomics. Anal. Chem. *75*, 663–670.

Ravelli, R.B.G., Gigant, B., Curmi, P.A., Jourdain, I., Lachkar, S., Sobel, A., and Knossow, M. (2004). Insight into tubulin regulation from a complex with colchicine and a stathmin-like domain. Nature *428*, 198–202.

Remy, M.-H., Merdes, A., and Gregory-Pauron, L. (2013). Assembly of gamma-tubulin ring complexes: implications for cell biology and disease. (Copyright © 2013, Elsevier Inc. All Rights Reserved.).

Rice, L.M., Montabana, E. a, and Agard, D. a (2008). The lattice as allosteric effector: structural studies of alphabeta- and gamma-tubulin clarify the role of GTP in microtubule assembly. Proc. Natl. Acad. Sci. U. S. A. *105*, 5378–5383.

Roque, H., Ward, J.J., Murrells, L., Brunner, D., and Antony, C. (2010). The fission yeast XMAP215 homolog Dis1p is involved in microtubule bundle organization. PLoS One *5*, e14201.

Rosenberg PhD Thesis, J.A. (2007). PhD Thesis.

Rothbauer, U., Zolghadr, K., Muyldermans, S., Schepers, A., Cardoso, M.C., and Leonhardt, H. (2008). A versatile nanotrap for biochemical and functional studies with fluorescent fusion proteins. Mol. Cell. Proteomics *7*, 282–289.

Roubin, R., Acquaviva, C., Chevrier, V., Sedjaï, F., Zyss, D., Birnbaum, D., and Rosnet, O. (2013). Myomegalin is necessary for the formation of centrosomal and Golgi-derived microtubules. Biol. Open *2*, 238–250.

Samejima, I., Lourenço, P.C.C., Snaith, H.A., and Sawin, K.E. (2005). Fission yeast mto2p regulates microtubule nucleation by the centrosomin-related protein mto1p. Mol. Biol. Cell *16*, 3040–3051.

Samejima, I., Miller, V.J., Groocock, L.M., and Sawin, K.E. (2008). Two distinct regions of Mto1 are required for normal microtubule nucleation and efficient association with the gamma-tubulin complex in vivo. J. Cell Sci. *121*, 3971–3980.

Samejima, I., Miller, V.J., Rincon, S. a, and Sawin, K.E. (2010). Fission yeast Mto1 regulates diversity of cytoplasmic microtubule organizing centers. Curr. Biol. *20*, 1959–1965.

Sato, M., Okada, N., Kakui, Y., Yamamoto, M., Yoshida, M., and Toda, T. (2009). Nucleocytoplasmic transport of Alp7/TACC organizes spatiotemporal microtubule formation in fission yeast. EMBO Rep. *10*, 1161–1167.

Sawin, K.E. (2005). Meiosis: organizing microtubule organizers. Curr. Biol. *15*, R633–5.

Sawin, K.E., and Tran, P.T. (2006). Cytoplasmic microtubule organization in fission yeast. Yeast *23*, 1001–1014.

Sawin, K.E., Lourenco, P.C.C., and Snaith, H.A. (2004). Microtubule nucleation at non-spindle pole body microtubule-organizing centers requires fission yeast centrosomin-related protein mod20p. Curr. Biol. *14*, 763–775.

Schiebel, E. (2000). gamma-tubulin complexes: binding to the centrosome, regulation and microtubule nucleation. Curr. Opin. Cell Biol. *12*, 113–118.

Schwanhäusser, B., Gossen, M., Dittmar, G., and Selbach, M. (2009). Global analysis of cellular protein translation by pulsed SILAC. Proteomics *9*, 205–209.

Seltzer, V., Janski, N., Canaday, J., Herzog, E., Erhardt, M., Evrard, J.-L., and Schmit, A.-C. (2007). Arabidopsis GCP2 and GCP3 are part of a soluble gamma-tubulin complex and have nuclear envelope targeting domains. Plant J. *52*, 322–331.

Shapshak, P. (2012). Molecule of the month, PDE4DIP. Bioinformation *8*, 740–741.

Shimada, H., Kuboshima, M., Shiratori, T., Nabeya, Y., Takeuchi, A., Takagi, H., Nomura, F., Takiguchi, M., Ochiai, T., and Hiwasa, T. (2007). Serum anti-myomegalin antibodies in patients with esophageal squamous cell carcinoma. Int. J. Oncol. *30*, 97–103.

Singh, S., Springer, M., Steen, J., Kirschner, M.W., and Steen, H. (2009). FLEXIQuant: a novel tool for the absolute quantification of proteins, and the simultaneous identification and quantification of potentially modified peptides. J. Proteome Res. *8*, 2201–2210.

Snaith, H. a, and Sawin, K.E. (2003). Fission yeast mod5p regulates polarized growth through anchoring of tea1p at cell tips. Nature *423*, 647–651.

Snaith, H.A., Anders, A., Samejima, I., and Sawin, K.E. (2010). New and old reagents for fluorescent protein tagging of microtubules in fission yeast; experimental and critical evaluation. Methods Cell Biol. *97*, 147–172.

Soejima, H., Kawamoto, S., Akai, J., Miyoshi, O., Arai, Y., Morohka, T., Matsuo, S., Niikawa, N., Kimura, A., Okubo, K., et al. (2001). Isolation of novel heart-specific genes using the BodyMap database. Genomics *74*, 115–120.

Sohrmann, M., Fankhauser, C., Brodbeck, C., and Simanis, V. (1996). The dmf1/mid1 gene is essential for correct positioning of the division septum in fission yeast. Genes Dev. *10*, 2707–2719.

Soldati, T., and Schliwa, M. (2006). Powering membrane traffic in endocytosis and recycling. Nat. Rev. Mol. Cell Biol. *7*, 897–908.

Song, Y., Kirkpatrick, L.L., Schilling, A.B., Helseth, D.L., Chabot, N., Keillor, J.W., Johnson, G.V.W., and Brady, S.T. (2013). Transglutaminase and polyamination of tubulin: posttranslational modification for stabilizing axonal microtubules. Neuron *78*, 109–123.

Spiegelman, B.M., Penningroth, S.M., and Kirschner, M.W. (1977). Turnover of tubulin and the N site GTP in Chinese hamster ovary cells. Cell *12*, 587–600.

Srsen, V., Fant, X., Heald, R., Rabouille, C., and Merdes, A. (2009). Centrosome proteins form an insoluble perinuclear matrix during muscle cell differentiation. BMC Cell Biol. *10*, 28.

Stearns, T., Evans, L., and Kirschner, M. (1991). Gamma-tubulin is a highly conserved component of the centrosome. Cell *65*, 825–836.

Stiess, M., and Bradke, F. (2011). Neuronal polarization: the cytoskeleton leads the way. Dev. Neurobiol. *71*, 430–444.

Stiess, M., Maghelli, N., Kapitein, L.C., Gomis-Rüth, S., Wilsch-Bräuninger, M., Hoogenraad, C.C., Tolić-Nørrelykke, I.M., and Bradke, F. (2010). Axon extension occurs independently of centrosomal microtubule nucleation. Science *327*, 704–707.

Sun, J., Zhang, X., Broderick, M., and Fein, H. (2003). Measurement of Nitric Oxide Production in Biological Systems by Using Griess Reaction Assay. Sensors *3*, 276–284.

Syred, H.M., Welburn, J., Rappsilber, J., and Ohkura, H. (2013). Cell cycle regulation of microtubule interactomes: multi-layered regulation is critical for the interphase/mitosis transition. Mol. Cell. Proteomics.

Tagwerker, C., Zhang, H., Wang, X., Larsen, L.S.Z., Lathrop, R.H., Hatfield, G.W., Auer, B., Huang, L., and Kaiser, P. (2006). HB tag modules for PCR-based gene tagging and tandem affinity purification in Saccharomyces cerevisiae. Yeast *23*, 623–632.

Takahashi, M., Yamagiwa, A., Nishimura, T., Mukai, H., and Ono, Y. (2002). Centrosomal proteins CG-NAP and kendrin provide microtubule nucleation sites by anchoring gamma-tubulin ring complex. Mol. Biol. Cell *13*, 3235–3245.

Tasto, J.J., Carnahan, R.H., McDonald, W.H., and Gould, K.L. (2001). Vectors and gene targeting modules for tandem affinity purification in Schizosaccharomyces pombe. Yeast *18*, 657–662.

Tatebe, H., Goshima, G., Takeda, K., Nakagawa, T., Kinoshita, K., and Yanagida, M. (2001). Fission yeast living mitosis visualized by GFP-tagged gene products. Micron *32*, 67–74.

Teixidó-Travesa, N., Villén, J., Lacasa, C., Bertran, M.T., Archinti, M., Gygi, S.P., Caelles, C., Roig, J., and Lüders, J. (2010). The gammaTuRC revisited: a comparative analysis of interphase and mitotic human gammaTuRC redefines the

set of core components and identifies the novel subunit GCP8. Mol. Biol. Cell *21*, 3963–3972.

Teixidó-Travesa, N., Roig, J., and Lüders, J. (2012). The where, when and how of microtubule nucleation - one ring to rule them all. J. Cell Sci. *125*, 4445–4456.

La Terra, S., English, C.N., Hergert, P., McEwen, B.F., Sluder, G., and Khodjakov, A. (2005). The de novo centriole assembly pathway in HeLa cells: cell cycle progression and centriole assembly/maturation. J. Cell Biol. *168*, 713–722.

Thingholm, T.E., Jensen, O.N., and Larsen, M.R. (2009). Analytical strategies for phosphoproteomics. Proteomics *9*, 1451–1468.

Thuriaux, P., Sipiczki, M., and Fantes, P.A. (1980). Genetical analysis of a sterile mutant by protoplast fusion in the fission yeast Schizosaccharomyces pombe. J. Gen. Microbiol. *116*, 525–528.

Tilney, L.G., Bryan, J., Bush, D.J., Fujiwara, K., Mooseker, M.S., Murphy, D.B., and Snyder, D.H. (1973). Microtubules: evidence for 13 protofilaments. J. Cell Biol. *59*, 267–275.

Toda, T., Umesono, K., Hirata, A., and Yanagida, M. (1983). Cold-sensitive nuclear division arrest mutants of the fission yeast Schizosaccharomyces pombe. J. Mol. Biol. *168*, 251–270.

Tolić-Nørrelykke, I.M., Sacconi, L., Thon, G., and Pavone, F.S. (2004). Positioning and elongation of the fission yeast spindle by microtubule-based pushing. Curr. Biol. *14*, 1181–1186.

Tropini, C., Roth, E. a, Zanic, M., Gardner, M.K., and Howard, J. (2012). Islands containing slowly hydrolyzable GTP analogs promote microtubule rescues. PLoS One *7*, e30103.

Tuteja, N., Chandra, M., Tuteja, R., and Misra, M.K. (2004). Nitric Oxide as a Unique Bioactive Signaling Messenger in Physiology and Pathophysiology. J. Biomed. Biotechnol. *2004*, 227–237.

Uehara, R., Nozawa, R., Tomioka, A., Petry, S., Vale, R.D., Obuse, C., and Goshima, G. (2009). The augmin complex plays a critical role in spindle microtubule generation for mitotic progression and cytokinesis in human cells. Proc. Natl. Acad. Sci. U. S. A. *106*, 6998–7003.

Vale, R.D. (2003). The molecular motor toolbox for intracellular transport. Cell *112*, 467–480.

Vale, R.D., Schnapp, B.J., Reese, T.S., and Sheetz, M.P. (1985). Movement of organelles along filaments dissociated from the axoplasm of the squid giant axon. Cell *40*, 449–454.

Vardy, L., and Toda, T. (2000). The ® ssion yeast g -tubulin complex is required in G 1 phase and is a component of the spindle assembly checkpoint. EMBO J. *19*.

Venkatram, S., Tasto, J.J., Feoktistova, A., Jennings, J.L., Link, A.J., and Gould, K.L. (2004). Identification and characterization of two novel proteins affecting fission yeast gamma-tubulin complex function. Mol. Biol. Cell *15*, 2287–2301.

Venkatram, S., Jennings, J.L., Link, A., and Gould, K.L. (2005). Mto2p, a novel fission yeast protein required for cytoplasmic microtubule organization and anchoring of the cytokinetic actin ring. Mol. Biol. Cell *16*, 3052–3063.

Verde, I., Pahlke, G., Salanova, M., Zhang, G., Wang, S., Coletti, D., Onuffer, J., Jin, S.L., and Conti, M. (2001). Myomegalin is a novel protein of the golgi/centrosome that interacts with a cyclic nucleotide phosphodiesterase. J. Biol. Chem. *276*, 11189–11198.

Vérollet, C., Colombié, N., Daubon, T., Bourbon, H.-M., Wright, M., and Raynaud-Messina, B. (2006). Drosophila melanogaster gamma-TuRC is dispensable for targeting gamma-tubulin to the centrosome and microtubule nucleation. J. Cell Biol. *172*, 517–528.

Vinh, D.B.N., Kern, J.W., Hancock, W.O., Howard, J., and Davis, T.N. (2002). Reconstitution and characterization of budding yeast gamma-tubulin complex. Mol. Biol. Cell *13*, 1144–1157.

Vinogradova, T., Miller, P.M., and Kaverina, I. (2009). Microtubule network asymmetry in motile cells: role of Golgi-derived array. Cell Cycle *8*, 2168–2174.

Vogel, J., Drapkin, B., Oomen, J., Beach, D., Bloom, K., and Snyder, M. (2001). Phosphorylation of gamma-tubulin regulates microtubule organization in budding yeast. Dev. Cell *1*, 621–631.

Wade, R.H. (2007). Microtubules: an overview. Methods Mol. Med. *137*, 1–16.

Wade, R.H. (2009). On and around microtubules: an overview. Mol. Biotechnol. *43*, 177–191.

Wadsworth, P., Lee, W.-L., Murata, T., and Baskin, T.I. (2011). Variations on theme: spindle assembly in diverse cells. Protoplasma *248*, 439–446.

Wang, H., and Nogales, E. (2005). Nucleotide-dependent bending flexibility of tubulin regulates microtubule assembly. Nature *435*, 911–915.

Wang, M., Roberts, D.L., Paschke, R., Shea, T.M., Masters, B.S., and Kim, J.J. (1997). Three-dimensional structure of NADPH-cytochrome P450 reductase: prototype for FMN- and FAD-containing enzymes. Proc. Natl. Acad. Sci. U. S. A. *94*, 8411–8416.

Wang, X., Ching, Y.P., Lam, W.H., Qi, Z., Zhang, M., and Wang, J.H. (2000). Identification of a common protein association region in the neuronal Cdk5 activator. J. Biol. Chem. *275*, 31763–31769.

Wang, Z., Wu, T., Shi, L., Zhang, L., Zheng, W., Qu, J.Y., Niu, R., and Qi, R.Z. (2010). Conserved motif of CDK5RAP2 mediates its localization to centrosomes and the Golgi complex. J. Biol. Chem. *285*, 22658–22665.

Wasteneys, G.O., and Ambrose, J.C. (2009). Spatial organization of plant cortical microtubules: close encounters of the 2D kind. Trends Cell Biol. *19*, 62–71.

Weil, C.F., Oakley, C.E., and Oakley, B.R. (1986). Isolation of mip (microtubule-interacting protein) mutations of Aspergillus nidulans. Mol. Cell. Biol. *6*, 2963–2968.

Weisenberg, R. (1975). The role of nucleotides in microtubule assembly. Ann. N. Y. Acad. Sci. *253*, 573–576.

Weisenberg, R.C., and Deery, W.J. (1976). Role of nucleotide hydrolysis in microtubule assembly. Nature *263*, 792–793.

Weisenberg, R.C., Borisy, G.G., and Taylor, E.W. (1968). The colchicine-binding protein of mammalian brain and its relation to microtubules. Biochemistry *7*, 4466–4479.

Welburn, J.P.I. (2013). The molecular basis for kinesin functional specificity during mitosis. Cytoskeleton (Hoboken).

Widlund, P.O., Stear, J.H., Pozniakovsky, A., Zanic, M., Reber, S., Brouhard, G.J., Hyman, A. a, and Howard, J. (2011). XMAP215 polymerase activity is built by combining multiple tubulin-binding TOG domains and a basic lattice-binding region. Proc. Natl. Acad. Sci. U. S. A. *108*, 2741–2746.

Wilson-Grady, J.T., Villén, J., and Gygi, S.P. (2008). Phosphoproteome analysis of fission yeast. J. Proteome Res. *7*, 1088–1097.

Wittmann, T., Hyman, a, and Desai, a (2001). The spindle: a dynamic assembly of microtubules and motors. Nat. Cell Biol. *3*, E28–34.

Wu, J.-Q., Kuhn, J.R., Kovar, D.R., and Pollard, T.D. (2003). Spatial and temporal pathway for assembly and constriction of the contractile ring in fission yeast cytokinesis. Dev. Cell *5*, 723–734.

Xiong, Y., and Oakley, B.R. (2009). In vivo analysis of the functions of gamma-tubulin-complex proteins. J. Cell Sci. *122*, 4218–4227.

Zhang, J., and Megraw, T.L. (2007). Proper recruitment of gamma-tubulin and D-TACC/Msps to embryonic Drosophila centrosomes requires Centrosomin Motif 1. Mol. Biol. Cell *18*, 4037–4049.

Zhang, X., Liu, D., Lv, S., Wang, H., Zhong, X., Liu, B., Wang, B., Liao, J., Li, J., Pfeifer, G.P., et al. (2009). CDK5RAP2 is required for spindle checkpoint function. Cell Cycle *8*, 1206–1216.

Zheng, L., Schwartz, C., Wee, L., and Oliferenko, S. (2006). The fission yeast transforming acidic coiled coil-related protein Mia1p/Alp7p is required for formation

and maintenance of persistent microtubule-organizing centers at the nuclear envelope. Mol. Biol. Cell *17*, 2212–2222.

Zheng, Y., Jung, M.K., and Oakley, B.R. (1991). Gamma-tubulin is present in Drosophila melanogaster and Homo sapiens and is associated with the centrosome. Cell *65*, 817–823.

Zheng, Y., Wong, M.L., Alberts, B., and Mitchison, T. (1995). Nucleation of microtubule assembly by a gamma-tubulin-containing ring complex. Nature *378*, 578–583.

Zimmerman, S., and Chang, F. (2005). Effects of {gamma}-tubulin complex proteins on microtubule nucleation and catastrophe in fission yeast. Mol. Biol. Cell *16*, 2719–2733.

Zimmerman, W.C., Sillibourne, J., Rosa, J., and Doxsey, S.J. (2004). Mitosis-specific anchoring of gamma tubulin complexes by pericentrin controls spindle organization and mitotic entry. Mol. Biol. Cell *15*, 3642–3657.